

# **Structural Analysis of an Ultra-Light Drift Chamber in Composite Materials for High Energy Particle Physics experiments**

Thesis by  
Rakesh Rawat (s289828)

Submitted to the  
Department of Structural, Geotechnical and Building Engineering  
(DISEG)

in partial fulfillment of the  
Requirements for the Degree of  
Master of Science in Civil Engineering  
(Structures and Infrastructures)



**Politecnico  
di Torino**

Supervisor: Prof. Zavarise Giorgio  
Prof. Mauro Corrado  
Co-supervisor: Prof. Franco Grancagnolo

POLITECNICO DI TORINO  
Turin, Italy

July 2023

©2023  
Rakesh Rawat (s289828)  
All rights reserved.

The author hereby grants to Politecnico di torino permission to reproduce and to distribute publicly paper and electronic copies of this thesis document in whole or in part in any medium now known or hereafter created.

## THESIS CERTIFICATE

This is to undertake that the thesis titled *Structural analysis of an ultra-light drift chamber in composite materials for High Energy Particle Physics experiments* submitted to the Department of Structural, Geotechnical and Building Engineering, Politecnico di torino, for the award of Master of Science in Civil Engineering (Structures and Infrastructures), is a bona fide record of the research work done by me under the supervision of Prof.Zavarise Giorgio, Prof.Mauro Corrado and Prof.Franco Grancagnolo. The contents of this thesis, in full or in parts, have not been submitted to any other Institute or University for the award of any degree or diploma.

Signature of the Author: \_\_\_\_\_

Rakesh Rawat  
s289828

Certified by: \_\_\_\_\_

Prof.Zavarise Giorgio	Prof.Mauro Corrado	Prof.Franco Grancagnolo
DISEG, Polito	DISEG, Polito	INFN, Italy

Accepted by: \_\_\_\_\_

# Abstract

Scientists will probably never know how big the universe is, but they are certainly very close to knowing how small the universe can be. Subatomic particles, which are the building blocks of the universe, have captivated physicists ever since the discovery of electrons by J.J. Thomson in 1897 (Nobel Prize, 1906). The discovery of these subatomic particles is made possible by a very precise and sensitive instrument called particle detectors. Their significance lies in their ability to detect and measure the properties of subatomic particles such as electrons, protons, neutrons, muons, and kaons, which are the fundamental constituents of the universe.

This thesis focuses on the design and analysis of the Ultra-light IDEA (Innovative Detector for Electron-positron Accelerator) drift chamber used in high-energy particle physics experiments. The aim of the thesis is to reduce the total deformation of the spokes that support the load from the 343,968 anodic and cathodic wires contributing to 10 tonnes of total load. Our goal is to reduce the total deformation from 2000 mm to a virtually imperceptible margin close to 0 mm (by 10,000 folds). The significance of this pursuit lies in the fact that failure in determining the position of the anodic wire means failure in determining the position of charged particles in space. On the other hand, the mass of the drift chamber must be kept to a minimum. If this were merely a structural design problem, it could have been solved effortlessly in a relatively short span of time. However, the ultimate goal of particle detection increases the complexity of the problem from being comically trivial to dauntingly enigmatic.

To achieve this goal, the thesis presents a novel concept of monolithic equivalent orthotropic material that significantly reduces simulation time by 360 folds. The thesis then attacks the problem from lesser known classical statistical concepts such as response surface methodology providing the groundwork for design exploration and the creation of meta-models. These meta-models are then used to perform multi modal optimization of mass and total deformation. When the total deformation of the spokes could not be further decreased, a cable prestressing is used. The cable prestressing is solved using metaheuristic algorithms such as Evolutionary algorithms where a 15 dimensions highly nonlinear optimization problem is solved. Additionally, to test and validate the simplifications adopted in the design procedure, a series of hypothesis testing is performed on the numerical model. A layered composite design is then presented, satisfying both the criteria from particle physics and the structural perspective. An cursory meso-scale failure study is conducted to investigate any failures or delaminations of the ply. Finally, a linear and nonlinear buckling analysis is done and buckling modes such as ovalization are discussed.

# Dedication

To all those brilliant minds working in Particle physics experiment who have traded suffering for awe, who have lost their grip and slipped into magnificence, for whom beauty is suffering. I have had this rare privilege to work with Professor Franco Grancagnolo, Professor Zavarise Giorgio and Professor Mauro Corrado on a year long journey on this indescribably beautiful problem. It was a year long very personal battle i was engaged in and i enjoyed every moment of it, however hard it was.

To my mother. To my brother. To Nivida, *noor* of my eyes.

# Acknowledgements

I would like to express my sincere appreciation to Professor Franco Grancagnolo and Istituto Nazionale di Fisica Nucleare (INFN) for granting me the opportunity to work on this problem. I extend my gratitude to the entire Enginsoft team for their invaluable assistance, with special thanks to Marco Spagnolo for his unwavering support. I am grateful to Professor Giuseppe Carlo Marano and Ph.D. student Marco Martino Rosso for their guidance and inspiration during the initial stages, which led me to discover my passion for structural engineering. Additionally, I would like to acknowledge the contributions of Professor Giulio Ventura and Professor Alberto Carpenteri for their inspiring lectures. My sincere appreciation also goes to Professor Anna Pandolfi and Professor Roberto Fedele for providing me with the opportunity to learn from them during the single Ph.D. courses.

I am filled with gratitude towards Professor Mauro Corrado, who not only imparted valuable knowledge but also taught me the art of conquering seemingly insurmountable challenges. His guidance and mentorship have been invaluable in shaping my approach to problem-solving.

Professor Zavarise Giorgio has been a guardian figure throughout my journey, displaying genuine care and deep concern for both me and my research. I am forever indebted to the unwavering support and encouragement he provided me along the way. His presence has been a constant source of inspiration, instilling in me the confidence to overcome obstacles and pursue excellence.

Lastly, I want to thank Politecnico di Torino. One of the striking features of the universities in Italy is inclusion and its contribution to creating an equal and just world. With minimum or no tuition fees, students like me from one of the world's poorest countries have been given the platform as richer ones, to ventilate our thoughts and ideas. It has ensured that students like me have strength and hope, who otherwise have had no future at all. It has guaranteed equal opportunities for those that have been denied opportunities in the past in their nation for decades. I believe that any university owes two fundamental things to its students: firstly, knowledge, research, and discovery—the answers; and secondly, the ability to question the very foundations and challenge them because "certainty is an illusion." I am confident that my experience at Politecnico di Torino has filled me with knowledge and also with doubt and invigorate me for the restless pursuit of truth.

# Contents

<b>1</b>	<b>Problem Statement</b>	<b>23</b>
1.1	Introduction to Particle detector . . . . .	23
1.2	Introduction to Drift Chambers . . . . .	26
1.3	IDEA drift chamber . . . . .	28
1.3.1	Design Aspects . . . . .	29
1.3.2	Goals and Objectives . . . . .	30
1.4	Organization of the Thesis . . . . .	31
<b>2</b>	<b>Preliminary Design: Development of a Finite Element Model</b>	<b>32</b>
2.0.1	Mathematical models and Numerical simulations . . . . .	33
2.0.2	Finite Element Method : Basic Idea and Features . . . . .	35
2.0.3	Variational Principles . . . . .	37
2.1	Problem Simplification and challenges . . . . .	40
2.2	Hypothesis Formulation . . . . .	42
2.3	IDEA Drift chamber: Loads and Criteria . . . . .	43
2.4	Initial Concept of the IDEA drift chamber . . . . .	45
2.5	Development of the Numerical Model . . . . .	48
2.5.1	Engineering Data . . . . .	49
2.5.2	Geometry . . . . .	50
2.5.3	Model Setup . . . . .	55
2.5.4	Analysis . . . . .	61
2.5.5	Solution Procedures and Algorithms . . . . .	64
2.6	Geometrical Nonlinearities . . . . .	68
2.7	Analysis of Cyclic symmetric structures . . . . .	70
2.8	Numerically Accurate Results . . . . .	74
2.8.1	Mesh Independent solution . . . . .	74
2.8.2	3D element shape and order . . . . .	76
2.8.3	Artificially high stresses . . . . .	77
2.8.4	Accurate Surface Stress Using Surface Coating . . . . .	78
2.8.5	Adaptive convergence . . . . .	78
2.8.6	Mesh Size : Parametric Study . . . . .	79
2.9	Results, Validity and Insights . . . . .	84
2.9.1	Linear Analysis . . . . .	84
2.9.2	Nonlinear Analysis . . . . .	85

## CONTENTS

---

2.9.3	Validation . . . . .	89
2.9.4	Conclusions . . . . .	90
<b>3</b>	<b>Preliminary Design Exploration: A statistical Approach</b>	<b>91</b>
3.1	Design Exploration:A Parametric Study . . . . .	92
3.1.1	Design of Experiments and Response surface Methodology . . . . .	94
3.2	Initial simulation : Base Model . . . . .	97
3.3	Identifying the design candidates . . . . .	99
3.4	Sample generation . . . . .	99
3.5	Running the simulation . . . . .	103
3.6	Methodology . . . . .	104
3.7	Sensitivity Analysis . . . . .	105
3.8	Results from the Sensitivity Analysis . . . . .	107
3.8.1	CoP Matrix . . . . .	107
3.8.2	Linear Correlation Matrix . . . . .	108
3.8.3	Best design from the Sensitivity Analysis . . . . .	109
3.9	Kriging Response Surface Methodology . . . . .	110
3.10	Creation of the Metamodels and Multi-objective optimization . . . . .	117
3.10.1	Creation of the Metamodels . . . . .	117
3.10.2	Optimization of the Metamodels . . . . .	122
3.11	Limitations from Linear Buckling Analysis . . . . .	125
3.11.1	Output from the Adaptive Metamodel of Optimal Prognosis(AMOP) . . . . .	127
3.11.2	Optimization of the Metamodel . . . . .	131
3.12	Use of Epoxy Carbon Unidirectional Prepeg . . . . .	133
3.13	Conclusions . . . . .	135
<b>4</b>	<b>Hypothesis Testing and Model Calibration</b>	<b>138</b>
4.1	Monolithic Equivalent Orthotropic Material . . . . .	139
4.2	Layered Composite Material . . . . .	139
4.3	Validation of the Monolithic design with Layered composite design at $0^\circ$ . . . . .	140
4.3.1	Validity of the Total deformation results . . . . .	140
4.3.2	Validity of the Buckling loads . . . . .	141
4.3.3	Mass of the system . . . . .	141
4.4	Calibration of the Layered composite design . . . . .	142
4.5	Validation of the Monolithic design with Layered composite design at [0/0/90/0/90] . . . . .	146
4.6	Conclusion . . . . .	149
<b>5</b>	<b>Preliminary Design Exploration: A metaheuristic Approach</b>	<b>151</b>
5.1	Optimization Techniques . . . . .	151
5.1.1	Constrained optimization . . . . .	153
5.1.2	Necessary and sufficient conditions for a non-linearly constrained minimum . . . . .	154
5.1.3	Non-linearly constrained minimization . . . . .	156
5.2	Optimization Algorithms . . . . .	157



## CONTENTS

---

5.2.1	Non-Linear Programming by Quadratic Lagrangian . . . . .	157
5.2.2	Evolutionary Algorithms . . . . .	162
5.3	Genetic Algorithms . . . . .	164
5.3.1	Implementation Technique . . . . .	165
5.3.2	Selection options . . . . .	169
5.3.3	Recombination . . . . .	170
5.4	Methodology . . . . .	170
5.5	Conclusion . . . . .	187
<b>6</b>	<b>Layered Composite Design</b>	<b>189</b>
6.1	Introduction . . . . .	189
6.2	Need of composite material in particle detector systems . . . . .	191
6.3	Historical Development of Composites . . . . .	193
6.4	Use of composite from Mechanical point of view . . . . .	194
6.5	Fibres and Matrix . . . . .	198
6.6	Physical Properties of Composite materials . . . . .	200
6.7	Macromechanical Analysis of composite lamina . . . . .	202
6.8	Hooke's law for Anisotropic, Orthotropic and Transverly isotropic material	205
6.9	Hooke's Law for a Two-Dimensional Unidirectional Lamina: Plane stress Assumption . . . . .	209
6.10	Hooke's Law for a Two-Dimensional Angle Lamina . . . . .	211
6.11	Micromechanical Analysis of Composites . . . . .	212
6.12	Design of composite . . . . .	216
6.13	Numerical modelling of composite structures: Micro, Macro and Meso level Approach . . . . .	220
6.13.1	ANSYS Composite PrepPost Workflows . . . . .	221
6.13.2	Implementation in Workbench . . . . .	222
6.14	Methodology . . . . .	224
6.14.1	Geometry creation in SpaceClaim . . . . .	224
6.14.2	Meshing in ANSYS Mechanical . . . . .	225
6.14.3	Layered Composite definition in ANSYS Composite PrepPost (ACP)	226
6.14.4	Exporting Model to Static Structural . . . . .	236
<b>7</b>	<b>Structural Analysis: A Macro Scale Approach</b>	<b>237</b>
7.1	Contact kinematics . . . . .	237
7.1.1	Location of contact detection . . . . .	238
7.1.2	Penetration . . . . .	239
7.1.3	Pinball Algorithm . . . . .	241
7.1.4	Contact Algorithms . . . . .	241
7.1.5	MPC184 - Multipoint Constraint . . . . .	243
7.2	Defining contacts . . . . .	243
7.3	Application of Pressure . . . . .	245
7.4	Application of Prestress on Cable elements . . . . .	246
7.5	Boundary condition . . . . .	247
7.6	Results . . . . .	247

## CONTENTS

---

7.6.1	Total deformation of the drift chamber with the edge of the outer cylinders fixed . . . . .	247
7.6.2	Total deformation of the drift chamber with the face of the outer cylinders fixed . . . . .	250
7.7	Conclusion . . . . .	252
<b>8</b>	<b>Failure Analysis of Composites</b>	<b>253</b>
8.1	Failure criterion . . . . .	253
8.1.1	Maximum strain criterion . . . . .	254
8.1.2	Maximum stress criterion . . . . .	254
8.1.3	Quadratic Failure Criteria . . . . .	254
8.2	Tsai-Wu Failure Criterion . . . . .	255
8.3	Tsai-Hill Failure Criterion . . . . .	257
8.4	Hoffman failure criterion . . . . .	258
8.5	Reserve factor . . . . .	259
8.6	Weighting Factors . . . . .	260
8.7	Results from the failure analysis . . . . .	260
8.7.1	Results: Inverse Reserve factor . . . . .	261
8.7.2	Results: Safety margin . . . . .	263
8.7.3	Results: Safety factor . . . . .	264
8.7.4	Results: Stress Analysis . . . . .	264
8.8	Conclusion . . . . .	268
<b>9</b>	<b>Buckling Analysis</b>	<b>269</b>
9.1	Introduction . . . . .	269
9.2	Linear Buckling Theory . . . . .	271
9.2.1	Results from Linear Buckling Analysis . . . . .	272
9.2.2	Ovalization . . . . .	276
9.3	Non linear Buckling Analysis . . . . .	279
9.3.1	Applying Load Increments . . . . .	280
9.3.2	Automatic Time Stepping . . . . .	280
9.3.3	Unconverged Solution . . . . .	280
9.3.4	Performing a Nonlinear Buckling Analysis . . . . .	281
9.3.5	Performing a Post-Buckling Analysis . . . . .	282
9.4	Results from Nonlinear buckling analysis . . . . .	284
9.5	Conclusion . . . . .	287
<b>10</b>	<b>Conclusions</b>	<b>288</b>

# List of Figures

1.1	Discovery of the positron by C.D. Anderson in 1932 by analyzing the condensation trail of a positively charged particle yet far less massive than proton [3]. Paul Dirac had predicted the existence of such antiparticle in 1932. . . . .	24
1.2	Quarks have spin 1/2, and must obey the Pauli exclusion principle hence cannot exist in identical states. So with three strange quarks, the property which distinguishes them must be capable of at least three distinct values. Discovery of the Omega baryon $\Omega^-$ validated the Quark model which predicted its existence[4]. . . . .	25
1.3	Schematic of the drift chamber. The cathode drift wires carry non uniform voltage whereas the field wires maintain an equipotential lines linear . Adapted from <i>William R Leo. Techniques for nuclear and particle physics experiments: a how-to approach. Springer Science Business Media, 2012 [7]</i> . . . . .	26
1.4	As the electrons moves towards anode from much smaller electric field to a very large electric field around anode region, with a velocity proportional to electric field applied, an avalanche is created. Such large gas amplification is obtained by using anode of very thin wires of the orders 20-100 $\mu\text{m}$ . Adapted from <i>Hermann Kolanoski and Norbert Wermes. Particle Detectors: Fundamentals and Applications. Oxford University Press, USA, 2020 [2]</i> . . . . .	27
1.5	Cylindrical drift chamber with cathode and anode wires parallel to magnetic field. Subsequently, the cut out shows the arrangement of drift cells. The electric field is then perpendicular to the magnetic field ( $\vec{E} \perp \vec{B}$ ). Adapted from <i>Hermann Kolanoski and Norbert Wermes. Particle Detectors: Fundamentals and Applications. Oxford University Press, USA, 2020 [2]</i> . . . . .	28
1.6	Schematic diagram of the IDEA detector Adapted from <i>Walaa Elmetenawee, Alessandro Corvaglia, Federica Cuna, Nicola De Filippis, Edoardo Gorini, Francesco Grancagnolo, Marcello Maggi, Alessandro Miccoli, Marco Panareo, Margherita Primavera, et al. The tracking performance for the idea drift chamber. arXiv preprint arXiv:2211.12568, 2022[8]</i> . . . . .	29

## LIST OF FIGURES

---

2.1	Schematic diagram of the Finite Element Process. Adapted from <i>klaus-Jürgen Bathe. Finite element procedures. klaus-Jurgen Bathe, 2006[11].</i>	36
2.2	A function with zero values at the endpoints (blue), and a piecewise linear approximation (red). Adapted from <i>Wikipedia. Finite element method — Wikipedia, the free encyclopedia[23].</i>	39
2.3	a) Footprint in lunar soil showing the dust lunar regolith. Adapted from <i>NASA photo AS11-40-5877.</i> b) Challenger space shuttle explodes and flies uncontrollably. Adapted from <i>WR Rogers. The rogers' commission report on the space shuttle challenger accident. US Government Accounting Office, 1987 [26]</i>	42
2.4	Drift cells arranged in 9 super layers at the end plate which are the origin of the load in drift chamber. Adapted from <i>Walter Blum, Werner Riegler, and Luigi Rolandi. Particle detection with drift chambers. Springer Science Business Media, 2008 [6]</i>	44
2.5	Wire pattern of the OPAL vertex chamber showing increasing wire load from one layer to another as the radius increases. This is the reason of uniformly varying pressure. Adapted from <i>Walter Blum, Werner Riegler, and Luigi Rolandi. Particle detection with drift chambers. Springer Science Business Media, 2008 [6].</i>	45
2.6	Initial concept of the IDEA drift chamber proposed by Istituto Nazionale di Fisica Nucleare (INFN) a) Endplate of the drift chamber showing outer ring, inner ring and spokes b) Isometric view of the IDEA drift chamber	46
2.7	a) Gas containment in which the gas vessel can freely deform without affecting the internal wire position and mechanical tension. b) Light Wire Cage support structure with Feed-through less wiring	47
2.8	a) Mu2e I-Tracker cage showing connectivity of the cables, spokes and outercylinder b) An analogy between Mu2e I-Tracker cage and a harp bridge c) A section of a wire cage support	47
2.9	a) Properties of the Carbon fiber modelled as an equivalent orthotropic material for cylinders and spokes b) Properties of the Structural steel which are used for the cables	50
2.10	a) Element orientation for the outer cylinder b) Element orientation for the inner cylinder	51
2.11	Schematic showing alignment of the surface section with (a) top, (b) middle and (c) bottom respectively	52
2.12	Inspection of the element coordinate system using element triads which shows the orientation with respect to global coordinate system. In our case, it varies according to time step and nodes.	53
2.13	a) A sector of our drift chamber representing cyclic symmetry. The two planes defined on XY plane are low and high region of cyclic symmetry. The dots represent that the coincident topology has been shared between the connecting parts b) Conformal mesh is generated in the ANSYS mechanical even when the quality of the element is worst.	54

## LIST OF FIGURES

---

2.14	Failure to comply with the unit conversion resulted Mars Climate Orbiter to miss the planned trajectory. No verification and validation had been done for the software. Figure adapted from <i>Mishap Investigation Board. Mars climate orbiter mishap investigation board phase i report november 10, 1999, 1999[27]</i> . . . . .	55
2.15	Different types of finite elements used in our numerical model . . . . .	58
2.16	Mesh/element quality of the outer (3 mm element size) and inner cylinder (1 mm element size). . . . .	59
2.17	Uniformly varying load is treated as series of equivalent uniformly distributed load . . . . .	60
2.18	A typical sparse matrix in finite element problem with non zero elements in black dots. Adapted from <i>Wikipedia. Sparse matrix — Wikipedia, the free encyclopedia[28]</i> . . . . .	66
2.19	Equivalent von-Mises stress at the outer cylinder calculated with averaged, nodal difference, elemental difference and unaveraged methods with 3 mm element size . . . . .	81
2.20	Equivalent von-Mises stress at the outer cylinder calculated with averaged, unaveraged methods and nodal difference with 1 mm element size. . . . .	82
2.21	Full scale model of the IDEA drift chamber made up of carbon subjected to a full load of 10 tonnes. The maximum deformation occurs on inner cylinder 1550.2 mm. The deformation is shown on a true scale. . . . .	84
2.22	Response of the full scale model when turning on the geometrical nonlinearities. . . . .	86
2.23	The convergence criterion is not met as the force convergence is above the force criterion . . . . .	87
2.24	Total deformation ( <i>133.27 mm</i> ) of the symmetric sector drift chamber subjected to uniformly distributed load . . . . .	88
2.25	Force convergence criterion is met after 16 substeps and 64 iterations. . . . .	89
3.1	Projection of trajectory of Lorenz system in phase space with "canonical" values of parameters $\rho = 28, \sigma = 10, \beta = 8/3$ (or 2.666667) and integration timestep 0.001. The system exhibits chaotic behavior for these (and nearby) values. . . . .	93
3.2	Outline of the input and the output parameters. . . . .	98
3.3	A window of SpaceClaim showing the Named selection required for automatic input in ANSYS Mechanical, Script parameters, the generated geometry and Python Script for geometry generation . . . . .	104
3.4	Project schematic for the Parametric design exploration. The values of the parameters are created by OptiSlang DOE wizard and these values are sent to SpaceClaim for geometry generation. Based on this the ANSYS Mechanical solves the model the Result set is updated. This completes one single iteration. . . . .	105
3.5	Input parameters for the Sensitivity analysis, their resolution and range. Continuous parameters are preferred as the response surface is a well defined surface, else slices will be formed. . . . .	106

## LIST OF FIGURES

---

3.6	Example of the first 10 Design results from the sensitivity analysis. . . . .	106
3.7	CoP Matrix results from the sensitivity analysis which shows the highest sensitivity of the parameter height , outer thickness and the radius of the cables. . . . .	107
3.8	Correlation Matrix from the sensitivity analysis showing linear correlation coefficients, histograms and anthill plots for all selected input and output parameters and their combinations respectively, combined into one plot. .	108
3.9	Parallel coordinates plot showing all the 100 designs evaluated during the sensitivity analysis. The plot displays a comprehensive representation of input, output, objectives, and constraints for all designs. Each parameter is accompanied by two sliders to set lower and upper bounds. Designs that fall outside of these bounds are also shaded in grey. . . . .	109
3.10	Response surface showing Isotropic Kriging approximation between the total deformation, height of the outer cylinder and the thickness of the outer cylinder . . . . .	115
3.11	Response surface showing Isotropic Kriging approximation between the total deformation, height of the outer cylinder and the radius of the cables. . . . .	115
3.12	Response surface showing Isotropic Kriging approximation between the total deformation, height of the outer cylinder and the breadth of the spokes. . . . .	116
3.13	Response surface showing Isotropic Kriging approximation between the total deformation, height of the outer cylinder and the height of the spokes. . . . .	116
3.14	Optimization criteria set for minimising the Total deformation and Total mass. Initially it will create a Meta Model and then optimise the response surface . . . . .	118
3.15	Parallel coordinates plot for the 10,000 design created by the metamodels . . . . .	119
3.16	Objective Pareto plot for the multiobjective optimization . . . . .	120
3.17	Parallel coordinates plots of the designs selected from the meta models with height of outer cylinder less than 200 mm and total displacement less than 27.1206 mm. . . . .	121
3.18	Parallel coordinates plots of the designs selected from the meta models radius of the cables less than 1.5 mm and total displacement less than 10 mm. . . . .	122
3.19	Criterion set for the multi-objective optimization using Genetic Algorithms. . . . .	123
3.20	Parallel coordinates plot of the optimization results subjected to the constraint. . . . .	124
3.21	Deformed shape of the spokes obtained from the Linear buckling analysis of the drift chamber for breadth of 5 mm and depth of 10 mm. Load multiplier is 0.92. . . . .	126
3.22	Project schematic in the ANSYS workbench for the Linear Buckling analysis. The parametric design is studied through Adaptive Metamodel of Optimal Prognosis (AMOP). . . . .	127

## LIST OF FIGURES

---

3.23	Correlation Matrix from the Adaptive Metamodel of Optimal Prognosis (AMOP) showing linear correlation coefficients, histograms and anthill plots for all selected input and output parameters and their combinations respectively, combined into one plot. . . . .	128
3.24	Response surface for the breadth, height and the load multiplier for Linear Buckling analysis. The response surface is obtained through Adaptive Metamodel of Optimal Prognosis (AMOP). . . . .	129
3.25	Parallel coordinates for the Linear Buckling analysis through the use of Adaptive Metamodel of Optimal Prognosis (AMOP). . . . .	130
3.26	Optimization criteria set for minimising the Total load multiplier and Total mass of the spokes. . . . .	131
3.27	Parallel coordinates plot of the optimization results obtained from the minimisation of Total load multiplier and Total mass of the spokes . . . .	132
3.28	Engineering properties of epoxy carbon unidirectional prepeg . . . . .	134
3.29	Buckled shape for the drift chamber and the load multipliers. The minimum load multiplier is 2.20. . . . .	136
3.30	Total deformation of 21.643 mm using epoxy carbon as our material for drift chamber. . . . .	137
4.1	Material properties of the Epoxy carbon prepeg used in ANSYS Composite PrepPost (ACP) . . . . .	143
4.2	Polar properties of the Stackup oriented at [0/0/0/0/0] . . . . .	143
4.3	Polar properties of the Stackup oriented at [0/0/90/0/0] . . . . .	146
4.4	Total deformation (2.87 mm) of the layered composite subjected to 10000 N	147
4.5	Total deformation (2.78 mm) of a symmetric sector of equivalent monolithic structure subjected to 10000 N . . . . .	148
4.6	Total deformation (24.34 mm) of the layered composite subjected to 100000 N . . . . .	148
4.7	Total deformation (25.39 mm) of a symmetric sector of equivalent monolithic structure subjected to 100000 N . . . . .	149
5.1	Tangent hyperplanes in a three-dimensional space with (a) one and (b) two constraints . . . . .	155
5.2	Ackley function reveals a complex landscape characterized by numerous local minima and a global minimum at the origin, challenging algorithms to navigate the function's intricate topology to find the optimal solution. .	162
5.3	Parameters and range for the evolutionary algorithm . . . . .	171
5.4	The maximum total deformation of the spokes is set as constraint . . . . .	172
5.5	Parameters setting for evolutionary algorithm. The starting population is 140 (10 N) and 70 (5 N) is the population in each generation. We adopt a mutation rate of 7% . . . . .	173
5.6	The starting population explores the space in 15 dimensions between 0°C to 400°C. . . . .	174
5.7	Second generation . . . . .	175
5.8	Third generation . . . . .	176

## LIST OF FIGURES

---

5.9	Fourth generation . . . . .	177
5.10	Fourteenth generation . . . . .	178
5.11	Twenty first generation . . . . .	179
5.12	Twenty second generation . . . . .	180
5.13	Twenty third generation . . . . .	181
5.14	All 1680 designs . . . . .	182
5.15	Input History for the thermal condition 8. The algorithm has practically stabilized and ceases to explore more design space. . . . .	183
5.16	Total deformation History showing very rapid convergence in the beginning. However, the algorithm ceases to give better results after 18 <sup>th</sup> generation. . . . .	184
5.17	The optimal solution obtained from the evolutionary algorithm: Average deformation (0.428763 mm) and maximum deformation (0.56466 mm). . . . .	188
6.1	A classification chart of the composites. Adapted from <i>Bhagwan D Agarwal, Lawrence J Broutman, and CW Bert. Analysis and performance of fiber composites. 1981[42].</i> . . . .	190
6.2	A carbon fiber of 6 $\mu\text{m}$ diameter carbon filament compared to 50 $\mu\text{m}$ diameter human hair. Adapted from <i>Wikipedia:Composite material [43].</i> . . . .	191
6.3	Specific strength as a function of time of use of materials. Adapted from <i>Eager, T.W., Whither advanced materials? Adv. Mater. Processes, ASM International, June 1991, 25–29.</i> . . . . .	196
6.4	A cross-section of a unidirectional fibre of the composite embedded in matrix. Adapted from <i>Bhagwan D Agarwal, Lawrence J Broutman, and CW Bert. Analysis and performance of fiber composites. 1981[42].</i> . . . .	198
6.5	Epoxy Prepregs pre-manufactured as tapes (76 to 1270 mm) consisting of fibers embedded in a polymer matrix . Adapted from <i>Autar K Kaw. Mechanics of composite materials. CRC press, 2005 [47].</i> . . . . .	200
6.6	Longitudinal stress-strain diagrams for a composite with (a) linear and (b) nonlinear matrix material. <i>Bhagwan D Agarwal, Lawrence J Broutman, and CW Bert. Analysis and performance of fiber composites. 1981[42].</i> . . . .	201
6.7	Typical laminate made up of three laminae. The direction of the fibers can be changed in each individual layer to adapt for the load bearing capacity. Adapted from <i>Autar K Kaw. Mechanics of composite materials. CRC press, 2005 [47].</i> . . . . .	203
6.8	Schematic of deformation in isotropic and anisotropic material. Adapted from <i>Daniel Gay. Composite materials: design and applications. CRC press, 2022[45].</i> . . . . .	204
6.9	Schematic of deformation in isotropic and anisotropic material. Adapted from <i>Daniel Gay. Composite materials: design and applications. CRC press, 2022 [45].</i> . . . . .	205
6.10	A unidirectional lamina as a transversely isotropic material with fibers arranged in a square array. Adapted from <i>Autar K Kaw. Mechanics of composite materials. CRC press, 2005 [47].</i> . . . . .	209



## LIST OF FIGURES

---

6.11	Plane stress conditions for a thin plate. Adapted from <i>Autar K Kaw. Mechanics of composite materials. CRC press, 2005 [47].</i> . . . . .	209
6.12	Orientation of the fibre in a unidirectional composite. Adapted from <i>Daniel Gay. Composite materials: design and applications. CRC press, 2022 [45].</i> . . . . .	212
6.13	Loading Curves of Metal and Unidirectional Composite. Adapted from <i>Daniel Gay. Composite materials: design and applications. CRC press, 2022[45].</i> . . . . .	214
6.14	a) Off axis modulus of the composite. b) Off axis rupture strength of composite. Adapted from <i>Daniel Gay. Composite materials: design and applications. CRC press, 2022 [45].</i> . . . . .	215
6.15	Effect of Ply orientation on composite structures. Adapted from <i>Daniel Gay. Composite materials: design and applications. CRC press, 2022[45].</i>	218
6.16	Effect of laminate lay up on the deformation. Adapted from <i>Daniel Gay. Composite materials: design and applications. CRC press, 2022[45].</i> . . .	219
6.17	Basic Workflow in the ANSYS Composite PrepPost (ACP) including Eigenvalue Buckling Analysis . . . . .	223
6.18	A sector of drift chamber used for the analysis. . . . .	224
6.19	Full geometry of the drift chamber using surfaces that act as a mould for the composite layers. No topology is shared between cables and the spokes.	225
6.20	Basic Workflow of the ANSYS Composite PrepPost (ACP) workflow using different types of Model. While transferring the model to Static Structural, the type of data , "Solid" or " Shell" to be exported should also be defined.	226
6.21	A window layout of the ANSYS Composite PrepPost (ACP) with Model Tree structure, including the composite layup, material properties, boundary conditions, and analysis settings. . . . .	227
6.22	Fabric Properties for the Epoxy Carbon Prepeg. . . . .	228
6.23	Representation of Elastic Properties of Epoxy Carbon Prepeg. . . . .	228
6.24	Five fabrics stacked up with a cross-ply at 90° in the middle. Each stackup has 1 mm thickness. . . . .	229
6.25	Stackup of the Production ply and Analysis ply. The polar properties of the stackup can be seen to be decreasing in 0° and increasing in 90°. . . .	230
6.26	Layup direction for the composite inner and outer cylinders. The outer cylinder is extruded outwards <i>shown by purple arrows</i> . The inner cylinder is extruded inwards <i>shown by purple arrows</i> . The green arrows represent the direction of fibers. For the inner and outer surfaces the fibers are in cylindrical direction. Incorrect definition of Layup direction will produce intersecting surfaces and the solver will be unable to give an output. . . .	232
6.27	Reference direction and fiber direction for the spokes. The reference direction of spokes are in radial direction. . . . .	232
6.28	Illustration of various solid extrusion methods available in ANSYS Composite PrepPost (ACP). . . . .	233

## LIST OF FIGURES

---

6.29	One of the spokes is defined in ANSYS Composite PrepPost (ACP) for Extrusion using thickness of the solid and shell normal is the offset direction. This is necessary for post processing the composite. . . . .	234
6.30	Full setup of the solid model : One of the spokes is defined in ANSYS Composite PrepPost (ACP) and extruded as solid model, whereas other 35 are defined in ANSYS Mechanical and composite properties are defined through command APDL. . . . .	234
7.1	Contact Detection Point Location at Gauss Point. Adapted from <i>ANSYS Inc. ANSYS mechanical user's guide, 2019[29]</i> . . . . .	238
7.2	Surface-Projection-Based Contact. Adapted from <i>ANSYS Inc. ANSYS mechanical user's guide, 2019[29]</i> . . . . .	239
7.3	Penetration Distance. Adapted from <i>ANSYS Inc. ANSYS mechanical user's guide, 2019[29]</i> . . . . .	240
7.4	Smoothing Convex corner. Adapted from <i>ANSYS Inc. ANSYS mechanical user's guide, 2019[29]</i> . . . . .	240
7.5	Translation of the spokes in the negative Y direction due to lack of contact between spokes and the cylinders . . . . .	243
7.6	Contact definition between the lower surface of the spokes and the nodes of the cables . . . . .	244
7.7	Initial information of the contacts defined on our model. The resulting penetration and gap can be read from the table provided. . . . .	245
7.8	Contact status check on our model. The status can be Over-constrained, Far, Near, Sliding and Sticking. . . . .	245
7.9	Application of linearly varying pressure of 0.36 MPa on the surface of the spokes. The application of pressure is defined using cylindrical coordinate system. . . . .	246
7.10	Total deformation ( <i>14.099 mm</i> ) of the drift chamber subjected to linearly varying pressure only. . . . .	248
7.11	Total deformation ( <i>0.63 mm</i> ) of the outer cylinder subjected to linearly varying pressure only. . . . .	248
7.12	Total deformation ( <i>0.67 mm</i> ) of the drift chamber subjected to linearly varying pressure and prestress. . . . .	249
7.13	Total deformation of the spokes ( <i>0.62 mm</i> ) subjected to linearly varying pressure and prestress. The deformation has been scaled 60 times higher otherwise it is visually imperceptible. . . . .	249
7.14	Total deformation ( <i>0.67 mm</i> ) of the drift chamber subjected to linearly varying pressure and prestress. . . . .	250
7.15	Total deformation ( <i>11.54 mm</i> ) of the drift chamber subjected to linearly varying pressure only with outer cylinders completely fixed . . . . .	251
7.16	Total deformation ( <i>4.871 mm</i> ) of the drift chamber subjected to linearly varying pressure and prestress with outer cylinders completely fixed . . . . .	251
7.17	Total deformation of the spokes ( <i>4.869 mm</i> ) subjected to linearly varying pressure and prestress with outer cylinders completely fixed. . . . .	252

## LIST OF FIGURES

---

8.1	Various failure criterion are turned on to check the composite failure . . .	260
8.2	Notations for various failures modes for composites [29]. . . . .	261
8.3	A very low inverse reserve factor indicating no failure in our composite .	261
8.4	Maximum value of inverse reserve factor occurs at the contact between spokes and inner cylinder. . . . .	262
8.5	Possible Maximum strain failure mode ( $e2t$ ) and Tsai Hill ( $th$ ) failure in the spoke as given by inverse reserve factor. . . . .	262
8.6	Possible Maximum strain failure mode ( $e2t$ ) in the outer cylinder as given by inverse reserve factor. . . . .	263
8.7	Safety margin in our composite drift chamber. . . . .	263
8.8	Safety factor in our composite drift chamber. . . . .	264
8.9	Equivalent von-Mises stress calculated on the entire spoke. . . . .	265
8.10	Normal stress on the Top ply reported in element coordinate system (X-axis). 265	
8.11	Normal stress on the Top middle reported in element coordinate system (X-axis). . . . .	266
8.12	Normal stress on the Top bottom reported in element coordinate system (X-axis). . . . .	266
8.13	Equivalent von-Mises stress calculated on the outer cylinder. . . . .	267
8.14	Equivalent von-Mises stress calculated on the inner cylinder. . . . .	267
9.1	(a) Non linear load deflection curve (b) Linear (Eigenvalue) buckling curve. Adapted from <i>ANSYS Inc. ANSYS mechanical user's guide, 2019 [29]</i> . . . . .	271
9.2	Buckling mode corresponding to first buckling load factor due to the application of force . . . . .	273
9.3	Buckling mode corresponding to second buckling load factor due to the application of force . . . . .	274
9.4	Buckling mode corresponding to third buckling load factor due to the application of force . . . . .	274
9.5	Buckling mode corresponding to first buckling load factor due to the application of uniformly varying pressure . . . . .	275
9.6	Buckling mode corresponding to second buckling load factor due to the application of uniformly varying pressure . . . . .	275
9.7	Buckling mode corresponding to third buckling load factor due to the application of uniformly varying pressure . . . . .	276
9.8	Eigenshapes of even order. Adapted from <i>Alberto Carpinteri. Advanced structural mechanics. CRC Press, 2017 [53]</i> . . . . .	277
9.9	Eigenshapes of the odd order. Adapted from <i>Alberto Carpinteri. Advanced structural mechanics. CRC Press, 2017 [53]</i> . . . . .	277
9.10	Buckling mode corresponding to first buckling load factor . . . . .	278
9.11	Buckling mode corresponding to first buckling load factor . . . . .	278
9.12	Buckling modes interact with the spokes and consequently spokes deform near the outer cylinder . . . . .	279
9.13	Schematic for the workflow in the ANSYS Workbench to perform Non-linear buckling Analysis . . . . .	283

## LIST OF FIGURES

---

9.14	Total deformation of the drift chamber with full application of load of 0.65 MPa. A very large deflection can be seen as we are also looking at a post buckling stage. . . . .	284
9.15	Total Deformation history of the structure . . . . .	284
9.16	Tabular data: Deformation history . . . . .	285
9.17	Total load history of the structure. At time 0.63 the load is 116000 N. This is slightly lower than that predicted by linear buckling theory. . . . .	285
9.18	Force Convergence graph showing multiple substeps converged and bi-sections . . . . .	286

# List of Tables

2.1	Parametric Study of the effect of the Mesh size on the convergence of displacement, stresses and axial force. . . . .	83
2.2	Three different mathematical models based on boundary condition and material choice and the corresponding outputs . . . . .	90
3.1	Best design obtained from the sensitivity analysis with least deformation of 5.89769 mm . . . . .	110
3.2	Best design model (486) obtained from the multi-objective optimization of the deformation and mass . . . . .	120
3.3	Best design model (694) obtained from the constrained multi-objective optimization of the Total deformation and Total mass . . . . .	124
3.4	Best design 49 model obtained from the multi-objective optimization of the Total deformation and Total mass . . . . .	129
3.5	Best design 49 model obtained from the multi-objective optimization of the Total deformation and Total mass . . . . .	133
3.6	Design parameters choosen for drift chamber using Epoxy Carbon Unidirectional Prepeg . . . . .	135
4.1	Design parameters choosen for drift chamber using Epoxy Carbon Unidirectional Prepeg . . . . .	139
4.2	Arrangement and orientation of the Ply in the various components of Drift chamber . . . . .	140
4.3	Validation and Analysis of the Monolithic Model with the Layered Composite structure ( <i>Large deflection was turned on in both cases</i> ). . . . .	140
4.4	Validation of the Monolithic design with Layered composite design at [0/0/90/0/90] . . . . .	147
5.1	Minimum value, Mean value and the standard deviation of the total deformation in each generation as the evolutionary algorithm searches for global local optima in the domain. . . . .	185
5.2	Values of the thermal condition used in the cables to apply the effect of prestress. Cable-1 is the outermost cable near the inner cylinder. Cable-14 is the innermost cable near the outer cylinder. . . . .	186

## LIST OF TABLES

---

5.3	Values of the thermal condition used in the cables to apply the effect of prestress. The average deformation in the spokes is 0.428763 mm and maximum deformation in the spokes is 0.56466 mm. . . . .	186
5.4	Values of the thermal condition used in the cables to apply the effect of prestress. The average deformation in the spokes is 0.42069 mm and maximum deformation in the spokes is 0.59195 mm. . . . .	187
6.1	Specific Modulus and Specific Strength of Typical Fibers, Composites, and Bulk Metals. Adapted from <i>Autar K Kaw. Mechanics of composite materials. CRC press, 2005 [47].</i> . . . . .	196
6.2	Mechanical properties of typical fibers and composites compared to steel and aluminum. Adapted from <i>Autar K Kaw. Mechanics of composite materials. CRC press, 2005 [47].</i> . . . . .	197
6.3	Load Durability Ratings for High Volume and High Performance Composites. Adapted from <i>Daniel Gay. Composite materials: design and applications. CRC press, 2022[45].</i> . . . . .	217
6.4	Arrangement of the Stackup and Ply in the various components of Drift chamber . . . . .	231
7.1	Values of the thermal condition used in the cables to apply the effect of prestress. Cable-1 is the outermost cable near the inner cylinder. Cable-14 is the innermost cable near the outer cylinder. . . . .	247

*I fell in love with this problem.*

# Chapter 1

## Problem Statement

This thesis focuses on design and analysis of Ultra light IDEA (Innovative Detector for Electron-positron Accelerator) drift chamber used in high energy particle physics experiment. Design and analysis of such precise and sophisticated instrument needs an impeccable structural design that considers not only the basic principles of the structural design, but also takes into account the principles of the particle detection. The thesis investigates the model of the IDEA drift chamber using composite materials, and addresses the structural design from static, dynamic and instability point of view in an intuitive, organised and logical manner using the tools of computational mechanics. However, it must not be mistaken with the full design of the model which is still a few miles ahead. In a series of chapters, the thesis presents and investigates the design and analysis of IDEA drift chamber in an eloquent manner.

### 1.1 Introduction to Particle detector

The visual perception of objects is due to the fact that light passes through series of parts of eyes : cornea, pupil, lens and then retina which contains more than two million nerves called photoreceptors [1]. These photoreceptors are responsible for transforming light signals into electrical impulses and neural signals. This is one of the most fundamental examples of electromagnetic interaction of particles and also particle detection [2]. The detection of elementary particles, nuclei and high energetic electromagnetic radiation,



designated as particles, in modern physics are done by Particle detectors.

Particle detectors are one of the most sophisticated as well as precise instrument present on this planet which detects, tracks and measures the properties of the subatomic particles, such as electrons, protons and neutrons by the measurement of the particle energy and other attributes such as momentum, spin, charge. The advancement of the nuclear and particle physics has a direct correlation with the development of these detectors. Particle physics began its journey by discovery of the radioactivity by H.Becquerel in 1896[2]. This discovery also became the basis for the discovery of the cosmic rays by V.Hess in 1912 (Nobel Prize, 1946). With availability of photographic plates and scintillating coatings around 1900s, Rutherford, Geiger and Mardsen detected scattering of the particles using Zinc Sulfide (ZnS) screen. By analyzing the photographic pictures, C.F Powell and co-workers discovered the pion in 1947 (Nobel Prize, 1950) by reconstructing the kinematics of the single charged particle. H.Geiger developed tubes based on gas amplification in strong electric field, which led to development of the Geiger-Müller tube. Development of “coincidence method” by W.Bothe in 1920s (Nobel Prize, 1954) paved path for the electronic recording.

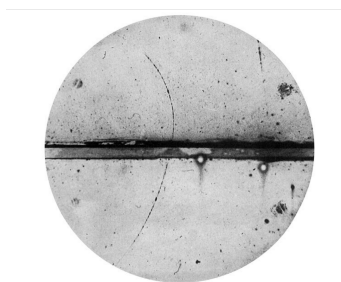


Figure 1.1: Discovery of the positron by C.D. Anderson in 1932 by analyzing the condensation trail of a positively charged particle yet far less massive than proton [3]. Paul Dirac had predicted the existence of such antiparticle in 1932.

Cloud chambers were first detectors where particle trajectories as “condensation trail” were visible (Figure 1.1). This led to discovery of first antiparticle, the positron, by An-

## CHAPTER 1. PROBLEM STATEMENT

---

derson in 1932. Cloud chamber was built by C.T.R Wilson (Nobel Prize, 1927), and later advanced by Blackett (Nobel Prize, 1948).

Bubble chamber (Figure 1.2) built by D.A Glaser (Nobel Prize, 1960), in 1950s became first detectors with which particle reactions were recorded completely with a bubble formation of the superheated liquid which could be photographed and analysed [2]. Both cloud and bubble chambers operate in a magnetic field in such a way that both momentum and charge can be determined by analysing track's curvature. As highly integrated electronics developed, Multi wire proportional chamber (MWPC) was built by G.Charpak (Nobel Prize, 1992). In 1980s, MWPC and its variants, in particular drift chambers, replaced bubble chamber.

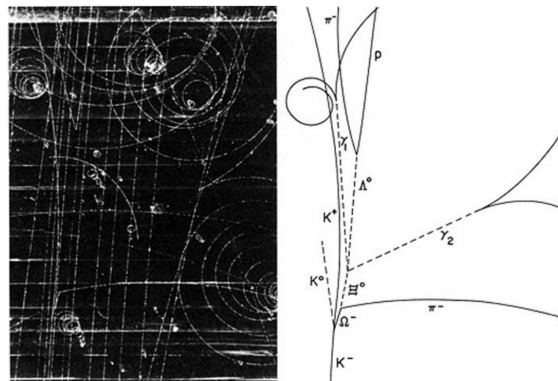


Figure 1.2: Quarks have spin  $1/2$ , and must obey the Pauli exclusion principle hence cannot exist in identical states. So with three strange quarks, the property which distinguishes them must be capable of at least three distinct values. Discovery of the Omega baryon  $\Omega^-$  validated the Quark model which predicted its existence[4].

These detectors can be ionization detectors and scintillation detectors, however detectors of other completely different principle like Čerevkov counter are also present. We limit our discussion to Gas-filled detectors as the Drift chamber belongs to this category.

## 1.2 Introduction to Drift Chambers

Drift chambers are very important apparatus (Figure 1.3) in particle physics experiment. They are electronic detector to measure the correct position of the moving charged particle. It was first studied by Bressani, Charpak, Rahm and Zupancic in 1969. The first functional drift chamber was built by Prof. A.H Walenta, Heintze and Schürlein in 1971[5]. As charged particles passes through the sensitive medium, in this case gas, it interacts with the surrounding atomic electrons electromagnetically, which creates an electron/ion pair as the charged particle moves along its path. Typically, an electric field (typically of the order few KeV per centimetre of gas) imparts kinetic energy to these particles and they start to drift towards positive electrode. If the electric field is strong enough, the particles drifting through the gas undergoes collisions with the neighboring atoms while moving towards the positive electrode. This results in an avalanche of electrons (Figure 1.4). The encounters are purely random and are characterized by a mean free flight path  $\lambda$  between ionizing encounters [6]. When these electrons reach the anode, a current is generated which is proportional to the number of ions created. This is the principle on which the measurement of the radiation fluxes are based upon[2]. However, for a single charged particle, the current is not sufficient, hence an intrinsic amplification is necessary in a very high field around anode [2]. In principle, the detector is a capacitor which discharges as the ionisation takes place [2]. Electrically, it behaves as a current source [2].

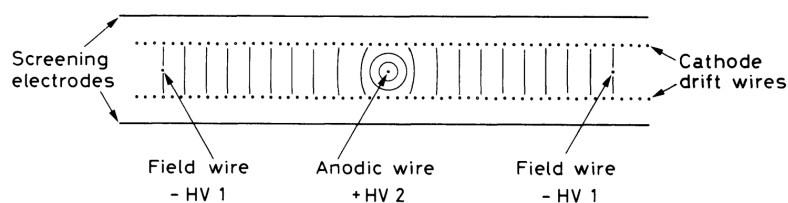


Figure 1.3: Schematic of the drift chamber. The cathode drift wires carry non uniform voltage whereas the field wires maintain an equipotential lines linear . Adapted from William R Leo. *Techniques for nuclear and particle physics experiments: a how-to approach*. Springer Science Business Media, 2012 [7]

These electrons drift with a known predictable speed while travelling to the anode. The time taken by the electron to reach the anode from the original source can now be measured. Based on the drift time and drift velocity ( $v_D$ ) the position of the particle can be calculated.

$$x = \int_{t_{start}}^{t_{stop}} v_D(t) dt \quad (1.1)$$

The precision of the position resolution does not depend upon the spacing of the signal electrodes, but rather on the precision of the time measurement of the electron drift [2]. The device based on this principle is called Drift chamber. The current spatial resolution is around 50 micrometers or better [5].

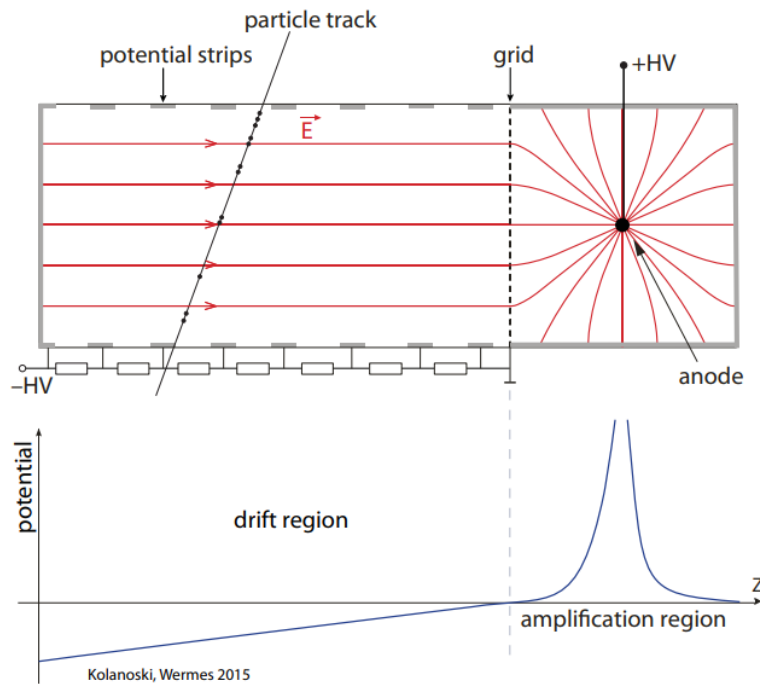


Figure 1.4: As the electrons moves towards anode from much smaller electric field to a very large electric field around anode region, with a velocity proportional to electric field applied, an avalanche is created. Such large gas amplification is obtained by using anode of very thin wires of the orders 20-100  $\mu\text{m}$ . Adapted from *Hermann Kolanoski and Norbert Wermes. Particle Detectors: Fundamentals and Applications. Oxford University Press, USA, 2020 [2]*.

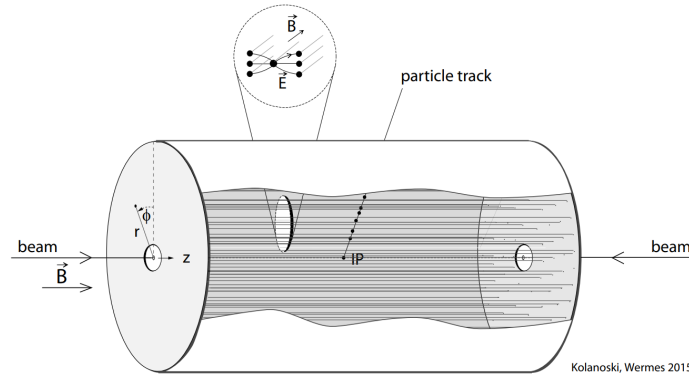


Figure 1.5: Cylindrical drift chamber with cathode and anode wires parallel to magnetic field. Subsequently, the cut out shows the arrangement of drift cells. The electric field is then perpendicular to the magnetic field ( $\vec{E} \perp \vec{B}$ ). Adapted from *Hermann Kolanoski and Norbert Wermes. Particle Detectors: Fundamentals and Applications. Oxford University Press, USA, 2020 [2]*.

The measurement and reconstruction of the trajectories of the charged particles requires coverage of the large volumes which is done by drift cells, each with signal wire (anode). The central anode wire is surrounded by the electrodes on cathode potential which can be formed by conductive surface on a carrier material. Based on the stacking of these drift cells, to cover larger volume, the layers can have planar or cylindrical shapes [2]. Cylindrical drift chambers (Figure 1.5), which are the drift chambers of our interest, are often used as a tracking chamber in collider experiments, in which the axis of the chamber is in the beam direction.

### 1.3 IDEA drift chamber

Prior to the IDEA drift chamber (Figure 1.6), several other chambers were proposed and/or used in various experiments. These include KLOE (1998) at Frascati  $\Phi$ -factory DAΦNE, CluCou Chamber proposed for the 4<sup>th</sup>-Concept at ILC (2009), I-tracker chamber proposed for the Mu2e experiment at Fermilab (2012) DCH for the MEG-II upgrade at PSI. The IDEA detector, which represents state of the art, is a versatile detector that

includes a silicon pixel vertex detector, a large and lightweight drift chamber, surrounded by silicon micro-strip detectors, a thin and lightweight superconducting solenoid coil, a  $\mu$ Rwell pre-shower detector, a dual-readout calorimeter, and a  $\mu$ Rwell muon system located within the magnet return yoke [8]. The IDEA drift chamber designed for experiments at future  $e^+e^-$  colliders, provides an efficient tracking, a high precision measurement of the momentum and robust particle identification by cluster counting technique [9]. The innovative approaches for wiring and assembly procedures makes it highly transparent, in terms of radiation lengths.

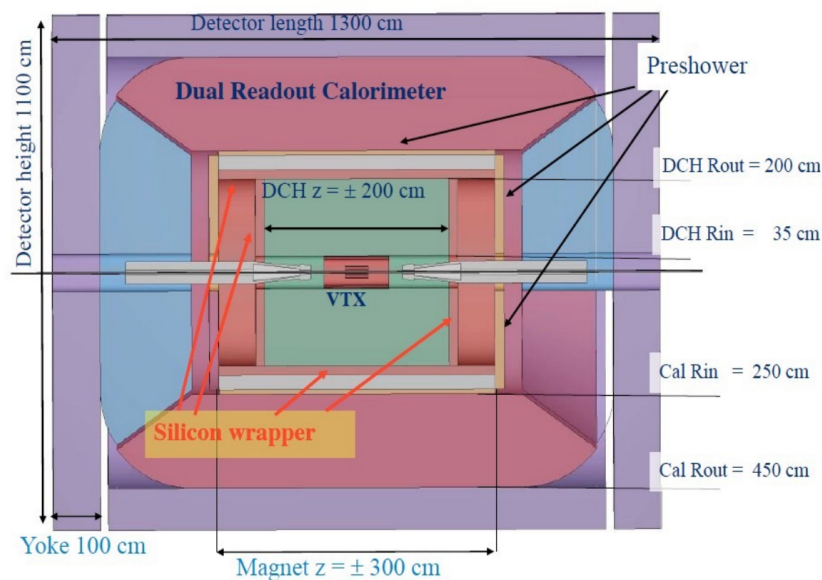


Figure 1.6: Schematic diagram of the IDEA detector Adapted from *Walaa Elmetenawee, Alessandro Corvaglia, Federica Cuna, Nicola De Filippis, Edoardo Gorini, Francesco Grancagnolo, Marcello Maggi, Alessandro Miccoli, Marco Panareo, Margherita Primavera, et al. The tracking performance for the idea drift chamber. arXiv preprint arXiv:2211.12568, 2022[8].*

### 1.3.1 Design Aspects

The IDEA central drift chamber is a unique volume, high granularity, full stereo, low mass cylindrical drift chamber with 2T solenoid field, with helium based gas mixture [10]. The drift chamber has inner radius  $R_{inner}=350$  mm and outer radius  $R_{outer}=2000$  mm with a

length  $L=4000$  mm. It consists of 112 co-axial layers, at alternating-sign stereo angles, arranged in 24 identical azimuthal sectors. It consists of almost 343,968 wires of  $20\mu\text{m}$  to  $50\mu\text{m}$  and to accommodate these large number of wires, the design of wiring procedure and the new construction technique of MEG-II drift chamber will be used [8]. To ensure the transparency, the function of gas containment and wire support are separated in the following way: The wires are connected to a self-sufficient lightweight structure (known as a wire cage), which is enclosed by a thin outer layer made of an appropriate material (known as a gas vessel) to hold the gas mixture. The wire tension stress is transmitted to the rim of the outer endplate through a system of tie-rods. A cylindrical carbon fiber support structure, which bears the entire load, is attached to the rim.

### 1.3.2 Goals and Objectives

IDEA drift chamber is based on MEG-II and is designed in such a way to meet the following objectives:

- a) Reduction of the material for the inner cylinder and end plates due to separation of gas containment - wire support.
- b) Feed-through-less wiring <sup>1</sup>: By utilizing thinner wires and a feed-through-less wiring configuration, it becomes possible to increase the chamber granularity and the ratio of field/sense wire. This has the advantage of reducing both multiple scattering and the overall tension on the end plates caused by the wires.
- c) Cluster timing <sup>2</sup>: The use of cluster timing can achieve a spatial resolution of less than  $< 100\mu\text{m}$  for 8 mm drift cells in helium-based gas mixtures.

---

<sup>1</sup>"Feed-through less wiring" refers to a type of wiring configuration where electrical wires pass through a sealed barrier without creating any openings or "feed-throughs" in the barrier. This type of wiring is often used in applications where it is necessary to prevent the transfer of gases, fluids, or other materials between two separate environments that are separated by the barrier. In feed-through less wiring, the wires are usually threaded through a small hole or conduit in the barrier and then sealed in place using a special material or process that creates a hermetic seal. This helps to maintain the integrity of both environments while allowing electrical signals or power to pass through the barrier

<sup>2</sup>Cluster timing refers to the measurement of the time at which particles hit the detectors and the determination of the time difference between the arrival times of particles at different locations in the detector. The accuracy of the timing measurement is critical for identifying the particle type and determining its energy.

d) Cluster counting <sup>3</sup>: allows to reach  $dN_c/dx$  resolution  $< 3\%$  for particle identification (a factor 2 better than  $dE/dx$  as measured in a beam test)

## 1.4 Organization of the Thesis

The first chapter provides an introduction to the IDEA drift chamber, outlining the goals and design objectives of this thesis. In the second chapter, a preliminary design of a finite element model is presented, along with the underlying hypotheses and simplifications made to achieve our objectives. Statistical concepts, including response surface methodology, metamodel creation, and multi-objective optimization, are introduced in the third chapter. The fourth chapter focuses on hypothesis testing and model calibration, conducted to verify the simplifications made in pursuit of our goals.

Moving on to the fifth chapter, we delve into the optimization of a highly nonlinear problem, specifically determining the cable prestressing forces to limit deflection in the drift chamber. The sixth chapter outlines a methodological approach for developing the composite structure, while the seventh chapter provides an overview of structural mechanics, including a brief introduction to contact kinematics. In the eighth chapter, a meso-scale analysis of the ply is presented, along with various failure criteria. The ninth chapter delves into a comprehensive analysis of buckling, covering both linear and nonlinear approaches. Finally, in the tenth chapter, we present our concluding remarks.

---

<sup>3</sup>In particle detection, cluster counting is a technique used to determine the number of clusters, or energy deposits, produced by particles interacting with a detector which can be used to identify the type of particle, determine its energy, and measure its trajectory.



## **Chapter 2**

# **Preliminary Design: Development of a Finite Element Model**

This chapter provides a critical overview of the assumptions made by the author, underlying principles on which the mathematical model is based, simplifications done to model and/or solve the problem efficiently, and the methodology to develop the finite element model. Even though the final goal of the IDEA drift chamber project is to use the composite materials, the chapter is based upon equivalent orthotropic material. The logical reasoning behind this is also explained in this chapter (Section 2.5.1). Also, the subsequent chapters (Chapters.3, Chapter.4 and Chapter.5) which are based on the concept of equivalent orthotropic material will provide a convincing proof on the choice of material in preliminary design stage.

Development of the Finite element method is a collaborative outcome of three separate research groups: applied mathematicians, physicists and engineers[11]. Finite element method involves idealization of the physical phenomena and processes to an analytical description called mathematical model. These mathematical models are precisely formulated understanding the phenomena and processes, as well as the laws governing them. The mathematical models thus developed are characterized by very complex differential and/or integral equations posed on geometrically complicated domains [12].

The concept of approximation is one of the founding pillars of finite element method. Greek Mathematician Archimedes (287-212 B.C.) determined the value of  $\pi$  by approximating the shape of a circle using straight lines. In 1697, Gottfried Leibniz solved the brachistochrone problem using similar approach. Variational methods developed by Ritz (1909), Galerkin (1915), Trefftz (1926), Courant (1943), and then Hellinger and Reissner (1953) was a precursor for the development of finite element method. In 1941, A. Hrennikof, published his first paper on plates and membrane in which he discretized the domain into lattice structure introducing the concept of mesh discretization [13]. On the same year, R. Courant solved a second order partial differential equation arising from Saint–Venant’s torsion problem of a cylinder using Rayleigh–Ritz variational method [14]. Between 1954 and 1956, John Argyris, formulated the classical force method of structural design for one-dimensional rigid frames using matrix notation [15]. R.W. Clough coined the phrase Finite Element Method in his paper paper entitled, “The Finite Element Method in Plane Stress Analysis” published in 1960[16]. In 1960, R.W. Clough and Wilson developed a finite element program for planar structures. The 1960s saw the development of three-dimensional finite element formulations for solid and fluid mechanics. In the 1970s and 1980s, nonlinear material models were introduced, enabling more accurate simulations of real-world structures [17]. In the 1990s, parallel computing enabled the solution of larger and more complex problems using the finite element method setting into motion whirlwind of development [17].

### **2.0.1 Mathematical models and Numerical simulations**

In an article in 2009, The New York times, Steven Strogatz wrote, “Since Newton mankind has come to realise that the laws of physics are always expressed in the language of differential equations. This is true for the equations governing the flow of heat, air and water; for the laws of electricity and magnetism; even for the unfamiliar and often counterintuitive atomic realm where quantum mechanics reigns.” This clearly explains that it is possible to mathematically express, in terms of differential equations, how the physical phenomena

## CHAPTER 2. PRELIMINARY DESIGN: DEVELOPMENT OF A FINITE ELEMENT MODEL

---

and processes work. This is done by developing mathematical models which is a set of differential equations that represents the physical phenomena or the processes to be studied in terms of the variables concerned with the output that we are interested in. They are often based in fundamental scientific laws of physics such as conservation of mass, energy and linear momentum [12]. The derivations of such governing equations for most problems may not be difficult, however their solution by exact methods is often difficult. In such cases, numerical methods are employed to find the solution of such equations. Numerical methods transform the governing set of differential equations into a discrete set of algebraic equations that can be solved by computers. Such process is called numerical simulation.

The Navier-Stokes equations for an incompressible fluid fluid flowing through a pipe with varying cross-sectional area in three dimensions are given by;

$$\rho(\partial \mathbf{u} / \partial t + \mathbf{u} \cdot \nabla \mathbf{u}) = -\nabla p + \mu \nabla^2 \mathbf{u} + f \quad (2.1)$$

$$\nabla \cdot \mathbf{u} = 0 \quad (2.2)$$

where  $\rho$  is the density of the fluid,  $u(x, y, z, t)$  is the velocity field of the fluid,  $p(x, y, z, t)$  is the pressure field of the fluid,  $\mu$  is the dynamic viscosity of the fluid,  $f(x, y, z, t)$  is any external force acting on the fluid, and  $\nabla^2 u$  is the Laplacian of the velocity field. These partial differential equations are highly nonlinear and have been solved analytically only for some simple geometries and boundary conditions. Such mathematical models cannot be solved for more realistic problems which have more complex geometric and boundary conditions without the application of numerical methods. This is the fundamental strength of the numerical methods. However, theoretical understanding of Navier-Stokes solutions is incomplete and mathematicians have not yet proven that smooth solutions always exist. This is called the Navier–Stokes existence and smoothness problem and is considered one of the Millennium Prize Problems selected by the Clay Mathematics Institute in 2000 [18]. While computers can indeed solve Navier-Stokes equations numerically by approximating the solution, it is not possible to solve them for all situations, especially for

turbulent flows. This is the reason why the problem is still unsolved and highlights the limitations of numerical methods. Numerical methods are solely based upon underlying principles of physics, and can only be used for problems whose governing equations are known. Otherwise, numerical methods produce results incoherent to reality and results may be misleading. In short, simulation is no substitute for math—it could never provide a proof[19]. The use of numerical methods and computer simulation to solve a mathematical model based upon certain fundamental laws is called numerical simulation [12]. Numerical simulation of physical systems is known as computational mechanics[11].

Finite difference method, finite element method, boundary element method, Monte Carlo method, molecular dynamics, computational fluid dynamics, finite volume method, discrete element method, spectral methods and lattice Boltzmann method are all numerical methods and have a distinct principle to solve the differential equations. Finite element method should not be confused with these existing numerical methods. Moreover, finite element analysis (FEA) is a model created usually using the software interface to simulate a structural design. Finite element method (FEM) is the underlying mathematical model on which finite element analysis (FEA) is based.

### **2.0.2 Finite Element Method : Basic Idea and Features**

Finite element method is a very general but powerful numerical method that can be applied to real world problems involving complicated physics, geometry and boundary conditions. The method involves dividing a given domain into subdomains and approximating the governing equations by means of variational methods. The subdomains are then connected in a way that the approximating function and possibly their derivatives are continuous at the connecting points. Finite element method has completely dominated other competing methods because of three powerful features [12]. First, a geometrically complex domain can be easily divided into very simple sub domains called finite elements, which can be viewed as an independent domain by itself. Second, the mathematical model defining the problem in each finite element is formulated in the form of differential equations which are

## CHAPTER 2. PRELIMINARY DESIGN: DEVELOPMENT OF A FINITE ELEMENT MODEL

converted into a set of discrete algebraic equations that can be easily solved by computer algorithms using numerical methods and quantities of interest can be calculated using approximation function. Third, the relationships between these finite element are formulated and the solution over each part is then assembled using inter-element relationship to obtain the solution to the whole domain.

A schematic diagram to summarize the process of finite element method is shown below (Figure 2.1). In addition to the basic features we described already, it adds one more important parameter called accuracy. For any finite element model, an accuracy criteria must be defined and the analysis must be refined until a desired level of accuracy is met. Numerical methods used to solve partial differential equations can produce accurate results when they have consistency, stability and convergence [20].

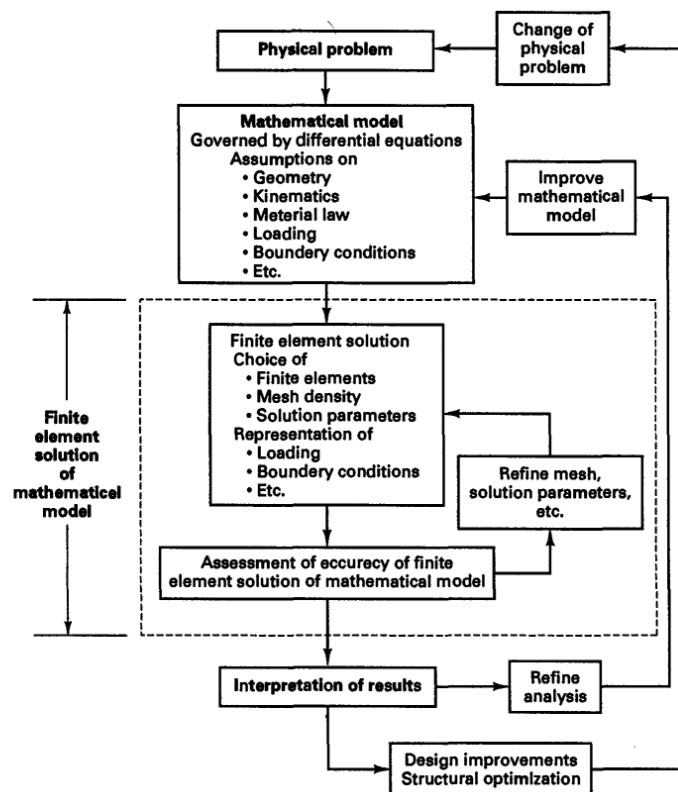


Figure 2.1: Schematic diagram of the Finite Element Process. Adapted from *klaus-Jürgen Bathe. Finite element procedures. klaus-Jurgen Bathe, 2006[11]*.

### 2.0.3 Variational Principles

Feynman's quip about calculus as God's language revealed and emphasized the infinite powers calculus had [21]. However, the solutions of differential equations are not only often unclear, but whether solutions are unique or exist at all are also notable subjects of interest [22]. Most systems of differential equations are unsolvable [19]. This is where variational principle comes into play. In mechanics, variational principles refers to the use of virtual work method or principle of total potential energy to determine the approximate solution to the problems. It is concerned with finding the extremum or stationarity of a functional with respect to the variables of the problem. The functional depends upon the nature of the problem such as governing differential equation, boundary conditions, and other constraints imposed. The variational formulation converts a strong form (continuous and satisfied pointwise) of differential equation based upon complex vector equilibrium equations into a weak form (may not be satisfied pointwise) of integral equations which can be easily solved which handles scalar quantities only.

For illustrative purpose let us consider a one-dimensional problem P

$$P : \begin{cases} u''(x) = f(x) \text{ in } (0, 1) \\ u(0) = u(1) = 0 \end{cases} \quad (2.3)$$

where  $f$  is given,  $u$  is an unknown function of  $x$ , and  $u''$  is the second derivative of  $u$  with respect to  $x$ . This boundary value problem (BVP) can be solved by computing antiderivatives but it works only in one spatial dimension and does not generalize to higher-dimensional problems or problems like  $u + u'' = f$ . Using FEM, one rephrases the original BVP in its weak form and then the weak form is discretized in a finite-dimensional space. The problem is converted to large but finite-dimensional linear problem whose solution will approximately solve the original BVP.

If  $u$  is a solution to P, then for any smooth function  $v$  that satisfies the displacement

boundary conditions, i.e.  $v = 0$  at  $x = 0$  and  $x = 1$ , we have

$$\int_0^1 f(x)v(x)dx = \int_0^1 u''(x)v(x)dx. \quad (2.4)$$

Conversely, if  $u$  with  $u(0) = u(1) = 0$  satisfies (2.4) for every smooth function  $v(x)$  then one may show that this  $u$  is a solution of P. We define a new operator or map  $\phi(u, v)$  such that:

$$\begin{aligned} \int_0^1 f(x)v(x)dx &= \int_0^1 u''(x)v(x)dx \\ &= u'(x)v(x)|_0^1 - \int_0^1 u'(x)v'(x)dx \\ &= - \int_0^1 u'(x)v'(x)dx \equiv -\phi(u, v) \end{aligned} \quad (2.5)$$

where we have used the assumption that  $v(0) = v(1) = 0$ . For a two dimensional problem,

$$\int_{\Omega} fvd s = - \int_{\Omega} \nabla u \cdot \nabla v d s \equiv -\phi(u, v)$$

where  $\nabla$  and  $\cdot$  denote gradient and dot product in the two-dimensional plane.

The problem P can now be solved by replacing the infinite dimensional linear problem (Equation 2.6) into a finite dimensional linear problem (Equation 2.7).

Find  $u \in H_0^1$  such that

$$\forall v \in H_0^1, -\phi(u, v) = \int f v \quad (2.6)$$

Find  $u \in V$  such that

$$\forall v \in V, -\phi(u, v) = \int f v \quad (2.7)$$

where  $V$  is a finite-dimensional subspace of  $H_0^1$ . There are many possible choices for  $V$ . However, for the finite element method we take  $V$  to be a space of piecewise polynomial

functions (Figure 2.2).

We take the interval  $(0, 1)$ , choose  $n$  values of  $x$  with  $0 = x_0 < x_1 < \dots < x_n < x_{n+1} = 1$  and we define  $V$  by:  $V = \{v : [0, 1] \rightarrow \mathbb{R} : v \text{ is continuous, } v|_{[x_k, x_{k+1}]}$  is linear for  $k = 0, \dots, n$ , and  $v(0) = v(1) = 0\}$  where we define  $x_0 = 0$  and  $x_{n+1} = 1$ . The functions in  $V$  are not differentiable. Indeed, if  $v \in V$  then the derivative is typically not defined at any  $x = x_k, k = 1, \dots, n$ . However, the derivative exists at every other value of  $x$  and one can use this derivative for the purpose of integration by parts.

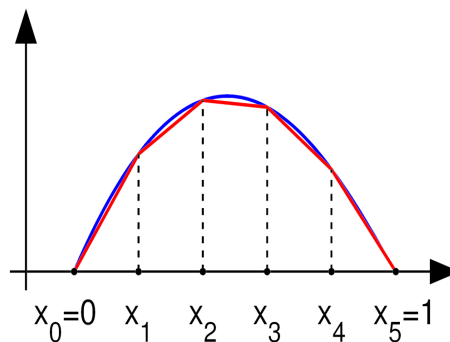


Figure 2.2: A function with zero values at the endpoints (blue), and a piecewise linear approximation (red). Adapted from *Wikipedia. Finite element method — Wikipedia, the free encyclopedia*[23].

In Figure 2.2, as the number of the subdivisions increases, the approximation of the maxima becomes better. If we use an approximation function that is an exact one, then only the stationarity of the functional is obtained. With less point, we are imposing a constraint based on the degree of the polynomial chosen, so the stationarity cannot be obtained exactly. In classical "variational formulations", the problem is translated to a functional or a variational principle which is equivalent to a governing differential equation. In modern "variational formulations", the use of equivalent weighted integral statement is preferred which may not be equivalent to variational principle [12]. Ritz and Galerkin method are well known variational formulation in which the variational formulations are generally expressed in terms of displacement. In such case, stress is much worse approximated than strain. Similarly the formulation can also be done in terms of stresses at the expense



of displacement. In mixed formulations, both can be approximated but are much more demanding.

## 2.1 Problem Simplification and challenges

Developing a numerical model for particle detectors is a challenging problem not only because of the difficulty in understanding the problem, but also because of difficulty in simplifying the problem. In words of Hans Hoffman, “The ability to simplify means to eliminate the unnecessary so that the necessary may speak.” A drift chamber consists of 112 co-axial layers, at alternating-sign stereo angles, arranged in 24 identical azimuthal sectors and almost 343,968 wires (Refer to Section 1.3.1 for details). The chamber has a gas containment (filled with helium gas) and wire cage structure. Very highly sensitive sensors to detect the presence of charged particle are also present. A numerical model abstracting all these features would not only be tedious and computationally difficult, but is also rather unnecessary. The art of abstraction lies in knowing what is essential and what is minutia, what is signal and what is noise, what is trend and what is wiggle [21]. It’s an art because such choices always involve an element of danger[21]. Abstraction must incorporate all the features that are essential in predicting the behaviour of the system to the desired level of accuracy. This is the first thing we keep in mind while developing our numerical model.

The second difficulty arises due to the extreme loads the structure is subjected to. A cantilever beam with length= 1650 mm, depth = 3 mm and breadth= 1 mm is subjected to a load of 4200 N. This induces an axial compression of 2000 N (280 MPa) and axial tension of 13000 N (1830 MPa) respectively. This is more than 10 times higher than what the normal beams are subjected to. In cables, the stresses are as high as 4100 MPa. With time, the creep is developed in these cables hence the load must be lower than 50% of the yield strength. Taking into account creep effects, the load is almost 33 times higher than expected.

## CHAPTER 2. PRELIMINARY DESIGN: DEVELOPMENT OF A FINITE ELEMENT MODEL

---

The third challenging problem is the design criteria. Generally, the maximum deflection of the beam is limited to  $\text{Span}/500$  [Eurocode 2], which is equivalent to 3.3 mm for 1650 mm long beam. But, in case of ours, the deflection must be very close to 0 mm (failure in determining the position of the anodic wire means failure in determining the position of charged particle in space). Now, the obvious solution is to increase the cross-sectional area until the deformation criteria is achieved. However, just as the name "ultra light drift chamber" emphasizes, one of the major goals is to optimize the mass, and this criteria restricts our design space. In addition, it must be noted that the ultimate goal is not to solve a structural problem, but to detect the particles. This ultimate goal of particle detection constrains our structural problem to a very small domain of solutions.

The final task is the interpretation of results, which involves analyzing the outputs generated by FEM to gain insights into the behavior of system and drawing conclusions based on these insights. It is crucial in assessing the accuracy and validity of the FEM model based upon the simplifications and hypothesis made. An interpretation is a human-dependent step and could be incomplete or even wrong, even though the FEM output may be correct. A simple example is that in case of linear analysis, stress state in a finite element model is given by Cauchy stress tensor having nine components which is overwhelming. That is why we prefer to use von-Mises stress which has only one scalar component. If von-Mises stresses are lower than yield, no problem would arise. However, if some part of the material has yielded, the stresses might be calculated by the solver based on linear projection of the strain using linear constitutive law. This means that the stresses can be much higher than yield which leads to incorrect conclusion. These are the kind of nuances the designer must be careful while interpreting the results. In several stages of model development, all our assumptions and hypothesis that we fed as an input are checked against the obtained output for their validation. In cases where our assumptions and hypothesis fail, further refinements are done to improve the finite element model.

## 2.2 Hypothesis Formulation

On July 20, 1969, during Apollo 11 mission, human set foot on the moon for the first time. During that mission, scientists had made a hypothesis that the lunar surface was covered in a layer of fine, powdery dust [24] (Figure 2.3 (a)). This hypothesis was based on observations made from Earth and from orbit, as well as the fact that the Moon has no atmosphere to blow away any loose material. If this hypothesis had been incorrect and the lunar surface had instead been rocky or uneven, the lunar module's landing gear which had been designed to sink would have failed, could have tipped over and the mission would have failed [25]. Since, the hypothesis was correct, numerical simulations generated for these gears were proved to be correct and the mission was and is still considered a giant leap for mankind.



(a)



(b)

Figure 2.3: a) Footprint in lunar soil showing the dust lunar regolith. Adaptdted from *NASA photo AS11-40-5877*. b) Challenger space shuttle explodes and flies uncontrollably. Adapted from *WR Rogers. The rogers' commission report on the space shuttle challenger accident. US Government Accounting Office, 1987 [26]*

Another example is of the Challenger space shuttle. Scientists had hypothesized that the

O-rings, which were used to seal the joints between sections of the solid rocket boosters, would maintain their integrity even in cold temperatures. However, on the day of the launch, January 28, 1986, the temperature was much colder than expected, and the O-rings failed to seal properly, leading to a catastrophic explosion (Figure 2.3 (b)), that killed all seven crew members aboard the shuttle [26]. This is considered one of the biggest catastrophic failures in the space mission history. This happened simply because the underlying hypothesis was incorrect. Even in such case, numerical simulations produced results which at that time were thought to be correct based on the human understanding of the O-rings.

So two important things are necessary to produce a correct result in simulation. One part is the correctness in how the finite element algorithms work and their implementation in the software. But another important aspect is the human understanding of the problem and the underlying hypothesis made to develop the numerical model, without which the numerical simulations only produce random numbers. The fulfillment of both of the above criteria can only produce a correct result.

### **2.3 IDEA Drift chamber: Loads and Criteria**

In a gas mixture, a charged particle (an electron, a proton, a muon, a kaon, . . . ) traversing the gas volume, ionises the gas leaving a trail of electron-positive ion pairs along its trajectory. If an electric field is generated the electrons, which move much faster than the positive ions, will immediately drift towards the anodic wires (positively charged), generating an electric signal which is properly amplified in order to be detected by the external sensors. Correlating the position of the hit wire and the time delay of the signal, it is possible to reconstruct in space, the position of the charged particles and its trajectory. The accuracy of the position is in the range of 100-200 micron. Therefore, the position of the anodic wire in space must be known with an accuracy better than 50 micron at most.

Now, a thin wire (20-50 micron diameter), suspended at its extremities (end plates)

## CHAPTER 2. PRELIMINARY DESIGN: DEVELOPMENT OF A FINITE ELEMENT MODEL

---

when subjected to gravity, as it is in a drift chamber, will bow in space according to a catenary. A 20 micron tungsten wire, 2 m long, will bow about 100 micron at its middle point, if tensioned with a load of approximately 25 grams. Higher loads will decrease the bowing, however, it increases the risk of yielding or breaking. This gives rise to a problem, since it is necessary to keep the anodic and cathodic wires parallel in space to preserve the constant electric field. Another problem arise due to the fact that the anodic and cathodic wire, being charged at opposite voltages, will be attracted to each other and, being suspended at their extremities, will get closer in the middle. This might cause a short circuit which can only be avoided if the mechanical tension in the wires is further increased. This is the origin of the load on the end plates of the drift chamber (Figure 2.4).

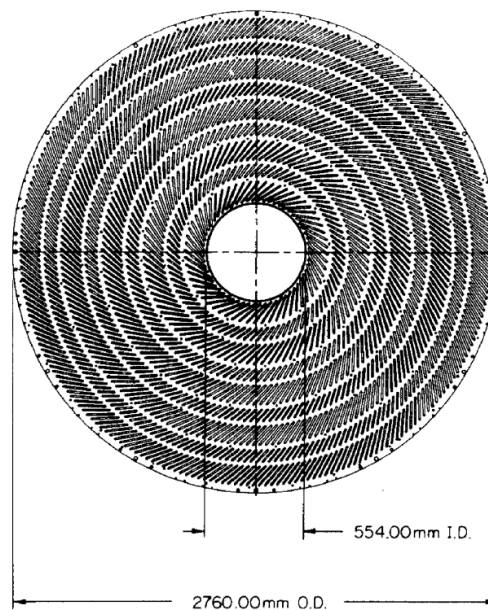


Figure 2.4: Drift cells arranged in 9 super layers at the end plate which are the origin of the load in drift chamber. Adapted from *Walter Blum, Werner Riegler, and Luigi Rolandi. Particle detection with drift chambers. Springer Science Business Media, 2008 [6]*

In our specific case, we have approximately 56,000 anodic wires (20 micron diameter tungsten) and 280,000 cathodic wires (40 and 50 micron diameter aluminum wires), at an average of 30 grams per wire, and we obtain approximately 10 tonnes of total load. The drift chamber is radially divided in 14 super-layers of wires, arranged azimuthally in an

## CHAPTER 2. PRELIMINARY DESIGN: DEVELOPMENT OF A FINITE ELEMENT MODEL

integer number of cells (a set a 5 cathodic wires surrounding an anodic wire) as shown in Figure 2.5. Clearly, from one super-layer to the next, the cell size increases with the radius of the chamber and in order to keep it approximately constant (around  $1.5 \text{ cm}^2$ ), Istituto Nazionale di Fisica Nucleare (INFN) has decided to increase the number of cells from one super-layer to the next. For our calculations, therefore, we can consider having the 10 tonnes load as uniformly distributed over the surface of the end plates ( $80,000 \text{ cm}^2$ ) in  $1.5 \text{ cm}^2$  units of 180 grams each.

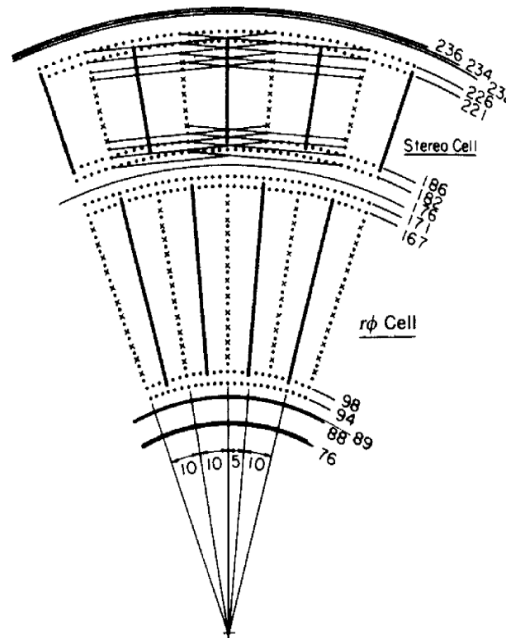


Figure 2.5: Wire pattern of the OPAL vertex chamber showing increasing wire load from one layer to another as the radius increases. This is the reason of uniformly varying pressure. Adapted from *Walter Blum, Werner Riegler, and Luigi Rolandi. Particle detection with drift chambers. Springer Science Business Media, 2008 [6].*

### 2.4 Initial Concept of the IDEA drift chamber

Istituto Nazionale di Fisica Nucleare (INFN) conceptualized the initial geometry of the IDEA drift chamber (Figure 2.6). Slightly bigger than MEG-II drift chamber (2018), IDEA drift chamber has inner and outer diameter of the cylinders equal to 700 mm and

## CHAPTER 2. PRELIMINARY DESIGN: DEVELOPMENT OF A FINITE ELEMENT MODEL

---

4000 mm respectively. The total length of the drift chamber is 4500 mm whereas the active length is 4000 mm only. The spokes which carry the main load are 1 mm x 3 mm, distributed radially from the inner to outer cylinder. Each spoke is supported by a system of very thin 0.5 mm diameter wires (Figure 2.7 (b)). The gas containment of the chamber (Figure 2.7 (a)) can be excluded from our problem and wire cage support (Figure 2.7 (b)) is of interest in this thesis. There are two end plates in the drift chamber of which we will focus our design in only one. This is our first simplification of the problem and the reason is due to the fact that both end plates are structurally similar, made up of same material and subjected to same load. The design of one should automatically satisfy the design of another. The end plate is made up of 24 spokes with a sectoral angle of  $15^\circ$  hence we reduce the problem to axisymmetric one. This is the second simplification. Both of these simplifications greatly reduce the dimensionality (1/48 times) of the problem.

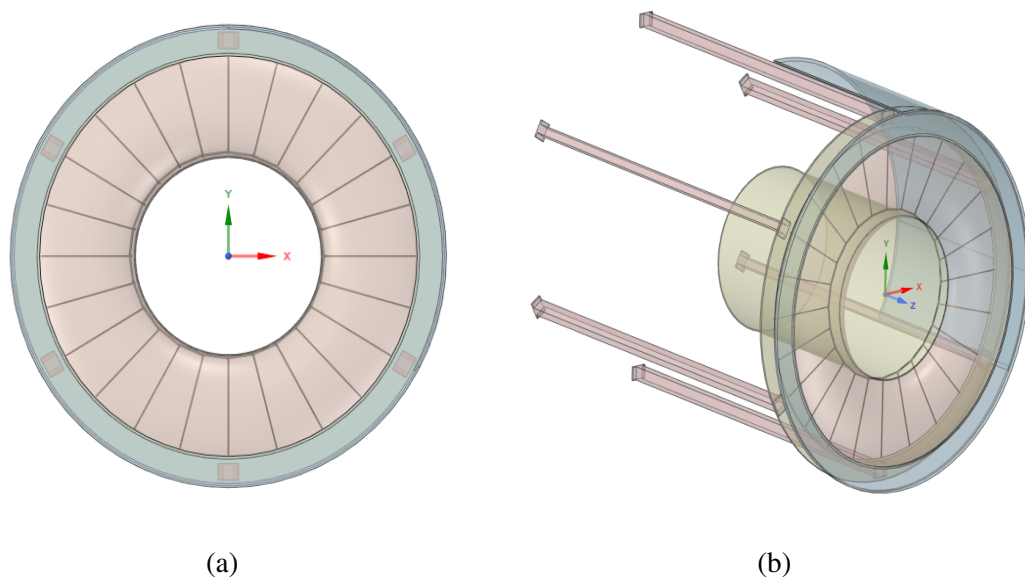


Figure 2.6: Initial concept of the IDEA drift chamber proposed by Istituto Nazionale di Fisica Nucleare (INFN) a) Endplate of the drift chamber showing outer ring, inner ring and spokes b) Isometric view of the IDEA drift chamber

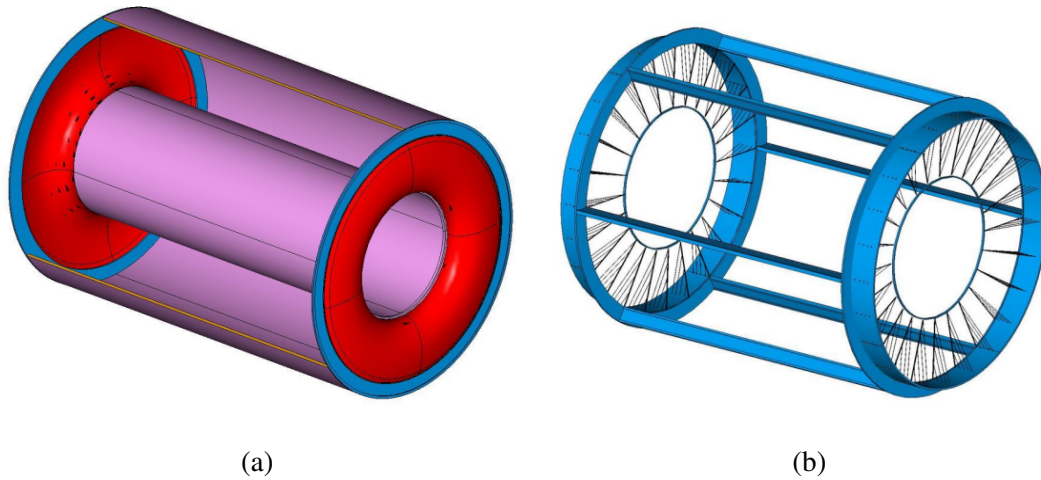


Figure 2.7: a) Gas containment in which the gas vessel can freely deform without affecting the internal wire position and mechanical tension. b) Light Wire Cage support structure with Feed-through less wiring

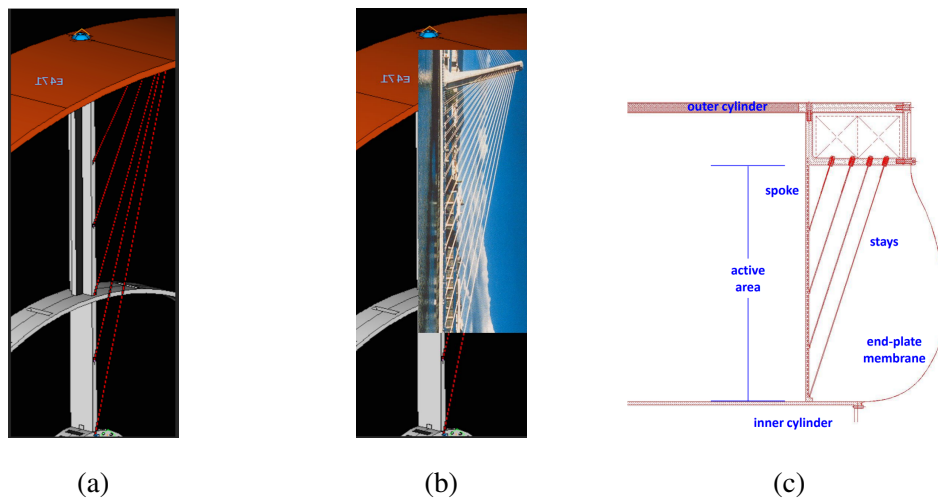


Figure 2.8: a) Mu2e I-Tracker cage showing connectivity of the cables, spokes and outercylinder b) An analogy between Mu2e I-Tracker cage and a harp bridge c) A section of a wire cage support

The cables together with the spokes and the outer ring (Figure 2.8 (a)-(c)) are analogous to the harp cable stayed bridge (Figure 2.8 (b)). The outer ring acts as a tower whereas the spokes acts as a deck. The forces in the cables are tuned in such a way that the deformation in the spokes is minimum.



## 2.5 Development of the Numerical Model

“For reasons nobody understands, the universe is deeply mathematical. Maybe God made it that way. Or maybe it’s the only way a universe with us in it could be, because nonmathematical universes can’t harbor life intelligent enough to ask the question. In any case, it’s a mysterious and marvelous fact that our universe obeys laws of nature that always turn out to be expressible in the language of calculus as sentences called differential equations [21].” The nature is filled with riddles we cannot solve, but it is also reassuring that the complexity we find in nature can be studied with the help of mathematical models and differential equations. Numerical model is a mathematical abstraction of a physical phenomena and process that explores its behaviour and predict its outcomes. Another aspect is to understand what to abstract. A full detailed abstraction may not necessarily mean a better numerical model. However, a very simplified model can miss the details governing the dynamics of our physical system. A right balance between these two is necessary. Sometimes simple models can outperform more complex mathematical models. This phenomenon is known as the "paradox of simplicity" and challenges the assumption that more complex models are always better. This highlights the importance of considering simplicity and interpretability when developing mathematical models. The following subsections provide a general idea of the approach taken to model the structure while ensuring certain design criteria and requirements are met. The aim of this section is to create a base model, on which a parametric study (Chapter.3) and an optimization of the cable tuning forces (Chapter.5) will be based upon.

**ANSYS Workbench** Computer simulations are carried out using ANSYS Workbench environment within which various modules are available each designed for a specific task. The geometry is created in SpaceClaim and the static structural analysis is done in ANSYS Mechanical. ANSYS Mechanical is a large-scale multipurpose finite element program which can be used for solving several classes of engineering problems. The user of the ANSYS can benefit of a very well explained user manual and the verification manual on benchmark problems reflects its credibility.

### 2.5.1 Engineering Data

The aim of the IDEA drift chamber project is to design an ultra-light drift chamber in composite materials which is an orthotropic layered material. But we begin our initial preliminary studies with a material having same orthotropic properties as composite (Figure 2.9 (a)), but to form the structure (surfaces and beams), no layers are used. In a simple way, it can be thought that we are using a general material like structural steel whose material properties are that of the composite. The reason to do so is that our initial design is deformation based and we are mainly concerned with analyzing the deformation and reducing it to minimum. Stresses and corresponding strains are also taken into account, but do not govern the initial preliminary design. Secondly, a full simulation time for composite model like ours takes more than half an hour whereas for orthotropic material with same elastic properties takes only few seconds. So performing parametric study and optimization on such orthotropic material would be an obvious choice. Finally, the understanding of such simple models to which we are very familiar with, can help us formulate the problems in a better way than layered composites. For example, to define the buckling, we need an axial force. However, for composite the output are the in plane stresses on each ply. So if we want the total axial force in cross-section, we would have to sum it up. However for solid models, the beam results directly gives us the axial force. For the cables, structural steel (Figure 2.9 (b)) is used.

## CHAPTER 2. PRELIMINARY DESIGN: DEVELOPMENT OF A FINITE ELEMENT MODEL

	A	B	C	D	E
1	Property	Value	Unit		
2	Density	1800	kg m <sup>-3</sup>		
3	Orthotropic Elasticity				
4	Young's Modulus X direction	2,3E+11	Pa		
5	Young's Modulus Y direction	2,3E+10	Pa		
6	Young's Modulus Z direction	2,3E+10	Pa		
7	Poisson's Ratio XY	0,2			
8	Poisson's Ratio YZ	0,4			
9	Poisson's Ratio XZ	0,2			
10	Shear Modulus XY	9E+09	Pa		
11	Shear Modulus YZ	8,2143E+09	Pa		
12	Shear Modulus XZ	9E+09	Pa		

(a)

	A	B	C	D	E
1	Property	Value	Unit		
2	Material Field Variables	Table			
3	Density	7850	kg m <sup>-3</sup>		
4	Isotropic Secant Coefficient of Thermal Expansion				
5	Coefficient of Thermal Expansion	1,2E-05	C <sup>-1</sup>		
6	Isotropic Elasticity				
7	Derive from	Young's Modulus and...			
8	Young's Modulus	2E+11	Pa		
9	Poisson's Ratio	0,3			
10	Bulk Modulus	1,6667E+11	Pa		
11	Shear Modulus	7,6923E+10	Pa		
12	Strain-Life Parameters				
20	S-N Curve	Tabular			
24	Tensile Yield Strength	2,5E+08	Pa		
25	Compressive Yield Strength	2,5E+08	Pa		
26	Tensile Ultimate Strength	4,6E+08	Pa		
27	Compressive Ultimate Strength	0	Pa		

(b)

Figure 2.9: a) Properties of the Carbon fiber modelled as an equivalent orthotropic material for cylinders and spokes b) Properties of the Structural steel which are used for the cables

### 2.5.2 Geometry

Geometry is created in SpaceClaim which can be used for direct 3D modelling for rapid concept design and geometry manipulation. The geometry is an assemblage of surface and line bodies hence is treated as multibody parts. The geometry of the model determines the shape of the finite elements used to represent the physical domain. Consequently, accuracy is heavily dependent on how well these elements represent the actual geometry.

## CHAPTER 2. PRELIMINARY DESIGN: DEVELOPMENT OF A FINITE ELEMENT MODEL

---

Also, computational effort is directly proportional to the complexity of the geometry.

### Surface Bodies

If one dimension is 10 times smaller than other one can be categorised as thin structures. Ideally, solid elements can be used to model them but they require an aspect ratio close to 1. Modelling thin structures using solid element will significantly increase the aspect ratio and we begin to observe poor results. The alternative could be to generate very fine mesh with good aspect ratio, but the computational time will increase a lot. The shell element can be efficient in such case which are spatially 3D but geometrically 2D elements. Their thickness is not defined explicitly but is directly taken into section property. Each node has 6 degrees of freedom. The shell element incorporates both membrane and bending behaviour. The membrane stiffness is higher than bending stiffness. Shell element also has a state of plane stress (zero stress in thickness direction). The element coordinate system must also be carefully checked and aligned as the results are reported in this coordinate system. The local Z axis (blue) will be normal to the surface and X axis (red) will be aligned in the circumferential direction (Figure 2.10 (a)(b)). The third axis will be perpendicular to both (green).

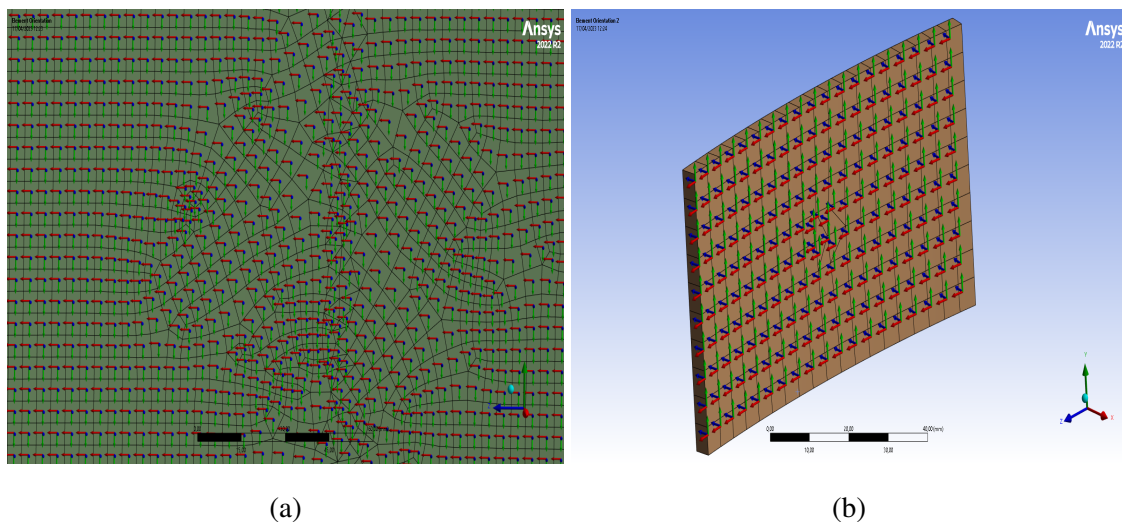


Figure 2.10: a) Element orientation for the outer cylinder b) Element orientation for the inner cylinder

## CHAPTER 2. PRELIMINARY DESIGN: DEVELOPMENT OF A FINITE ELEMENT MODEL

---

The outer and the inner cylinders are created as surfaces with 4 mm thickness and flexible stiffness behaviour meaning the surface is allowed to deform. Surface bodies have a normal direction indicated by green. The shell midsection is aligned with the surface body is our choice. However, using the offset type, the shell can be aligned to top (Figure 2.11 (a)) , middle (Figure 2.11 (b)) , bottom (Figure 2.11 (c)) or user defined . An eccentricity is generated when shell is aligned with top, bottom or any other user defined plane.

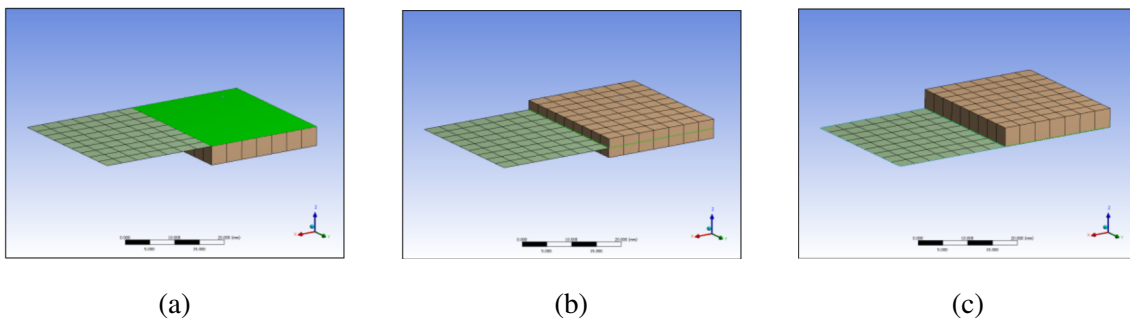


Figure 2.11: Schematic showing alignment of the surface section with (a) top, (b) middle and (c) bottom respectively

### Line Bodies

For slender geometry ( Slenderness Ratio  $=GAL^2/EI \geq 30$  ) , line bodies may yield computationally efficient as well as numerically accurate results. The cables and the spokes are created as line bodies and can further be defined as Beam, Pipe, Link/Truss, Cable etc. Spokes are created as Beam elements (BEAM 189) which is suitable for thin and moderately thick beam structures whereas Cables<sup>1</sup> are created as Truss elements (LINK 180). While it is possible to accurately capture the response of the beam like structure accurately using Beam elements, attributes such as highly local deformation cannot be captured with this element. Using solid elements for very slender structures poses the same modelling problem of modelling surface bodies as mentioned in Paragraph Surface Bodies. The output quantities for beam ( axial , bending , torsion and shear) is directly

---

<sup>1</sup>Cables refer to the structural element supporting the spokes. They do not necessarily mean Cable as in finite element. Instead they are modelled with Truss elements.

## CHAPTER 2. PRELIMINARY DESIGN: DEVELOPMENT OF A FINITE ELEMENT MODEL

calculated <sup>2</sup>. For slender structures, axial and bending behaviour can be separately studied which is tedious in solid modelling. The final advantage is that the cross section properties can be assigned and changed iteratively which is important in preliminary design studies. However, it should be noted that the output has a simplified stress state (3 components of stress only) and reported on element coordinate system. The X axis is along the axis of the beam and other two axes are in plane perpendicular to each other (Figure 2.12).

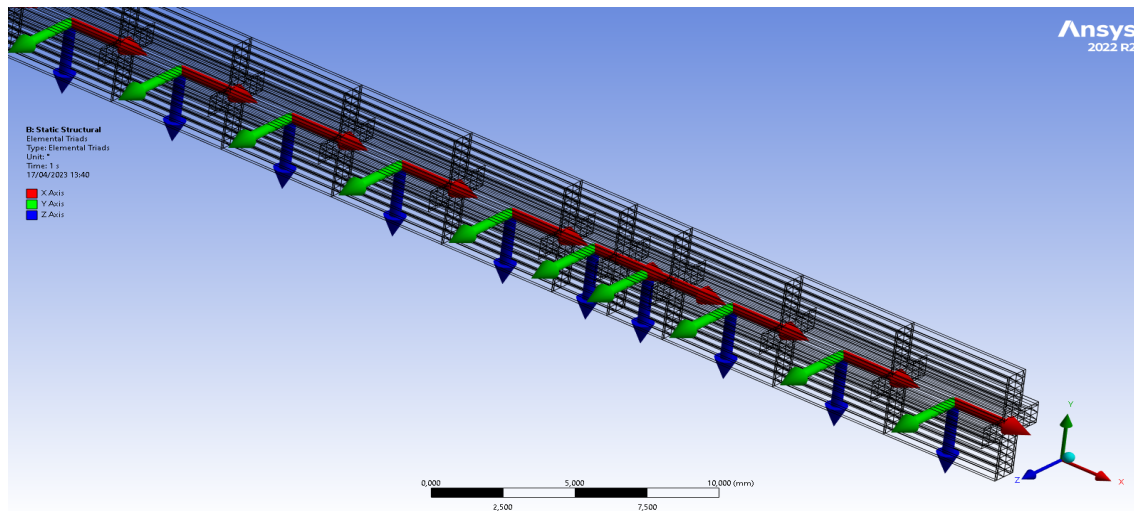


Figure 2.12: Inspection of the element coordinate system using element triads which shows the orientation with respect to global coordinate system. In our case, it varies according to time step and nodes.

For the cables, a circular cross section with 0.5 mm diameter is assigned using a beam profile <sup>3</sup> and then a truss element is assigned to it. For the Spokes, the cross section to the line element has been assigned by extraction of the solid. It can be noted that the cross section coordinate system of the SpaceClaim and the static structural are different. The cross section lies in XY plane in SpaceClaim and Z is the edge tangent. The cross section lies in YZ plane in ANSYS mechanical and X is the edge tangent. This means the Moment of inertia about  $I_{xx}$  in SpaceClaim becomes  $I_{yy}$  in ANSYS Mechanical. After creating a geometry, two planes can be defined on the higher and lower edge which will

<sup>2</sup>Path dependent results such as Shear-Moment diagrams for symmetry imposed bodies is not available in ANSYS Mechanical

<sup>3</sup>Beam profile has to be used to define a cross section to an element and later be assigned the proper finite element type

be later used to define cyclic symmetry in our structure. There are some limitations on the numerical model due to the choice of line bodies. The first one is that only uniformly distributed line pressure can be applied instead of uniformly varying line pressure on the spokes. The second is that mesh convergence studies cannot be performed.

### Assembly of the components: Coincident Topology Sharing

In order to develop a connection or interaction between independent parts, a connection has to be defined even if the parts are touching each other. If the interactions are not defined correctly, the simulation results will be misleading or wrong. For large assemblies, this can be tedious and time-consuming work. We have two options to define the connection between neighbouring parts. The first one is to create a shared topology in SpaceClaim (Figure 2.13 (a)).

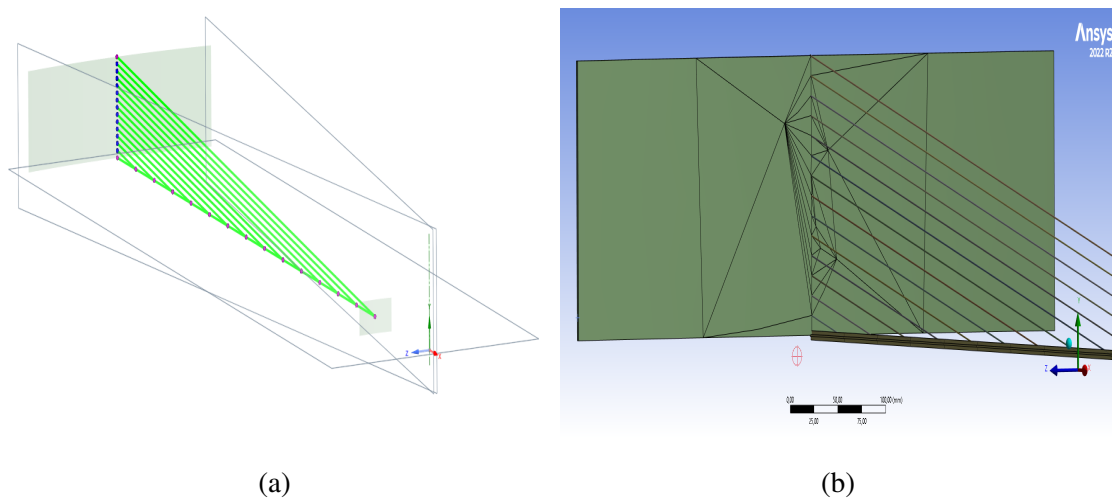


Figure 2.13: a) A sector of our drift chamber representing cyclic symmetry. The two planes defined on XY plane are low and high region of cyclic symmetry. The dots represent that the coincident topology has been shared between the connecting parts b) Conformal mesh is generated in the ANSYS mechanical even when the quality of the element is worst.

The parts are bonded or welded together and the interface between two parts is shared. It has shared nodes on the interface between two parts as a result the mesh generated is conformal (continuous) between the two parts (Figure 2.13 (b)). The degrees of freedom

## CHAPTER 2. PRELIMINARY DESIGN: DEVELOPMENT OF A FINITE ELEMENT MODEL

---

are continuous and noise around the contact region are suppressed. The second one is to define contacts manually in ANSYS Mechanical which is described in detail in Chapter.7 (section 7.1). Currently, we prefer to use the Coincident topology sharing.

### 2.5.3 Model Setup

Once the geometry has been prepared, the next step is to export the model in the static structural within the Workbench environment. However, it is important to note that the active unit system specified in the previous sessions (e.g: SpaceClaim) are consistent. Also, even if the material has been previously defined in Engineering data, for secondary imports, a manual assignment is necessary. The stiffness behaviour of the parts are set to be flexible, the default coordinate system is the Global coordinate system (0,0,0) and the reference temperature is taken is 22 degrees Celsius.

#### Consistent Unit System

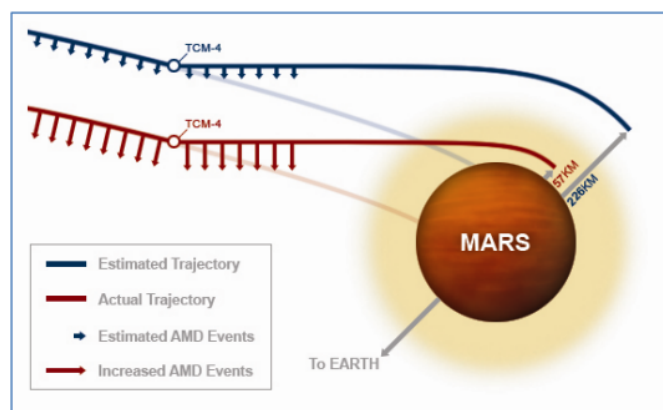


Figure 2.14: Failure to comply with the unit conversion resulted Mars Climate Orbiter to miss the planned trajectory. No verification and validation had been done for the software. Figure adapted from *Mishap Investigation Board. Mars climate orbiter mishap investigation board phase i report november 10, 1999, 1999*[27]

On September 23, 1999, Mars Climate Orbiter, launched by NASA, after entering Mars orbit was lost. Later, investigation revealed that the failure resulted due to the signal from



## CHAPTER 2. PRELIMINARY DESIGN: DEVELOPMENT OF A FINITE ELEMENT MODEL

---

Earth being sent in English units (pound-seconds) without being converted into the metric standard (Newton-seconds) [27]. This caused the Spacecraft to miss the trajectory by nearly 150 Kilometers.

Unit system is a very fundamental but crucial concept. In physics quantities such as length, mass, time, temperature and electric current are the base quantities of the measurement and are called fundamental quantities and their corresponding units are known as the fundamental units. Other physical quantities can be measured by using derived units which are obtained by combining these fundamental units. A unit system is said to be consistent if the derived units of the chosen system can be expressed in terms of the fundamental units without conversion factors. Finite element solvers only understand the values and not the units. Hence, without the proper conversion factors, there would be a unit mismatch. Such errors are common in finite element programs without in built unit system. Particular care has to be taken for the conversion factor. In addition, during computation there might be round off and truncation error and such errors are cumulative in nature. Typically, the most accurate results are obtained if the units are chosen such that the values of the input quantities to the numerical simulation are close to unity. By having the input quantities close to unity, the influence of round-off errors and truncation errors are reduced. In case of ours, the value of load can be converted to 2.52 N/mm (equivalent UDL) therefore we use the Newton, millimeter and seconds.

### **Mesh Setup**

Meshing is a process in which our geometry (domain) is spatially discretized into finite elements and nodes. The mesh along with material properties defines the stiffness and the mass distribution in our structure. Mesh plays an important part in obtaining a precise and accurate solution. Too coarse mesh may produce incorrect results or not even produce result at all due to excessive element distortion or lower element quality causing convergence issues. On the other hand, very fine mesh can make the computational task demanding. In some cases, we can run out of memory too. A mesh convergence study must be done and the solution must be mesh independent. In ANSYS Workbench, both the

## CHAPTER 2. PRELIMINARY DESIGN: DEVELOPMENT OF A FINITE ELEMENT MODEL

---

SpaceClaim and ANSYS Mechanical can be used to develop high quality meshes. In our case, we simply choose the ANSYS Mechanical to generate the Mesh. For the spokes, we have used BEAM189, 3-Node nonlinear beam element. Even though ANSYS Mechanical uses Timoshenko Beam theory by default which is suitable for thick beams to include the shear deformation effects. This element corresponds to Euler beam when the beam is very slender and shear strain is zero. The governing equations of Timoshenko beam theory in terms of the deflection  $w$  and rotation  $\Psi$  are;

$$-\frac{d}{dx} \left[ GAK_s \left( \Psi + \frac{dw}{dx} \right) \right] + c_f w = q \quad (2.8)$$

$$-\frac{d}{dx} \left( EI \frac{d\Psi}{dx} \right) + GAK_s \left( \Psi + \frac{dw}{dx} \right) = 0 \quad (2.9)$$

where  $G$  is the shear modulus and  $K_s$  is the shear correction coefficient, which is introduced to account for the difference in the constant state of shear stress timoshenko beam theory and parabolic variation of the shear stress computed by the elasticity theory. For short and chubby beams (i.e., length-to-height ratio less than 20),  $\Psi \neq -(dw/dx)$  and the difference,  $\Psi + (dw/dx)$ , is the transverse shear strain. When the shear strain is zero (i.e., for long slender beams), substituting equation 2.9 into equation 2.8, we obtain governing equation of the Euler-Bernoulli beam theory.

$$\frac{d^2}{dx^2} \left( EI \frac{d^2 w}{dx^2} \right) + c_f w = q(x) \text{ for } 0 < x < L \quad (2.10)$$

The cables supporting the spokes are LINK180 elements with 2 nodes, no bending or shear effects, no pressures, and the entire element has only one integration point. The element is not capable of carrying bending loads. The stress is assumed to be uniform over the entire element. For the surfaces, SHELL281 is used which is 8 node shell element. A membrane option is also available for this element and uses an equivalent energy method to compute shear-correction factors.

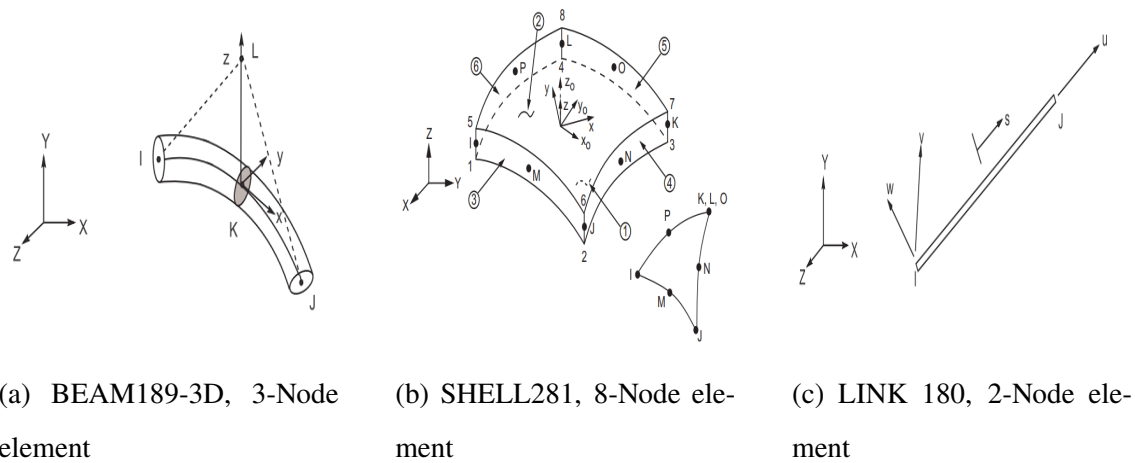


Figure 2.15: Different types of finite elements used in our numerical model

### Element Testing

The element generated by the meshing options must be checked for their appropriate shape. The appropriateness of an element is calculated by using shape parameters and help us also to define the quality of our mesh (Figure 2.16) . The acceptability depends on element shape limits whose default values are functions of element type and settings.

**Aspect Ratio** Aspect ratio is one of the easiest to understand shape measure in finite element. An equilateral triangle and a square quadrilateral has an aspect ratio of 1. Deviation from these shape will increase the aspect ratio. Aspect ratio of an element alone does not have a correlation with numerical accuracy unless the aspect ratio is  $> 1000$ . In such case, numerical round off errors are introduced. For preliminary stage , an aspect ratio less than 5 for majority of elements (90 % and above ) is acceptable.

**Angle deviation** Angle deviation is computed only for shell elements and is based the largest deviation from  $90^\circ$  of any of the 4 corner angles of the element. The best configuration is  $0^\circ$  and deviations from this means lower quality.

**Jacobian Ratio** Jacobian ratio is widely used mesh metric and indicates the mapping between the element space and the real space. Nonetheless, it is also directly related to the

## CHAPTER 2. PRELIMINARY DESIGN: DEVELOPMENT OF A FINITE ELEMENT MODEL

---

geometry of the element created. Based upon the sampling location which may be nodes or in some cases gaussian integration points, a determinant of the jacobian is computed. This determinant represents the mapping between the element natural coordinate and real space. For ideal shape element, the determinant is constant.

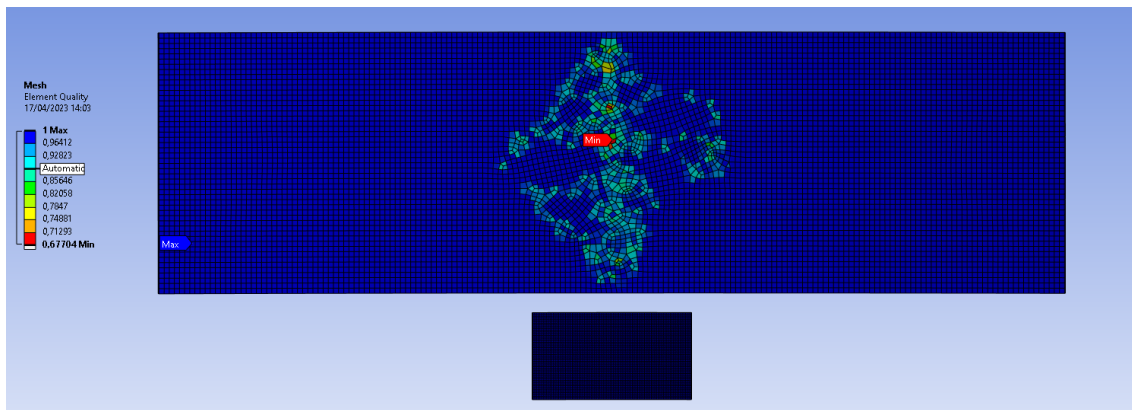


Figure 2.16: Mesh/element quality of the outer (3 mm element size) and inner cylinder (1 mm element size).

### Loading

We have mentioned previously in the Section 2.1 about the loads in a detailed way. The loads are uniformly varying with maximum value (5.050 N/mm) at the outer cylinder to a minimum value (0 N/mm) at the inner cylinder. The spokes are modelled with line element hence only uniformly distributed line pressure is allowed. We model the load as an uniformly distributed line pressure with an equivalent value of uniformly varying line pressure (Figure 2.17). In both case, we expect the deformation to be almost equivalent. The assumption is reasonable in preliminary stage of design.

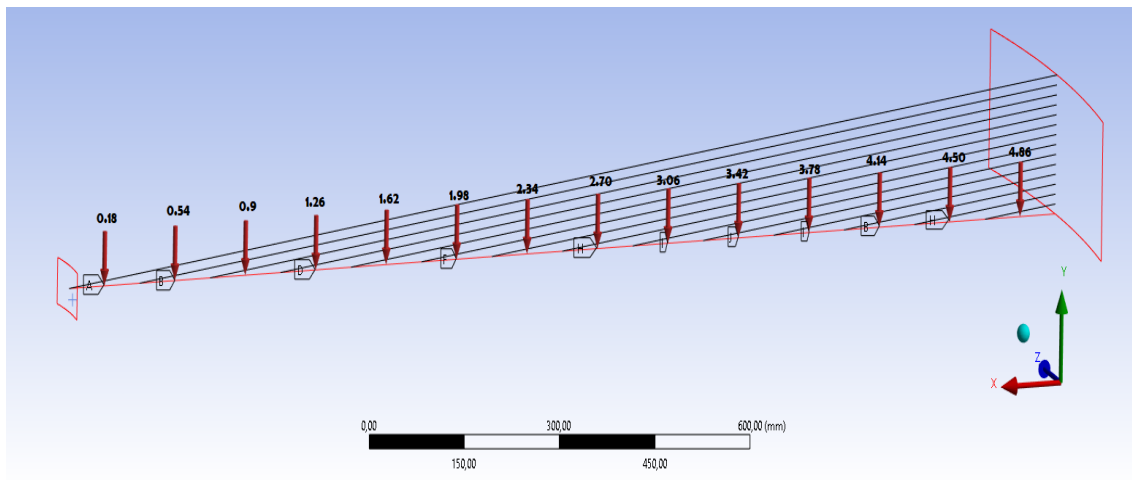


Figure 2.17: Uniformly varying load is treated as series of equivalent uniformly distributed load

Application of pressure can induce additional stiffness contribution in structure called the "Pressure load stiffness" effect if the load is defined normal to the face or edge. This is because pressure acts as a follower load, which means that it continues to act in a direction normal to face or edge even when the structure is in deformed configuration. However, pressure loads defined with the vector components act in a constant direction even as the structure deforms. The loads are applied in a single time step. However, sometimes convergence issues may arise when high loads are applied in a single time step. In such cases, the load can be applied in several stages. However, the computational time will increase significantly. It is very important to note that even the unconverged solution will be given as an output. Such output must be read properly from the output files and the underlying reason must be investigated.

### Boundary conditions

In mathematics, in order to solve a set of differential equations, a condition has to be met at all or part of the boundary of a region in which the solution is sought. This set of conditions is called boundary conditions. In mechanics, boundary conditions are also conditions stated in terms of variables. Most common boundary condition is Dirichlet boundary conditions, which consist of imposing the displacement. Neumann condition,

also called “natural” because it naturally appears in the the weak formulation, is generally used in cases in which a temporal dependency is solved. It is usually an easy task to identify the type of boundary condition to be applied in common engineering problems such as pier of a bridge or foundation of a building unless the problem is rather sophisticated. In many engineering problems, choosing the right type of boundary conditions are very obvious, due to the fact that the basic theoretical principles as well as engineering practices have validated and justified the assumptions over decades. However, in a problem like ours, the definition of the correct boundary condition is not trivial. It has to be carefully chosen, justified and validated. There are two initial boundary conditions that we choose to implement. The first one is fixing the face of the outer cylinder so as to make it completely undeformable and the second one is fixing the edge of the outer cylinder so as to take into account the deformability of the outer cylinder and see its effect. Although, the drift chamber does not have the outer face completely fixed in reality, exploring this boundary condition might be helpful. Sometimes the boundary conditions may not be sufficient to constrain the degrees of freedom of a body. This is indicated by a message “NEGATIVE PIVOT . . .” In virtually all circumstances, matrices representing the complete structure with the appropriate boundary conditions must be positive definite.

#### 2.5.4 Analysis

The analysis of the numerical model is related to solving the equilibrium equations for the primary unknown quantity which is displacement and then solving secondary quantities such as strains and stresses with respect to that.

##### Solving for unknown reaction and forces

In case of static linear analyses,

$$[K]\{u\} = \{F\} \quad (2.11)$$

$$\text{or, } [K]\{u\} = \{F^a\} + \{F^f\} \quad (2.12)$$

## CHAPTER 2. PRELIMINARY DESIGN: DEVELOPMENT OF A FINITE ELEMENT MODEL

---

where;

$[K]$  = total stiffness matrix =  $\sum_{m=1}^N [K_e]$

$\{u\}$  = nodal degree of freedom (DOF) vector

$N$  = number of elements

$[K_e]$  = element stiffness

$\{F^r\}$  = nodal reaction load vector

The total applied load vector,  $\{F^a\}$ ,

$$\{F^a\} = \{F^{nd}\} + \{F^e\} \quad (2.13)$$

where;

$\{F^{nd}\}$  = applied nodal load vector

$\{F^e\}$  = total of all element load vector effects (pressure, acceleration, gravity)

If sufficient boundary conditions are specified, Equation 2.11 yields a unique solution  $\{u\}$  at each node in the model.

Rewriting Equation 2.12 by separating out the matrix and vectors into those DOFs with and without imposed values,

$$\begin{bmatrix} [K_{cc}] & [K_{cs}] \\ [K_{cs}]^T & [K_{ss}] \end{bmatrix} \begin{Bmatrix} \{u_c\} \\ \{u_s\} \end{Bmatrix} = \begin{Bmatrix} \{F_c^a\} \\ \{F_s^a\} \end{Bmatrix} + \begin{Bmatrix} \{F_c^r\} \\ \{F_s^r\} \end{Bmatrix} \quad (2.14)$$

where;

$s$  = DOFs with imposed values (specified DOFs)

$c$  = DOFs without imposed values (computed DOFs)

Note that  $\{u_s\}$  is known, but may or may not be equal to  $\{0\}$ . Since the reactions at DOFs without imposed values must be zero, Equation 2.14 can be written as:

$$\begin{bmatrix} [K_{cc}] & [K_{cs}] \\ [K_{cs}]^T & [K_{ss}] \end{bmatrix} \begin{Bmatrix} \{u_c\} \\ \{u_s\} \end{Bmatrix} = \begin{Bmatrix} \{F_c^a\} \\ \{F_s^a\} \end{Bmatrix} + \begin{Bmatrix} \{0\} \\ \{F_s^r\} \end{Bmatrix} \quad (2.15)$$

The first row of Equation 2.15 may be solved for  $\{u_c\}$  :

$$\{u_c\} = [K_{cc}]^{-1} (- [K_{cs}] \{u_s\} + \{F_c^a\}) \quad (2.16)$$

### Reaction Forces

The reaction vector  $\{F_s^r\}$ , for linear models from the second row of Equation 2.15:

$$\{F_s^r\} = [K_{cs}]^T \{u_c\} + [K_{ss}] \{u_s\} - \{F_s^a\} \quad (2.17)$$

The nodal reaction load vector may be alternatively obtained by combining Equation 2.12 and Equation 2.13 to get:

$$\{F^r\} = [K] \{u\} - \{F^{nd}\} - \{F^e\} \quad (2.18)$$

where only the loads at imposed DOFs are output. The transient/dynamic effects can also be added wherever applicable:

$$\{F^r\} = [M] \{u\} + [C] \{u\} + [K] \{u\} - \{F^{nd}\} - \{F^e\} \quad (2.19)$$

where;

$[M]$  = total mass matrix

$[C]$  = total damping matrix

The element static nodal loads are:

$$\{F_e^k\} = - [K_e] \{u\} + \{F^e\} \quad (2.20)$$

where;

$\{F_e^k\}$  = element nodal loads

e = subscript for element matrices and load vectors



The element damping and inertial loads are:

$$\begin{aligned}\{F_e^c\} &= - [C_e] \{\dot{u}\} \\ \{F_e^m\} &= - [M_e] \{\ddot{u}\}\end{aligned}$$

where;

$\{F_e^D\}$  = element damping nodal load

$F_e^I$  = element inertial nodal load.

Thus,

$$\{F^r\} = - \sum_{e=1}^N [\{F_e^K\} + \{F_e^C\} + \{F_e^m\}] - \{F^{nd}\} \quad (2.21)$$

The derivatives of the nodal DOF with respect to time are:

$\{\dot{u}\}$  = first derivative of the nodal DOF with respect to time, e.g. velocity

$\{u\}$  = second derivative of the nodal DOF with respect to time, e.g. acceleration

### 2.5.5 Solution Procedures and Algorithms

The system of simultaneous linear equations generated by the finite element procedure has to be solved for  $\{u\}$ . This is done by using a direct elimination process or an iterative method. The direct elimination process is a Gaussian process and involves decomposition of the stiffness matrix  $[K]$  into lower and upper triangular matrices,  $[K] = [L][U]$  followed by forward and back substitutions to compute the displacement vector  $\{u\}$ .

On the other hand, an iterative method involves an initial prediction  $\{u\}_1$ , for the displacement vector  $\{u\}$  and then a successive steps of iteration are performed using  $\{u\}_2$ ,  $\{u\}_3, \dots$  such that, in the limit,  $\{u\}_n = \{u\}$  as  $n$  tends to infinity. The solution converges based on specified tolerance after a finite number of iterations. The iterative solvers are fast in comparison to direct solvers which are by default solvers for ANSYS. We will exploit this benefit of iterative solvers in subsequent chapters.

### Direct Solver

Sparse Direct Solver is the available solver in ANSYS and exploits the fact that stiffness matrices are normally sparsely populated. This allows in solving the simultaneous equations efficiently. The equation is solved by triangular decomposition of matrix  $[K]$  to yield the following equation:

$$[L][U]\{u\} = \{F\} \quad (2.22)$$

where;

$[L]$  = lower triangular matrix

$[U]$  = upper triangular matrix

By substituting:

$$\{w\} = [U]\{u\} \quad (2.23)$$

we can obtain  $\{u\}$  by first solving the triangular matrix system for  $\{w\}$  by using the forward pass operation given by:

$$[L]\{W\} = \{F\} \quad (2.24)$$

and then computing  $\{u\}$  using the back substitution operation on a triangular matrix given by:

$$[U]\{u\} = \{w\} \quad (2.25)$$

When  $[K]$  is symmetric, the above procedure could use the substitution:

$$[K] = [L][L]^T \quad (2.26)$$

However, it is modified as:

$$[K] = [L'] [D] [L']^T \quad (2.27)$$

where;

$[D]$  = a diagonal matrix

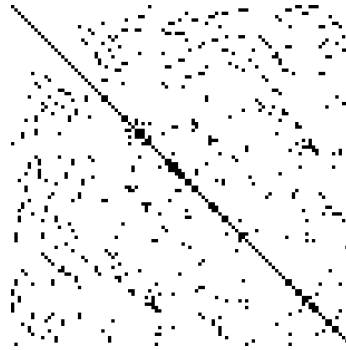


Figure 2.18: A typical sparse matrix in finite element problem with non zero elements in black dots. Adapted from *Wikipedia. Sparse matrix — Wikipedia, the free encyclopedia*[28].

The diagonal terms of  $[D]$  may be negative in the case of some nonlinear analysis. In that case,  $[L']$  is generated without the consideration of a square root of negative number. Therefore, Equation 2.22 through Equation 2.25 become:

$$[L'] [D] [L']^T \{u\} = \{F\} \quad (2.28)$$

$$\{w\} = [D] [L']^T \{u\} \quad (2.29)$$

$$[L'] \{W\} = \{F\} \quad (2.30)$$

and

$$[D] [L']^T \{U\} = \{F\} \quad (2.31)$$

$[K]$  is normally sparsely populated with non-zero coefficients dominantly located around the main diagonal (Figure 2.18). The Sparse Direct Solver handles only the nonzero entries in  $[K]$ . During the Cholesky decomposition of  $[K]$  shown in Equation 2.22 or Equation 2.28, nonzero coefficients appear in  $[L]$  or  $[L']$  at locations where  $[K]$  matrix had zero entries[29]. The Sparse Direct Solver algorithm minimizes this fill-in by reordering the equation numbers in  $[K]$  and consequently the performance of a direct solution method is greatly enhanced[29]. The rows and columns of  $[K]$  and the rows of  $\{F\}$  are rearranged with the objective of minimizing fill-in. So, when the decomposition step in Equation 2.22 or Equation 2.28 is performed on the reordered  $[K]$  matrix, the fill-in that occurs

in  $[L]$  or  $[L']$  matrix is kept to a minimum [29]. This greatly enhances the performance of the Sparse Direct Solver. To achieve minimum fill-in, different reordering algorithms are available in the literature [30]. The Sparse Direct Solver is based on two different reordering techniques: Minimum Degree ordering and the METIS ordering [29]. This is automatically chosen by the solver algorithm.

### Iterative Solver

In computational mathematics, iterative solvers refer to a class of solvers which use an initial value to generate an approximate solution in which the  $n^{\text{th}}$  solution is based upon the previous  $(n-1)^{\text{th}}$  one. Iterative solvers may result in less I/O or disk usage, less total elapsed time, and more scalable parallel performance but lack the robustness in comparison to direct solvers. For nearly-singular matrices or matrices that include Lagrangian multipliers, iterative solvers are not effective or may even fail. However, iterative methods are often the only choice for nonlinear equations and are also often useful for linear problems involving many variables (sometimes on the order of millions), where direct methods would be prohibitively expensive (and in some cases impossible) even with the best available computing power [31].

There are various alternatives for iterative solvers in ANSYS usually based on the conjugate gradient (CG) method such as Jacobi Conjugate Gradient (JCG) solver which is suitable for well-conditioned problems [32]. Another solver is the Preconditioned Conjugate Gradient (PCG) solver which performs reasonably well for all types of problems including the ill-conditioned beam/shell structural analysis. The third solver is the Incomplete Cholesky Conjugate Gradient (ICCG) solver which is more efficient and robust than the JCG solver for solving ill-conditioned matrices. The form of equations to be solved iteratively is given as :

$$[K]\{u\} = \{F\} \quad (2.32)$$

where;

$[C]$  = global coefficient matrix

$\{u\}$  = unknown vector

$\{F\}$  = global load vector

In case of CG method, the solution can be expressed as a series of vectors  $\{p_i\}$  :

$$\{u\} = \alpha_1 \{p_1\} + \alpha_2 \{p_2\} + \dots + \alpha_m \{p_m\} \quad (2.33)$$

where  $m$  is no larger than the matrix size  $n$ . In an infinite precision machine, the solution is guaranteed to converge in  $n$  or fewer iterations. On a machine with finite precision, sometimes it may require more than  $n$  iterations to converge. A maximum of  $2n$  iterations is permitted by the solvers and if the solution does not converge an error message is generated. This may be due to an insufficient number of boundary constraints. A condition number of  $[K]$  is equal to the ratio of the maximum eigenvalue of  $[K]$  to the minimum eigenvalue of  $[K]$  and the rate of convergence is proportional to the square root of this number. A preconditioning procedure is generally used to reduce the condition number of linear Equation 2.32.

## 2.6 Geometrical Nonlinearities

If, in the initial linear analysis, the deformed shape of the structure is very different from the unloaded one hence the theory of small deformation is not valid. In such case, it is very important to take into account the geometrical nonlinearities present in the structure. This is done by activating the large deflection on for the Analysis and is used throughout the design stages. Also, Line bodies, as in our case, set to Link/Truss or Cable may not be able to solve if large deflection is turned off. In order to understand geometrical stiffness, the basic idea is that stiffness of a structure is a function of the displacement and as the displacement changes, so does the stiffness. Four types of geometrical non-linearities may be present in the structure.

1) Large strain involves accounting for finite strains, which can lead to changes in the shape of the object being analyzed, such as changes in area or thickness. Deflections and

## CHAPTER 2. PRELIMINARY DESIGN: DEVELOPMENT OF A FINITE ELEMENT MODEL

---

rotations can also be very large.

2) Large rotation refers to situations where the rotations are significant but the mechanical strains that cause stresses are small and are evaluated using linear expressions. The object being analyzed is assumed to undergo rigid body motions, but not changes in shape. This type of analysis is based on the original configuration of the object.

3) Stress stiffening is the stiffening or weakening of structure due to its stress state. In very thin structure (like ours), the bending stiffness is very small in comparison to the axial stiffness and coupling between in-plane and traverse displacements takes place hence stress stiffening comes into play. Stress stiffness matrix is computed based on previous equilibrium equations. Hence, at least two iterations are necessary to solve the model. However this does not guarantee the convergence of the solution. In case of very thin composite structures, coupled with pressure, the solver may not be unable to compute the solution in a single time step. In such cases, it is recommended to use time stepping procedure or at least set the Auto time stepping to program controlled or On.

If membrane stresses should become compressive rather than tensile, then terms in the stress stiffness matrix may “cancel” the positive terms in the regular stiffness matrix and therefore yield a non-positive definite total stiffness matrix, which indicates the onset of buckling. If this happens, it is indicated with the message: “Large negative pivot value....., at node..... may be because buckling load has been exceeded”. It must be noted that a stress stiffened model with insufficient boundary conditions to prevent rigid body motion may yield the same message.

4) Spin softening is also used when both strains and rotations are small, but it accounts for the coupling between transverse vibrational motion and centrifugal force due to angular velocity.

### Pressure Load Stiffness

Forces are treated numerically by equivalent pressure over an area. However, pressure is a "follower" load and is normal to the surface even in the deformed configuration causing a preload stiffness and even with a seemingly equivalent pressure and loads, the buckling loads may be quite different. Significant effect can be seen in nonlinear and eigenvalue buckling analysis. However, sometimes it may be necessary to use the follower force, so it is recommended to know the underlying assumptions on the type of problem to be solved.

## 2.7 Analysis of Cyclic symmetric structures

For a cyclic symmetric or periodic structure such as our IDEA drift chamber, the numerical simulation can be performed for the complete structure by modelling only one sector of it. The same sector is repeated N number of times using cylindrical coordinate system defined by user to yield the full structure. Constraint relationships are to be defined for the lower and the higher edge or face and this constraint relationship is satisfied to obtain the nodal displacement. The response of the full model is thus the linear combination of several independent responses, known as solution harmonics and are represented by harmonic indices. The number of harmonic indices must be lower than the number of the segments in our cyclic structure. The method was adapted from Dickens [33]. Constraint equations relating the lower and higher angle edges of the two sectors are written:

$$\begin{pmatrix} u'_A \\ u'_B \end{pmatrix} = \begin{bmatrix} \cos k\alpha & \sin k\alpha \\ -\sin k\alpha & \cos k\alpha \end{bmatrix} \begin{pmatrix} u_A \\ u_B \end{pmatrix} \quad (2.34)$$

where;

$u_A, u_B$  = calculated displacements on lower angle side of basic and duplicated sectors (  $A$  and  $B$ , respectively)

$u'_A, u'_B$  = displacements on higher angle side of basic and duplicated sectors (  $A$  and  $B$ , respectively) determined from constraint relationships

## CHAPTER 2. PRELIMINARY DESIGN: DEVELOPMENT OF A FINITE ELEMENT MODEL

---

$$k=\text{harmonic index } =0,1,2 \dots \begin{cases} N/2 & \text{if } N \text{ is even} \\ \frac{N-1}{2} & \text{if } N \text{ is odd} \end{cases}$$

$$\alpha = 2\pi/N = \text{sector angle}$$

$N$  = number of sectors in  $360^\circ$

The mode shape in each sector is obtained from the eigenvector solution. The displacement components ( $x$ ,  $y$ , or  $z$ ) at any node in sector  $j$  for harmonic index  $k$ , in the full structure is given by:

$$u = u_A \cos(n-1)k\alpha - u_B \sin(n-1)k\alpha \quad (2.35)$$

where;

$n$  = sector number, varies from 1 to  $N$

$u_A$  = basic sector displacement

$u_B$  = duplicate sector displacement

If the mode shapes are normalized to the mass matrix in the mode analysis, the normalized displacement components in the full structure is given by

$$u_{\text{normalized}} = \begin{cases} \frac{u}{\sqrt{N}} & \text{if } k = 0 \text{ or } k = N/2 \\ \frac{u}{\sqrt{N/2}} & \end{cases} \quad (2.36)$$

The equation of motion for harmonically-varying forced response is:

$$\left( [K^s] - \Omega^2 [M^s] \right) \{u^s\} = \{F^s\} \quad (2.37)$$

where;

$[K^s]$  = stiffness matrix

$[M^s]$  = mass matrix

$\{F^s\}$  = load vector

$\{u^s\}$  = displacement vector

$\Omega$  = forcing frequency



## CHAPTER 2. PRELIMINARY DESIGN: DEVELOPMENT OF A FINITE ELEMENT MODEL

---

The superscript  $s$  implies the matrices refer to the entire  $360^\circ$  system. Equation 2.37 can be transferred into modal space by:

$$\{u^s\} = [\Phi^s] \{a^s\} \quad (2.38)$$

where;

$[\Phi^s]$  = the set eigenvectors of the full system

$\{a^s\}$  = the vector of modal coordinates

Substituting this into Equation 2.37 and pre-multiplying by  $[\Phi^s]^\top$  yields the forced response equation in terms of modal coordinates:

$$\left( [\Lambda^s] - \Omega^2 [I] \right) \{a^s\} = [\Phi^s]^\top \{F^s\} \quad (2.39)$$

where;

$[\Lambda^s]$  = the diagonal matrix for the system natural frequencies squared

$[I]$  = the identity matrix

The number of eigenvectors (modes) used in Equation 2.39 is much less than the total number of degrees of freedom, so that Equation 2.39 is significantly smaller system than Equation 2.37.

A cyclic symmetric structure has the following transformation from cyclic coordinates to physical coordinates:

$$\{\mathbf{x}\} = ([F] \otimes [I]) \{\tilde{x}_h\} \quad (2.40)$$

where;

$\{\tilde{x}_h\}$  = cyclic (or harmonic) coordinates for harmonic index  $h$

$[F]$  = real-valued Fourier matrix

$\otimes$  denotes the Kronecker product

The system eigenvectors can also be expressed in terms of their harmonics:

$$[\Phi^s] = ([F] \otimes [I]) \tilde{B}_{\text{diag}} ([\tilde{\Phi}]_h) \quad (2.41)$$

## CHAPTER 2. PRELIMINARY DESIGN: DEVELOPMENT OF A FINITE ELEMENT MODEL

---

where;

$[\tilde{\Phi}]_h$  = the real-valued cyclic modes corresponding to harmonic  $h$

$\tilde{B}_{\text{diag}}()$  = a pseudo-block diagonal matrix.

A block is  $1 \times 1$  for  $h = 0$  and  $N/2$  if  $N$  is even, and  $2 \times 2$  otherwise.  $N$  is the number of sectors. Substituting Equation 2.41 into Equation 2.39 gives the frequency response equation in cyclic coordinates:

$$\left( [\Lambda^s] - \Omega^2 [1] \right) \{a^s\} = \{f^s\} \quad (2.42)$$

where the modal load  $\{f^\beta\}$  is:

$$\{f^s\} = \tilde{B}_{\text{diag}} \left( ([\tilde{\Phi}]_h^\top) \right) ([F]^\top \otimes [I]) \{F^s\} \quad (2.43)$$

The forcing function is assumed to be time harmonic as well as spatially harmonic in the circumferential direction. The force on any sector  $n$  can then be related to the force on the basic sector by only a phase shift:

$$\{F_n\} = \{F\} e^{i\phi(n-1)} \quad (2.44)$$

where;

$\{F\}$  = complex load vector on the basic sector

$\phi = \frac{2\pi C}{N}$  = phase of excitation on sector  $n$

$C$  = engine order (EO) excitation

$N$  = number of sectors

Using Equation 2.42 and Equation 2.43:

$$\{f^s\} = \tilde{B}_{\text{diag}} \left( ([\tilde{\Phi}]_h^\top) \right) ([F]^\top \otimes [I]) \{F^s\} \quad (2.45)$$

Equation 2.45 can be written as the sum of each sector:

$$\{f^s\} = \sum \tilde{B}_{\text{diag}} \left( ([\tilde{\Phi}]_h^\top) \right) ([F_n]^\top \otimes [I]) \{F_n\} \quad (2.46)$$

where;

$[F_n]$  = the  $n^{\text{th}}$  row of the Fourier matrix  $[F]$

Once the vector of modal coordinates  $\{a^s\}$  is obtained for a given excitation frequency  $\Omega$ , we can expand back to the physical solution quantities for the entire structure. The displacements of sector  $n$  are determined by:

$$\{u_n\} = ([F_n] \otimes [I]) \tilde{B}_{\text{diag}} ([\tilde{\Phi}]_h) \{a^s\} \quad (2.47)$$

Stresses and strains can be similarly evaluated by using the stress and strain mode shapes for  $[\tilde{\Phi}]_h$ .

## 2.8 Numerically Accurate Results

Obtaining numerically accurate results is of paramount importance for usefulness, reliability and safety of the engineering design. Numerical accuracy depends upon type and size and a trade-off is necessary between numerically accurate solution and computational cost. Also interpretation of the results plays an important role to obtain the numerically accurate results.

### 2.8.1 Mesh Independent solution

Specifying an appropriate mesh size is critical to obtain accurate results in reasonable time. Coarse mesh may produce incorrect results if higher stress gradients too large. Fine mesh may cause increase of computational cost. In order to meet the end goal which is to obtain the mesh independent solution, we can start by a coarse mesh and refining it until further refinement do not change the output results appreciably. The element size has a greater effect in derived quantities such as stress and strains and post processing techniques such as results averaged, unaveraged or nodal difference can be used in order to obtain the correct mesh size hence numerically accurate solution.

The first thing we can do is to check if the gradients are too high through the element. In the

## CHAPTER 2. PRELIMINARY DESIGN: DEVELOPMENT OF A FINITE ELEMENT MODEL

---

limit of infinite mesh density, the gradients theoretically disappears and the element has constant stress. However, we do not need infinite mesh density (hence zero gradients) to obtain numerically accurate solution. The displacement is an unknown quantity which is solved at the nodes of the finite element. Using strain displacement matrix, the strains for each element are computed at the gaussian integration points. Using constitutive equations for material model the stress is calculated. These computed values of derived quantities are extrapolated to the corner nodes using shape functions of the element. Often, the highest values are on the outside surfaces of the mesh. We wish to obtain the values at the nodes which lie on the surface of the mesh. The difficulty is that every element has its own value at the nodes and also the element share a common node. This causes a dilemma to which value should be used at the shared common node. Two approaches are taken by the solver. The first is averaging the stresses/strains in which we lose the peak but have a single value per node to consider resulting in smooth and continuous contour plots from elements to elements. The second one is unaveraged which gives a range of values from lowest to highest at a common shared node and discontinuous contour plots from elements to elements. In mesh independent solution, both of these will show the same values and disparity in above two indicates that we do not have sufficient mesh density.

There are also methods like nodal difference and elemental differences that can be exploited to obtain the numerically accurate results. Nodal difference computes the maximum difference between the unaveraged computed result for all elements that share a particular node. Elemental Difference computes the maximum difference between the unaveraged computed result for all nodes in an element, including mid side node. After computing all these values, the second thing we have to look is if the stress gradients are only high in some parts of elements, finer mesh should be used only there instead of whole body. Also, adaptive sizing can be turned on followed by smooth transition of the mesh. The whole process must be repeated until mesh independent solution is achieved.

### 2.8.2 3D element shape and order

During automatic mesh generation both hexahedral and tetrahedral elements are generated and a combination of more than one element shape is present. It is often thought that hexahedral elements are better suited than tetrahedral elements. For a simple regular sweepable body (having two opposite topologically similar faces), a quadrilateral element is generated on one face and extruded to the other face to produce a hexahedral element. When the complexity in geometry increases, we may resort to tetrahedral or a combination of various element types. In any case, it is important to know the effect of choice of element type on our results. A solid is made up of nodes, each having 3 degrees of freedom in X, Y, and Z direction, at which the displacements and the reaction forces are calculated. The integration points are within the element at which derived quantities are calculated using shape functions. A 4 noded tetrahedral element also called lower order or linear tetrahedral element since the shape function is a linear polynomial one. It has only one gaussian integration point so stress and strain are constant within the element. To calculate the stress and strain gradient accurately using these element an extremely fine mesh is needed. In bending dominated problems, these linear elements fail to accurately capture the curvature hence are prone to shear locking. This causes spurious shear stresses and overly stiff behaviour no matter how fine the mesh is.

Linear 8 noded hexahedral elements are not prone to above problems hence are recommended in linear stress and dynamic analyses. However, we are not restricted to linear element in today's world. Higher order elements whose shape functions are quadratic can be used. These are modified form of linear element with an additional mid side node in between. For example, a second order 10 noded tetrahedral element (4 gaussian integration points) is obtained from a 4 noded tetrahedral element by adding a mid side node. Increased number of gaussian integration points means the distribution of the stresses and strains within the element and increased number of nodes means the element is able to capture the curvature more smoothly in case of bending problems. In addition, wedge and pyramid elements may also be formed during mesh generation. Excess of either of

these elements will cause an error and should be replaced by tetrahedral elements manually.

In ANSYS Mechanical, Quadratic elements are used by default. For sweepable bodies, hexahedral dominated mesh is generated, whereas for a complex geometry tetrahedral dominated mesh is generated. Tetrahedral elements can have an easier mesh transition from coarse to fine mesh region. The greater advantage lies in the fact that we can have optimal mesh generation by greater number of elements in high stress gradients only. However, in hexahedral mesh the refinement propagates in the sweeping direction.

### **2.8.3 Artificially high stresses**

In some cases, the artificially induced stresses grow as the mesh becomes finer. This creates a confusion as we are expecting results to be correct if the mesh is finer. The primary unknown quantity such as displacement and rotation at each node is directly calculated from the global stiffness matrix converge to a unique solution as the mesh becomes finer. The stress and strains are derived quantities and are not calculated from the global stiffness matrix due to which they may not converge to a unique solution from a finer mesh. The common cause for artificially high stresses include application of loads or constraints on a vertex or node, sharp corners or edges, contacts, over constraint due to improper boundary conditions. Stress singularity should not be confused with stress risers which have a larger but finite stress and may even have closed form mathematical solution. To avoid the stress singularity, we can refer to St.Venant's principle which states that the stresses on a boundary reasonably distant from an applied load are not significantly altered if this load is changed to a statically equivalent load. The distribution of stress and strain is altered only near the regions of load application. That means wherever stress singularity occurs, the mesh can be made finer and the distant stresses can only be scoped in the results.

### **2.8.4 Accurate Surface Stress Using Surface Coating**

In the finite element method, the stress and strains are extrapolated from the gaussian integration points to the surface of the element. For coarse mesh with large stress gradient, this may not be sufficient accurate enough. This can be efficiently handled by using surface coating (shell elements) in the post processing. Surface coatings do not increase the stiffness of the system and share the same deformation as underlying solids. Since, no out of plane extrapolation is done, the surface stresses calculated are accurate. Surface coatings should be used for surfaces whose element size in normal to the surface direction is large.

### **2.8.5 Adaptive convergence**

The success of finding a solution does not guarantee the success in finding a numerically accurate solution. Adaptive convergence means that the output does not change or converges to a value with decreasing element size for a well defined model. In finite element there is no exact solution to compare how accurate our solution is due to complexity in material behaviour, non linear contacts and non linear deformation. In such case, we look upon relative accuracy of the models between one mesh size to another. It involves solving the model iteratively with different mesh sizes and computing relative error until the user defined accuracy is achieved. In the past, the refinement regions were predicted with trial and error to produce numerically accurate results. However, in ANSYS this can be done automatically. In each iteration, only the elements on which the relative error is larger than specified is refined. Adaptivity is more robust with tetrahedron elements. It should be noted for each output result, the adaptivity convergence may vary. Keeping all the factors described above to obtain a numerically accurate results, we first check the averaged, unaveraged, nodal difference and element difference solution. We focus our mesh study on the outer cylinder because the domain of inner cylinder is very small. Also for the line elements, the few number of elements are enough to capture their behaviour.

### 2.8.6 Mesh Size : Parametric Study

To understand whether or not the mesh size is fine enough, a convergence study has to be done. It can be noted that the convergence study in ANSYS Mechanical is incompatible with the line elements. In order to overcome this, instead we carry out a parametric study in which mesh size is defined as an input parameter and resulting effects on various other output variables can be studied. For spokes and cables, we know that line elements are able to capture the behaviour of the structure even with few elements and are computationally inexpensive too. In case of inner cylinder, the domain is very small in comparison to the outer cylinder so even using very fine mesh is not a problem. In case of outer cylinder, as the spokes are loaded, it deforms (Max.deformation in outer cylinder is 13 mm) and an interaction occurs between spokes, cables and outer cylinder. Another reason is that this is the largest domain that is present in our numerical model that governs the numerical accuracy of our mathematical model. This is the main reason, we focus our study on the outer cylinder. From, Figure 2.19, it is clear that a discrepancy exists between maximum von-Mises stress calculated by averaged (2034.7 MPa) and unaveraged (2406.1 MPa) results. The nodal difference (1730.5 MPa) and elemental difference (1550.5 MPa) also suggest that the mesh is not fine enough or it may also be due to artificial high stress. The results have to be further investigated.

To do so, a parametric study is done using mesh size ranging from 50 mm to 1 mm and their results are tabulated in Table 2.1. From the Table 2.1, we can observe that in case of line elements even a coarse mesh of 50 mm is predicting with a reasonable accuracy as does 1 mm mesh size. In case of maximum equivalent stress and average equivalent stress at outer cylinder, the average and unaveraged value have almost converged. However, the nodal difference still persists (1981 MPa) and this value is decreasing as the mesh becomes finer suggesting that no artificial stress exists and further mesh refinement is necessary. If we look at the Table 2.1, we can see that using 50 mm mesh size, 189 elements were created and the maximum deformation was 142.993 mm with a solution time of 5 seconds. With 1 mm mesh size, a deformation of 133.226 mm was obtained, with 85442 elements



## CHAPTER 2. PRELIMINARY DESIGN: DEVELOPMENT OF A FINITE ELEMENT MODEL

---

and a solution time of 12892 seconds. This solution time is 17088.4 times higher than previous one. Now, we have already stated that mathematical models have to be refined until a tolerance or an accuracy criteria is met and there is always a trade-off between numerical accuracy and computational cost. With a reasonable degree of confidence, we can say that the solution using 1 mm mesh size is numerically accurate and we do not further refine the mesh size in this stage of design.

## CHAPTER 2. PRELIMINARY DESIGN: DEVELOPMENT OF A FINITE ELEMENT MODEL

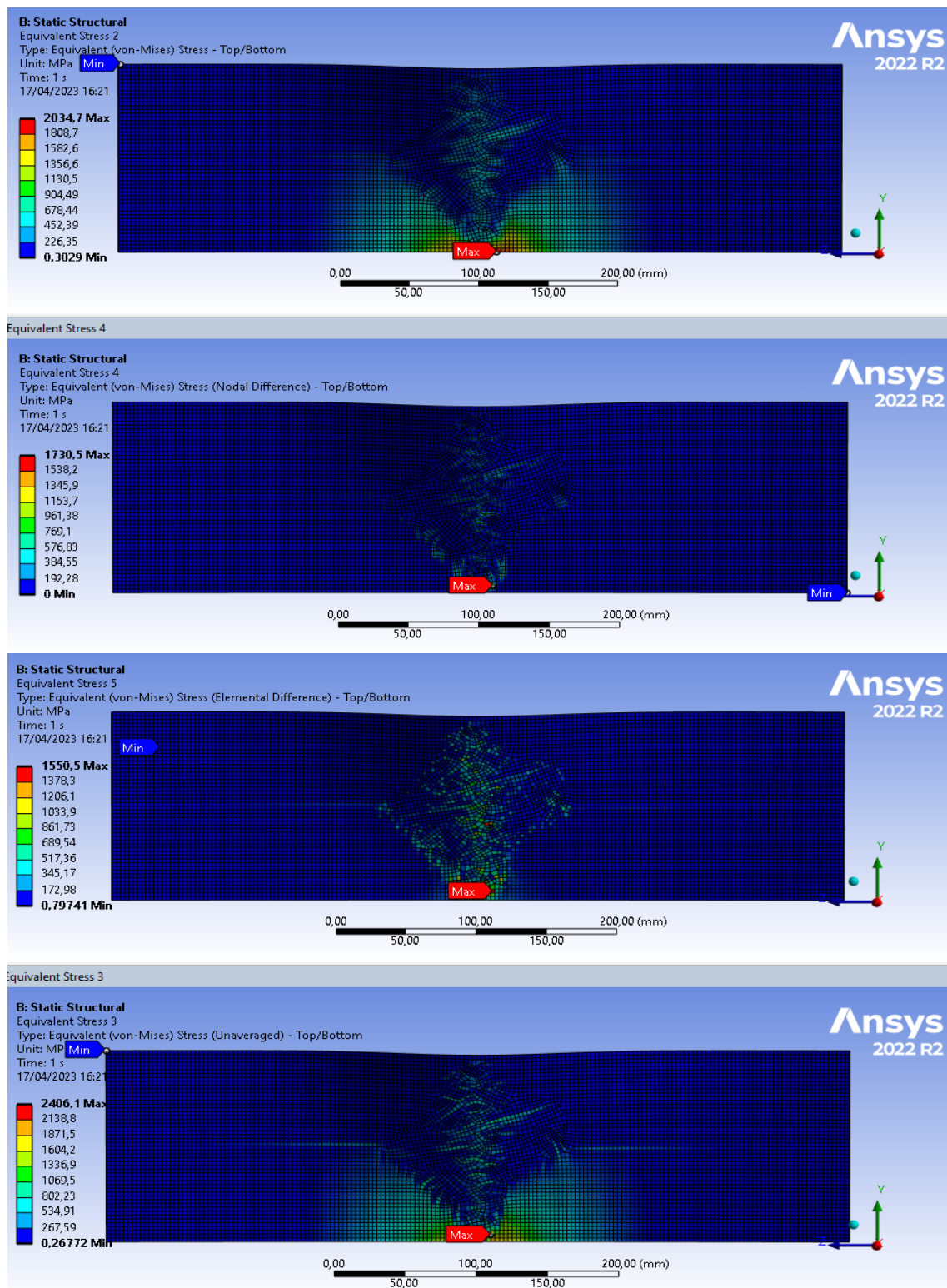


Figure 2.19: Equivalent von-Mises stress at the outer cylinder calculated with averaged, nodal difference, elemental difference and unaveraged methods with 3 mm element size

## CHAPTER 2. PRELIMINARY DESIGN: DEVELOPMENT OF A FINITE ELEMENT MODEL

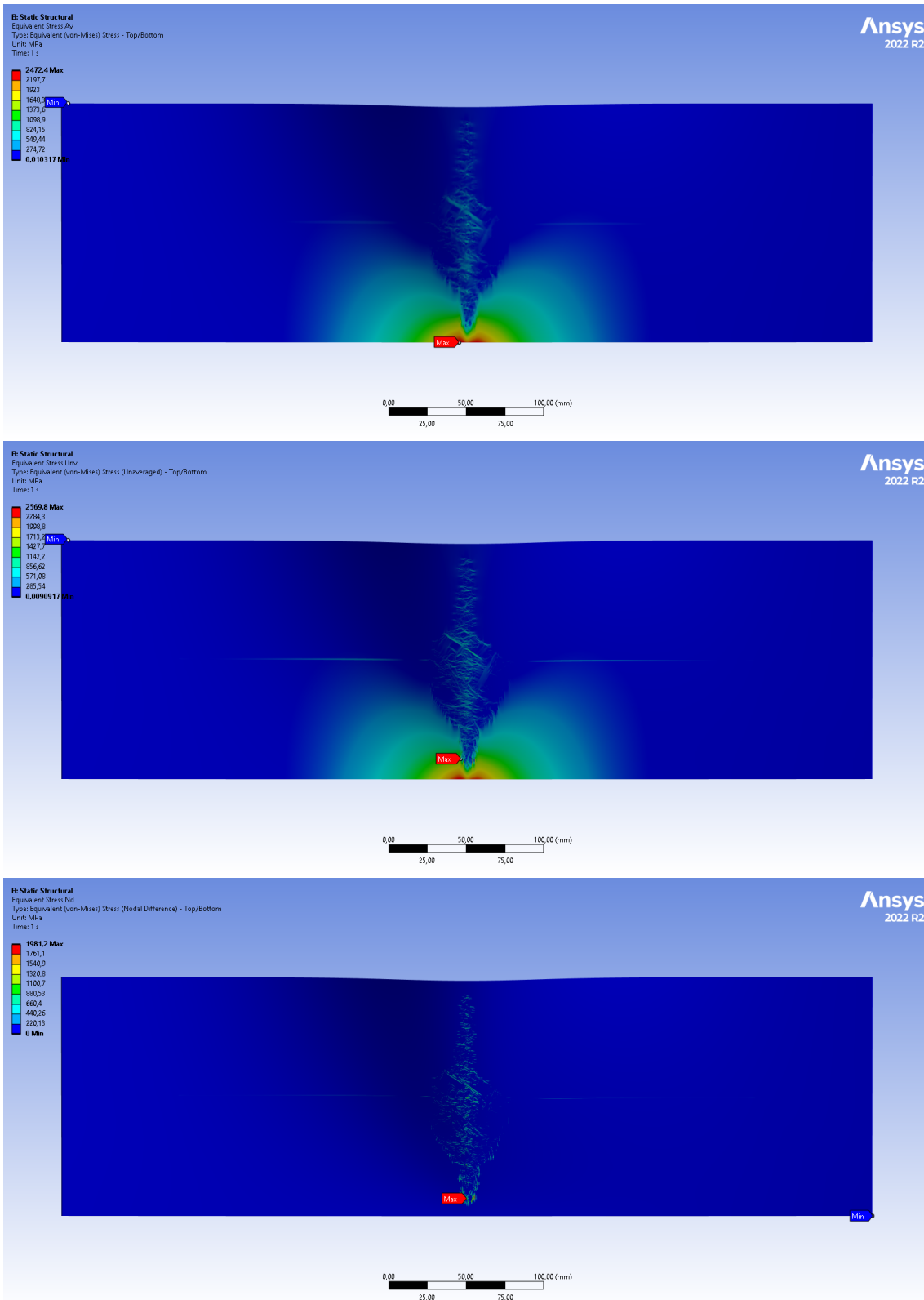


Figure 2.20: Equivalent von-Mises stress at the outer cylinder calculated with averaged, unaveraged methods and nodal difference with 1 mm element size.

CHAPTER 2. PRELIMINARY DESIGN: DEVELOPMENT OF A FINITE ELEMENT MODEL

Design No	Mesh Size	Total deformation Model	Equivalent Stress Maximum in Outer Cylinder			Equivalent Stress Average in Outer Cylinder			Maximum Axial Force Spokes	Equivalent Stress Maximum Cables	Mesh Quality		Solution Elapsed Time	Number Mesh Elements
			Averaged	Unaveraged	Nodal diff	Averaged	Unaveraged	Nodal diff			Min	Average		
DP 0	50	142.993	1763	3233	2932	223	286	201	12132	3197	0.13	0.80	5	189
DP 1	45	145.261	821	1824	1694	219	273	190	12139	2992	0.34	0.89	7	206
DP 2	40	139.848	1777	3293	2996	226	282	200	12126	3204	0.39	0.92	12	216
DP 3	35	139.495	1329	3262	2937	213	261	197	12145	3184	0.47	0.93	7	251
DP 4	30	138.848	1273	2367	2069	212	253	178	12219	2880	0.46	0.92	12	266
DP 5	25	142.349	1259	2249	1939	194	228	141	12175	2853	0.44	0.95	9	320
DP 6	20	139.726	2028	2994	2603	157	180	104	12233	3056	0.68	0.97	17	425
DP 7	15	130.568	1750	3104	3007	162	177	81	12559	3146	0.04	0.96	27	607
DP 8	10	135.217	2376	2497	2058	143	151	52	12368	3227	0.67	0.99	22	1120
DP 9	5	135.033	1976	2386	1908	140	144	34	12294	3246	0.60	0.99	77	3838
DP 10	4	133.568	1860	2249	2043	137	141	30	12476	3221	0.60	0.99	324	5900
DP 11	3	134.377	2042	2683	2330	139	141	26	12311	3225	0.67	0.99	291	10228
DP 12	2	137.256	1681	2156	1998	136	139	24	12243	3275	0.67	0.99	2149	22337
DP 13	1	133.266	2472	2570	1981	131	132	7	12283	3152	0.59	1.00	12892	85442

Table 2.1: Parametric Study of the effect of the Mesh size on the convergence of displacement, stresses and axial force.

## 2.9 Results, Validity and Insights

### 2.9.1 Linear Analysis

Without turning on the Large deflection, an analysis is carried out in a single time step to calculate the total deformation on the model (Figure 2.21). A full scale model is built and loaded with uniformly distributed line pressure. This model also helps in validation of cyclic symmetric model. The mesh is just fine to capture the geometry and the sole purpose is to just get an insight into our structure, without imposing any accuracy criteria.

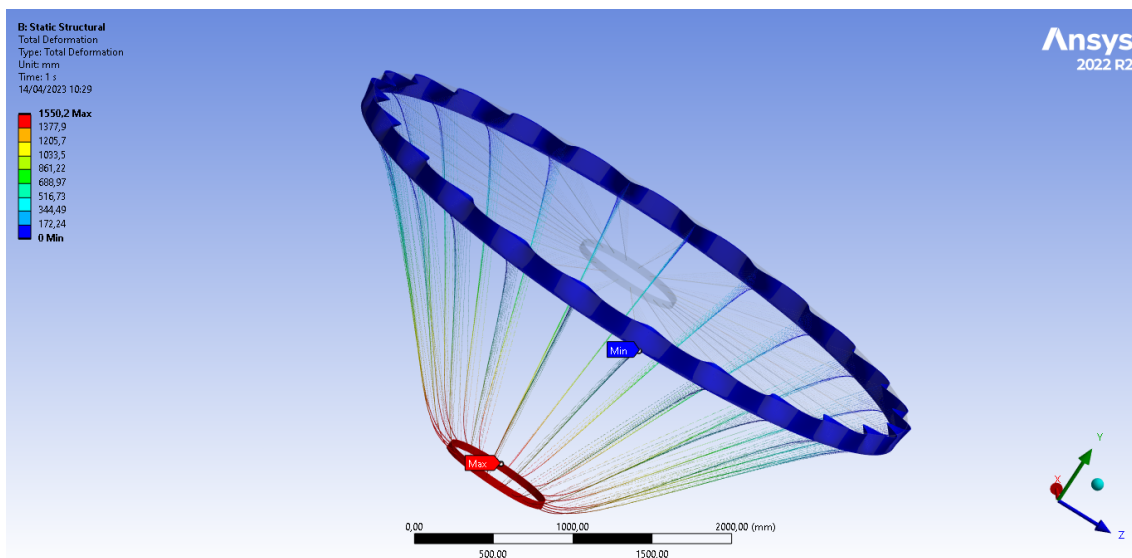


Figure 2.21: Full scale model of the IDEA drift chamber made up of carbon subjected to a full load of 10 tonnes. The maximum deformation occurs on inner cylinder 1550.2 mm. The deformation is shown on a true scale.

A warning message "Line bodies with type set to Link/Truss or Cable may not be able to solve if Large Deflection is turned off in the Analysis Settings for the model." Based on our theoretical understanding, the small deformation theory is valid when the deformations are so small that the undeformed and deformed geometry of the model is almost the same. In our case, the model's deformed and undeformed configuration are very different. In such case, linear analysis cannot predict a true behaviour of our system and this is evident from the obtained results. So, we turn on the large deformation in the analysis setting

activating the geometrical nonlinearities.

It should be noted that when the deformation results are very small, the results from linear analysis and that from activating Large deflection are almost the same. However, turning on large deflection is always recommended except in cases like linear buckling analysis. Another important point is that a model should be first run in the linear analysis as it is easy to find errors in the model with small computational time. when the model runs correctly, a nonlinear analysis can be carried out. Another important case is that for very large iteration studies like optimization of cable tuning forces, where thousands of iterations are necessary, linear analysis can be carried out and the solution can be constrained to a domain. This can then be followed by further iterations from turning on the large deformation.

### 2.9.2 Nonlinear Analysis

After activating the geometrical nonlinearities, the solver is unable to correctly solve the model. In some cases, no graphical output is generated. The solution information must be checked in the output file. An unconverged solution message due to various modelling issues might be the probable cause. In our case, our initial suspicion is due to the application of very high loads on such slender structure. This may cause excessive distortion leading the displacement to be very high and unrealistic. It is always a good idea to read the information, warning and error message generated during the solution process. The following message from the solver is generated in the output file.

```
*** ERROR *** CP = 30.344 TIME= 10:41:27 The value of UZ at node 42260 is
4514112.77. It is greater than the current limit of 1000000 (which can be reset on the
NCNV command). This generally indicates rigid body motion as a result of an uncon-
strained model. Verify that your model is properly constrained.
```

```
*** ERROR *** CP = 30.344 TIME= 10:41:27 *** MESSAGE CONTINUATION —
```

## CHAPTER 2. PRELIMINARY DESIGN: DEVELOPMENT OF A FINITE ELEMENT MODEL

---

DIAGNOSTIC INFORMATION \*\*\* Rigid body motion can also occur when net section yielding has occurred resulting in large displacements for small increments of load or when buckling has occurred. You can plot the time history curve for node 42260 in the UZ direction to check for stiffness (slope of the curve) approaching zero.

\*\*\* WARNING \*\*\* CP = 30.344 TIME= 10:41:27 The unconverged solution (identified as time 1 substep 999999) is output for analysis debug purposes. Results should not be used for any other purpose.

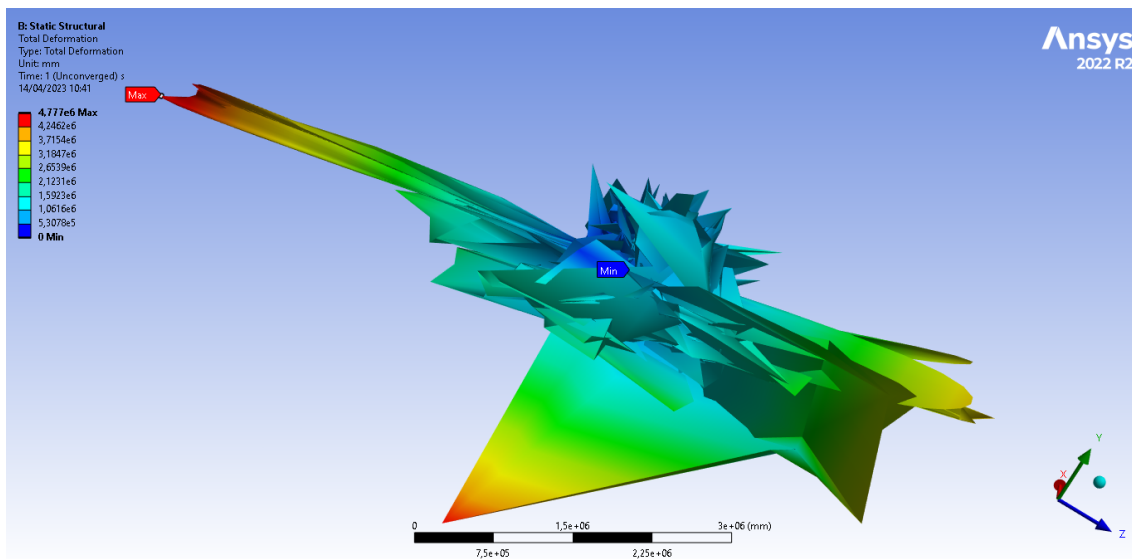


Figure 2.22: Response of the full scale model when turning on the geometrical nonlinearities.

The solver indicates a rigid body motion at a node which may be due to unconstrained model or yielding. We have already solved our model in linear analysis and are certain about functionality of the model and validity of the boundary conditions. We should be able to suspect the truth long before we are able to prove it. Our initial suspicion is that because the load is applied in a single time step there is a potential discrepancy between applied and internal element forces in a nonlinear analysis. This is shown by the force convergence graph (Figure 2.23) in which Force convergence is above the force criterion and does not meet the requirements

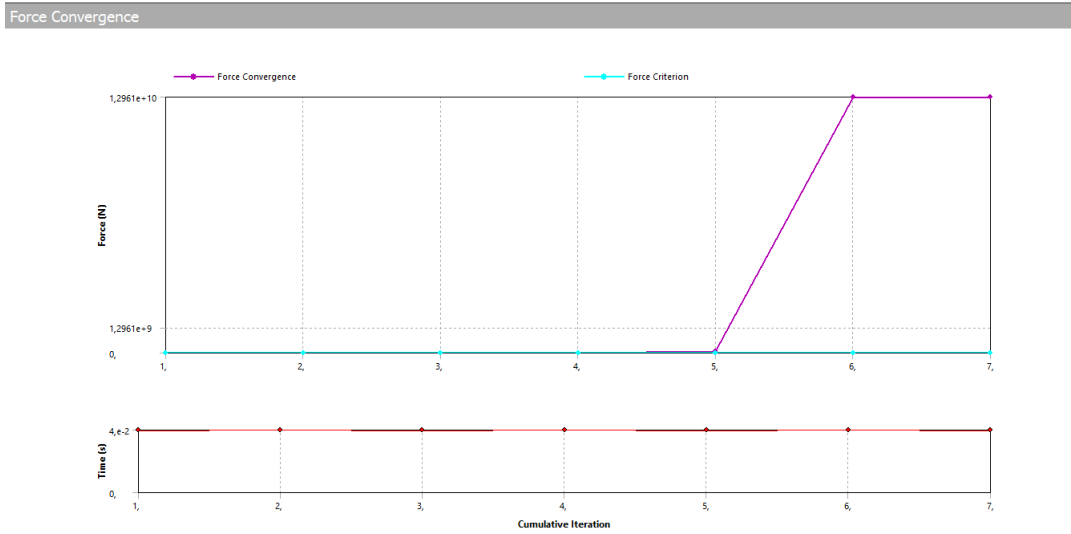


Figure 2.23: The convergence criterion is not met as the force convergence is above the force criterion

### Time/Load stepping procedures

Time stepping (or load stepping ) is a procedure in which the time step size and/or the applied loads are automatically determined in response to the current state of the analysis under consideration. There are two important features of the automatic time stepping algorithm. The first feature concerns the ability to estimate the next time step size  $\Delta t_{n+1}$ , based on current  $t_n$  and past analysis  $\Delta t_n$  conditions, and make proper load adjustments. The second feature is time step bisection whose main purpose is to decide whether or not to reduce the present time step size,  $\Delta t_n$ , and redo the computation within that substep with a smaller step size. This is done when proper convergence is not achieved or not anticipated during the equilibrium iterations. Multiple bisections can also occur during a substep. We divide the load in 5 initial substeps with 1 being the minimum substep and 10000 being maximum. Since a load step has an associated time span we can also equivalently specify the initial, minimum and maximum time step sizes.



## CHAPTER 2. PRELIMINARY DESIGN: DEVELOPMENT OF A FINITE ELEMENT MODEL

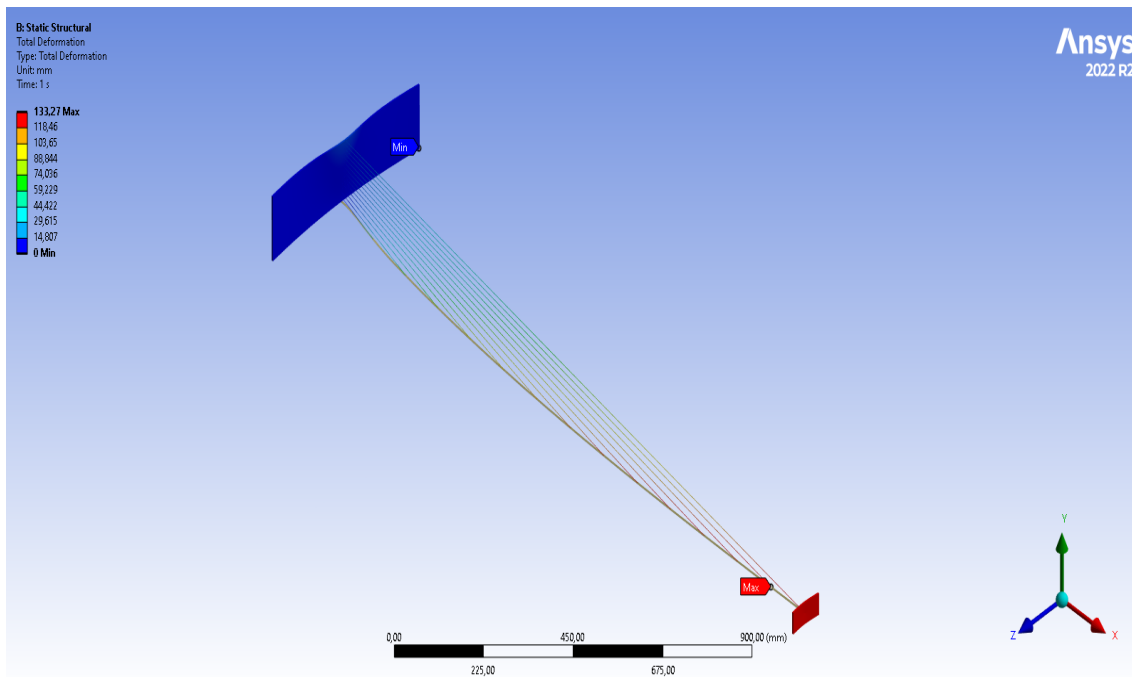


Figure 2.24: Total deformation ( $133.27\text{ mm}$ ) of the symmetric sector drift chamber subjected to uniformly distributed load

Using automatic time stepping procedure, the solution was converged and a total deformation of  $133.27\text{ mm}$  was obtained at inner cylinder (Figure 2.24). Compared to  $1552\text{ mm}$  in linear analysis, the solution discrepancy is quite high. This also stresses the importance of using geometrical nonlinearities. Here, we can also stress that the accuracy of these time stepping procedures are dependent on the time step; however, at the expense of the computational cost. A converged solution does not mean the most accurate one. Also, the definition of the convergence in time stepping procedures and in mesh size study is very different. Automatic time stepping should not be used for problems having localized dynamic behavior in which the low-frequency energy content may dominate the high-frequency areas, in structures subjected to seismic loading where the time step tends to changes continually as different frequencies are excited and in rigid body motion problems.

When solving nonlinear analysis, an iterative procedure (equilibrium iterations) is carried out at each substep described above. A converged solution is the one in which

## CHAPTER 2. PRELIMINARY DESIGN: DEVELOPMENT OF A FINITE ELEMENT MODEL

out-of-balance loads are less than the specified convergence criteria (Figure 2.25). These convergence controls are "step aware" and can be different for each step. Force residual relative tolerance dictates the threshold value for force residual convergence in Newton-Raphson convergence. A smaller value will lead to more iterations but a smaller residual.

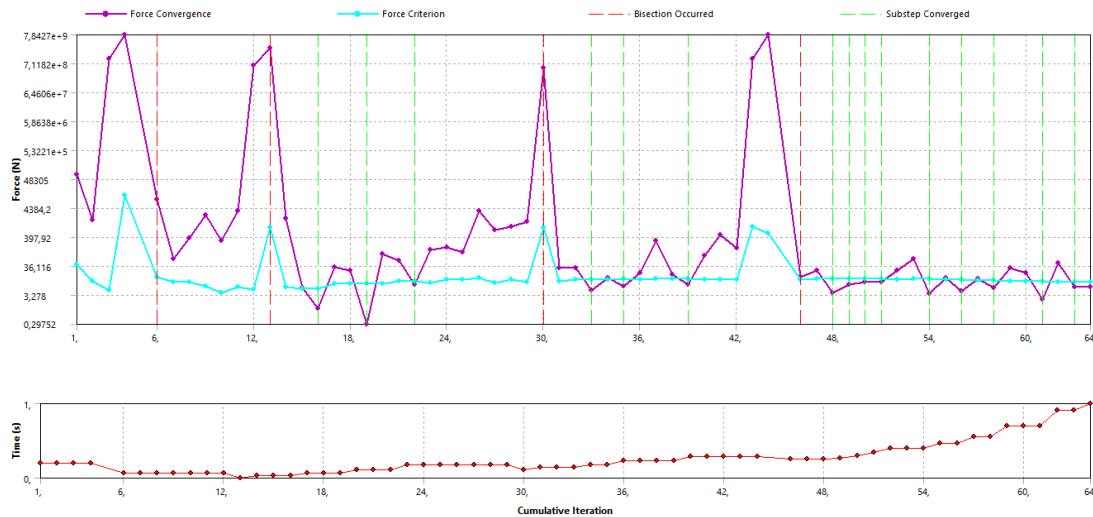


Figure 2.25: Force convergence criterion is met after 16 substeps and 64 iterations.

### 2.9.3 Validation

Generally, validation of the finite element model is done checking reaction forces. In our case, we study three different models. The first model is the one previously described, made with composite and steel in which a fixed boundary condition was applied at the lower edge of the outer cylinder. The second model is exactly the same one but with a fixed boundary condition at the face of the outer cylinder. This is similar to considering a very rigid outer cylinder. Our goal will be to see the evolution of the stresses and strain as the model evolves on subsequent chapters from a flexible one to a stiffer one. The third model is completely built with structural steel and we compare the results with composite. It will not only help in the validation of our finite element model, but also the validation of the material choice i.e composites.

## CHAPTER 2. PRELIMINARY DESIGN: DEVELOPMENT OF A FINITE ELEMENT MODEL

	Edge fixed	Face fixed	Edge fixed
Material type	Composite and steel	Composite and steel	structural steel
Max. Total deformation in model (mm)	135.03	96.83	108.37
Max. Total deformation in outer cylinder (mm)	14.73	-	7.84
Min. Axial force in Spokes (N)	-365.87	-1957.80	-1312.40
Max. Axial force in Spokes (N)	12294.00	13497.00	13103.00
Max. Equivalent stress in Cables (MPa)	3245.70	3350.90	3330.50
Avg. Equivalent stress in Cables (MPa)	71.49	89.95	82.88
Max. Equivalent stress in Inner cylinder (MPa)	1646.70	1885.20	1952.90
Avg. Equivalent stress in Inner cylinder (MPa)	280.11	317.02	335.90
Max. Equivalent stress in Outer cylinder (MPa)	1976.00	-	1618.30
Avg. Equivalent stress in Outer cylinder (MPa)	139.77	-	224.33
Mass (kg) per sector	0.69587	0.69587	2.7773
Volume (mm <sup>3</sup> ) per sector	3.54E+05	3.54E+05	3.54E+05

Table 2.2: Three different mathematical models based on boundary condition and material choice and the corresponding outputs

Now if we look at the results, we see that by applying a fixed boundary condition on the whole face of outer cylinder, the total deformation is lower compared to the first model. This is an expected behaviour and encourages us to improve the stiffness of the outer cylinder. But this has caused, an increase in the axial forces in the spokes both in tension and in compression. This would also increase a tendency of the spokes to buckle. The second aspect is that, referring to the Figure 2.9, steel has higher stiffness in Y and Z axis by one order and almost same stiffness in X axis as composite so the deformation must be lower than composite and somewhat closer to closer. Indeed, we get a deformation of 108.37 mm which is 0.8 times than that of composite.

### 2.9.4 Conclusions

In this preliminary design stage, we are almost certain but not completely sure that the analysis carried out is numerically accurate. But, in order to get an insight about the behaviour of the system, we are almost successful. We see that the structure has completely collapsed in terms of stresses as well as meeting the deformation criteria.

## Chapter 3

# Preliminary Design Exploration: A statistical Approach

In structural engineering, any design criteria can be met by changing some input variables randomly. For example in this drift chamber problem, we can solve this structure by increasing the thickness (rigidity) of the outer cylinder and spokes. Also, if the cables fail, we can increase their diameter too. This is how a problem is solved in most structural engineering problems. We have already mentioned in Chapter 2 Section 2.1 that the ultimate goal is not to solve a structural problem, but to detect the particles. This increases the complexity of the problem from comically trivial to dauntingly enigmatic. In 1945, Mathematician George Pólya published the book *How To Solve It*, one of the most published books on problem solving technique , in which he states, “ My method to overcome a difficulty is to go round it.” In this chapter, our *mantra* is to go around our problem in order to solve this seemingly impossible task. The chapter attacks the problem from statistical approach and rare concepts such as Response Surface Methodology and Design of Experiments are applied to solve not just a single problem but to go around it in order to get an insight into a *what if* question.

### 3.1 Design Exploration: A Parametric Study

Before the advent of chaos theory, the Newtonian view of the world was characterized by the belief that the behavior of any physical system could be predicted with complete accuracy, given a sufficiently precise understanding of its initial conditions and the laws governing its behavior. Only centuries later, Heisenberg came up with the idea of uncertainty but that was in the scale of atoms, insignificant in large bodies. In 1991 when Edward Lorenz, father of the modern chaos theory was awarded Kyoto prize, the committee stated his idea of deterministic chaos, “profoundly influenced a wide range of basic sciences and brought about one of the most dramatic changes in mankind’s view of nature since Sir Isaac Newton.” Lorenz introduced the concept of Lorenz attractor which is a set of chaotic solution to Lorenz system which can have an intricate structure and can even appear fractal-like<sup>1</sup>, providing a new way to visualize and understand chaotic systems. The discovery of this Lorenz attractor was done by design exploration. For three constants  $\sigma$ ,  $\rho$ , and  $\beta$  which are system’s input parameters proportional to the Prandtl number, Rayleigh number, and certain physical dimensions of the layer itself, Lorenz carried out simulation. Based on different values of these input parameters Lorenz obtained different solutions, but not all solutions were chaotic. Through, design exploration he understood the chaotic nature of the system. Had only one value been used, or values at only certain locations were used the behaviour of the system would have been perceived in different way. This process of varying input parameters in some possible ranges in order to see how the system responds is called design exploration. These are very less used concepts especially in structural mechanics.

---

<sup>1</sup>The curve is infinitely long on finite dimensional space so that it starts filling the space in higher dimension. The dimension of the Lorenz attractor is observed to be around 2.06

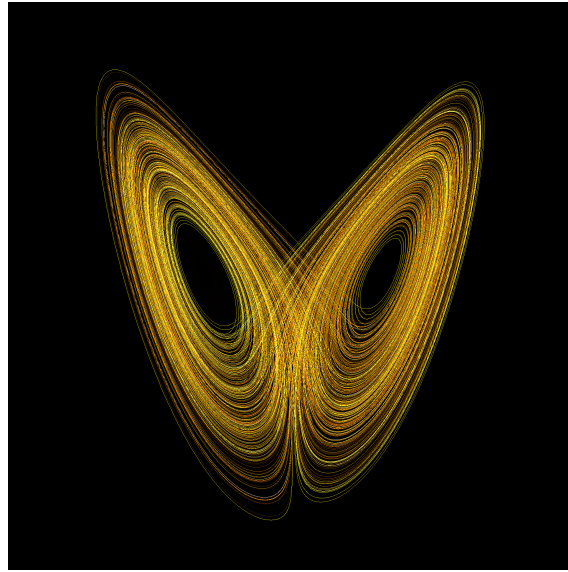


Figure 3.1: Projection of trajectory of Lorenz system in phase space with "canonical" values of parameters  $\rho = 28, \sigma = 10, \beta = 8/3$  (or 2.666667) and integration timestep 0.001. The system exhibits chaotic behavior for these (and nearby) values.

Simulation models often have many input factors, and determining which ones have a significant impact on performance measures (responses) of interest can be a difficult task. The common approach of changing one factor at a time is statistically inefficient and, more importantly, is very often just incorrect because for many models factors interact to impact on the responses [34]. It is absolutely necessary to study the influence of the design (input) parameters on the output in an exhaustive manner so as to understand our structure and its behaviour. "Design is an iterative process, and exploration is a key part of that process." It creates a design space from which by logical reasoning, design parameters can be chosen so as to satisfy the desired objectives.

The process of design exploration involves using Design of Experiments (DOE) and Response surfaces to analyze the correlation between design variables and output . By understanding how output variable varies with changes in design variables, it becomes simpler to identify the adjustments necessary to meet output constraints. Response surfaces once generated eliminate the need for additional simulations for new configurations.

This is the principle of Simulation Driven Product Development [29]. It should not be confused with optimization which gives a single design point, whereas the design exploration gives us a range of design points. The ultimate goal of design exploration might be an optimization problem to get the most efficient design, but before that the designer needs an overview of the response and all the *what if* questions. Then only, after analyzing all the situations, the designer might proceed with the optimization with certain constraints imposed to get the best design, or may choose any of the possible alternative combination of input variable to get the output.

### 3.1.1 Design of Experiments and Response surface Methodology

Response surface methodology (RSM) is a concept introduced by George E. P. Box and K. B. Wilson in 1951. It is a mathematical model relating the response of output variable (response variable) as a function of input variables using response surface. The classical Response surfaces were developed using linear polynomial models, mainly first-degree and second-degree models, with continuous response variables assumed. However, after 1970s a lot of upgradation in the method has been done to cover wider range of experiments. The response surface is typically a polynomial equation describing the relationship between the input variables and the response variable. Higher degree polynomial means more complex model but higher flexibility. The response surface methodology has three parts;

(a) Design of Experiments: It involves creating a set of input parameters from the subset in order to study the response of the system. For each input parameter, a range is specified and from this range a combination of the input parameters is generated. Various Design of Experiments such as Central Composite Design (CCD), Optimal Space-Filling Design (OSF), Box-Behnken Design, Sparse Grid Initialization, Latin Hypercube Sampling Design (LHS) are in use today.

(b) Building Meta Models: Meta models are created by the use of statistical analysis

### CHAPTER 3. PRELIMINARY DESIGN EXPLORATION: A STATISTICAL APPROACH

---

(regression analysis) such as Standard Response Surface - Full 2nd-Order Polynomial, Kriging, Non-Parametric Regression, Neural Network, Sparse Grid. Regression analysis can be used to create meta models which can accurately capture the behaviour of the system to build the response surface.

(c) Optimization of the response surface: This is where the core competency of the Response surface methodology lies. Only when we know all possible combination of design variables and their corresponding responses, we can decide with logical reasoning the selection of the input variables. There are various optimization techniques we can adopt to get the best design. These optimization algorithms minimize or maximize the variables based upon the response surfaces. We can use Multi-Objective Genetic Algorithm (MOGA), Nonlinear Programming by Quadratic Lagrangian (NLPQL) , Mixed-Integer Sequential Quadratic Programming (MISQP) , Adaptive Single-Objective Optimization (ASO) , Adaptive Multiple-Objective Optimization (AMO) etc to solve an optimization problem. Optimization algorithms are problem dependent and sometimes may not be able to find the optimal solution. The suitability of the optimization algorithms should be checked first based upon the nature of the benchmark problems they have been verified against. It can be noted that once the response surface is generated, each of the optimization method can be used with minimum computational time. The computational time is usually associated in building meta models.

Response surface is typically analyzed by a systematic and structured approach called Design of Experiments (DOE), which facilitates selection of proper set of experimental conditions to measure the response variable(s) while varying the input variable(s). A careful selection of Design of Experiment is necessary to minimize the number of experiments (iterations) required to accurately model the response surface. The careful part can be stressed because only with a proper selection of Design of Experiment, we can create a precise response surface. Careful planning of Design of Experiments includes several parameters:



### CHAPTER 3. PRELIMINARY DESIGN EXPLORATION: A STATISTICAL APPROACH

---

(a) Input variables: In a very simple problem, the input variables whose influence on output variable is expected, has to be identified. But sometimes, in complex problems, the influence of an input parameter is not obvious and we might often disregard them, which leads to incorrect experiment. All the input variables that have an influence on the output must be taken into account. However, using a lot of input variables will make the task tedious. Sensitivity analysis can be a good starting point to see the strength of influence of input parameters on output and then Design of experiments can be carried out with more sensitive variables and the experiment can be made sophisticated.

(b) Range: A practical range on which the input parameters can be varied to meet the design criteria should be specified. A very narrow range can give almost the same results. A wide range with few sample points can on other hand produce inaccurate response surface. Therefore, the range of input variable should be properly decided so as to represent the dynamics of the system.

(c) Replication: This refers to the number of times each experiment is repeated. Replication is important to ensure that the results are statistically significant and reproducible. The number of replicates needed depends on the variability of the system and the desired level of precision.

(d) Randomization: One of our main focus is the randomization of the input variables which refers to the process of obtaining unbiased input variables from the range in which the experiments are conducted. It can be noted that a lot of significant mathematical efforts have been made to obtain random unbiased sample in last few decades.

(e) Blocking: Blocking is a method used in which the domain is divided into blocks and a study is carried out in each block. This decreases the influence of variability. For example to check the effectiveness of a new medication, it is important to categorize by age or gender to prevent any variations in response that may be caused by these factors.

(f) Sample size: Depending upon how nonlinear the response is and the degree of the polynomial we are using, significant number of sample size might be necessary. Enough sample size must be specified to create the best fitting response surfaces. It is based on user's judgement of the problem. However when very large number of the sample size is specified, if the solver reaches a certain convergence based on statistical parameter, the iteration is stopped.

With proper selection of the above parameters, it is possible to obtain relevant and statistically significant results. Once the response surface is created, an optimization technique is generally employed to obtain the optimal value of input variables using gradient descent, response surface methodology itself, or other optimization algorithms.

## 3.2 Initial simulation : Base Model

Any complex design process begins with a simple simulation model known as base model, on which the all the input parameters (geometric, material, load and boundary conditions) and required output parameters (deformations, stresses) are defined and at least one simulation run is carried out. For the parametric study, we add one more step and define these input and output quantities as parametric variables. In our case, the input parametric variables are

- a) Height and thickness of the outer cylinder;
- b) Dimensions (breadth and depth) of the spokes;
- c) Dimensions (radius) of the cables;
- d) Thickness of the inner cylinder.

In ANSYS OptiSlang <sup>2</sup>, for each input variable defined as a parameter, a default of +/- 10% of the current value of each input parameter is used to initialize the parameter

---

<sup>2</sup>ANSYS OptiSlang is an extension in the ANSYS Workbench that includes a powerful simulation workflow environment. The software consists simulation driven workflow generation using parametric models for sensitivity analysis, optimization, and robustness evaluation.

### CHAPTER 3. PRELIMINARY DESIGN EXPLORATION: A STATISTICAL APPROACH

range. This can be manually adjusted and the adjustment must be such that the first simulation model has the input variables at the midpoint of the range; however, this is not a necessity. Each input parameters can be independently discrete or continuous within a range specified. The output parameter (also called performance indicator) is the total deformation in the spokes and the mass of the model (Figure 3.2) . No optimization is sought in these output variables. So the goal is to define the relationship between these six input parametric variables and two outputs. Now, we already have a model that can be run by the solver without any errors. This was introduced in the Chapter 1 and when we define our variables as parameters, this model becomes our base model.

	A	B	C	D
1	ID	Parameter Name	Value	Unit
2	[-] Input Parameters			
3	[-] Geometry (A1)			
4	P20	Height	200	
5	P21	Outerthickness	5	
6	P22	Innerthickness	5	
7	P25	Cirde_R	0,001	m
8	[-] Static Structural (B1)			
9	P32	Rectangle B	10	mm
10	P33	Rectangle H	10	mm
11	P34	Cirde R	1	mm
*	New input parameter	New name	New expression	
13	[-] Output Parameters			
14	[-] Static Structural (B1)			
15	P26	Total Deformation Maximum	52,069	mm
16	P37	Geometry Mass	4,4627	kg
*	New output parameter		New expression	
18	Charts			

Figure 3.2: Outline of the input and the output parameters.

However, we realise that parametric study means iterating the base model. Each time a geometry will have to be varied in the SpaceClaim, imported to the ANSYS Mechanical and the solver generates an output in the ANSYS Workbench. All these steps have to be automatized so no human interaction is permitted. To generate a parametric geometry, a python code is used. This code takes an input from the ANSYS workbench, updates the

geometry and exports to ANSYS mechanical. After solving the model, the outputs are again exported to ANSYS Workbench.

### **3.3 Identifying the design candidates**

Using the base model and the parameters defined, we can now generate a Response surface and with the aid of the response surface, we define a design space. Based on these two criterion, a Design of Experiment (DOE) will generate the design space. The design space is an approximation of the response of the system when subjected to the varying combination of the input parameters. The accuracy depends on complexity of the variations of the output parameters, number of points in the original DOE, and choice of the response surface type.

### **3.4 Sample generation**

A combination of the input variables within the range defined by the user generates a sample. Even from the same sample space, different samples can be generated and the relationship between input and output can be entirely different. This creates a problem in computer simulation in order to choose a combination of these input variables to accurately represent the response surface. Sample generation is an important step and helps in ascertaining the correct relationship between input and output variables. The question arises how to generate the sampling points evenly in order to capture the actual relationship. When modeling real world phenomena with a computer code one is often faced with the problem of what values to use for the inputs. In computer simulations, three important sample generators are used: Monte Carlo sampling, Latin Hypercube sampling and Optimal Space Filling Design sampling.

#### **Latin Hypercube sampling method**

Latin Hypercube sampling was proposed by McKay, Beckman and Conover (Los Alamos National Laboratory, 1979) as an alternative to simple Monte Carlo to characterise the un-

### CHAPTER 3. PRELIMINARY DESIGN EXPLORATION: A STATISTICAL APPROACH

---

certainty in inputs and is considered superior in generating a near-random sample from a multidimensional distribution in computer experiments and simulations. A sample space is divided into equal intervals or strata and a sample is taken from each stratum. The result is a multi dimensional array of randomly generated input variables from each row or column.

More precisely, for positive integers  $d$  and  $n$ , let:

1.  $\pi_k, 1 \leq k \leq d$ , be random permutations of  $\{1, \dots, n\}$  each uniformly distributed over all the  $n!$  possible permutations;
2.  $U_{i_1, \dots, i_d, j}, 1 \leq i_1, \dots, i_d \leq n, 1 \leq j \leq d$ , be  $[0, 1]$  uniform random variables;
3. the  $U_{i_1, \dots, i_d, j}$ 's and  $\pi_k$ 's all be stochastically independent.

A Latin hypercube sample of size  $n$  (taken from the  $d$ -dimensional hypercube  $[0, 1]^d$ ) is defined to be  $\{X(\pi_1(i), \pi_2(i), \dots, \pi_d(i)) : 1 \leq i \leq n\}$ , where for all  $1 \leq i_1, \dots, i_d \leq n$

$$X_j(i_1, \dots, i_d) = (i_j - U_{i_1, \dots, i_d, j}) / n \quad \forall 1 \leq j \leq d,$$
$$X(i_1, \dots, i_d) = (X_1(i_1, \dots, i_d), \dots, X_d(i_1, \dots, i_d))'.$$

Formally, let us consider a  $d$ -dimensional input space with  $n$  sample points. The  $i$ -th sample point is denoted by  $\mathbf{x}_i = (x_{i,1}, x_{i,2}, \dots, x_{i,d})$ , where  $i = 1, 2, \dots, n$ . In LHS, each dimension is divided into  $k$  intervals, denoted by  $[l_{1,j}, u_{1,j}], [l_{2,j}, u_{2,j}], \dots, [l_{k,j}, u_{k,j}]$ , where  $j = 1, 2, \dots, d$ . Then, one point is randomly selected from each interval to form the sample points.

The LHS method ensures that each row and each column of the above matrix contains exactly one sample point. This property makes LHS more efficient than other sampling methods that generate purely random samples, as it covers the input space more evenly.

### **Optimal Space Filled Latin Hypercube sampling method**

Classical DOE techniques (e.g., factorial, fractional factorial, or optimal designs) are designed to explain variability and estimate factor effects via the construction of statistical regression models [35]. Classical DOE may not be effective for sample generation when the results may be highly non-linear. If a model is deterministic, meaning that every time the model is run with identical input values, the output is the same, then replication is unnecessary and wasteful. Note that in classical DOE, replication is a core tenet due to the noisy (non-deterministic) nature of the output. Most classical DOE designs are boundary-filling rather than space-filling and thus are not ideal for capturing local phenomena which are common in nonlinear model. The Optimal Space Filling Latin Hypercube Sampling (OSFLHS) method is a modified version of LHS that aims to improve the sample point distribution in such cases.

Because of this objective to fill the space, the general class of experimental designs for computer experiments is called space-filling designs (SFDs). SFDs support the creation of a statistical emulator, or meta-model, which can be used to estimate uncertainty and predict the output of the simulation in both tested and untested conditions. If the emulator is robust enough, it can also serve as a surrogate for the model or simulation itself, which can save time and cut costs by avoiding the need to repeatedly re-run the simulation. Regular LHS creates a design in which all samples occupy unique rows and columns in a space defined only by continuous variables.

Sample size determination is a key aspect of planning any test. If we start with an initial size that is too small, we may not capture the true behavior of the response surface, and these inaccurate predictions can lead us to focus on inappropriate regions of the parameter space or report misleading results. Conversely, too large of a sample size is wasteful, especially when the computational budget is limited [36]. While important, the literature currently lacks clear formal guidance for choosing the right sample size for deterministic computer experiments, unlike for classical DOE. In the absence of a simple one-size-fits-

### CHAPTER 3. PRELIMINARY DESIGN EXPLORATION: A STATISTICAL APPROACH

---

all solution, we offer several ideas for how to approach sample size determination for SFDs.

As a simple rule of thumb, the number of runs ( $N$ ) for an effective initial computer experiment should be at least 10 times the number of variables ( $d$ ), i.e.,  $N=10 \times d$  [37]. If resources are especially limited, such that this minimum cannot be attained, testers could instead plan for 10 times the expected number of active variables, as the sparsity of effects principle suggests that systems and processes are often dominated by relatively few main effects and low-order interactions. Note, however, that this rule provides the lower bound, rather than the upper bound; sample sizes based on the  $N=10 \times d$  rule are especially likely to prove insufficient when probing more complex response surfaces. This rule of thumb is also intended for situations where most or all factors are continuous. Cases with several categorical variables would require more samples. In that situation, multiply the number of samples used for a single category by the number of categories being investigated to get a minimum for  $N$ .

Finally, subject matter experts' expectations for model behavior in response to changing inputs may further inform sample size selection. Relatively smaller sample sizes (such as  $N=10 \times d$ ) can be justified when largely linear and low-order effects are expected. Conversely, if highly non-linear response surfaces are expected, increasing the number of samples to fill the parameter space is even more crucial.

The OSFLHS method involves two steps. First, a set of initial LHS sample points is generated in the usual way. Then, an optimization algorithm is applied to adjust the position of each sample point to maximize the distance to its nearest neighbor. This ensures that the sample points are spaced as evenly as possible within the given constraints.

Formally, let us denote the set of initial LHS sample points by  $\mathbf{X} = \{\mathbf{x}_1, \mathbf{x}_2, \dots, \mathbf{x}_n\}$ , and the set of optimized sample points by  $\mathbf{Y} = \{\mathbf{y}_1, \mathbf{y}_2, \dots, \mathbf{y}_n\}$ . The optimization problem can be formulated as follows:

$$\begin{aligned} \text{maximize:} \quad & \min_{i,j=1,\dots,n,i \neq j} \|\mathbf{y}_i - \mathbf{y}_j\| \\ \text{subject to:} \quad & \mathbf{y}_i \in [l_{k,i}, u_{k,i}]^d, \quad i = 1, \dots, n \end{aligned} \tag{3.1}$$

Here, the objective is to maximize the minimum distance between any two sample points. The constraint ensures that each sample point remains within its assigned interval. The optimization problem can be solved using various algorithms, such as gradient descent, simulated annealing, or genetic algorithms. Once the optimized sample points  $\mathbf{Y}$  are obtained, they can be used in the same way as the initial LHS sample points  $\mathbf{X}$  to explore the input space or perform sensitivity analysis.

### 3.5 Running the simulation

Simulations can be performed in two ways. The first one is to run all the simulations for all the sample points. The second one is to check the mean and standard deviation convergences at each iteration against level of accuracy specified. Once the mean and standard deviation are stable for all output parameters, the correlation is converged and we stop our simulation. After this we can create meta models and optimization procedures. Initial simulation should only be run few design points and checked/verified that all the geometric, loading etc conditions are updated. Special attention should be given to cross section update and material assignment. The problem with cross section is that eventhough the iteration may seem to continue, it might be working with the by default cross section generated in the first iteration. The second thing is material data has to be manually entered in ANSYS when geometry is updated. Now if human interaction is necessary, it cannot be even called iteration. To avoid this, assign by default material should be set Yes. The default material should be changed from the Engineering data. In our case, we have seen in Chapter 2, that using the composite material, a very fine discretization of time step is necessary hence a single iteration will take a very long time which is not a practical approach. Even if we plan to do so, the deformation in the range of our design space is



## CHAPTER 3. PRELIMINARY DESIGN EXPLORATION: A STATISTICAL APPROACH

large enough that moment disequilibrium may arise hence the design points may fail.

### 3.6 Methodology

A python script is written in SpaceClaim that generates the geometry. Each component is assigned a named selection so that an iteration can be done without manual interruption. A parametric geometry is then setup so that these parameters will be varied to run the parametric analysis as shown in Figure 3.3. Once the geometry is updated, the geometry is exported to ANSYS mechanical and static structural analysis is carried out. The total deformation and the mass of the drift chamber are two output parameters that have to be studied. Once the output is generated it is stored in the OptiSlang. Another set of input parameter is then given to the SpaceClaim for next analysis and the iteration goes on. The project schematic for this cycle is shown in Figure 3.4. It should be noted that during the generation of the second model, the first model is already there in SpaceClaim, so on the top of the python code, a script to delete the existing geometry is written.

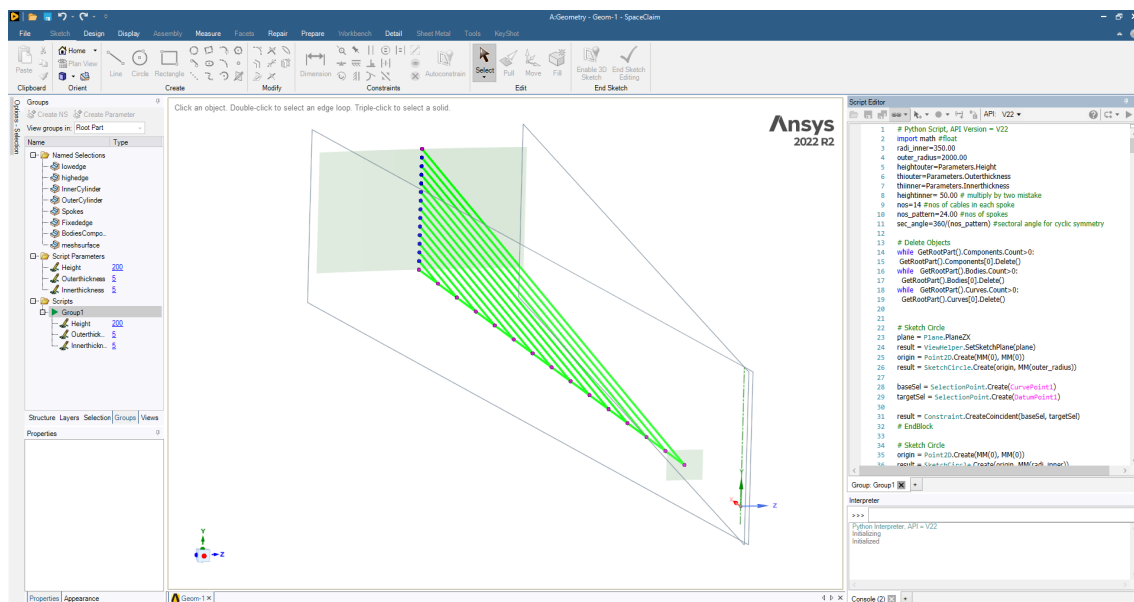


Figure 3.3: A window of SpaceClaim showing the Named selection required for automatic input in ANSYS Mechanical, Script parameters, the generated geometry and Python Script for geometry generation

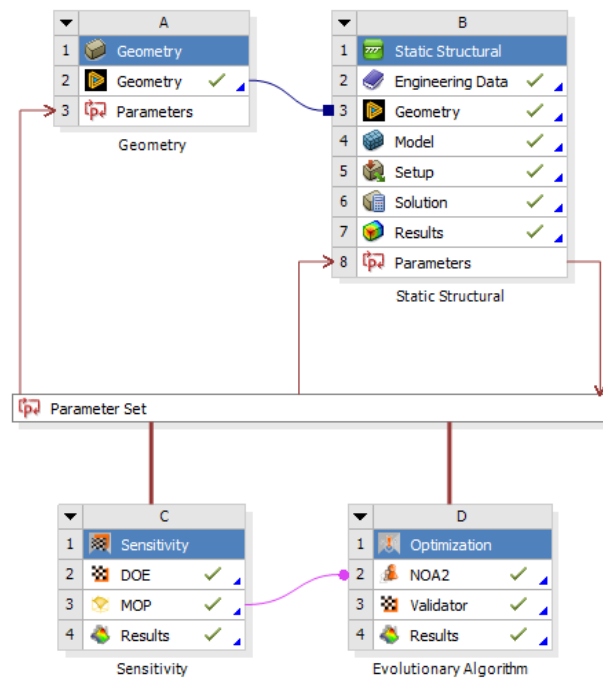


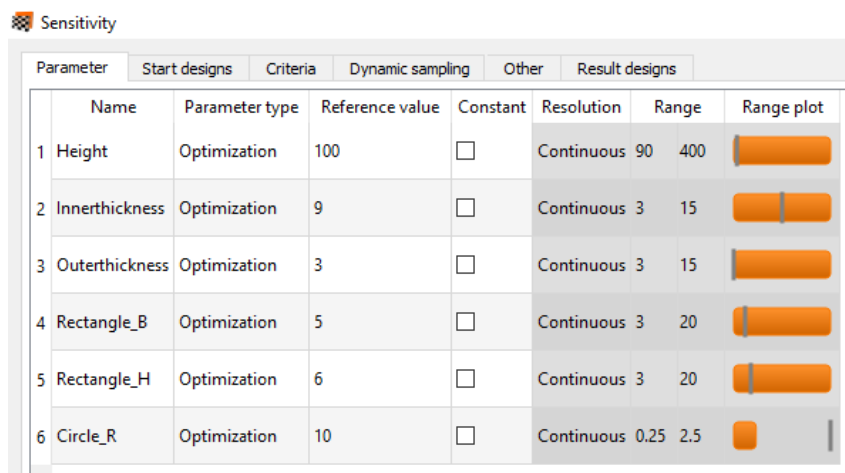
Figure 3.4: Project schematic for the Parametric design exploration. The values of the parameters are created by OptiSlang DOE wizard and these values are sent to SpaceClaim for geometry generation. Based on this the ANSYS Mechanical solves the model the Result set is updated. This completes one single iteration.

### 3.7 Sensitivity Analysis

Increasing the number of the inputs parameters, means increasing the number of design points which not only decreases the efficiency of the analysis process, but also the output becomes intractable. Creating the response surfaces with more than 10 or 15 input parameters is an expensive process. Hence, we include only the important input parameter whose impact on the response of the system is significant. This significantly reduces the sampling points as well as hundreds of unnecessary simulations. Now, what should be considered significant is based on our judgement. Hence, as mentioned previously in Chapter.1, an insight and instinct are two important things to solve this problem. A parameter correlation is such tool to help us asses the impact of each individual parameter

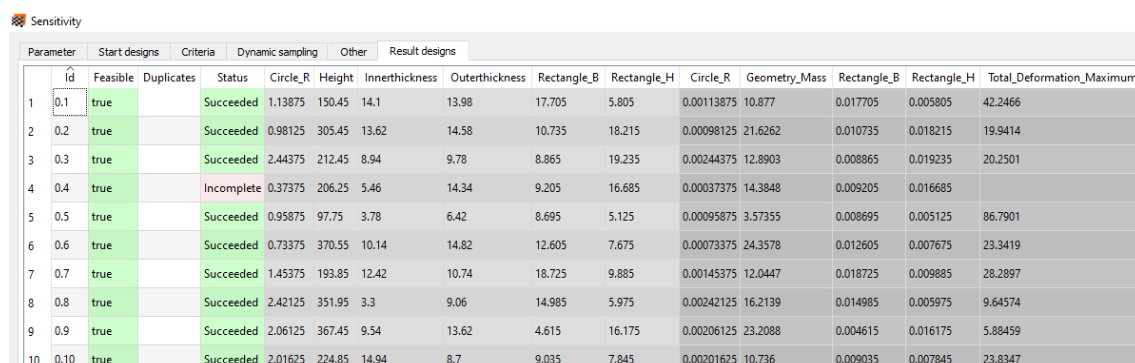
## CHAPTER 3. PRELIMINARY DESIGN EXPLORATION: A STATISTICAL APPROACH

as well as identify the degree to which the relationship is linear or quadratic. However, with just six input variables and only two output parameter, few number of iterations can generate a fairly accurate responses hence response surface in less computational cost. In reverse, these response surfaces can be employed to check the sensitivity of the input parameter. Figure 3.5 shows the input parameters, their resolution and the ranges. A wide range of the design space has been explored. Figure 3.6 shows a tabulated relationship between the input and the output of the sensitivity analysis.



Parameter	Start designs	Criteria	Dynamic sampling	Other	Result designs		
Name	Parameter type	Reference value	Constant	Resolution	Range		Range plot
1 Height	Optimization	100	<input type="checkbox"/>	Continuous	90	400	
2 Innerthickness	Optimization	9	<input type="checkbox"/>	Continuous	3	15	
3 Outerthickness	Optimization	3	<input type="checkbox"/>	Continuous	3	15	
4 Rectangle_B	Optimization	5	<input type="checkbox"/>	Continuous	3	20	
5 Rectangle_H	Optimization	6	<input type="checkbox"/>	Continuous	3	20	
6 Circle_R	Optimization	10	<input type="checkbox"/>	Continuous	0.25	2.5	

Figure 3.5: Input parameters for the Sensitivity analysis, their resolution and range. Continuous parameters are preferred as the response surface is a well defined surface, else slices will be formed.



Parameter	Start designs	Criteria	Dynamic sampling	Other	Result designs									
Id	Feasible	Duplicates	Status	Circle_R	Height	Innerthickness	Outerthickness	Rectangle_B	Rectangle_H	Circle_R	Geometry_Mass	Rectangle_B	Rectangle_H	Total_Deformation_Maximum
1	0.1	true	Succeeded	1.13875	150.45	14.1	13.98	17.705	5.805	0.00113875	10.877	0.017705	0.005805	42.2466
2	0.2	true	Succeeded	0.98125	305.45	13.62	14.58	10.735	18.215	0.00098125	21.6262	0.010735	0.018215	19.9414
3	0.3	true	Succeeded	2.44375	212.45	8.94	9.78	8.865	19.235	0.00244375	12.8903	0.008865	0.019235	20.2501
4	0.4	true	Incomplete	0.37375	206.25	5.46	14.34	9.205	16.685	0.00037375	14.3848	0.009205	0.016685	
5	0.5	true	Succeeded	0.95875	97.75	3.78	6.42	8.695	5.125	0.00095875	3.57355	0.008695	0.005125	86.7901
6	0.6	true	Succeeded	0.73375	370.55	10.14	14.82	12.605	7.675	0.00073375	24.3578	0.012605	0.007675	23.3419
7	0.7	true	Succeeded	1.45375	193.85	12.42	10.74	18.725	9.885	0.00145375	12.0447	0.018725	0.009885	28.2897
8	0.8	true	Succeeded	2.42125	351.95	3.3	9.06	14.985	5.975	0.00242125	16.2139	0.014985	0.005975	9.64574
9	0.9	true	Succeeded	2.06125	367.45	9.54	13.62	4.615	16.175	0.00206125	23.2088	0.004615	0.016175	5.88459
10	0.10	true	Succeeded	2.01625	224.85	14.94	8.7	9.035	7.845	0.00201625	10.736	0.009035	0.007845	23.8347

Figure 3.6: Example of the first 10 Design results from the sensitivity analysis.

## 3.8 Results from the Sensitivity Analysis

### 3.8.1 CoP Matrix

The CoP matrix in OptiSlang provides a way to analyze the sensitivity of system outputs (responses) to changes in the input variables (parameters). It allows users to assess the impact of different input variations on the performance of the system and identify the most influential parameters affecting the system's response.

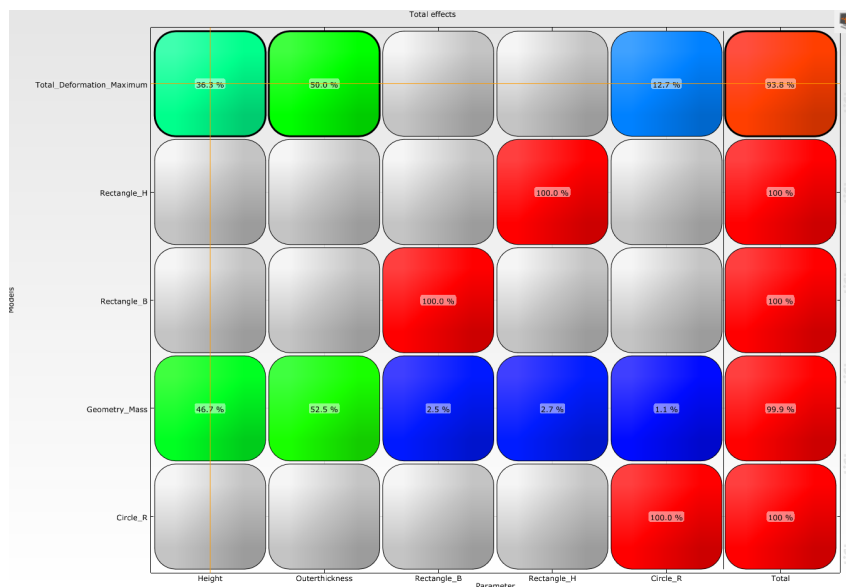


Figure 3.7: CoP Matrix results from the sensitivity analysis which shows the highest sensitivity of the parameter height, outer thickness, and the radius of the cables.

Analyzing the CoP matrix (Figure 3.7), we can conclude that the Height and the thickness of the outer cylinder are most important parameters for controlling the total deformation in the model and also contribute significantly to the total mass of the model. Using values of height around 400 mm and thickness higher than 13 mm, we can reduce the Total deformation to less than 6 mm. Accordingly, these are the parameters that have the most significant influence on the system's performance and we focus optimization efforts accordingly. The CoP values are typically normalized, enabling a direct comparison of different parameters' sensitivities.

From the above CoP Matrix, we can conclude that the effect of increasing the dimensions of the spokes has a very little effect for controlling the Total deflection. This may be due to the fact that the spokes are held in position by the cables. Also the slenderness of the spokes might be a factor due to which it is not able to contribute to limiting the Total deformation in the model. This defies the usual instinct hence this is a very useful finding.

### 3.8.2 Linear Correlation Matrix

The linear correlation matrix in OptiSlang provides a numerical representation of the correlation coefficients between pairs of parameters or between parameters and responses (Figure 3.8). The correlation coefficient quantifies the strength and direction of the linear relationship between two variables. It ranges from -1 to 1, where -1 indicates a perfect negative correlation, 1 indicates a perfect positive correlation, and 0 indicates no correlation.

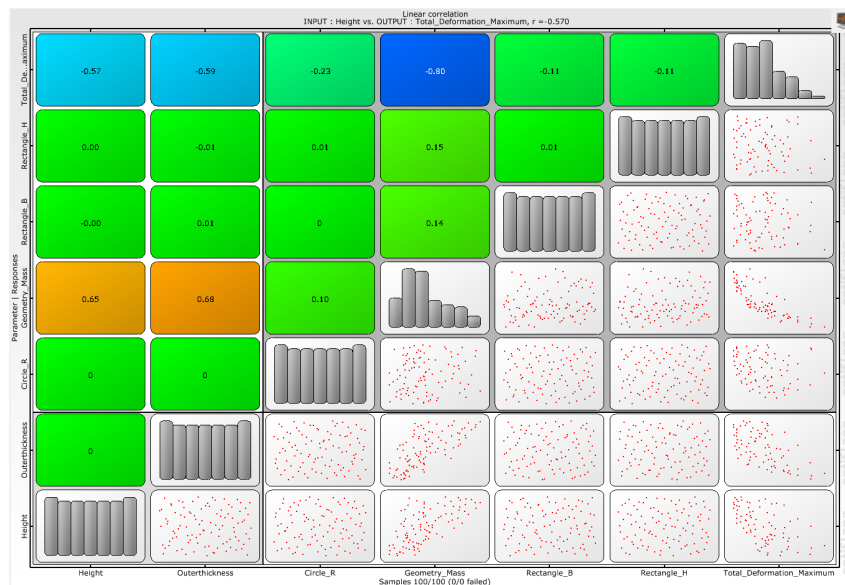


Figure 3.8: Correlation Matrix from the sensitivity analysis showing linear correlation coefficients, histograms and anthill plots for all selected input and output parameters and their combinations respectively, combined into one plot.

From the above linear correlation matrix, we see that height and thickness of the outer

## CHAPTER 3. PRELIMINARY DESIGN EXPLORATION: A STATISTICAL APPROACH

cylinder and radius of the cables are three most important parameters contributing to the Total deformation and Mass of the drift chamber. Also we see that there exists a strong negative linear correlation between Total deformation and Mass of the drift chamber. This means that if we increase the Mass it will help in decreasing the Total deformation. However, our goal is to have a minimum mass and minimum deformation which counteracts the negative linear correlation relationship between them. This is solved by using pareto optimality solution (Refer to Section 3.10.1).

### 3.8.3 Best design from the Sensitivity Analysis

Based on the design of experiments performed on the 100 different samples, all the designs are shown on the parallel coordinates plot below (Figure 3.9). If we consider to limit the deformation to the minimum then the best design is Design 20.

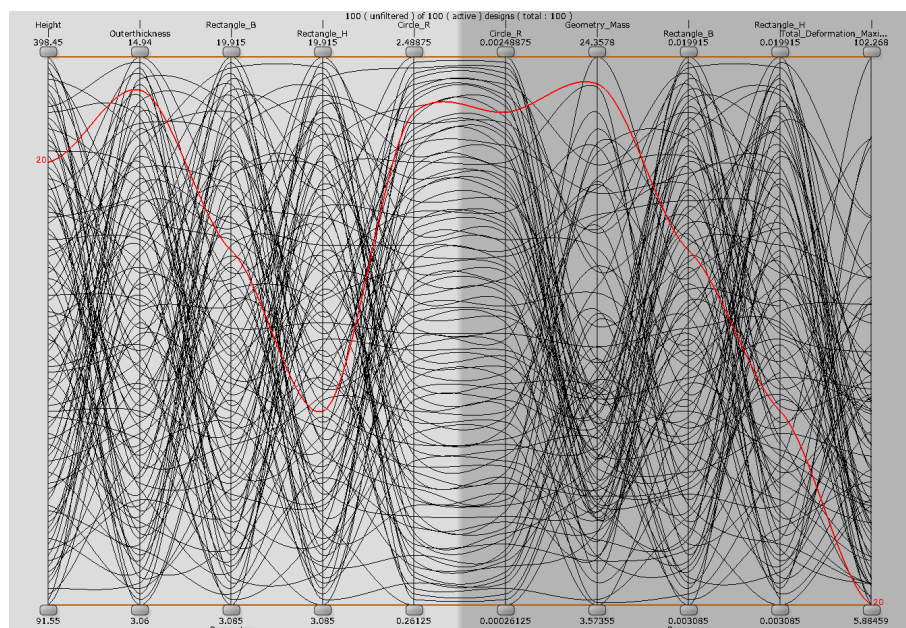


Figure 3.9: Parallel coordinates plot showing all the 100 designs evaluated during the sensitivity analysis. The plot displays a comprehensive representation of input, output, objectives, and constraints for all designs. Each parameter is accompanied by two sliders to set lower and upper bounds. Designs that fall outside of these bounds are also shaded in grey.

## CHAPTER 3. PRELIMINARY DESIGN EXPLORATION: A STATISTICAL APPROACH

---

From the above analysis, considering the model having least Total deformation as the best model,

<b>Parameters:</b>	
Height:	339.55 mm
Innerthickness:	7.02 mm
Outerthickness:	14.22 mm
Rectangle_B:	13.965 mm
Rectangle_H:	9.035 mm
Circle_R:	2.26375 mm

<b>Responses:</b>	
Geometry_Mass:	23.3293 kg per sector
Total_Deformation_Maximum:	5.89769 mm

Table 3.1: Best design obtained from the sensitivity analysis with least deformation of 5.89769 mm

### 3.9 Kriging Response Surface Methodology

When the samples are generated, an iteration is carried out and responses of the system are recorded. The iteration continues until all the sample input generates an output<sup>3</sup> or some statistical convergence is obtained. Then we have a set of input points and output points. For each output parameter and all the inputs, a regression analysis is done to obtain the so called response surface. An analogy can be made with respect to curve fitting approach. One method to obtain these response surface is by using kriging method. Kriging Response Surface (KRS) methodology is a statistical approach that combines kriging with response surface methodology (RSM) to model the relationship between the response variable and the input variables. The KRS methodology is based on two well-established statistical methods: kriging and Response Surface Methodology. Kriging is actually a geostatistical method that uses the spatial correlation between the data points to interpolate values at unobserved locations. RSM is a statistical approach that models the relationship between the response variable and the input variables using a set of mathematical functions. By

---

<sup>3</sup>However, if the values of the input generated are incompatible not necessarily only from a geometric perspective, a failed design is generated. This failed design can be retained and again be tried by the solver if needed.

combining kriging and RSM, the KRS methodology aims to create a more accurate and efficient method for modeling the relationship between the input variables and output variables.

**Kriging Methodology** Kriging is a method that estimates the unknown function,  $f(\mathbf{X})$ , by combining the observed data with a set of weights that depend on the spatial correlation between the data points. The weights are calculated using a covariance function,  $C(h)$ , which measures the similarity between the input variables at two different locations separated by a distance  $h$ . The kriging estimate,  $\hat{y}(\mathbf{X})$ , can be expressed as follows:

$$\hat{y}(\mathbf{X}) = \sum_i w_i (Y_i - \mu) + \mu \quad (3.2)$$

where  $Y_i$  is the observed value at location  $i$ ,  $\mu$  is the mean of the response variable, and  $w_i$  are the weights calculated using the covariance function. Kriging involves creating a linear model of spatial dependence between the measured data points and using that model to make predictions at unsampled locations. Let  $Z(s)$  denote the random variable representing the measured value at location  $s$ . The Kriging prediction at an unsampled location  $s^*$  can be expressed as:

$$Z(s^*) = \sum_{i=1}^n \lambda_i Z(s_i) \quad (3.3)$$

where  $n$  is the number of sampled locations,  $s_i$  and  $Z(s_i)$  are the sampled locations and values, respectively, and  $\lambda_i$  are the Kriging weights, which are determined by minimizing the prediction error, subject to the constraint that the weights sum to one:  $\sum_{i=1}^n \lambda_i = 1$

The Kriging weights are given by:

$$\lambda_i = \frac{\text{cov}(Z(s_i), Z(s^*))}{\sum_{j=1}^n \text{cov}(Z(s_i), Z(s_j))} \quad (3.4)$$

where  $\text{cov}(Z(s_i), Z(s_j))$  is the covariance between the values at locations  $s_i$  and  $s_j$ , and  $\text{cov}(Z(s_i), Z(s^*))$  is the covariance between the value at location  $s_i$  and the unsampled



location  $s^*$ . The spatial covariance function, which describes the correlation between the values at different locations, is typically assumed to be stationary and is estimated from the data using methods such as variogram analysis.

Instead of Kriging another similar technique called Inverse distance weighted (IDW) also exists which assumes that the value at an unsampled location is proportional to the weighted average of the values at the neighboring sampled locations. Let  $Z(s_i)$  denote the measured value at location  $s_i$  and  $d(s_i, s^*)$  denote the Euclidean distance between location  $s_i$  and the unsampled location  $s^*$ . The IDW prediction at location  $s^*$  can be expressed as:

$$Z(s^*) = \frac{\sum_{i=1}^n w_i Z(s_i)}{\sum_{i=1}^n w_i} \quad (3.5)$$

where  $w_i$  is the weight assigned to the  $i$ -th sampled location, which is determined as:

$$w_i = \frac{1}{d(s_i, s^*)^p} \quad (3.6)$$

where  $p$  is a user-defined power parameter that controls the influence of distant locations on the prediction. A higher value of  $p$  gives more weight to nearby locations and less weight to distant locations.

Kriging is a more sophisticated method that can provide accurate predictions even in regions with sparse data, but it requires a lot of data to estimate the spatial covariance function accurately. On the other hand, IDW is a simpler method that is easy to use and computationally efficient, but it does not take into account any spatial dependence structure in the data and can produce unrealistic results in areas with extreme values or discontinuities. Therefore, we adopt kriging and proceed with this one. However, there are several methods and once the iterations are created, other methods can also be taken into account without any expense of simulation time.

**Response Surface Methodology** Response surface methodology (RSM) is a statistical approach that models the relationship between the response variable and the input variables using a set of mathematical functions. The most common function used in RSM is the second-order polynomial function, which can be expressed as follows:

$$y = \beta_0 + \sum_{i=1}^k \beta_i x_i + \sum_{i=1}^k \beta_{ii} x_i^2 + \sum_{i=1}^k \sum_{j=i+1}^k \beta_{ij} x_i x_j + \epsilon$$

where  $y$  is the response variable,  $\mathbf{X} = (x_1, x_2, \dots, x_k)$  are the input variables,  $\beta_i$  are the linear coefficients,  $\beta_{ii}$  are the quadratic coefficients,  $\beta_{ij}$  are the interaction coefficients, and  $\epsilon$  is the error term.

**Kriging Response Surface Methodology** The Kriging Response Surface (KRS) methodology combines kriging and RSM to create a more accurate and efficient method for modeling the relationship between the response variable and the input variables.

$$y(\mathbf{x}) = f(\mathbf{x}) + \varepsilon \quad (3.7)$$

where  $y(\mathbf{x})$  is the output of the process at input location  $\mathbf{x}$ ,  $f(\mathbf{x})$  is a deterministic function representing the underlying response surface, and  $\varepsilon$  is a normally distributed error term with zero mean and variance  $\sigma^2$ . The function  $f(\mathbf{x})$  can be represented as a linear combination of basis functions:

$$f(\mathbf{x}) = \sum_{i=1}^n w_i b_i(\mathbf{x}) \quad (3.8)$$

where  $b_i(\mathbf{x})$  are basis functions,  $w_i$  are weights, and  $n$  is the number of basis functions. The weights and basis functions are chosen to minimize the prediction error of the kriging model.

Once the kriging model is constructed, it can be used as a surrogate for the true response surface to optimize the process using RSM techniques. This involves selecting a set of input locations to evaluate the process and updating the kriging model with the

new data. The RSM optimization algorithm then uses the kriging model to determine the optimal input values for the process. Kriging RSM is a powerful methodology for optimizing complex processes with nonlinear response surfaces. By combining kriging and RSM, it is possible to efficiently optimize processes that would be computationally infeasible to optimize directly.

The KRS methodology involves the following steps:

1. Design of experiments: A set of input variables are chosen, and a set of experiments are designed to collect data on the response variable for different combinations of the input variables.
2. Model fitting: The data is used to fit a KRS model, which involves estimating the unknown function  $f(\mathbf{X})$  and the covariance function  $C(h)$ .
3. Model validation: The KRS model is validated using a set of validation data that were not used in model fitting. The validation data is used to estimate the prediction error of the model.
4. Optimization: The KRS model is used to optimize the response variable by finding the combination of input variables that maximize or minimize the response variable.

The kriging response surface methodology can handle non-linear relationships between the response variable and the input variables. It can handle noisy data and missing values. It provides an estimate of the prediction error, which can be used to assess the quality of the model. However, it assumes that the relationship between the response variable and the input variables is smooth, which may not always be the case. This method requires a large number of experiments to accurately estimate the unknown function  $f(\mathbf{X})$  and the covariance function  $C(h)$ . In our case, we define four isotropic kriging response surface between the input and the output variables. These are shown from Figure 3.10 to Figure

## CHAPTER 3. PRELIMINARY DESIGN EXPLORATION: A STATISTICAL APPROACH

3.13.

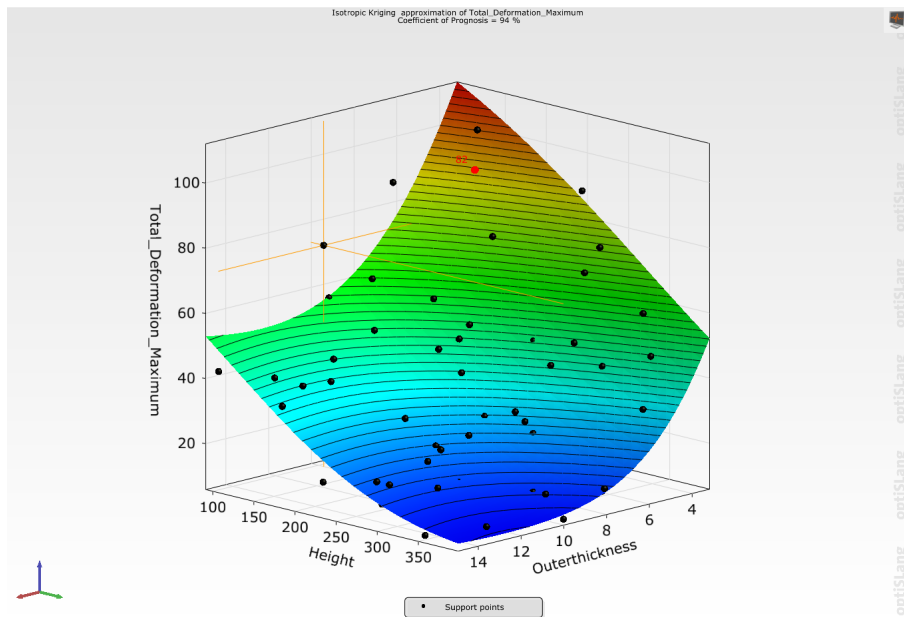


Figure 3.10: Response surface showing Isotropic Kriging approximation between the total deformation, height of the outer cylinder and the thickness of the outer cylinder .

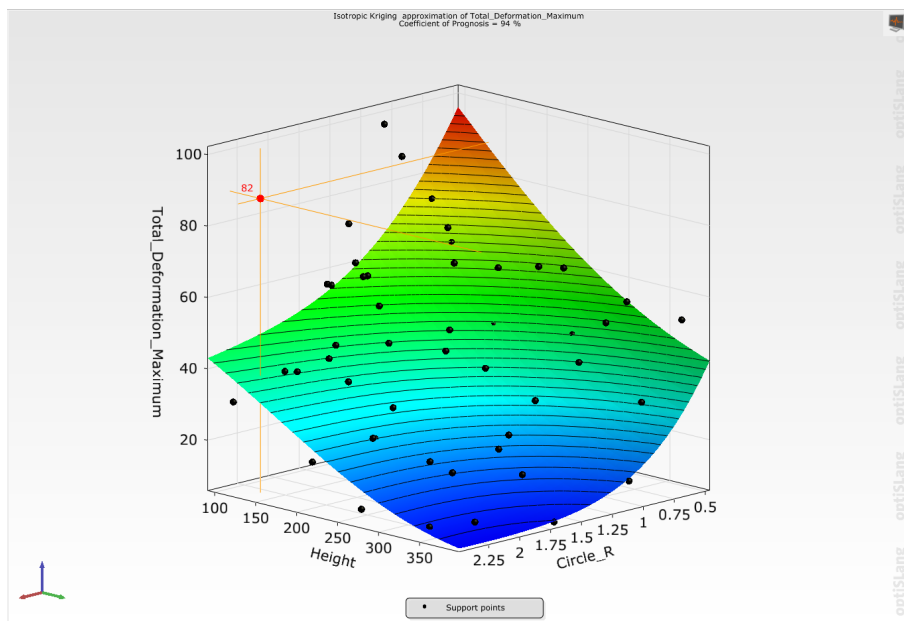


Figure 3.11: Response surface showing Isotropic Kriging approximation between the total deformation, height of the outer cylinder and the radius of the cables.

### CHAPTER 3. PRELIMINARY DESIGN EXPLORATION: A STATISTICAL APPROACH

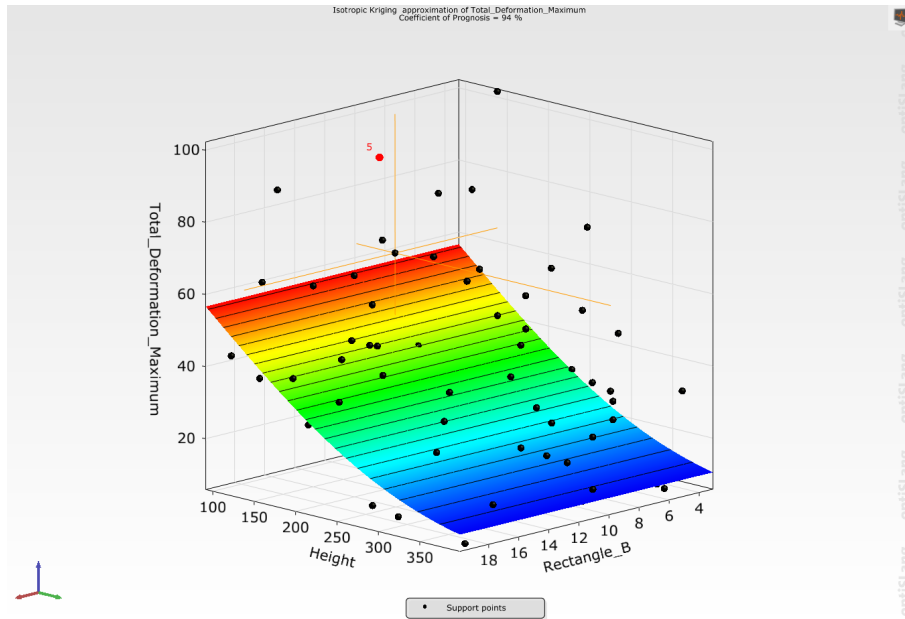


Figure 3.12: Response surface showing Isotropic Kriging approximation between the total deformation, height of the outer cylinder and the breadth of the spokes.

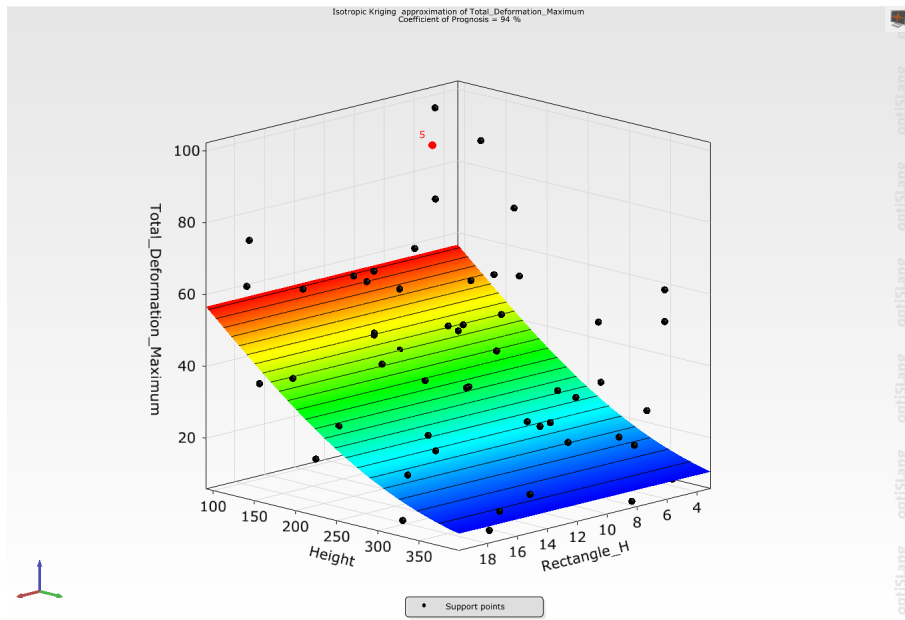


Figure 3.13: Response surface showing Isotropic Kriging approximation between the total deformation, height of the outer cylinder and the height of the spokes.

## **3.10 Creation of the Metamodels and Multi-objective optimization**

### **3.10.1 Creation of the Metamodels**

Response Surface Methodology involves designing a series of experiments to collect data on the response variable and the input variables. The data collected is then used to develop a regression equation, which is a mathematical expression that describes the relationship between the response variable and the input variables. The regression equation is then used to create a response surface. Once the response surface is generated using certain mathematical model, create a so called surrogate model or meta model. Once a meta model is created it can be used to make predictions about the response variable for new input values instantaneously without any simulation (Figure 3.15). In parametric design exploration, meta models give an answer to every possible design combination and the optimization of these models also gives us the best models. In our case, Figure 3.14 shows the optimization is sought on whole design space minimising the Total mass and Total deformation. But the use of meta models becomes almost necessary in situations when complex time consuming and computationally expensive simulations are to be done. In such cases, meta models can be employed to analyze, understand and optimize the behavior of such complex model under any design combination. The output of the meta models is not exact as it is only an approximation of the response of the system and the design can further be checked by using that design in actual simulation. The difference is the error and it can be improved by inserting more points. The objective pareto plot shows these designs (Figure 3.16). However, it should be understood that these meta models approximate the response accurate enough that designer gets an overall idea on the direction where the optimized value can be found.

### CHAPTER 3. PRELIMINARY DESIGN EXPLORATION: A STATISTICAL APPROACH

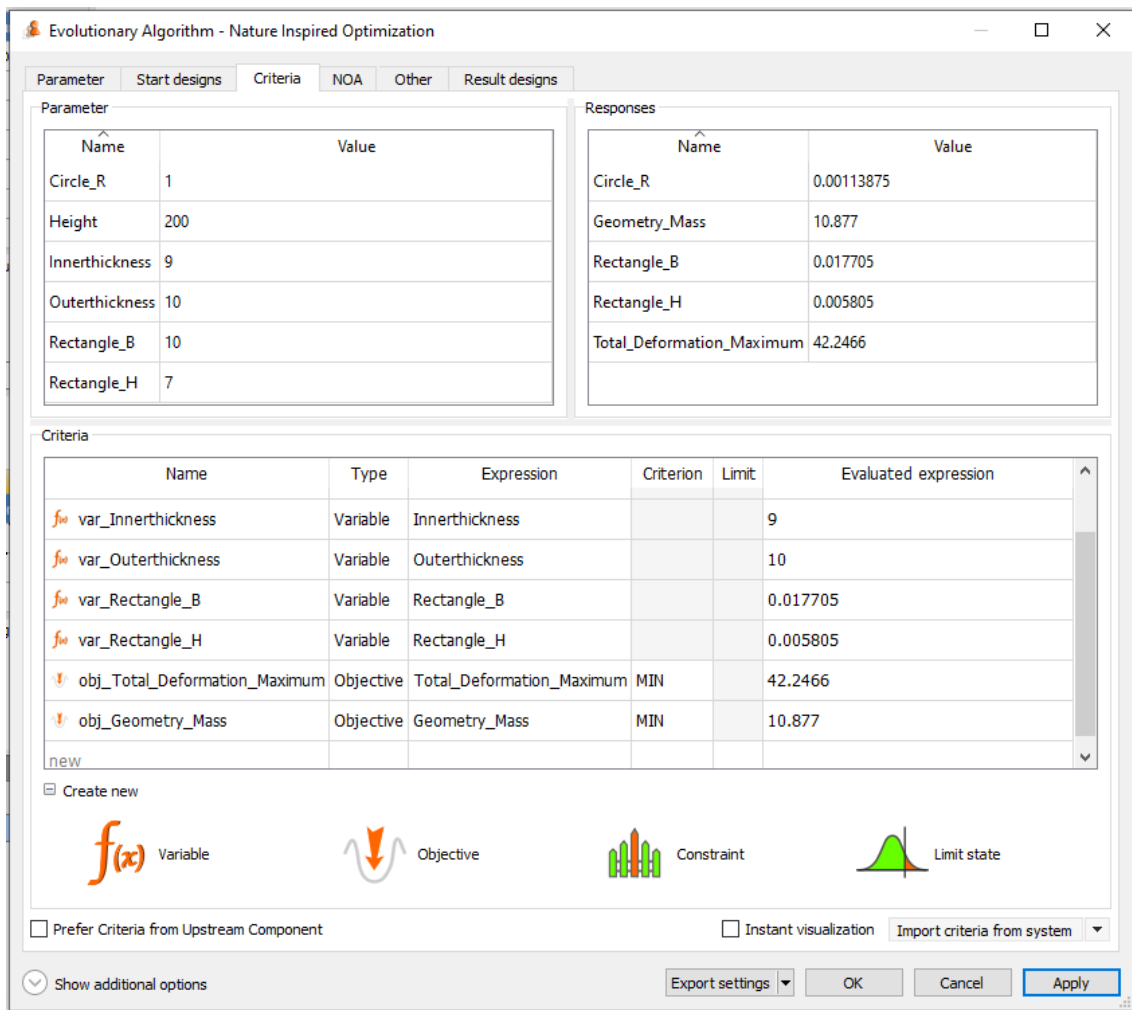


Figure 3.14: Optimization criteria set for minimising the Total deformation and Total mass. Initially it will create a Meta Model and then optimise the response surface

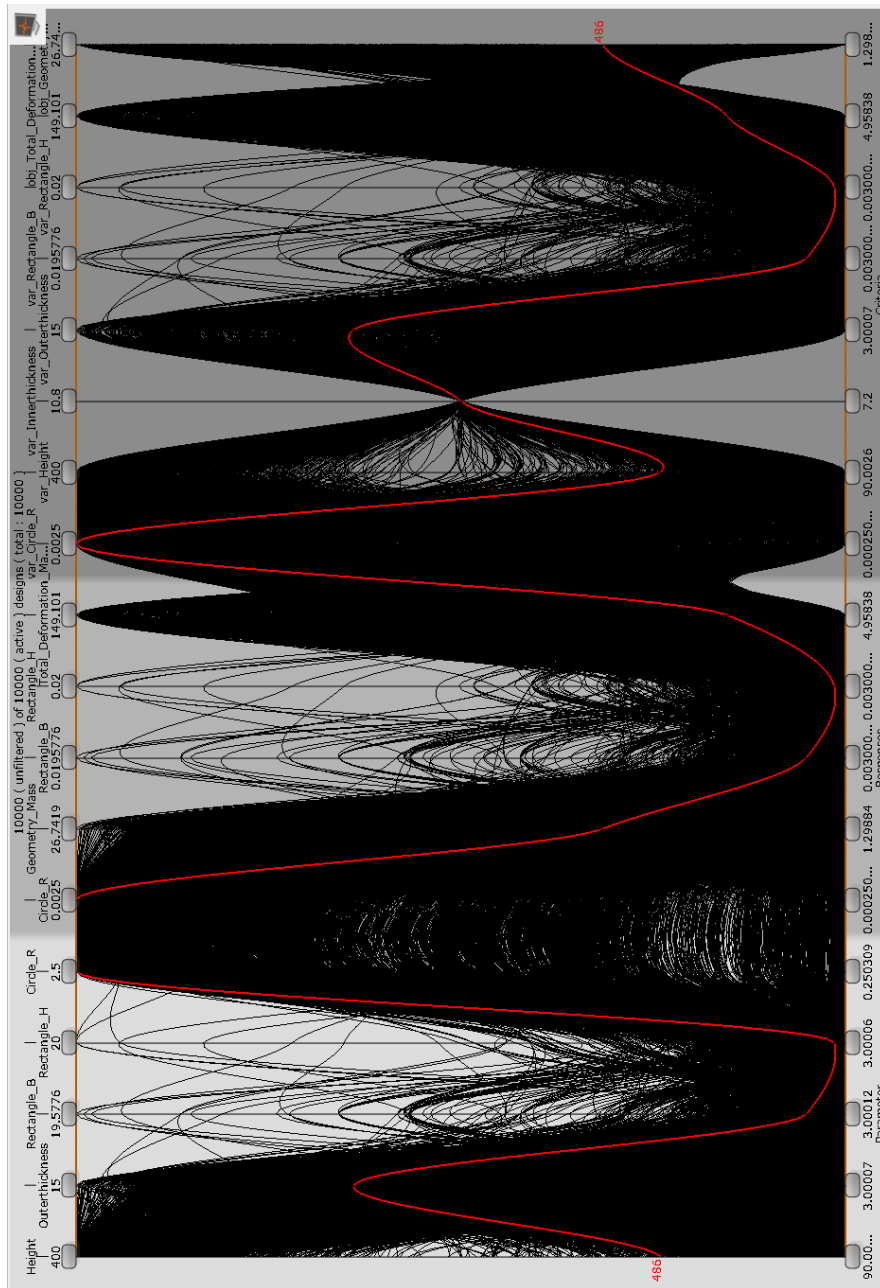


Figure 3.15: Parallel coordinates plot for the 10,000 design created by the metamodels



## CHAPTER 3. PRELIMINARY DESIGN EXPLORATION: A STATISTICAL APPROACH

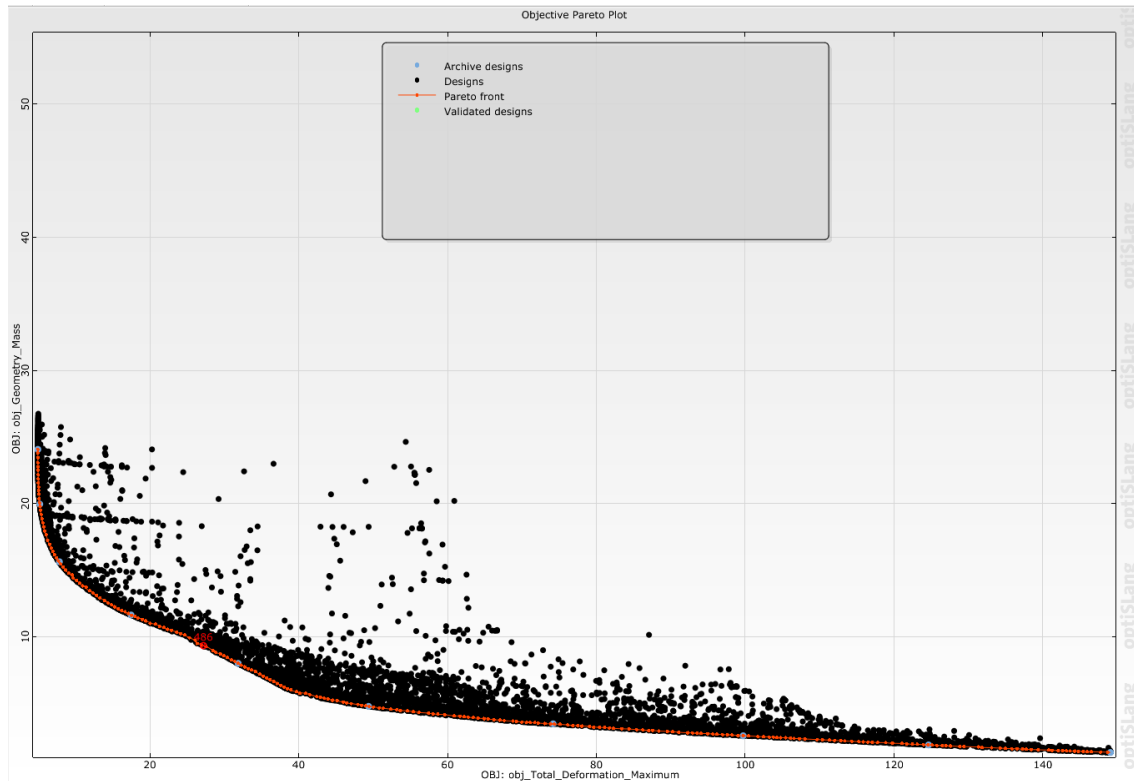


Figure 3.16: Objective Pareto plot for the multiobjective optimization

From the above analysis, using the meta model to minimise the Total deformation as well as Total mass, the best model is design no 486. However, several other best designs are also given.

---

### Parameters:

Height:	164.527 mm
Innerthickness:	9 mm
Outerthickness:	10.6708 mm
Rectangle_B:	3.83952 mm
Rectangle_H:	3.24668 mm
Circle_R:	2.5 mm

---

### Responses:

Geometry_Mass:	9.32653 kg per sector
Total_Deformation_Maximum:	27.2034 mm

---

Table 3.2: Best design model (486) obtained from the multi-objective optimization of the deformation and mass

### CHAPTER 3. PRELIMINARY DESIGN EXPLORATION: A STATISTICAL APPROACH

Two design philosophy can be adopted to seek the best design. One using the height of outer cylinder less than 200 mm (Figure 3.17) in which the Total deformation is around 27 mm. Another is using a radius of 1.5 mm cables (Figure 3.18) in which the deformation can be limited to less than 10 mm but the height of the outer cylinder must be around 400 mm in that case. So all these design exploration gives us an insight into what combination can be used in order to achieve our goal.

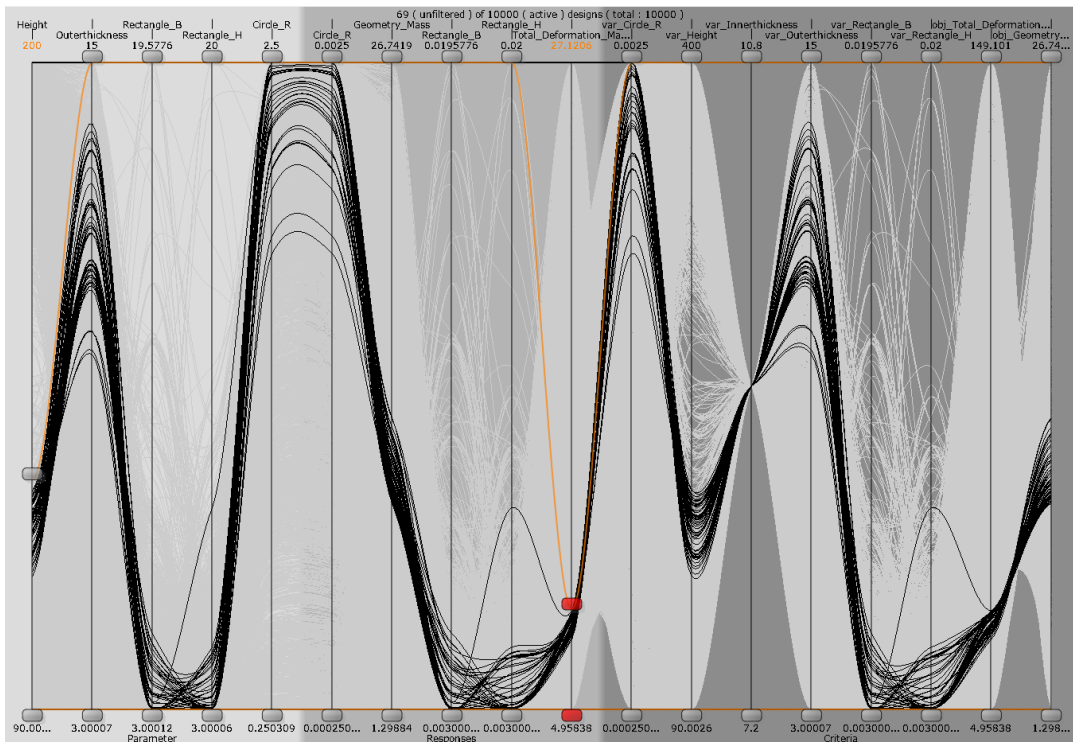


Figure 3.17: Parallel coordinates plots of the designs selected from the meta models with height of outer cylinder less than 200 mm and total displacement less than 27.1206 mm.

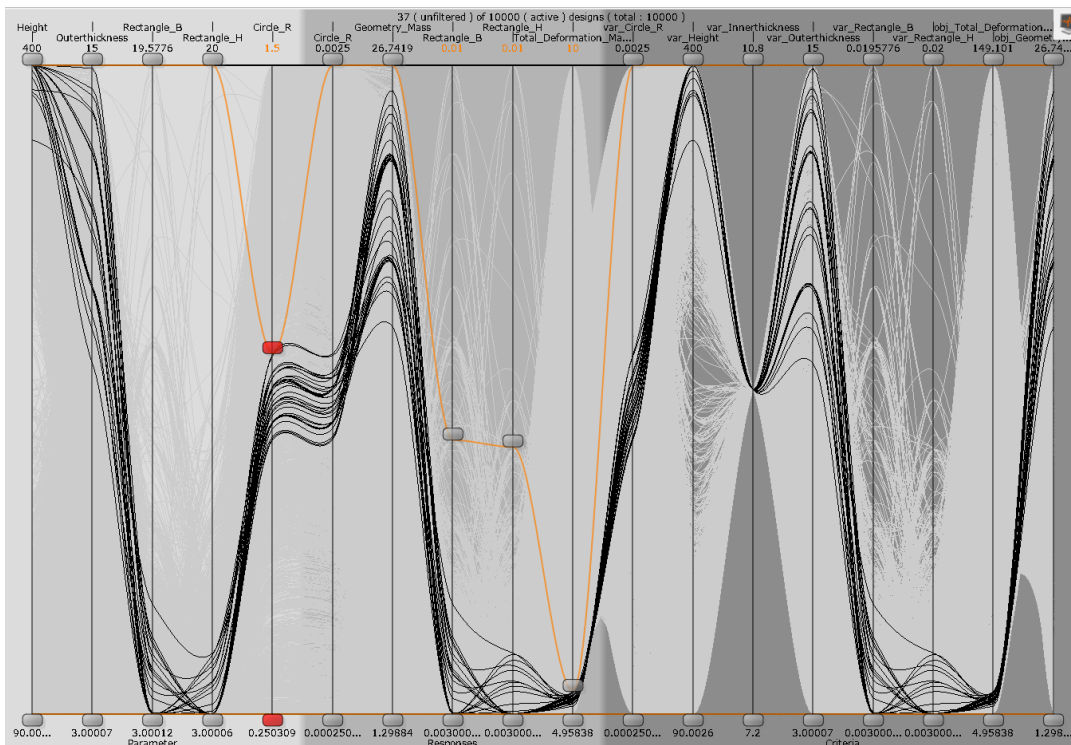


Figure 3.18: Parallel coordinates plots of the designs selected from the meta models radius of the cables less than 1.5 mm and total displacement less than 10 mm.

### 3.10.2 Optimization of the Metamodels

Previously no constraints on the input variables were used hence the optimization was performed in the whole response surface in order to minimise the Total deformation and Total Mass. However, we also have constraints in the input variables. This is shown in Figure 3.19. We already have a meta model and using genetic algorithm, we get 10000 feasible design points that satisfy our constraints. From the Parallel coordinates plot (Figure 3.20), we select the best design as Design 9989.

## CHAPTER 3. PRELIMINARY DESIGN EXPLORATION: A STATISTICAL APPROACH

The screenshot displays the 'Criteria' tab of the 'Evolutionary Algorithm - Nature Inspired Optimization' software. It shows the following data:

**Parameter Table:**

Name	Value
Circle_R	1
Height	100
Innerthickness	9
Outerthickness	3
Rectangle_B	5
Rectangle_H	6

**Responses Table:**

Name	Value
Circle_R	0.00113875
Geometry_Mass	10.877
Rectangle_B	0.017705
Rectangle_H	0.005805
Total_Deformation_Maximum	42.2466

**Criteria Table:**

Name	Type	Expression	Criterion	Limit	Evaluated expression
constr_Circle_R	Constraint	Circle_R	≤	1.5	0.00113875 ≤ 1.5
constr_Height	Constraint	Height	≤	200	100 ≤ 200
constr_Innerthickness	Constraint	Innerthickness	≤	10	9 ≤ 10
constr_Outerthickness	Constraint	Outerthickness	≤	15	3 ≤ 15
constr_Rectangle_B	Constraint	Rectangle_B	≤	10	0.017705 ≤ 10
constr_Rectangle_H	Constraint	Rectangle_H	≤	20	0.005805 ≤ 20
obj_Total_Deformation_Maximum	Objective	Total_Deformation_Maximum	MIN		42.2466
obj_Geometry_Mass	Objective	Geometry_Mass	MIN		10.877
new					

**Legend:**

- $f(x)$  Variable
- Downward arrow Objective
- Three bars Constraint
- Graph Limit state

Additional options:  Prefer Criteria from Upstream Component,  Instant visualization,  Show additional options,

Figure 3.19: Criterion set for the multi-objective optimization using Genetic Algorithms.

## CHAPTER 3. PRELIMINARY DESIGN EXPLORATION: A STATISTICAL APPROACH

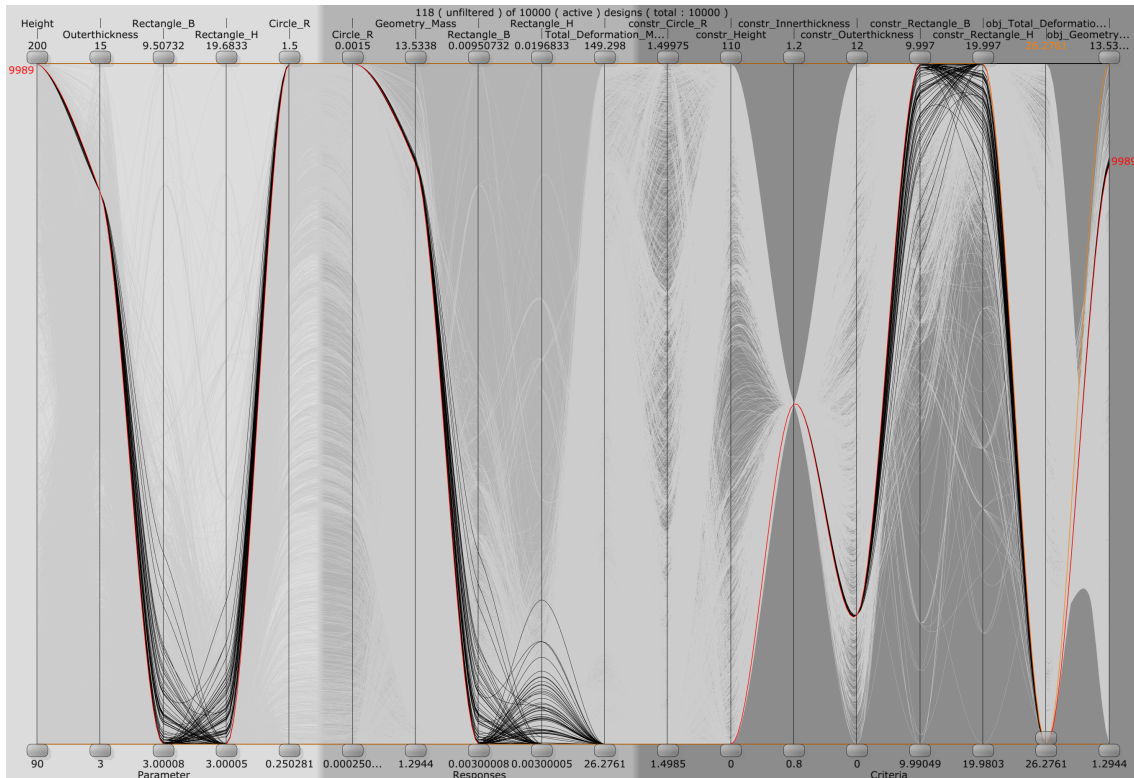


Figure 3.20: Parallel coordinates plot of the optimization results subjected to the constraint.

From the above analysis, Performing a multiobjective optimization of Total deformation as well as mass the best model is design no 694,

---

### Parameters:

---

Height:	200 mm
Innerthickness:	9 mm
Outerthickness:	12.7215 mm
Rectangle_B:	3.00113 mm
Rectangle_H:	3.00175 mm
Circle_R:	1.5 mm

---

### Responses:

---

Geometry_Mass:	11.7135 kg per sector
Total_Deformation_Maximum:	26.2761

---

Table 3.3: Best design model (694) obtained from the constrained multi-objective optimization of the Total deformation and Total mass

### 3.11 Limitations from Linear Buckling Analysis

For the above design 694, if we perform the linear buckling analysis, the load multiplier is less than 1. This is due to the fact that the beam is very slender. For our spokes, disregarding the stiffness of the cables,

Length of the beam ( $L$ ): 1650 mm = 1.65 meters

Cross-sectional dimensions: 3 mm x 3 mm

Area ( $A$ ) of the cross section:

$$A = \text{width} \times \text{height} = 3 \text{ mm} \times 3 \text{ mm} = 9 \text{ mm}^2$$

Moment of inertia ( $I$ ) of the cross section: Since the cross section is a square, the moment of inertia can be calculated using the formula:  $I = \frac{\text{width}^4}{12}$

$$I = \frac{(3 \text{ mm})^4}{12} = \frac{81 \text{ mm}^4}{12}$$

$$I = \frac{9 \text{ mm}^4}{12} = 6.75 \text{ mm}^4$$

Now, we can calculate the minimum radius of gyration ( $r$ ):

$$r = \sqrt{\frac{I}{A}} = \sqrt{\frac{6.75 \text{ mm}^4}{9 \text{ mm}^2}} = \sqrt{0.75 \text{ mm}^2} \approx 0.866 \text{ mm}$$

### CHAPTER 3. PRELIMINARY DESIGN EXPLORATION: A STATISTICAL APPROACH

---

Finally, we can calculate the slenderness ratio ( $\lambda$ ):

$$\lambda = \frac{L}{r} = \frac{1.65 \text{ meters}}{0.866 \text{ mm}} \approx 1903.83$$

Therefore, the slenderness ratio of the carbon composite beam is approximately 1900.83. Due to this even with lower value of loads, the drift chamber would completely buckle (Figure 3.21).

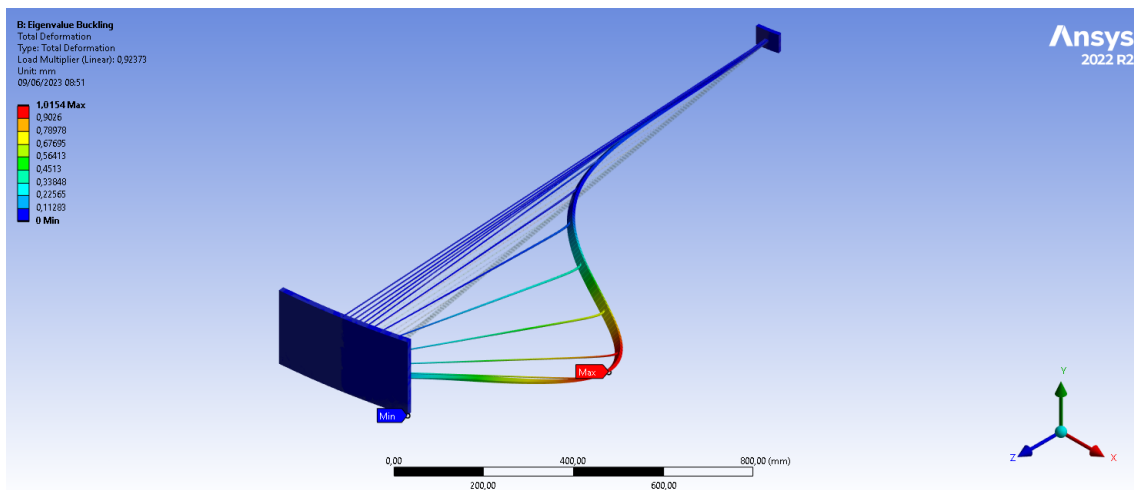


Figure 3.21: Deformed shape of the spokes obtained from the Linear buckling analysis of the drift chamber for breadth of 5 mm and depth of 10 mm. Load multiplier is 0.92.

In order to solve this issue, we increase the number of spokes from 24 to 36. Due to this the load in each spoke decreases from 4166.78 N to 2777.78 N. Now using a model consisting of 36 spokes, loaded with uniformly varying line pressure, a parametric analysis is done. The input parameters are the thickness of the outer cylinder, breadth and height of the rectangular cross-section of the spokes. The output parameter is the Load Multiplier. Using Design Exploration method mentioned in Section 3.1 to 3.10 above, we perform the parametric analysis to understand the effect of the input parameters on our output. The design exploration is done through the use of Adaptive Metamodel of Optimal Prognosis(AMOP) and 300 design iterations are performed on the design space

(Figure 3.22).

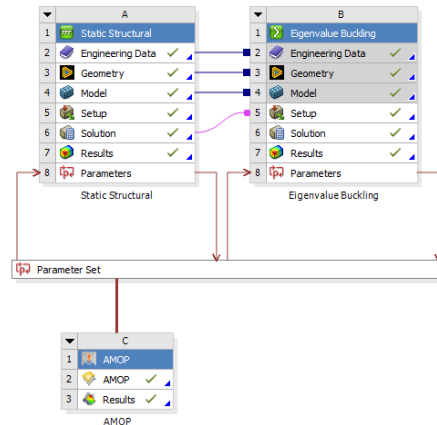


Figure 3.22: Project schematic in the ANSYS workbench for the Linear Buckling analysis. The parametric design is studied through Adaptive Metamodel of Optimal Prognosis (AMOP).

For the buckling analysis, we have used a linear pressure varying from 0.12036 N/mm at the inner edge to 3.2496 N/mm at the outer edge. In addition, it should be noted that the Large deflection is turned off which means that non linearities are not taken into account. Even though using the symmetric sector, non symmetric buckling modes will be missed, we focus our study on the lowest load multiplier only.

### 3.11.1 Output from the Adaptive Metamodel of Optimal Prognosis (AMOP)

Using the definition of the Correlation matrix, we can see that the effect of thickness of the outer cylinder has almost null effect on the load multiplier (Figure 3.23). Similarly, the breadth and height of the spokes are two important parameters affecting the load multiplier each one with a linear correlation of -0.81.



### CHAPTER 3. PRELIMINARY DESIGN EXPLORATION: A STATISTICAL APPROACH

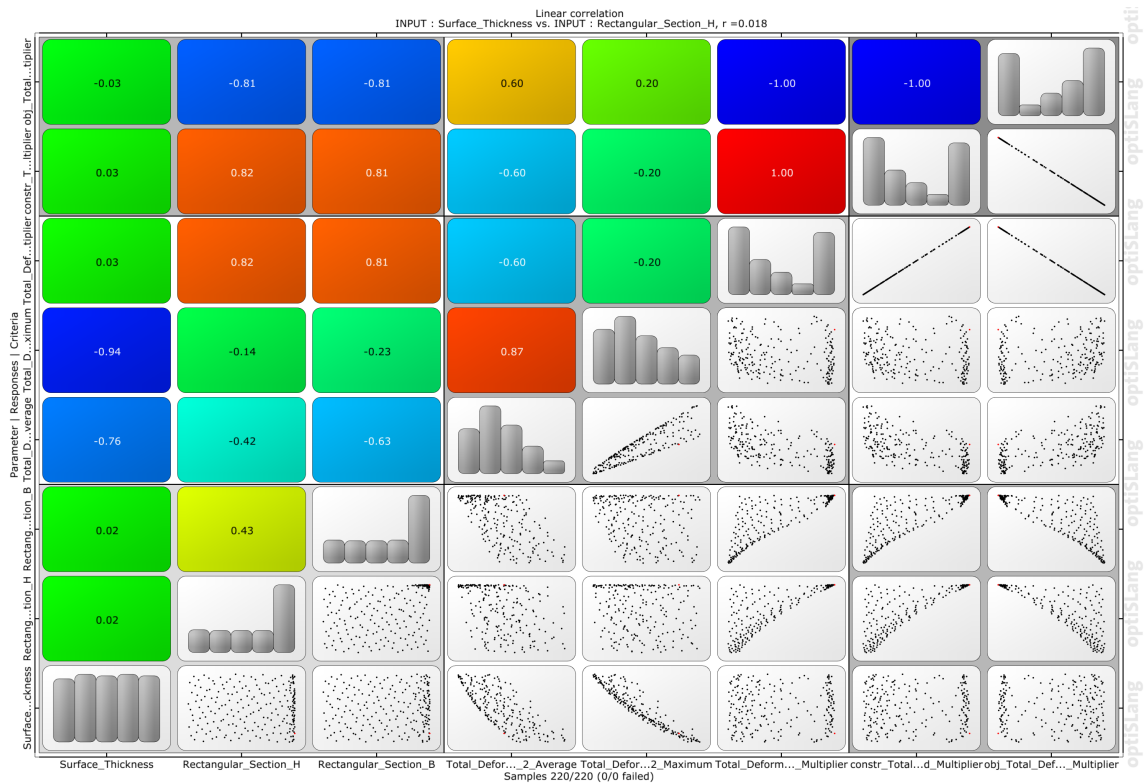


Figure 3.23: Correlation Matrix from the Adaptive Metamodel of Optimal Prognosis (AMOP) showing linear correlation coefficients, histograms and anthill plots for all selected input and output parameters and their combinations respectively, combined into one plot.

Another important output from the Adaptive Metamodel of Optimal Prognosis(AMOP) is the Response surface (Figure 3.24). The response surface shows that the even load multiplier as high as 11.8232 can be obtained using breadth of 20 mm and depth of 20mm. The lowest value of load multiplier is 1.08996 which is obtained using breadth of 5.24038 mm and depth of 11.3141 mm. The lowest value of load multiplier is 1.08996 which is obtained using breadth of 5.24038 mm and depth of 11.3141 mm. A load multiplier 2.03749 is obtained using breadth of 8.99038 mm and depth of 11.9551 mm. A parallel coordinate plot for the best design is also shown in Figure 3.25.

## CHAPTER 3. PRELIMINARY DESIGN EXPLORATION: A STATISTICAL APPROACH

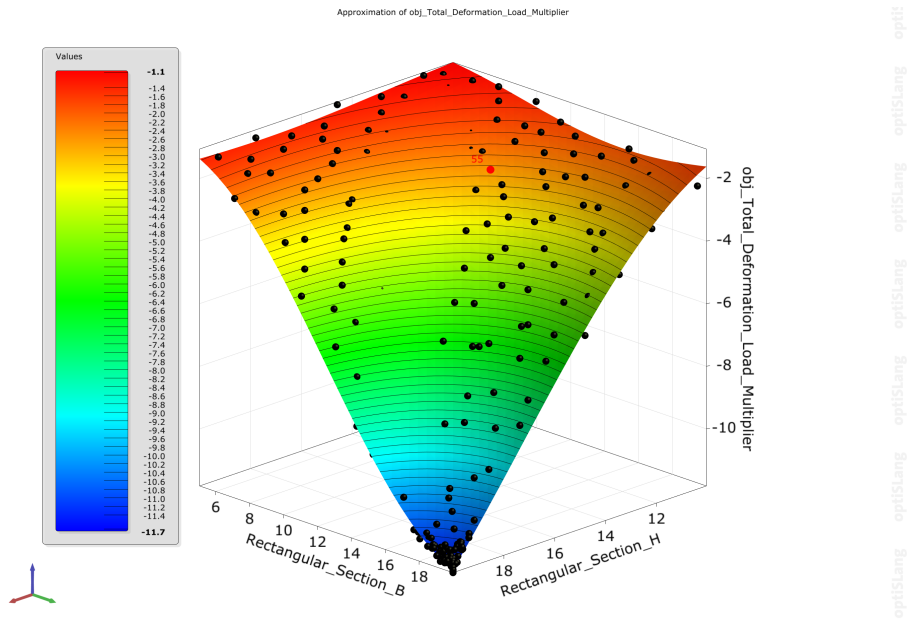


Figure 3.24: Response surface for the breadth, height and the load multiplier for Linear Buckling analysis. The response surface is obtained through Adaptive Metamodel of Optimal Prognosis (AMOP).

From the parallel coordinates plot in Figure 3.25, the best design is Design 49 for which the parameters are tabulated below,

<b>Parameters:</b>	
Height:	200 mm
Innerthickness:	10 mm
Outerthickness:	13.9263 mm
Rectangle_B:	8.31731 mm
Rectangle_H:	13.3654 mm
Circle_R:	1.5 mm
<b>Responses:</b>	
Maximum_Deformation:	15.4265 mm
Total_Deformation_Load_Multiplier:	2.51231

Table 3.4: Best design 49 model obtained from the multi-objective optimization of the Total deformation and Total mass

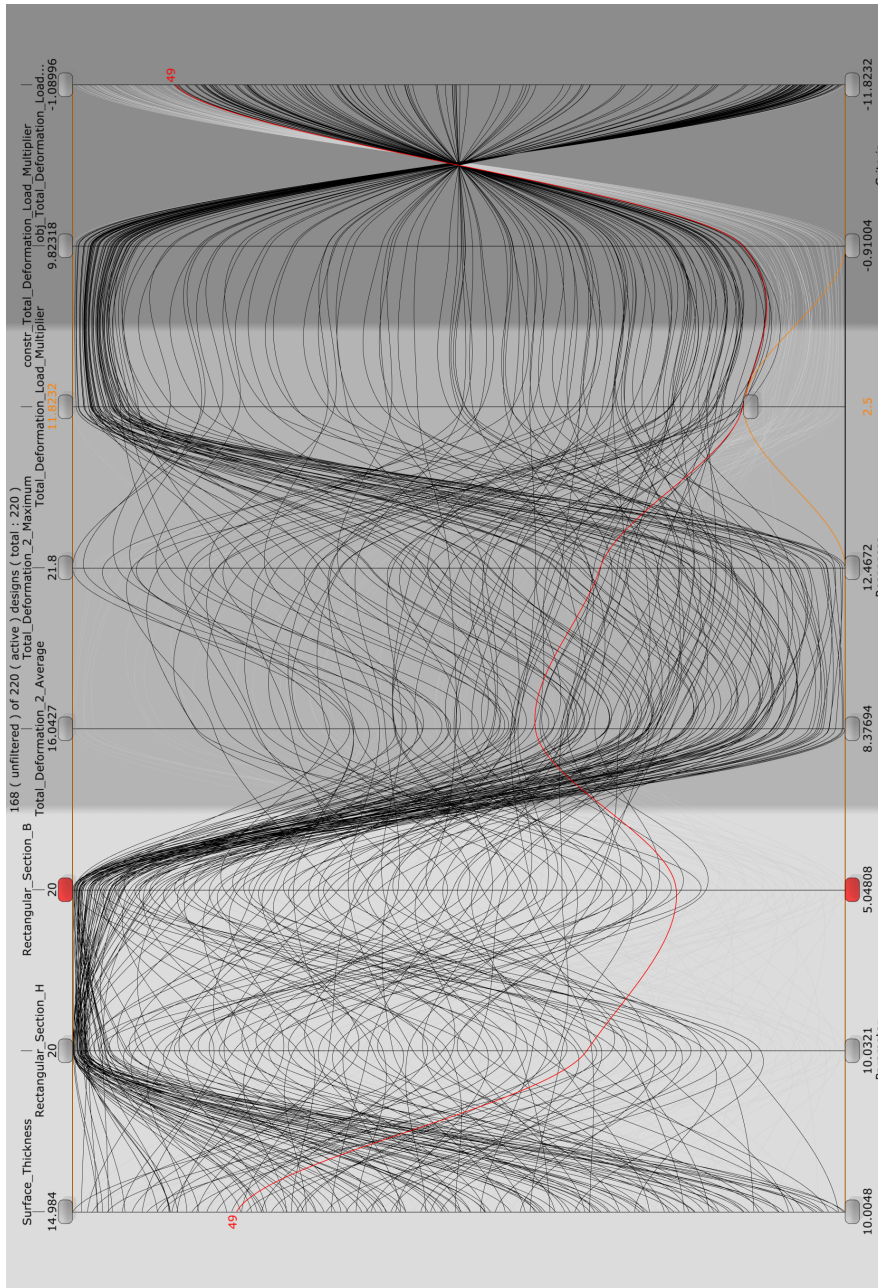


Figure 3.25: Parallel coordinates for the Linear Buckling analysis through the use of Adaptive Metamodel of Optimal Prognosis (AMOP).

### 3.11.2 Optimization of the Metamodel

Even though from the Adaptive Meta model of Optimal Prognosis (AMOP), we have more than 190 designs for which the load multiplier is greater than 2, we perform a multi-objective optimization for which the mass of the spokes and load multiplier is minimum. We already stated that the effect of the surface thickness on load multiplier is null. Also, increasing the surface thickness greatly increases the geometric mass, so even if it had effect on the load multiplier, we would try to keep it to minimum. The multi-objective optimization is performed using genetic algorithms and 100 iterations are performed (Figure 3.26). The load multiplier is set to 2.5 because in non linear analysis, the buckling load is less than that predicted by the linear buckling analysis (Figure 3.25).

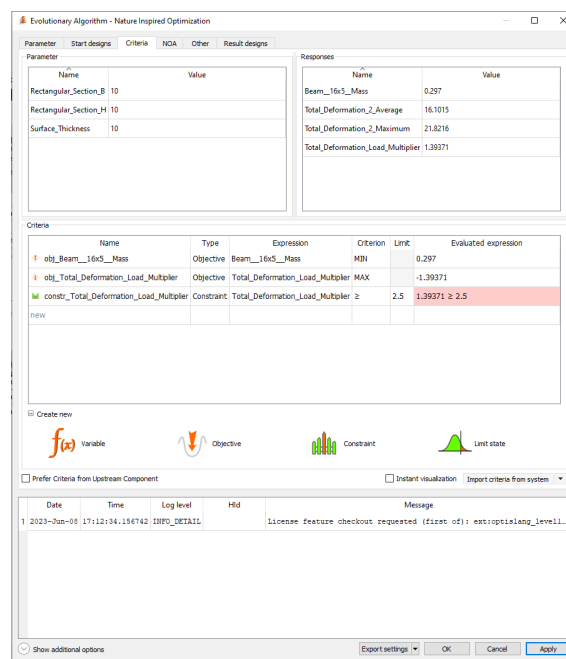


Figure 3.26: Optimization criteria set for minimising the Total load multiplier and Total mass of the spokes.

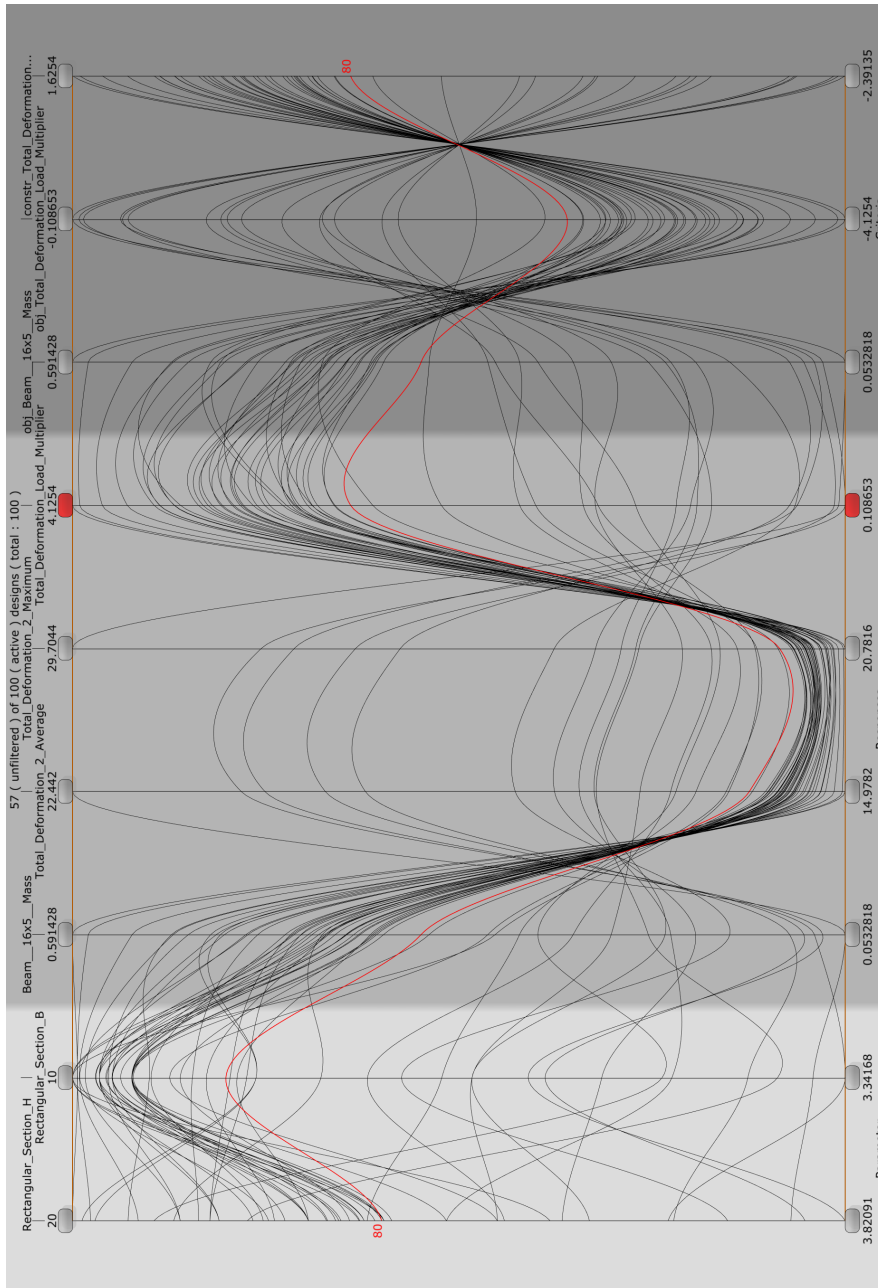


Figure 3.27: Parallel coordinates plot of the optimization results obtained from the minimisation of Total load multiplier and Total mass of the spokes .

## CHAPTER 3. PRELIMINARY DESIGN EXPLORATION: A STATISTICAL APPROACH

---

From the above analysis, the best design is Design 80 for which the parameters are tabulated below,

<b>Parameters:</b>	
Height:	200 mm
Innerthickness:	10 mm
Outerthickness:	10 mm
Rectangle_B:	8.67848 mm
Rectangle_H:	13.5258 mm
Circle_R:	1.5 mm

<b>Responses:</b>	
Maximum_Deformation:	21.5406 mm ( Linear Analysis)
Maximum_Deformation:	21.5406 mm ( Non-Linear Analysis)
Beam_Mass:	0.348627 kg
Total_Deformation_Load_Multiplier:	2.68032

Table 3.5: Best design 49 model obtained from the multi-objective optimization of the Total deformation and Total mass

### 3.12 Use of Epoxy Carbon Unidirectional Prepeg

In order to futher reduce the mass of the drift chamber, we change the engineering material from carbon fiber with a density of  $1800 \text{ kg/m}^3$  to Epoxy Carbon Unidirectional Prepeg with a density of  $1490 \text{ kg/m}^3$  . The properties of the Epoxy Carbon Unidirectional Prepeg is shown in the Figure 3.28.

## CHAPTER 3. PRELIMINARY DESIGN EXPLORATION: A STATISTICAL APPROACH

Properties of Outline Row 7: Epoxy Carbon UD (230 GPa) Prepreg			
	A	B	C
	Property	Value	Unit
1	Density	1490	kg m <sup>-3</sup>
2	Orthotropic Secant Coefficient of Thermal Expansion		
3	Coefficient of Thermal Expansion		
4	Coefficient of Thermal Expansion X direction	-4,7E-07	C <sup>-1</sup>
5	Coefficient of Thermal Expansion Y direction	3E-05	C <sup>-1</sup>
6	Coefficient of Thermal Expansion Z direction	3E-05	C <sup>-1</sup>
7	Orthotropic Elasticity		
8	Young's Modulus X direction	1,21E+11	Pa
9	Young's Modulus Y direction	8,6E+09	Pa
10	Young's Modulus Z direction	8,6E+09	Pa
11	Poisson's Ratio XY	0,27	
12	Poisson's Ratio YZ	0,4	
13	Poisson's Ratio XZ	0,27	
14	Shear Modulus XY	4,7E+09	Pa
15	Shear Modulus YZ	3,1E+09	Pa
16	Shear Modulus XZ	4,7E+09	Pa
17	Orthotropic Stress Limits		
18	Tensile X direction	2,231E+09	Pa
19	Tensile Y direction	2,9E+07	Pa
20	Tensile Z direction	2,9E+07	Pa
21	Compressive X direction	-1,082E+09	Pa
22	Compressive Y direction	-1E+08	Pa
23	Compressive Z direction	-1E+08	Pa
24	Shear XY	6E+07	Pa
25	Shear YZ	3,2E+07	Pa
26	Shear XZ	6E+07	Pa
27	Orthotropic Strain Limits		
28	Tensile X direction	0,0167	
29	Tensile Y direction	0,0032	
30	Tensile Z direction	0,0032	
31	Compressive X direction	-0,0108	
32	Compressive Y direction	-0,0192	
33	Compressive Z direction	-0,0192	
34	Shear XY	0,012	
35	Shear YZ	0,011	
36	Shear XZ	0,012	
37	Tsai-Wu Constants		
38	Coupling Coefficient XY	-1	
39	Coupling Coefficient YZ	-1	
40	Coupling Coefficient XZ	-1	
41	Puck Constants		
42	Material Classification	Carbon	
43	Compressive Inclination XZ	0,3	
44	Compressive Inclination YZ	0,25	
45	Tensile Inclination XZ	0,35	
46	Tensile Inclination YZ	0,25	
47			

Figure 3.28: Engineering properties of epoxy carbon unidirectional prepreg

## CHAPTER 3. PRELIMINARY DESIGN EXPLORATION: A STATISTICAL APPROACH

---

Now, the final section chosen for the drift chamber using Epoxy Carbon Unidirectional Prepeg considering optimization of Total deformation, Total mass and the load multiplier are shown in Table 3.6. The results are also shown in Figure 3.29 and Figure 3.30

<b>Parameters:</b>	
Height:	200 mm
Innerthickness:	10 mm
Outerthickness:	14.4 mm
Rectangle_B:	9.6 mm
Rectangle_H:	16.6 mm
Circle_R:	1.5 mm

<b>Responses:</b>	
Maximum_Deformation:	22.995 mm ( Linear Analysis)
Maximum_Deformation:	21.643 mm ( Non-Linear Analysis)
Total_Mass:	2.6269 kg per sector
Total_Deformation_Load_Multiplier:	2.2068

Table 3.6: Design parameters chosen for drift chamber using Epoxy Carbon Unidirectional Prepeg

### 3.13 Conclusions

Even though the parametric design exploration helped us to select the best optimal dimensions of the drift chamber, due to the constraints in selecting the dimensions, the total deformation of the model is still too high. Initially, in Chapter 2, our maximum deformation was 135.03 mm. In this Chapter 3, we reduce the deformation to 21.643 mm by using a design exploration and optimization procedure. However, the ultimate goal is to limit the deformation to 200 microns (0.2 mm) which is 1000 times lower than what we have achieved until now.



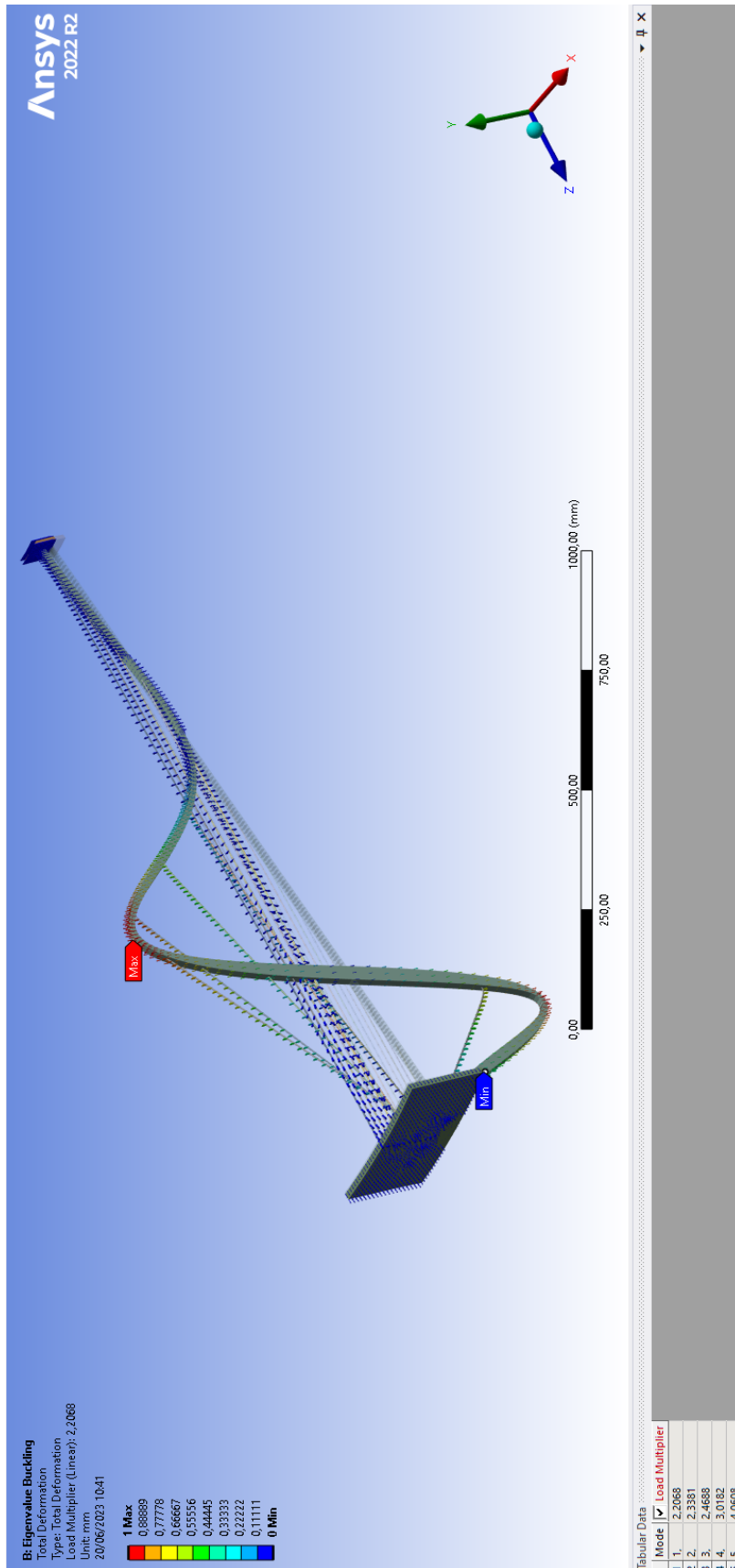


Figure 3.29: Buckled shape for the drift chamber and the load multipliers. The minimum load multiplier is 2.20.

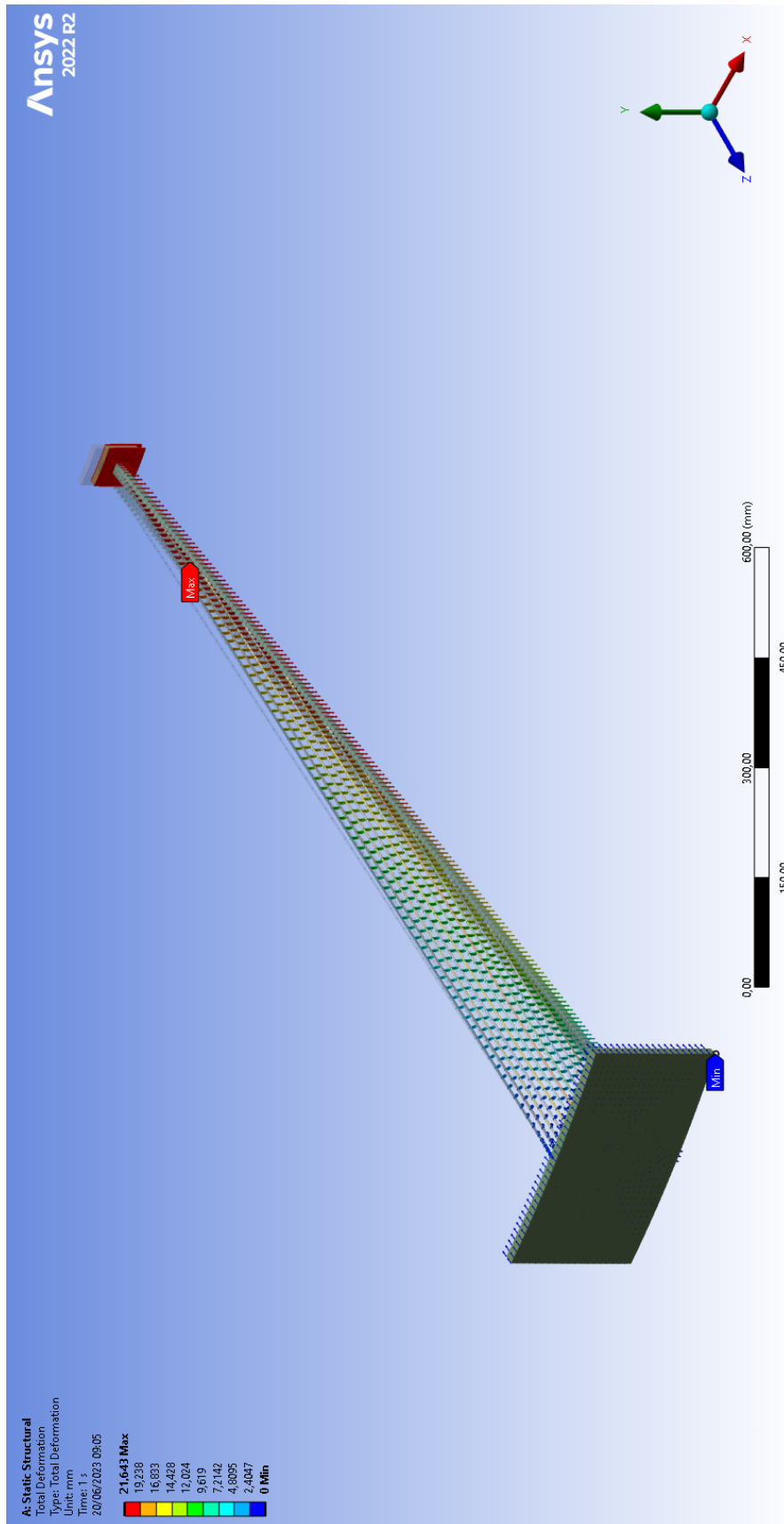


Figure 3.30: Total deformation of 21.643 mm using epoxy carbon as our material for drift chamber.

## Chapter 4

# Hypothesis Testing and Model Calibration

The previous chapters were based on the simplification that using a monolithic equivalent orthotropic material properties would yield the same result as a layered composite structure. This approach and the hypothesis so formulated has not been tested until now. If our hypothesis is correct, we already have a design for which the total deformation and the buckling criterion are fulfilled. If the outputs are completely different, all the results up to Chapter.4 will be incorrect. That is why we mentioned previously, in Chapter.2 , that simplification is an art because such choices always involve an element of danger[21]. The chapter primarily centers around rigorously validating our hypothesis through comprehensive numerical simulation, wherein we conduct a side-by-side comparison of both monolithic and composite models keeping in mind the precision we need . The chapter further acknowledges that the final layered composite structure will be different from the current model as angle lamina (cross-ply) may also be used . In such cases, the monolithic model will have to be developed based on the principles of composite laminate theory. A calibration will be done to develop a monolithic model, specifically tailored for a layered composite structure having an arbitrary angle lamina.

## 4.1 Monolithic Equivalent Orthotropic Material

Monolithic Equivalent Model corresponds to the layered composite design with fibres oriented at  $0^\circ$  only. This is our hypothesis. Based on this hypothesis, we already have the final design for a layered composite structure based on multi objective optimization of mass, total deformation and buckling load multiplier. The following Table 4.1 shows the geometric dimensions, total deformation, total mass and the load multiplier of our adopted design. The parameters are the same as shown in Chapter.3 (Table 3.6):

<b>Parameters:</b>	
Height:	200 mm
Innerthickness:	10 mm
Outerthickness:	14.4 mm
Rectangle_B:	9.6 mm
Rectangle_H:	16.6 mm
Circle_R:	1.5 mm
<b>Responses:</b>	
Maximum_Deformation:	22.995 mm ( Linear Analysis)
Maximum_Deformation:	21.643 mm ( Non-Linear Analysis)
Total_Mass:	2.6269 kg per sector
Total_Deformation_Load_Multiplier:	2.2068

Table 4.1: Design parameters chosen for drift chamber using Epoxy Carbon Unidirectional Prepeg

## 4.2 Layered Composite Material

We develop a composite model made from Epoxy carbon prepeg to test our hypothesis. For this design, a ply of 0.2 mm thickness is used. All the fibres are oriented at  $0^\circ$  and the ply configuration is shown in Table 4.2. The remaining parameters are same as that of Table 4.1.

Component Type	Orientation of Ply	No. of Ply	Total thickness (mm)
Outer Cylinder	0°	72	14.40
Inner Cylinder	0°	50	10.00
Spokes	0°	83	16.60

Table 4.2: Arrangement and orientation of the Ply in the various components of Drift chamber

### 4.3 Validation of the Monolithic design with Layered composite design at 0°

#### 4.3.1 Validity of the Total deformation results

Now, in order to validate the models, both the models are loaded with uniformly distributed load from 50,000 N to 100,000 N with an increment of 10,000 N. After each increment, Total deformation of the models are recorded. The Total load vs Total deformation for both models are shown in Table 4.3:

	Monolithic Model	Layered composite model
Total load (N)	Total deformation (mm)	Total deformation (mm)
100000	28.923	28.882
90000	26.445	26.234
80000	23.868	23.983
70000	21.217	21.432
60000	18.484	18.345
50000	15.651	15.343

Table 4.3: Validation and Analysis of the Monolithic Model with the Layered Composite structure (*Large deflection was turned on in both cases*).

The variation in deformation under certain load conditions exceeds the desired design precision of 0.2 mm. This disparity between the two numerical models can be attributed to several factors, including different mesh sizes, the application of line pressure in the monolithic model versus surface pressure in the composite model and the definition of non-linear contacts within the composite model. It should be noted that the similarity can

only be achieved in case the contacts are bonded and multi point constraint (MPC). When it is *Program controlled*, the similarity cannot be seen and sometimes the disparity can be very large. This will be discussed in detail in Chapter.7 (section 7.1).

### 4.3.2 Validity of the Buckling loads

When examining a single symmetric sector of a structure, there is a possibility of missing anti-symmetric buckling modes. Symmetric buckling modes display deformation patterns that possess symmetry about a central axis or plane. A single symmetric sector captures only the symmetric buckling modes. In our previous Chapter.3, we examined only one symmetric sector and determined the buckling load. Anti-symmetric buckling modes that are anti-symmetric about a central axis or plane, indicating opposing displacements on different sides of the structure, might be missing. Consequently, there is a potential risk of not accounting for these modes and their effects.

To accurately capture the buckling behavior of our structure, it is necessary to consider both symmetric and anti-symmetric modes. Only by analyzing the entire model, we can be sure to identify and assess all relevant buckling modes, ensuring a more comprehensive understanding of the structure's stability. For the composite models, in which non linear contacts are also defined, linear buckling analysis can also be misleading. So, we can argue that the models cannot be expected to be exactly same from buckling criterion and this is further described in detail in Chapter.9. In this chapter, we still maintain our focus on the total deformation of the spokes.

### 4.3.3 Mass of the system

Usually, the calculation of mass can be incorrect or significantly different in models imported from ANSYS Composite PrepPost (ACP). The geometry of Static Structural imported from the ANSYS Composite PrepPost (ACP) will show an incorrect value ( *in this case 29 kg*). In both scenarios, it is absolutely necessary to validate the mass based on the solver output only, ensuring that both numerical models are identical. The mass of

both the models were found to be correct upto third decimal and can be taken as 94.5684 kg.

## 4.4 Calibration of the Layered composite design

Based on the monolithic design and validation of our hypothesis, we have a layered composite design shown in Table 4.1 and Table 4.2. But for the layered composite design a cross-ply at  $90^\circ$  may be necessary from design point of view to increase the transverse stiffness (*this in turn decreases the desired longitudinal stiffness*). Monolithic designs are not only accurate but are also tremendously fast. This is very important in situations where thousands of iterations have to be performed. With a layered composite design, even a single run time can take hours whereas monolithic design just take few seconds. So our goal is to develop a monolithic equivalent of a layered composite design having a ply orientation of  $\begin{bmatrix} 0 & 0 & 90 & 0 & 0 \end{bmatrix}$ .

This can be done by two approaches.

1) Neglecting the thickness of  $90^\circ$  ply and using a reduced thickness in the monolithic design. That means using only 80% of the ply thickness. This can be a very simple approach and the Total deformation can be expected to be around the same (*but not exactly as the  $90^\circ$  ply has some stiffness contribution in the longitudinal direction too*). This can be adopted for preliminary design approach. However, we need a precision of 200 microns (0.2 mm) so this approach cannot be definitely used.

2) Calculating the E1, E2 and G12 of the stackup and using that material properties for the monolithic design.

**Unidirectional Stackup** The properties for a single fibre of epoxy are shown in Figure 4.1. For a stackup of 1 mm made with 5 ply of 0.2mm with an orientation of [0/0/0/0/0], the properties will remain same. The polar properties (Figure 4.2), normalised stiffness

(Equation 4.1) and compliance matrix (Equation 4.2) are directly obtained from the Engineering data of the ANSYS Composite PrepPost (ACP).

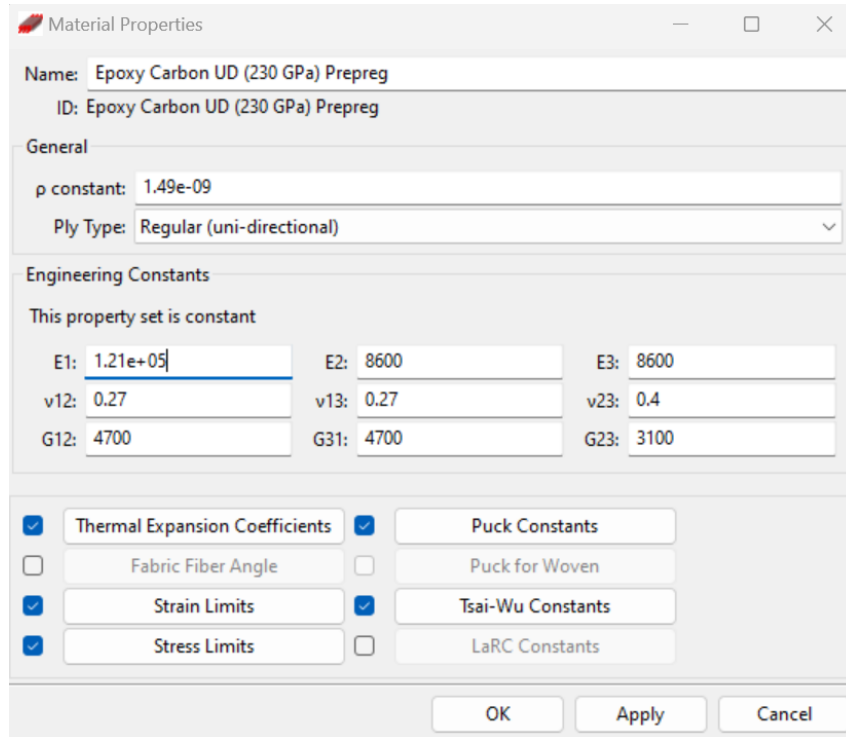


Figure 4.1: Material properties of the Epoxy carbon prepreg used in ANSYS Composite PrepPost (ACP)

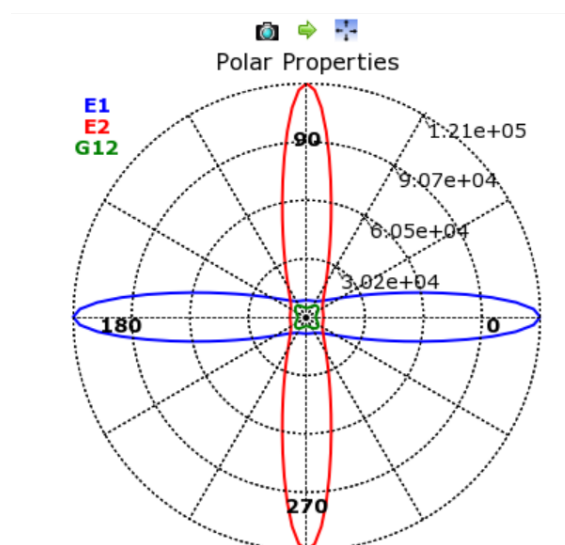


Figure 4.2: Polar properties of the Stackup oriented at [0/0/0/0/0]



$$[S] = \begin{bmatrix} 1.2163 \times 10^5 & 2334.1 & 0 & -1.5142 \times 10^{-11} & -2.8392 \times 10^{-13} & 0 & 0 & 0 \\ 2334.1 & 8644.8 & 0 & -2.8392 \times 10^{-13} & -9.464 \times 10^{-13} & 0 & 0 & 0 \\ 0 & 0 & 4700 & 0 & 0 & -4.732 \times 10^{-13} & 0 & 0 \\ -1.5142 \times 10^{-11} & -2.8392 \times 10^{-13} & 0 & 1.2163 \times 10^5 & 2334.1 & 0 & 0 & 0 \\ -2.8392 \times 10^{-13} & -9.464 \times 10^{-13} & 0 & 2334.1 & 8644.8 & 0 & 0 & 0 \\ 0 & 0 & -4.732 \times 10^{-13} & 0 & 0 & 4700 & 0 & 0 \\ 0 & 0 & 0 & 0 & 0 & 0 & 3100 & 0 \\ 0 & 0 & 0 & 0 & 0 & 0 & 0 & 4700 \end{bmatrix} \quad (4.1)$$

$$[C] = \begin{bmatrix} 8.2645 \times 10^{-06} & -2.2314 \times 10^{-06} & 0 & 3.0855 \times 10^{-21} & -7.5165 \times 10^{-22} & 0 & 0 & 0 \\ -2.2314 \times 10^{-06} & 0.00011628 & 0 & -7.5165 \times 10^{-22} & 3.8173 \times 10^{-20} & 0 & 0 & 0 \\ 0 & 0 & 0.00021277 & 0 & 0 & 6.4265 \times 10^{-20} & 0 & 0 \\ 3.0855 \times 10^{-21} & -7.5165 \times 10^{-22} & 0 & 8.2645 \times 10^{-06} & -2.2314 \times 10^{-06} & 0 & 0 & 0 \\ -7.5165 \times 10^{-22} & 3.8173 \times 10^{-20} & 0 & -2.2314 \times 10^{-06} & 0.00011628 & 0 & 0 & 0 \\ 0 & 0 & 6.4265 \times 10^{-20} & 0 & 0 & 0.00021277 & 0 & 0 \\ 0 & 0 & 0 & 0 & 0 & 0 & 0.00032258 & 0 \\ 0 & 0 & 0 & 0 & 0 & 0 & 0 & 0.00021277 \end{bmatrix} \quad (4.2)$$

**Cross ply Stackup** With the [0/0/90/0/0] ply orientation, the normalised laminate stiffness and compliance matrix should be calculated based on the properties shown in Figure 4.1. To calculate the compliance and stiffness matrix for a composite material, we need to consider the individual properties of the constituent materials and their arrangement in the composite.

Assuming a unidirectional composite with fiber orientation along the x-axis, the stiffness matrix [S] can be expressed as:

$$[S] = \begin{bmatrix} \frac{1}{E_{11}} & -\frac{\nu_{12}}{E_{11}} & -\frac{\nu_{13}}{E_{11}} & 0 & 0 & 0 \\ -\frac{\nu_{21}}{E_{22}} & \frac{1}{E_{22}} & -\frac{\nu_{23}}{E_{22}} & 0 & 0 & 0 \\ -\frac{\nu_{31}}{E_{33}} & -\frac{\nu_{32}}{E_{33}} & \frac{1}{E_{33}} & 0 & 0 & 0 \\ 0 & 0 & 0 & \frac{1}{G_{23}} & 0 & 0 \\ 0 & 0 & 0 & 0 & \frac{1}{G_{13}} & 0 \\ 0 & 0 & 0 & 0 & 0 & \frac{1}{G_{12}} \end{bmatrix} \quad (4.3)$$

where,  $E_{11}$ ,  $E_{22}$ , and  $E_{33}$  represent the Young's moduli of the composite material along the x, y, and z axes, respectively.  $\nu_{12}$ ,  $\nu_{13}$ , and  $\nu_{23}$  denote the Poisson's ratios, and  $G_{12}$ ,  $G_{13}$ , and  $G_{23}$  are the shear moduli.

To obtain the compliance and stiffness matrix for a lamina at an arbitrary angle, we can use the transformation matrix [T]. The transformation matrix relates the material properties of the lamina at the reference orientation to the lamina at the desired angle  $\theta$ . The transformation matrix [T] can be expressed as:

$$[T] = \begin{bmatrix} \cos^2(\theta) & \sin^2(\theta) & 2 \sin(\theta) \cos(\theta) & 0 & 0 & 0 \\ \sin^2(\theta) & \cos^2(\theta) & -2 \sin(\theta) \cos(\theta) & 0 & 0 & 0 \\ -\sin(\theta) \cos(\theta) & \sin(\theta) \cos(\theta) & \cos^2(\theta) - \sin^2(\theta) & 0 & 0 & 0 \\ 0 & 0 & 0 & \frac{1}{2} \sin(2\theta) & 0 & 0 \\ 0 & 0 & 0 & 0 & \frac{1}{2} \sin(2\theta) & 0 \\ 0 & 0 & 0 & 0 & 0 & \frac{1}{2} \sin(2\theta) \end{bmatrix} \quad (4.4)$$

The compliance matrix for the lamina at an arbitrary angle, can be calculated using the following equation:

$$[S]_{\text{lamina}} = [T]^{-1} \cdot [S]_{\text{reference}} \quad (4.5)$$

The stiffness matrix for the lamina at an arbitrary angle, can be calculated using the following equation:

$$[C]_{\text{lamina}} = [T] \cdot [C]_{\text{reference}} \cdot [T]^{-1} \quad (4.6)$$

Based on these equations (Equation 4.1 - 4.6), the material properties of the ply is calculated. The polar properties (Figure 4.3), normalised stiffness (Equation 4.7) and compliance matrix (Equation 4.8) show that the stackup has a reduced longitudinal stiffness but an increased transverse stiffness.

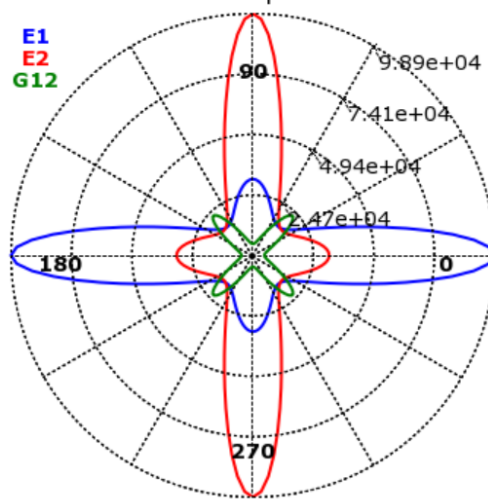


Figure 4.3: Polar properties of the Stackup oriented at [0/0/90/0/0]

$$[S] = \begin{bmatrix} 99033 & 2334.1 & 3.7833 \times 10^{-14} & -1.5142 \times 10^{-11} & -2.8392 \times 10^{-13} & -1.3659 \times 10^{-30} & 0 & 0 \\ 2334.1 & 31242 & 1.3458 \times 10^{-12} & -2.8392 \times 10^{-13} & -1.7035 \times 10^{-12} & -4.8588 \times 10^{-29} & 0 & 0 \\ 3.7833 \times 10^{-14} & 1.3458 \times 10^{-12} & 4700 & -1.3659 \times 10^{-30} & -4.8588 \times 10^{-29} & -4.732 \times 10^{-13} & 0 & 0 \\ -1.5142 \times 10^{-11} & -2.8392 \times 10^{-13} & -1.3659 \times 10^{-30} & 1.2073 \times 10^5 & 2334.1 & 1.5133 \times 10^{-15} & 0 & 0 \\ -2.8392 \times 10^{-13} & -1.7035 \times 10^{-12} & -4.8588 \times 10^{-29} & 2334.1 & 9548.7 & 5.3834 \times 10^{-14} & 0 & 0 \\ -1.3659 \times 10^{-30} & -4.8588 \times 10^{-29} & -4.732 \times 10^{-13} & 1.5133 \times 10^{-15} & 5.3834 \times 10^{-14} & 4700 & 0 & 0 \\ 0 & 0 & 0 & 0 & 0 & 0 & 3420 & 1.9594 \times 10^{-14} \\ 0 & 0 & 0 & 0 & 0 & 0 & 1.9594 \times 10^{-14} & 4380 \end{bmatrix} \quad (4.7)$$

$$[C] = \begin{bmatrix} 1.0115 \times 10^{-05} & -7.5573 \times 10^{-07} & 1.3498 \times 10^{-22} & 3.8093 \times 10^{-21} & -4.3331 \times 10^{-22} & 2.9887 \times 10^{-38} & 0 & 0 \\ -7.5573 \times 10^{-07} & 3.2065 \times 10^{-05} & -9.1756 \times 10^{-21} & -3.9048 \times 10^{-22} & 1.719 \times 10^{-20} & -1.9744 \times 10^{-36} & 0 & 0 \\ 1.3498 \times 10^{-22} & -9.1756 \times 10^{-21} & 0.00021277 & 3.1541 \times 10^{-38} & -2.0209 \times 10^{-36} & 6.4265 \times 10^{-20} & 0 & 0 \\ 3.8093 \times 10^{-21} & -3.9048 \times 10^{-22} & 3.1541 \times 10^{-38} & 8.3225 \times 10^{-06} & -2.0344 \times 10^{-06} & 2.0622 \times 10^{-23} & 0 & 0 \\ -4.3331 \times 10^{-22} & 1.719 \times 10^{-20} & -2.0209 \times 10^{-36} & -2.0344 \times 10^{-06} & 0.00010522 & -1.2046 \times 10^{-21} & 0 & 0 \\ 2.9887 \times 10^{-38} & -1.9744 \times 10^{-36} & 6.4265 \times 10^{-20} & 2.0622 \times 10^{-23} & -1.2046 \times 10^{-21} & 0.00021277 & 0 & 0 \\ 0 & 0 & 0 & 0 & 0 & 0 & 0.0002924 & -1.3081 \times 10^{-21} \\ 0 & 0 & 0 & 0 & 0 & 0 & -1.3081 \times 10^{-21} & 0.00022831 \end{bmatrix} \quad (4.8)$$

## 4.5 Validation of the Monolithic design with Layered composite design at [0/0/90/0/90]

The equivalent elastic properties mentioned in Equation 4.7 can be assigned to a monolithic model. If there are some discrepancies, the elastic properties can be tuned and calibrated to match the output from these two models. Now, a composite model with an orientation

## CHAPTER 4. HYPOTHESIS TESTING AND MODEL CALIBRATION

of [0/0/90/0/90] with 16 stackup (16 mm thickness) is developed. Alongside, a monolithic model with equivalent elastic properties is developed. Both models are loaded with various forces and the total deformation is reported in Table 4.4.

	Total Load (N)	Spokes			Outer Cylinder		
		Min (mm)	Max (mm)	Average (mm)	Min (mm)	Max (mm)	Average (mm)
Composite design	100000	0	24.339	14.757	0	1.2846	0.4742
Monolithic design		0	25.385	15.375	0	1.2649	0.33894
Composite design	70000	1.23E-03	17.913	10.681	0	0.9274	0.340
Monolithic design		0	18.309	10.922	0	0.8913	0.24046
Composite design	60000	1.53E-03	15.63	9.2621	0	0.8034	0.29447
Monolithic design		0	17.206	10.256	0	0.84069	0.22506
Composite design	50000	1.28E-03	13.26	7.8075	0	0.67658	0.24747
Monolithic design		0	13.356	7.8823	0	0.64765	0.1733
Composite design	30000	7.73E-04	8.271	4.801	0	0.41502	0.15116
Monolithic design		0	8.1818	4.7763	0	0.39178	0.10481
Composite design	10000	2.59E-04	2.8733	1.6412	0	0.14145	5.13E-02
Monolithic design		0	2.7856	1.6081	0	0.13163	3.52E-02

Table 4.4: Validation of the Monolithic design with Layered composite design at [0/0/90/0/90]

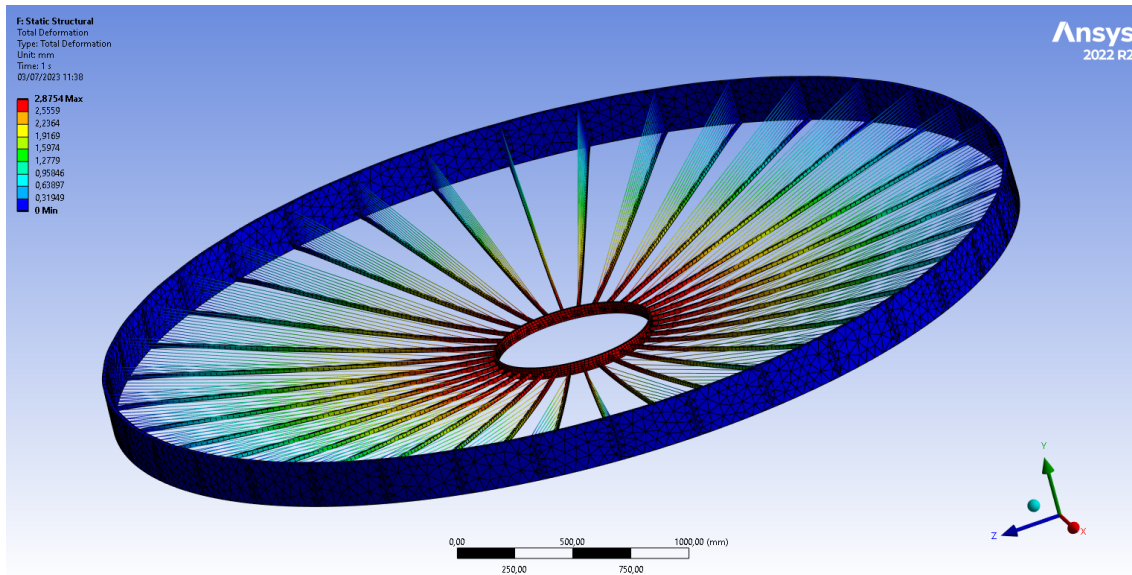


Figure 4.4: Total deformation (2.87 mm) of the layered composite subjected to 10000 N

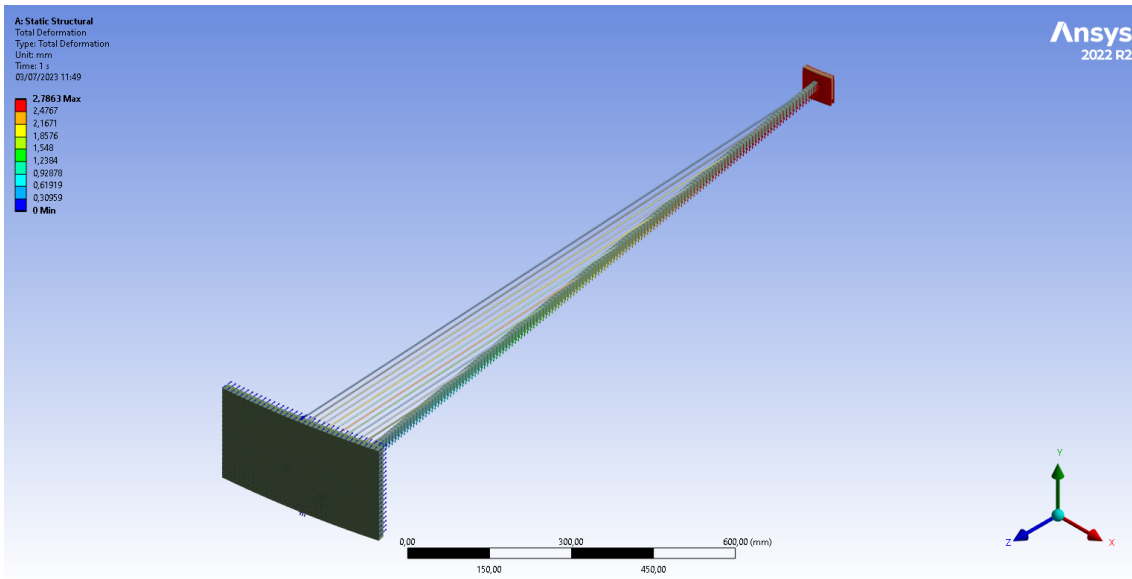


Figure 4.5: Total deformation (2.78 mm) of a symmetric sector of equivalent monolithic structure subjected to 10000 N

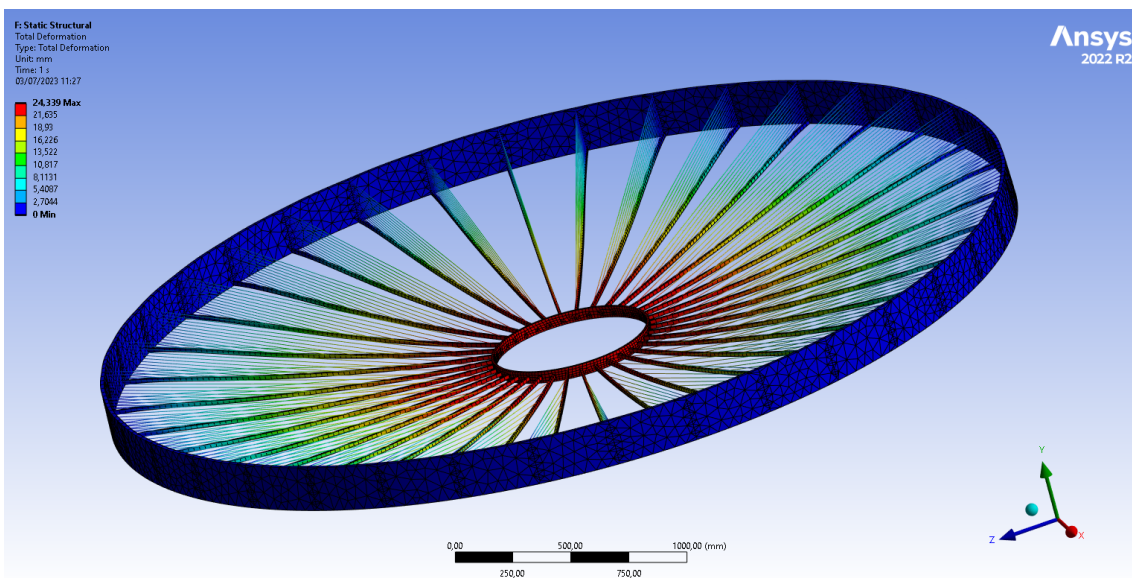


Figure 4.6: Total deformation (24.34 mm) of the layered composite subjected to 100000 N

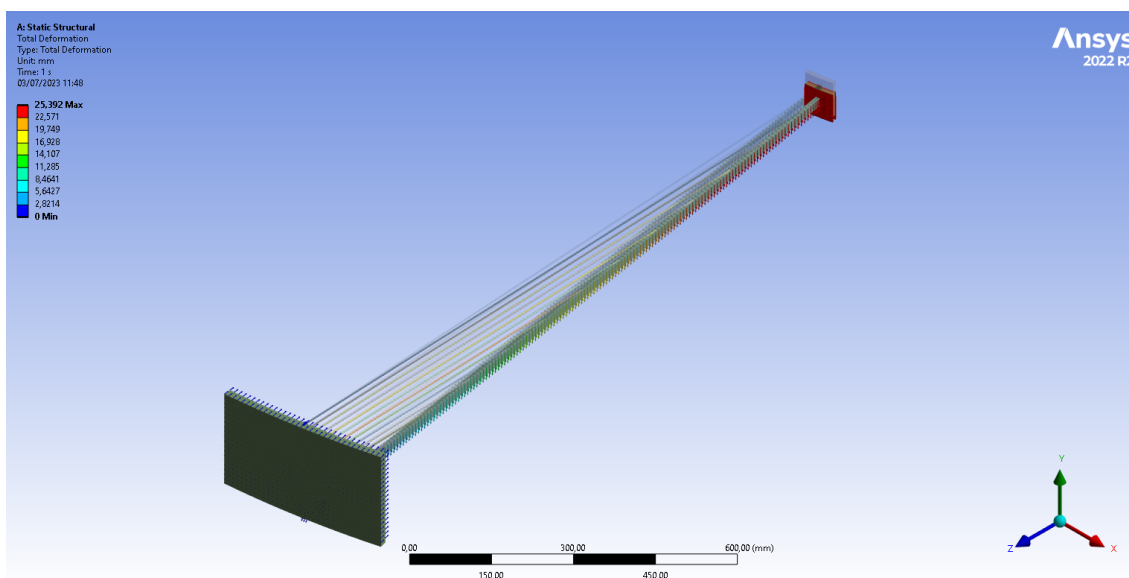


Figure 4.7: Total deformation ( $25.39 \text{ mm}$ ) of a symmetric sector of equivalent monolithic structure subjected to  $100000 \text{ N}$

The two models exhibit almost perfect similarities in the realm of small deformations (Figure 4.4-4.5), but when it comes to large deformations, there is a noticeable difference of  $1 \text{ mm}$  in Maximum Spokes deformation (Figure 4.6-4.7). This disparity could be attributed to nonlinear contacts or other factors that hold equal probability. While we can adjust and calibrate the model to accommodate the large deformation range, there is a potential risk of compromising accuracy in the small deformation range. However, since our final model will primarily operate within the small deformation range, we are willing to take this risk during the design phase.

## 4.6 Conclusion

In order to analyze the total deformation, only a macro analysis approach is necessary. In such case, monolithic designs can be developed which are characterized by their remarkable accuracy and exceptional speed (by almost 360 folds). These designs are developed by assigning equivalent properties based on the classical laminate theory. However, it is crucial to recognize that while the layered composite model can be replicated to very high

precision, it cannot be fully replicated. Consequently, it is imperative that we consistently validate our design values and responses exclusively using the layered composite model. This verification process is essential and cannot be avoided in the overall process.

# Chapter 5

## Preliminary Design Exploration: A metaheuristic Approach

This chapter provides a detail overview on the strategies that are applied to solve the problem related to minimizing the deformation of the spokes. Since, the material and subsequently its weight has to be kept minimum, the problem to minimize the deformation is solved using prestressing force in the cables. The ultra light drift chamber is very sensitive to the prestressing force and only a right combination of these prestressing force in the cables will limit the deformation. Otherwise, the spokes will have even higher deformation, inherit imperfection that will lower the buckling load as well as pose problems in relation to layout of the wires. To find the correct prestressing force in 14 cables to limit the Total deformation, we solve a 15 dimensional optimization problem. The problem is highly non linear and the solution strategies include optimization techniques from classical to the metaheuristic ones.

### 5.1 Optimization Techniques

Fletcher and Powell (1963) published the works of Davidon (1959), which marked a significant milestone in the history of solving optimization problems using computers. It was the first time that the minimum of a smooth non-linear function could be located without the knowledge of second derivatives [38]. Sixty years later, better models for



solving constrained and unconstrained, linear and non-linear optimization problems have been developed, and the growth in this field continues without abatement.

Non-linear optimization focuses on finding the maximum or minimum values of a given non-linear function, known as the objective function, with any number of independent variables or decision variables. When certain conditions are imposed to solve such problems, it is referred to as constrained non-linear optimization. Since our goal is to find the minimum, it is crucial to understand the different types of minima in an optimization problem. A strong minimum occurs when the objective function locally increases in all directions. On the other hand, a weak minimum is characterized by the objective function remaining locally the same in some directions but increasing locally in others. A non-linear function can have multiple points exhibiting weak minimum, all of which are known as local minima. Among these, if the objective function attains its lowest value, it is called the global minimum.

A point  $\mathbf{x}^*$  is considered a strong minimum of a function  $F(\mathbf{x})$  if there exists a scalar  $\delta > 0$  such that  $F(\mathbf{x}^*) < F(\mathbf{x}^* + \Delta\mathbf{x})$  for all  $\Delta\mathbf{x}$  satisfying  $0 < \|\Delta\mathbf{x}\| \leq \delta$ .

A point  $\mathbf{x}^*$  is considered a weak minimum of a function  $F(\mathbf{x})$  if it is not a strong minimum, and there exists a scalar  $\delta > 0$  such that  $F(\mathbf{x}^*) \leq F(\mathbf{x}^* + \Delta\mathbf{x})$  for all  $\Delta\mathbf{x}$  satisfying  $0 < \|\Delta\mathbf{x}\| \leq \delta$ .

For convex problems and linear programs, the local minima are also the global minima. However, most algorithms for nonlinear problems only search for local minima where the objective function is smaller than nearby feasible points, and therefore, they do not find the global minima [39]. Recognizing and locating global minima in such problems is highly challenging. As a result, the problem of finding global minima in nonlinear optimization is a major challenge, and many successful global optimization algorithms involve solving multiple local optimization problems. Problems with multiple local minima are referred to as multimodal optimization problems [40].

While most practical problems, including ours, focus on continuous optimization problems where the independent variable varies continuously over a domain, combinatorial problems, where the independent variable is restricted to a finite set, are also of great importance [40].

### 5.1.1 Constrained optimization

In unconstrained optimization problem, the independent variables  $x$  are allowed to take any finite value. For many problems this kind of approach is not useful because it is known a priori from properties of the system under study that certain points are unacceptable as solutions. Restrictions on the value of  $x$  are formulated as constraints and constrained optimization is the study of methods for solving this type of problems.

Constraints are specified as a set of functions  $c_i(\mathbf{x})$ , where  $i = 1$  to  $m$ , conveniently collected together as an  $m$ -vector

$$\mathbf{c}(\mathbf{x}) = \begin{bmatrix} c_1(\mathbf{x}) \\ \vdots \\ \vdots \\ \vdots \\ c_m(\mathbf{x}) \end{bmatrix} \quad (5.1)$$

which must be satisfied either as equalities

$$\mathbf{c}(\mathbf{x}) = \mathbf{0} \quad (5.2)$$

or inequalities

$$c(x) \geq 0 \quad (5.3)$$

Feasible points satisfy all the given constraints, and the collection of feasible points forms the feasible region. The constraints define a set of hypersurfaces in an  $n$ -dimensional

space, and the feasible region is the area where all these hypersurfaces intersect [38]. In the case of inequality constraints, the points reside on a specific side of these hypersurfaces.

### 5.1.2 Necessary and sufficient conditions for a non-linearly constrained minimum

A set of non-linear equality constraints will yield a curved hypersurface at intersection and no feasible directions from any point exists. For the non-linear inequalities, feasible directions may exist, but may not be necessarily reached along such distances [38]. A feasible point  $\mathbf{x}^*$  is said to be a non-linearly constrained strong minimum of a function  $F(\mathbf{x})$  if  $F(\mathbf{x}^*) < F(\mathbf{x})$  for all feasible points  $\mathbf{x} \neq \mathbf{x}^*$  in some neighbourhood of  $\mathbf{x}^*$ .

#### First-order necessary conditions for equality and inequality constraints

From a given point that satisfies a non-linear equality constraint, a feasible move is initially tangent to the hypersurface. The subspace thus generated by all these tangents is known as tangent hypersurface (see Figure 5.1 (a)). For more than one constraint, the tangent hyperplane is generated by vectors tangent to all of the constraints. Under the regularity assumption, the dimension of the tangent hyperplane is  $n - m$ . Thus, in Figure 5.1 (a) it is a plane, while in Figure 5.1 (b), where there are two constraints it is a line. In general, a basis matrix  $\mathbf{Z}$  for the tangent hyperplane at any point  $\mathbf{x}$  satisfies

$$\mathbf{A}^T(\mathbf{x})\mathbf{Z} = \mathbf{0} \quad (5.4)$$

For linear equality constraints, the feasible region is identical to the tangent hyperplane, as are the coefficient vectors to the constraint first derivative vectors. We can therefore intuitively transfer the first-order necessary conditions unchanged to the present case, that is

$$\nabla L(x^*) = \mathbf{g}(\mathbf{x}^*) - \mathbf{A}(\mathbf{x}^*)\lambda = 0 \quad (5.5)$$

for some Lagrange multipliers  $\lambda$ .

The matrix of constraint first derivative vectors  $\mathbf{A}(\mathbf{x})$  is now no longer constant. For inequality constraints, this implies that the present argument suggests again that the conditions

$$\nabla L(\mathbf{x}^*) = \mathbf{g}(\mathbf{x}^*) - \mathbf{A}_q(\mathbf{x}^*) \lambda_q = 0 \quad (5.6)$$

and

$$\lambda_q \geq 0 \quad (5.7)$$

are both necessary. These conclusions can be rigorously confirmed.

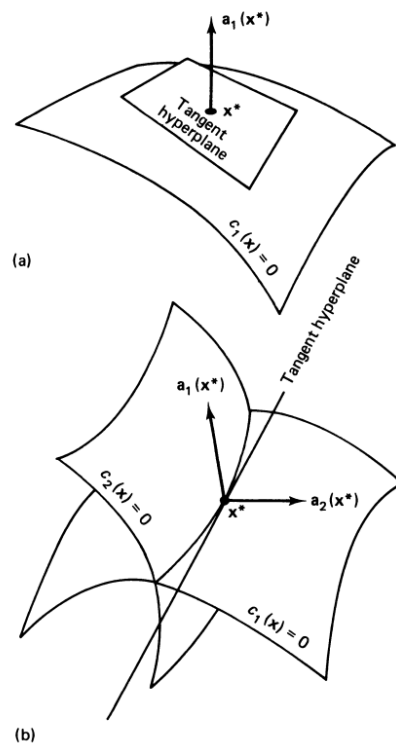


Figure 5.1: Tangent hyperplanes in a three-dimensional space with (a) one and (b) two constraints

### Second-order conditions for equality and inequality constraints

The treatment of Lagrangian functions suggests that the second-order sufficiency condition for an equality constrained strong minimum at a stationary point  $\mathbf{x}^*$  is that  $\mathbf{Z}^T [\nabla^2 L(\mathbf{x}^*)] \mathbf{Z}$

is positive definite and we can derive the following equation;

$$\nabla^2 L(\mathbf{x}) = \mathbf{G}(\mathbf{x}) - \sum_{i=1}^m \lambda_i \mathbf{B}_i(\mathbf{x}) \quad (5.8)$$

and  $\mathbf{Z}$  is a matrix whose columns form a basis for the tangent hyperplane. This conclusion is confirmed by rigorous analysis. The corresponding condition for inequality constraints also carries across as one might expect. Having identified a set of active constraints  $\mathbf{c}_q(\mathbf{x})$  for which  $\lambda_q \geq 0$ , it is sufficient that  $\mathbf{Z}_{q'}^T [\nabla^2 L(x^*)] \mathbf{Z}_{q'}$  be positive definite, where

$$\nabla^2 L(\mathbf{x}) = \mathbf{G}(\mathbf{x}) - \sum_{i=1}^q \lambda_i \mathbf{B}_i(\mathbf{x}) \quad (5.9)$$

The second-order necessary condition is that  $\mathbf{Z}_q^T [\nabla^2 L(x^*)] \mathbf{Z}_q$  be positive semi-definite.

### 5.1.3 Non-linearly constrained minimization

Modelling is a process of identifying objective, variables, and constraints for a given problem[39]. The construction of such mathematical model is often one of the most important step in the optimization process. A simplistic model will not give useful insights whereas a complex model may be difficult to solve. There is also not a single algorithm that is tailored to solve class of optimization problems. Each kind of algorithm is tailored to suit each class of optimization problem and the choice of the algorithms often determines the speed of the computation and, whether the problem is solved at all or not. The solution approaches to the non-linearly constrained minimization problems can be classified into two distinct categories[38]. The first one is the transformation methods in which the objective function is modified in such a way to have an unconstrained minimum at the minimum of the original constrained problem. If the modifications are done in sequence, we call it sequential method. The second type is a linear approximation of the constraints and subsequent application of projection, hence called projection methods. Both of the problem can further be sub-divided based on the role of Lagrangian function on the minimization process. However, in reality the categorisation may not always be clear cut based

on the complexity of the algorithms[38].

After an optimization algorithm succeeds in finding the solution, elegant mathematical expressions called optimality conditions are used to check that the set of variables are indeed the solution to the given optimization problem[39]. Sensitivity analysis can further aid in refinement of the model.

## 5.2 Optimization Algorithms

Optimization traces its roots back to the calculus of variations and the work of Euler and Lagrange. From then till now, all optimization algorithms are similar in nature. All optimization algorithms are iterative and all begin with an initial guess of the solution and then generate a sequence of improved solution called estimates or iterates, until the iteration stops with or without finding the optimal solution[39]. What differentiates each optimization algorithm from the next one is the way they generate these estimates or iterates and move forward. This completely determines the robustness, efficiency and accuracy of the solution[39].

### 5.2.1 Non-Linear Programming by Quadratic Lagrangian

Non-Linear Programming by Quadratic Lagrangian is a gradient based, single objective optimizer based on quasi newton methods developed by Klaus Schittkowski. The assumption is made that the objective function and constraints have continuous differentiability. The approach involves creating a series of subproblems in quadratic programming by approximating the Lagrangian function quadratically and linearizing the constraints. Quasi-Newton formula is used to update second order information, and an additional line search is employed to stabilize the method [29]. Since it is a gradient based optimization, the accuracy of the solution depends upon the accuracy of the gradients. Analytical gradients are unavailable for most of the practical problems so it is crucial that the numerical gradients i.e finite difference based gradients are as accurate as possible. Consider the

CHAPTER 5. PRELIMINARY DESIGN EXPLORATION: A METAHEURISTIC APPROACH

---

following single-objective nonlinear optimization problem. It is assumed that the problem is smooth and analytic throughout and is a problem of  $N$  decision variables.

Minimize:

$$f = f(\{x\}) \quad (5.10)$$

Subject to:

$$\begin{aligned} g_k(\{x\}) &\leq 0, \forall k = 1, 2, \dots, K \\ h_l(\{x\}) &= 0, \forall l = 1, 2, \dots, L \end{aligned} \quad (5.11)$$

where,

$$\{x_L\} \leq \{x\} \leq \{x_U\} \quad (5.12)$$

Where,  $K$  and  $L$  are the numbers of inequality and equality constraints. In many cases the inequality constraints are bound above and below, in such cases, it is customary to split the constraint into two inequality constraints. In order to approximate the quadratic sub-problem, assuming the presence of only equality constraints, the Lagrangian for Equation 5.12 can be written as:

$$\Lambda(\{x\}, \{\lambda\}) = f(\{x\}) + \{\lambda\}^T \{h(\{x\})\} \quad (5.13)$$

Where,  $\{\lambda\}$  is a  $L$  dimensional vector (non-zero) which are used as Lagrange multipliers. Thus, Equation 5.13 becomes a functional, which depends on two sets of independent vectors. In order to minimize this expression, we seek the stationarity of this functional with respect to the two sets of vectors. These expressions give rise to two sets of vector expressions as the following:

$$\begin{aligned} \Lambda(\{x\}, \{\lambda\})_{,\{x\}} &= \{\nabla \Lambda\} = \{\nabla f\} + [H]\{\lambda\} = \{0\} \\ \Lambda(\{x\}, \{\lambda\})_{,\{\lambda\}} &= \{h(\{x\})\} = \{0\} \end{aligned} \quad (5.14)$$

Equation 5.14 defines the Karush-Kuhn-Tucker (KKT) conditions which are the necessary conditions for the existence of the optimal point. The first equation comprises "  $N$  "

CHAPTER 5. PRELIMINARY DESIGN EXPLORATION: A METAHEURISTIC APPROACH

---

nonlinear algebraic equations and the second one comprises " L " nonlinear algebraic equations. The matrix [H] is a (N\* L) matrix defined as the following:

$$[H_{(N^* L)} = [\{\nabla h_1(\{x\})\}, \{\nabla h_2(\{x\})\}, \{\nabla h_3(\{x\})\}, \dots] \quad (5.15)$$

Thus, in Equation 5.15, each column is a gradient of the corresponding equality constraint. For our convenience, the nonlinear equations of 5.14 can be written as the following:

$$\{F(\{Y\})\} = \{0\} \quad (5.16)$$

where, Equation 5.16 is a (N+L) system of nonlinear equations. The independent variable set {Y} can be written as:

$$\{Y\} = \begin{Bmatrix} \{x\} \\ \{\lambda\} \end{Bmatrix} \quad (5.17)$$

while the functional set {F} is written as the following:

$$\{F\} = \begin{Bmatrix} \{\nabla \wedge\} \\ \{h\} \end{Bmatrix} \quad (5.18)$$

Referring to the section on Newton based methods, the vector {Y} is updated as the following:

$$\{Y_{j+1}\} = \{Y_j\} + \{\Delta Y_j\} \quad (5.19)$$

The increment of the vector is given by the iterative scheme in Newton's Iterative Method. Referring to Equation 5.16 , Equation 5.17, and Equation 5.18, the iterative equation is expressed as the following:

$$[\nabla F_j] \{\Delta Y_j\} = - \{F(\{Y_j\})\} \quad (5.20)$$

Note that this is only a first order approximation of the Taylor expansion of Equation 5.16. This is in contrast to Newton's iterative method where a quadratic approximation is done. This is because in Equation 5.17, a first order approximation has already been done. The



matrices and the vectors in Equation 5.20 can be expanded as the following:

$$\{\Delta Y\} = \begin{Bmatrix} \{\Delta x\} \\ \{\Delta \lambda\} \end{Bmatrix} \quad (5.21)$$

and

$$[\nabla F] = \begin{bmatrix} [\nabla^2 \Lambda]_{(N^* N)} & [H]_{(N^* L)} \\ [H]^T_{(L^* N)} & [0]_{(L^* L)} \end{bmatrix}_{((N+L^* (N+L))} \quad (5.22)$$

This is obtained by taking the gradients of Equation 5.18 with respect to the two variable sets. The sub-matrix  $[\nabla^2 \Lambda]_{(N^* N)}$  is the  $(N^* N)$  Hessian of the Lagrange function in implicit form.

To demonstrate how Equation is formed, let us consider the following simple case. Given a vector of two variables  $x$  and  $y$ , we write:

$$\{V\} = \begin{Bmatrix} \{a(x, y)\} \\ \{b(x, y)\} \end{Bmatrix} = \begin{Bmatrix} a1(x, y) \\ a2(x, y) \\ b1(x, y) \\ b2(x, y) \end{Bmatrix} \quad (5.23)$$

It is required to find the gradient (i.e. Jacobian of the vector function  $V$ ). To this effect, the derivation of the Jacobian is evident because in the present context, the vector  $V$  indicates a set of nonlinear (algebraic) equations and the Jacobian is the coefficient matrix which "links" the increment of the independent variable vector to the dependent variable vector. Thus, we can write:

$$\{\Delta V\} = \begin{Bmatrix} \{\Delta a(x, y)\} \\ \{\Delta b(x, y)\} \end{Bmatrix} = \begin{bmatrix} \frac{\partial a1}{\partial x} & \frac{\partial a1}{\partial y} \\ \frac{\partial a2}{\partial x} & \frac{\partial a2}{\partial y} \\ \frac{\partial b1}{\partial x} & \frac{\partial b1}{\partial y} \\ \frac{\partial b2}{\partial x} & \frac{\partial b2}{\partial y} \end{bmatrix} \begin{Bmatrix} \Delta x \\ \Delta y \end{Bmatrix} \quad (5.24)$$

Thus, the Jacobian matrix is formed. In some applications, the equation is written in the

following form:

$$\{\Delta V\} = \begin{Bmatrix} \{\Delta a(x, y)\} \\ \{\Delta b(x, y)\} \end{Bmatrix} = \begin{bmatrix} \frac{\partial a1}{\partial x} & \frac{\partial a2}{\partial x} & \frac{\partial b1}{\partial x} & \frac{\partial b2}{\partial x} \\ \frac{\partial a1}{\partial y} & \frac{\partial a2}{\partial y} & \frac{\partial b1}{\partial y} & \frac{\partial b2}{\partial y} \end{bmatrix}^T \begin{Bmatrix} \Delta x \\ \Delta y \end{Bmatrix} \quad (5.25)$$

where, the column "i" indicates the gradient of the "i-th" component of the dependent variable vector with respect to the independent vector. This is the formalism we use in determining Equation 5.22. Equation 5.20 may be rewritten as the following:

$$\begin{bmatrix} [\nabla^2 \Lambda]_{(N \times N)} & [H]_{(N \times L)} \\ [H]^T_{(L \times N)} & [0]_{(L \times L)} \end{bmatrix}^{(j)} \begin{Bmatrix} \{\Delta x\} \\ \{\Delta \lambda\} \end{Bmatrix}^{(j)} = - \begin{Bmatrix} \{\nabla \Lambda\} \\ \{h\} \end{Bmatrix}^{(j)} \quad (5.26)$$

Solution of Equation 5.26 iteratively will solve Equation 5.27 in a series of linear steps till the point when the increment is negligible. The update schemes for the independent variable and Lagrange multiplier vectors  $x$  and  $\lambda$  are written as the following:

$$\begin{aligned} \{x_{j+1}\} &= \{x_j\} + \{\Delta x_j\} \\ \{\lambda_{j+1}\} &= \{\lambda_j\} + \{\Delta \lambda_j\} \end{aligned} \quad (5.27)$$

The individual equations of the Equation 5.26 are written separately now. The first equation (corresponding to minimization with respect to  $x$ ) may be written as:

$$\begin{aligned} [\nabla^2 \Lambda]_j \{\Delta x\}_j + [H]_j \{\Delta \lambda\}_j &= -\{\nabla \Lambda\}_j \\ [\nabla^2 \Lambda]_j \{\Delta x\}_j + [H]_j \{\Delta \lambda\}_j &= -\{\nabla f\}_j - [H]_j \{\lambda\}_j \\ [\nabla^2 \Lambda]_j \{\Delta x\}_j + [H]_j \{\lambda\}_{j+1} &= -\{\nabla f\}_j \end{aligned} \quad (5.28)$$

The last step in Equation 5.28 is done by using Equation 5.27. Thus, using Equation 5.28 and Equation 5.26, the iterative scheme can be rewritten in a simplified form as:

$$\begin{bmatrix} [\nabla^2 \Lambda]_{(N \times N)} & [H]_{(N \times L)} \\ [H]^T_{(L \times N)} & [0]_{(L \times L)} \end{bmatrix}^{(j)} \begin{Bmatrix} \{\Delta x\}^{(j)} \\ \{\lambda\}^{(j+1)} \end{Bmatrix} = - \begin{Bmatrix} \{\nabla f\} \\ \{h\} \end{Bmatrix}^{(j)} \quad (5.29)$$

Thus, Equation 5.29 can be used directly to compute the  $(j + 1)$  th value of the Lagrange multiplier vector. Note that by using Equation 5.29, it is possible to compute the update of  $x$  and the new value of the Lagrange multiplier vector  $\lambda$  in the same iterative step. Equation 5.29 shows the general scheme by which the KKT optimality condition can be solved iteratively for a generalized optimization problem.

### 5.2.2 Evolutionary Algorithms

Let us consider a classical problem in optimization called two-dimensional Ackley function given by;

$$f(x, y) = e - 20 \exp \left( -0.2 \sqrt{\frac{x^2 + y^2}{2}} \right) - \exp \left( \frac{\cos(2\pi x) + \cos(2\pi y)}{2} \right) \quad (5.30)$$

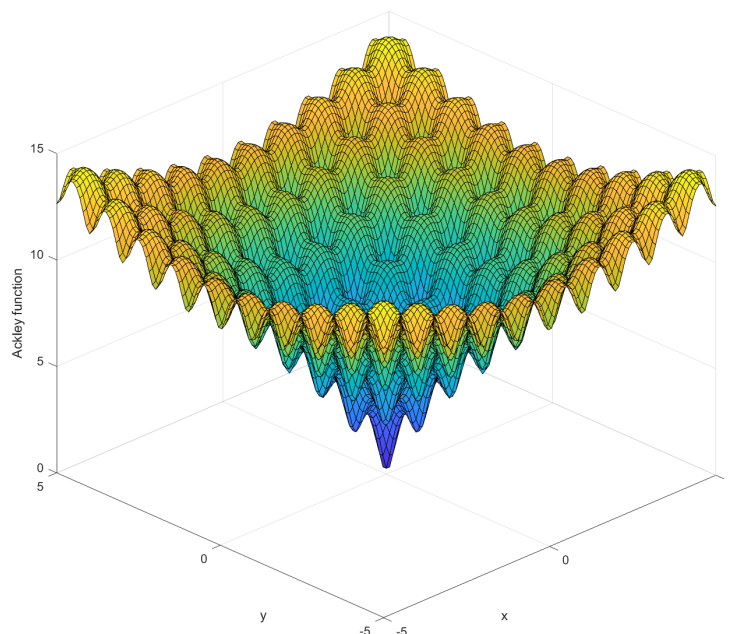


Figure 5.2: Ackley function reveals a complex landscape characterized by numerous local minima and a global minimum at the origin, challenging algorithms to navigate the function's intricate topology to find the optimal solution.

The Ackley function is a mathematical function commonly used to evaluate optimization algorithms. The above plot (Figure 5.2) of the two-dimensional Ackley function is called a fitness landscape which describes how a fitness or cost function varies with independent variables [40]. Even in two dimensions, the Ackley function shows numerous minima. In 20 or 30 dimensions, the number of minima could be unimaginable. We could attack this problem by taking the derivative of  $f(x, y)$  with respect to  $x$  and  $y$ , and then solving for  $f_x(x, y) = f_y(x, y) = 0$  to find the local minima. However, solving these simultaneous equations could be difficult. The Ackley function is a commonly used test function for optimization algorithms. It is a non-convex, multimodal function that has many local minima and one global minimum.

The conclusion of using the Ackley function in optimization is that it presents a challenging optimization problem that can test the effectiveness of optimization algorithms in finding the global minimum. This is where Evolutionary algorithms are useful.

### **Intelligence**

Intelligence is a complex and multifaceted concept, and its definition has evolved over time. At its core, intelligence involves the ability to learn from experience, solve problems, and adapt to new situations. It also encompasses other qualities such as creativity, reasoning, and social skills. With the motivation to encompass the intelligence issues in computer, which they lacked initially, fuzzy systems, neural networks and evolutionary algorithms were developed [40]. In the context of Evolutionary Algorithms (EAs), intelligence is often characterized by several key features. Adaptation refers to the ability of an algorithm to change and improve over time in response to feedback from its environment. Randomness allows the algorithm to explore different solutions and avoid getting stuck in local optima. Communication and feedback enable the algorithm to interact with its environment and learn from its experiences. Exploration and exploitation are two complementary strategies that EAs use to balance the search for new solutions and the exploitation of existing ones.

### 5.3 Genetic Algorithms

Genetic algorithms (GAs) are the earliest, most well-known, and most widely used EAs based on the principle of natural selection propounded by Charles Darwin in 1859, which on its time of publication was the most revolutionary as well as controversial scientific theory of all times [40]. Genetic algorithms simulate the natural selection, also known as survival of the fittest in order to solve the optimization problem. However, it would be more correct to say that these algorithms depend on the works of Charles Darwin, father of evolution as well as Gregor Mendel, father of genetics. *"Darwin, a child of privilege, developed the theory of natural selection, but it would be left to a child of poverty, Gregor Mendel, to prove it [40]"*. Research in computer simulations of genetics began in 1940s and led to a tremendous amount of research during 1970s and 1980s [40].

According to the theory of natural selection, all individuals are made up of different genetic structures and they pass some of these genetic traits to the offspring. If these traits are useful, their offspring are more likely to survive and reproduce more offspring, which leads to that genetic trait being predominant within that population. However, sometimes the genes are not transferred intact from parents to offspring, but are altered in some ways. These alterations are called mutations which may be beneficial or harmful. Similarly, to solve an optimization problem, we create a candidate population which we call individuals. The good or fit individuals which are an approximation to a good solution mate which is called cross-over and transfer their better genes to offspring. This event is called one generation of Genetic algorithm. Some offspring have high fitness while others will have low fitness. Low-fitness individuals have a high probability of dying in their generation; that is, they are removed from the GA simulation. High-fitness individuals survive to cross over with other high-fitness individuals, and thereby produce a new generation of individuals. This process is continued until the GA finds an acceptable solution to the optimization problem called near-optimal solution.

The final step in the GA is called mutation. In most GA implementations, mutation

is also rare (on the order of 2%). But we cannot say, in general, what the correct setting should be for a GA mutation rate. The best mutation rate depends on the problem, population size, encoding, and other factors. Regardless of its frequency, mutation is important because it allows the evolutionary process to explore new potential solutions to the problem. If some genetic information is missing from the population, mutation provides the possibility of injecting that information into the population. This is important in biological evolution, but even more important in GAs. This is because GAs typically have such small population sizes that inbreeding can easily become a problem, and evolutionary dead ends are more common in GAs than in biological evolution. In biological evolution we typically talk about populations of millions, while in GAs we talk about populations of dozens or hundreds.

To implement mutation, we select a mutation probability, say 1%. This means that after the crossover process produces offspring, each bit in each child has a 1% probability of flipping to the opposite value (a 1 changes to a 0, or a 0 changes to a 1). Mutation is simple, but it's important to select a reasonable mutation probability. Too high of a mutation probability makes the GA behave like a random search, which is not usually a great way to solve a problem. Too low of a mutation probability results in problems with inbreeding and evolutionary dead ends, which also prevents the GA from finding a good solution.

### 5.3.1 Implementation Technique

#### Initialization

Evolutionary algorithms begin with random population which is easiest and most popular initialization method. However, initialization can greatly affect the success of the Evolutionary algorithms. The first approach could be to generate  $5N$  random individuals and keep the best  $N$  as the initial population. The second option could be to generate random individuals, locally optimize them and perform gradient descent, then use resulting population as our initial population. The third is to use expert solutions or candidate solutions

from any other source to seed our initial population. This is called direct initialization. In our case, we begin with 140 as starting population size and then use 70 as the next population.

### **Convergence criteria**

We should always decide when to stop the algorithm. There are several criteria that can be defined to define the convergence in evolutionary algorithms.

- a) Preset number of generations.
- b) When a "good-enough" solution is found.
- c) The best individual fitness does not change after a certain number of generations.
- d) Population's fitness values does not change appreciably for a certain number of generations.

We can stop the EA after the standard deviation of the population's fitnesses stops decreasing, or drops below some threshold. This indicates that the population has reached a certain level of uniformity. We can also use some combination of the above criteria. To indirectly measure the fitness, we look at the standard deviation of the data and see whether the solution is converging, diverging or is stuck in a local optima. In cases, where we find that the solution is no more improving, we stop the iteration and begin with another set of parameters in search of the global optima.

### **Elitism**

The principle of evolutionary algorithm is natural selection, so the best individuals must survive. Elitism is the process of incorporating the method that best individuals survive and are retained from one generation to the next. Let us suppose we have an excellent solution  $x_i$  at  $i^{\text{th}}$  generation. Now since the solution at  $(i + 1)^{\text{th}}$  generation may or may not be better than  $x_i$ , we want to preserve the  $x_i$  solution. Otherwise,  $x_i$  will recombine with others and produce children, and we will lose  $x_i$ . This idea was first proposed by De Jong

in 1975.

### **Steady state algorithms**

Generally we suppose that the next generation replaces the previous generation entirely, except the elite individuals and such algorithms are called generational algorithms. However, this does not occur in nature. In nature the generations are staggered, and death and birth occur continuously. This motivated the scientists to implement the steady state genetic algorithms. In evolutionary algorithms, a steady-state algorithm is a variant where only a subset of individuals in the population is replaced at each iteration, maintaining a relatively stable population size. Instead of replacing the entire population, a fixed number of individuals, typically the least fit ones, are selected and replaced with new individuals generated through genetic operators such as mutation and crossover. This approach allows for a continuous exploration and exploitation of the search space, often resulting in faster convergence and better utilization of computational resources compared to other evolutionary algorithms.

### **Population Diversity**

Population diversity refers to strategies for managing duplicate individuals in the population and modifying selection and recombination techniques to foster diversity in problems with multiple modes. Initially, the focus is on addressing duplicate individuals. Subsequently, two approaches for promoting diversity in evolutionary algorithm (EA) populations can be discussed: restrictions on recombination and techniques for maintaining population niches, encompassing fitness sharing, clearing, and crowding methods.

**Duplicate Individuals** In a population that is repeatedly recombined from one generation to the next, uniformity often results. This means that the entire population becomes a population of clones. Uniformity occurs more often in discrete-domain problems than in continuous-domain problems, but it can occur in both types of problems. Uniformity limits the EA from further exploration of the search space. Although the candidate solution to which an EA converges is usually a good solution, there may be much better solutions



in other regions of the search space; therefore, even after the EA finds a good solution, we hope that it will keep exploring in an attempt to find even better solutions. When uniformity occurs before we have found a satisfactory solution to our optimization problem, it is called premature convergence [41]. We can prevent this with higher mutation rates, but if we use too high of a mutation rate our EA will degenerate into a random search. One common way to prevent premature convergence is to continuously search for duplicate individuals and replace them in the population.

**Niche-Based and Species-Based Recombination** The conventional implementation of evolutionary algorithms (EAs) typically involves selecting parent individuals and combining them to produce offspring, without considering the degree of similarity or dissimilarity between the parents. In contrast, in biological systems, parents often exhibit some level of similarity while also avoiding excessive closeness. For instance, mating between different species or close relatives is uncommon. Firstly, the resulting child may yield a suboptimal solution to the optimization problem since the midpoint between two highly fit individuals may possess low fitness. Secondly, the crossover process could lead to the loss of genetic information that might be crucial for solving the problem at hand.

Species-based recombination, on the other hand, involves partitioning the population into discrete subpopulations, or species, based on a more strict measure of similarity among individuals, such as their genetic distance or reproductive isolation. Within each species, individuals are allowed to mate and exchange genetic material, but mating between individuals from different species is either discouraged or disallowed altogether. Both niche-based and species-based recombination can be useful in genetic algorithms for maintaining genetic diversity and preventing premature convergence to suboptimal solutions. However, the specific approach that is most effective will depend on the particular problem being addressed and the characteristics of the population and search space.

It is important to recognize that niche-based and species-based strategies are contrasting approaches to addressing the same problem. Niche-based recombination operates on

the belief that when we combine individuals with high fitness, the resulting offspring is likely to be fit only if the parents are similar to each other. On the other hand, species-based recombination follows the philosophy that when we combine fit individuals, it is crucial to ensure that the parents are distinct from each other to facilitate effective exploration of the search space. The choice between these approaches depends on the specific characteristics and requirements of the problem at hand.

### 5.3.2 Selection options

Before combining individuals in evolutionary algorithms (EAs) to create offspring, it is necessary to determine which individuals will serve as parents. Roulette-wheel selection is the standard method used in genetic algorithms (GAs) and various other selection algorithms exist and are utilized in EAs. Most selection methods exhibit bias towards fitter individuals in the population. In other words, regardless of the selection algorithm employed, a more fit individual typically has a higher probability of being chosen compared to a less fit individual.

If a selection method exhibits excessive bias towards fit individuals, the population may converge too quickly towards a uniform solution, limiting the exploration of the search space. On the other hand, if a selection method lacks sufficient bias towards fit individuals, the EA may struggle to effectively exploit the information present in the most fit individuals.

Selection pressure, denoted as  $\phi$ , serves as a useful metric for quantifying the differences between various selection algorithms.

$$\phi = \frac{\text{Pr( selection of most fit individual )}}{\text{Pr( selection of average individual )}} \quad (5.31)$$

It is defined as the ratio between the probability of selecting the most fit individual and the average individual's probability of being selected for recombination. Selection pressure measures the relative probability of highly fit individuals participating in recombination.

**Rank based selection** Rank-based selection is a type of selection method used in evolutionary algorithms (EAs) that assigns individuals in the population ranks based on their fitness levels. Instead of directly using fitness values for selection, the individuals are ordered according to their fitness ranks. This approach aims to strike a balance between exploitation (selecting highly fit individuals) and exploration (allowing less fit individuals a chance for selection).

### 5.3.3 Recombination

Recombination, also known as crossover, is a fundamental operation in genetic algorithms (GAs). It involves the combination of genetic material from two or more parent individuals to create offspring with a new set of characteristics. In a genetic algorithm, a population of potential solutions is evolved over generations to find an optimal or near-optimal solution to a given problem. Each individual in the population represents a potential solution and is encoded as a string of genetic information, often referred to as a chromosome. During the recombination process, two parent individuals are selected from the population, and portions of their chromosomes are exchanged or combined to create new offspring individuals. The specific method of recombination varies depending on the encoding scheme used and the nature of the problem being solved. In our case, we use uniform and simulated binary recombination method.

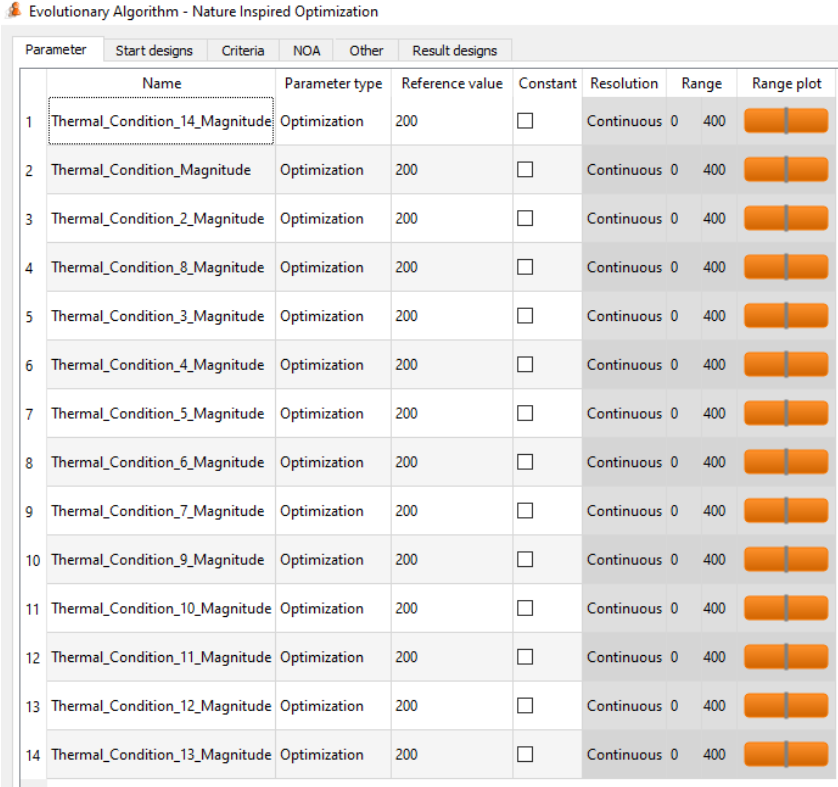
## 5.4 Methodology

The effect of prestress can be applied by the direct application of force or by the use of thermal gradient technique. Both yield the same value of prestressing force. However, if the range of prestressing force for each of these 14 parameter starts from 0 N to 3000 N, then there are  $3001^{14} \approx 3.502 \times 10^{41}$  possible combinations. If we use a temperature in the range of 0°C to 400°C then there are  $401^{14} \approx 7.865 \times 10^{27}$  possible combinations. Therefore, by changing the range from force to temperature, the number of combinations would be reduced significantly.

## CHAPTER 5. PRELIMINARY DESIGN EXPLORATION: A METAHEURISTIC APPROACH

---

The second thing is to define the constraint. Although, our aim is to reduce the average total deformation of spokes to be less than 200 microns, we use the maximum total deformation of the spokes to be less than 200 microns because if the maximum total deformation is less than 200 microns, then automatically the average total deformation of spokes to be less than 200 microns. We define the thermal conditions in each cables as parameter (Figure 5.3) and define the constraint (Figure 5.4). In parallel, we also check the values of axial force induced in the spokes.



The screenshot shows the 'Evolutionary Algorithm - Nature Inspired Optimization' software interface. It features a table with 14 rows, each representing a parameter. The columns are: Parameter, Name, Parameter type, Reference value, Constant, Resolution, Range, and Range plot. All parameters are of type 'Optimization' with a reference value of 200. The resolution is 'Continuous' and the range is from 0 to 400. Each parameter has a corresponding 'Range plot' button.

Parameter	Name	Parameter type	Reference value	Constant	Resolution	Range	Range plot
1	Thermal_Condition_14_Magnitude	Optimization	200	<input type="checkbox"/>	Continuous	0 400	
2	Thermal_Condition_Magnitude	Optimization	200	<input type="checkbox"/>	Continuous	0 400	
3	Thermal_Condition_2_Magnitude	Optimization	200	<input type="checkbox"/>	Continuous	0 400	
4	Thermal_Condition_8_Magnitude	Optimization	200	<input type="checkbox"/>	Continuous	0 400	
5	Thermal_Condition_3_Magnitude	Optimization	200	<input type="checkbox"/>	Continuous	0 400	
6	Thermal_Condition_4_Magnitude	Optimization	200	<input type="checkbox"/>	Continuous	0 400	
7	Thermal_Condition_5_Magnitude	Optimization	200	<input type="checkbox"/>	Continuous	0 400	
8	Thermal_Condition_6_Magnitude	Optimization	200	<input type="checkbox"/>	Continuous	0 400	
9	Thermal_Condition_7_Magnitude	Optimization	200	<input type="checkbox"/>	Continuous	0 400	
10	Thermal_Condition_9_Magnitude	Optimization	200	<input type="checkbox"/>	Continuous	0 400	
11	Thermal_Condition_10_Magnitude	Optimization	200	<input type="checkbox"/>	Continuous	0 400	
12	Thermal_Condition_11_Magnitude	Optimization	200	<input type="checkbox"/>	Continuous	0 400	
13	Thermal_Condition_12_Magnitude	Optimization	200	<input type="checkbox"/>	Continuous	0 400	
14	Thermal_Condition_13_Magnitude	Optimization	200	<input type="checkbox"/>	Continuous	0 400	

Figure 5.3: Parameters and range for the evolutionary algorithm

## CHAPTER 5. PRELIMINARY DESIGN EXPLORATION: A METAHEURISTIC APPROACH

The screenshot displays the 'Evolutionary Algorithm - Nature Inspired Optimization' software interface. The 'Criteria' tab is selected, showing a table of optimization criteria. The 'constr\_Spokes\_Deformation\_Maximum' criterion is highlighted in red, indicating it is the active constraint. The 'Responses' tab shows the current values for various parameters, including 'Total\_Deformation\_3\_Maximum' at 0.808028.

Name	Type	Expression	Criterion	Limit	Evaluated expression
obj_Spokes_Deformation_Average	Objective	Spokes_Deformation_Average	MIN		7.89433
obj_Spokes_Deformation_Maximum	Objective	Spokes_Deformation_Maximum	MIN		22.1302
constr_Spokes_Deformation_Maximum	Constraint	Spokes_Deformation_Maximum	≤	0.2	22.1302 ≤ 0.2

Figure 5.4: The maximum total deformation of the spokes is set as constraint

## CHAPTER 5. PRELIMINARY DESIGN EXPLORATION: A METAHEURISTIC APPROACH

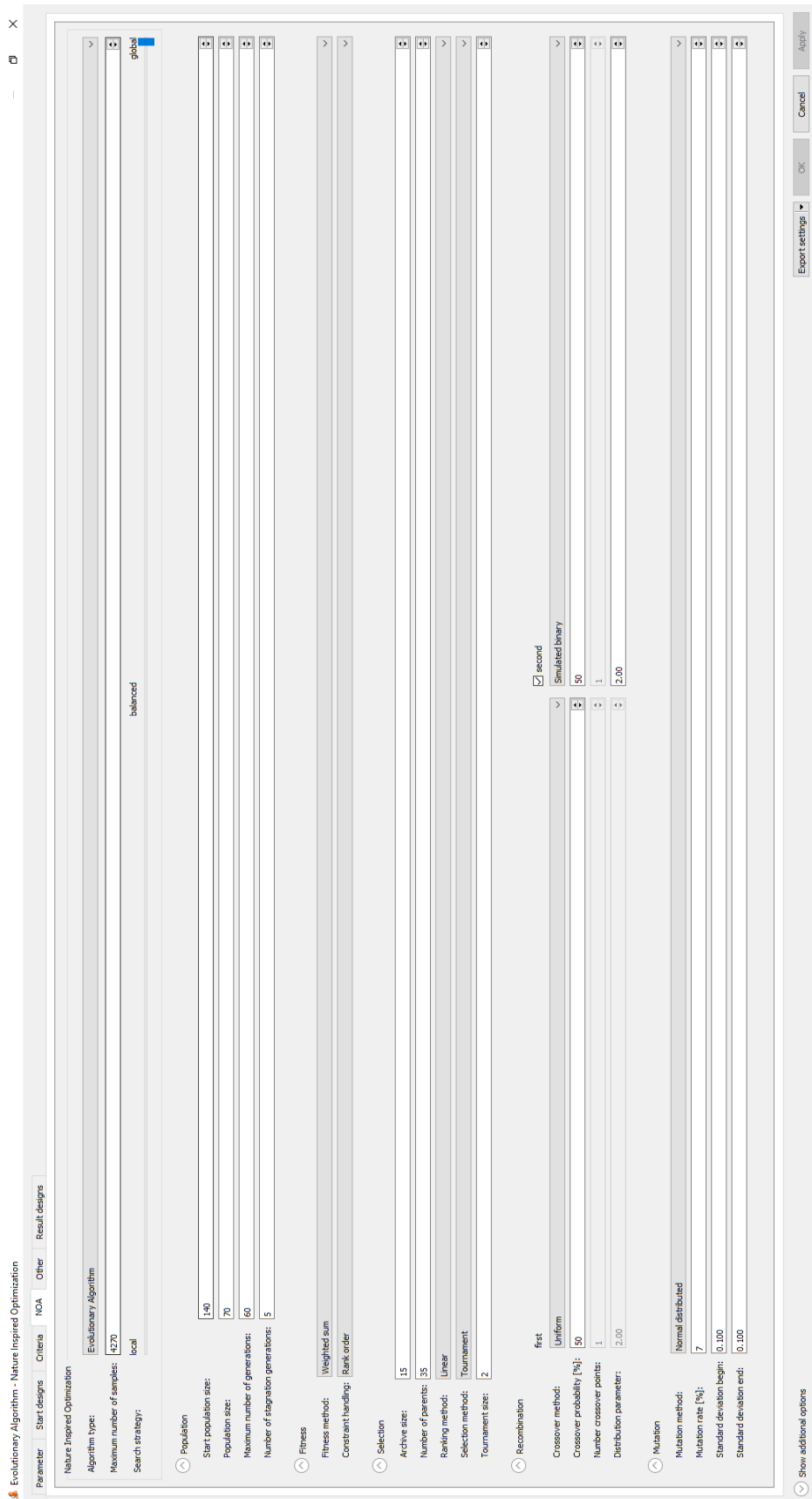


Figure 5.5: Parameters setting for evolutionary algorithm. The starting population is 140 ( $10N$ ) and 70 ( $5N$ ) is the population in each generation. We adopt a mutation rate of 7% .













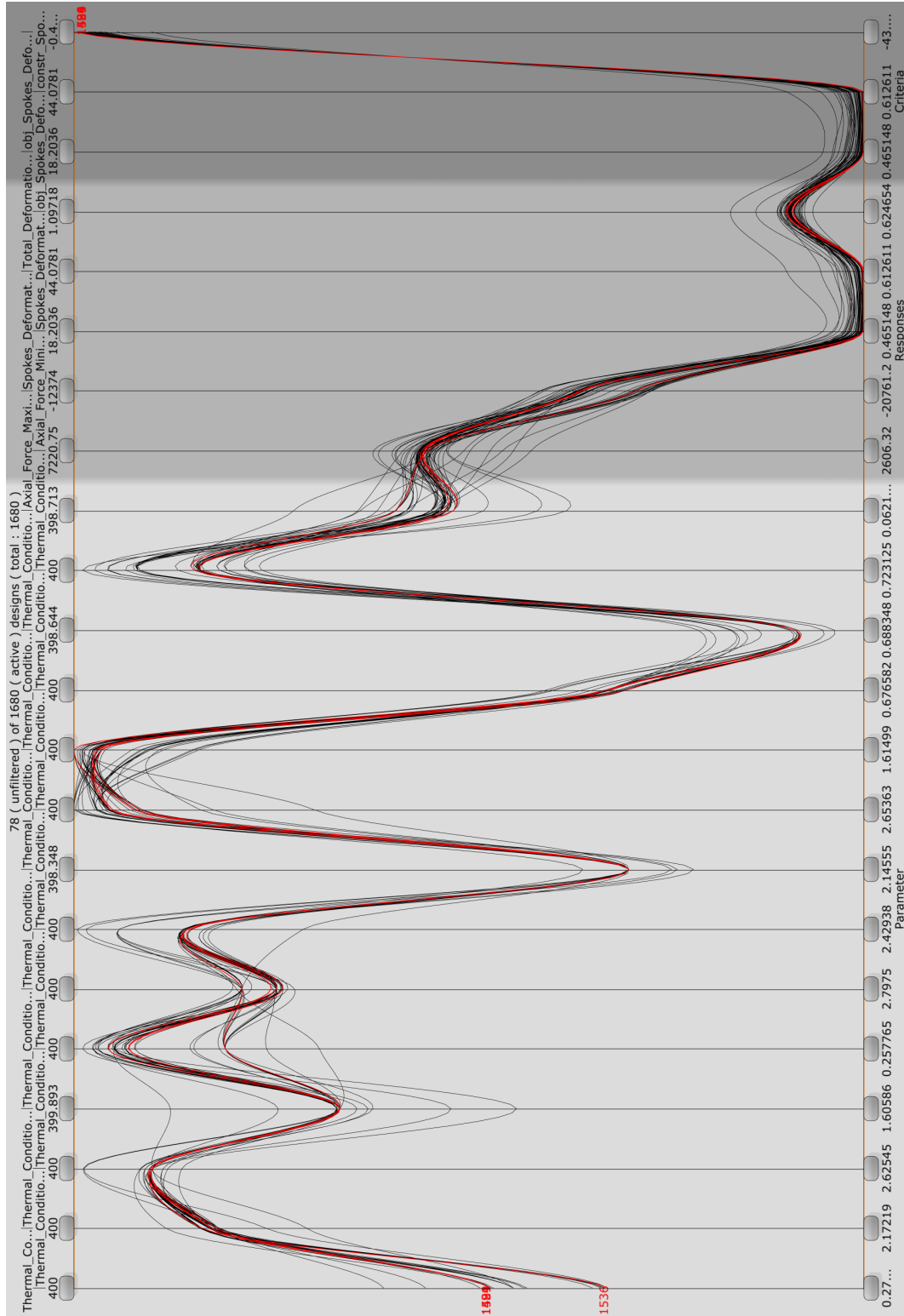


Figure 5.11: Twenty first generation



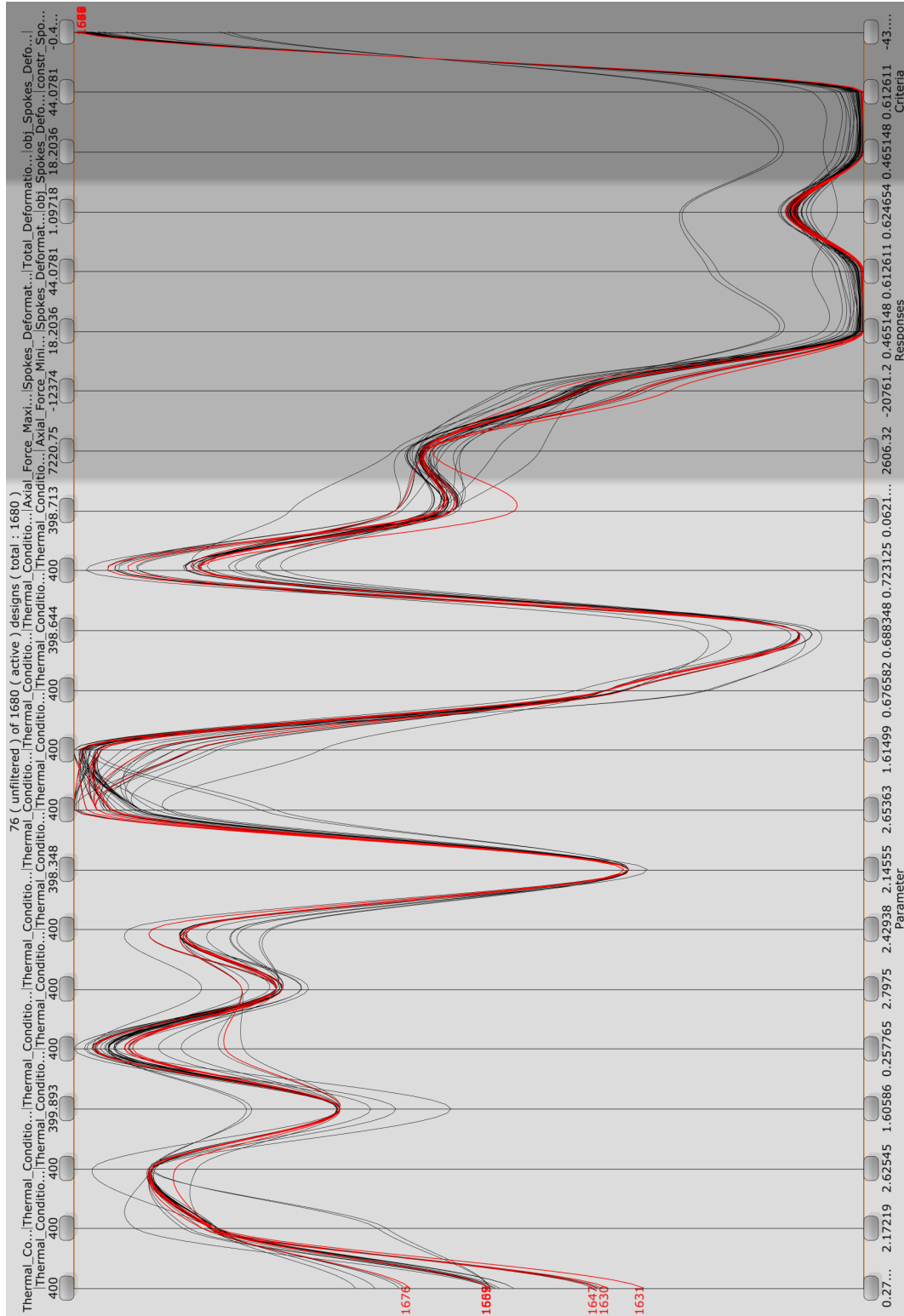


Figure 5.13: Twenty third generation



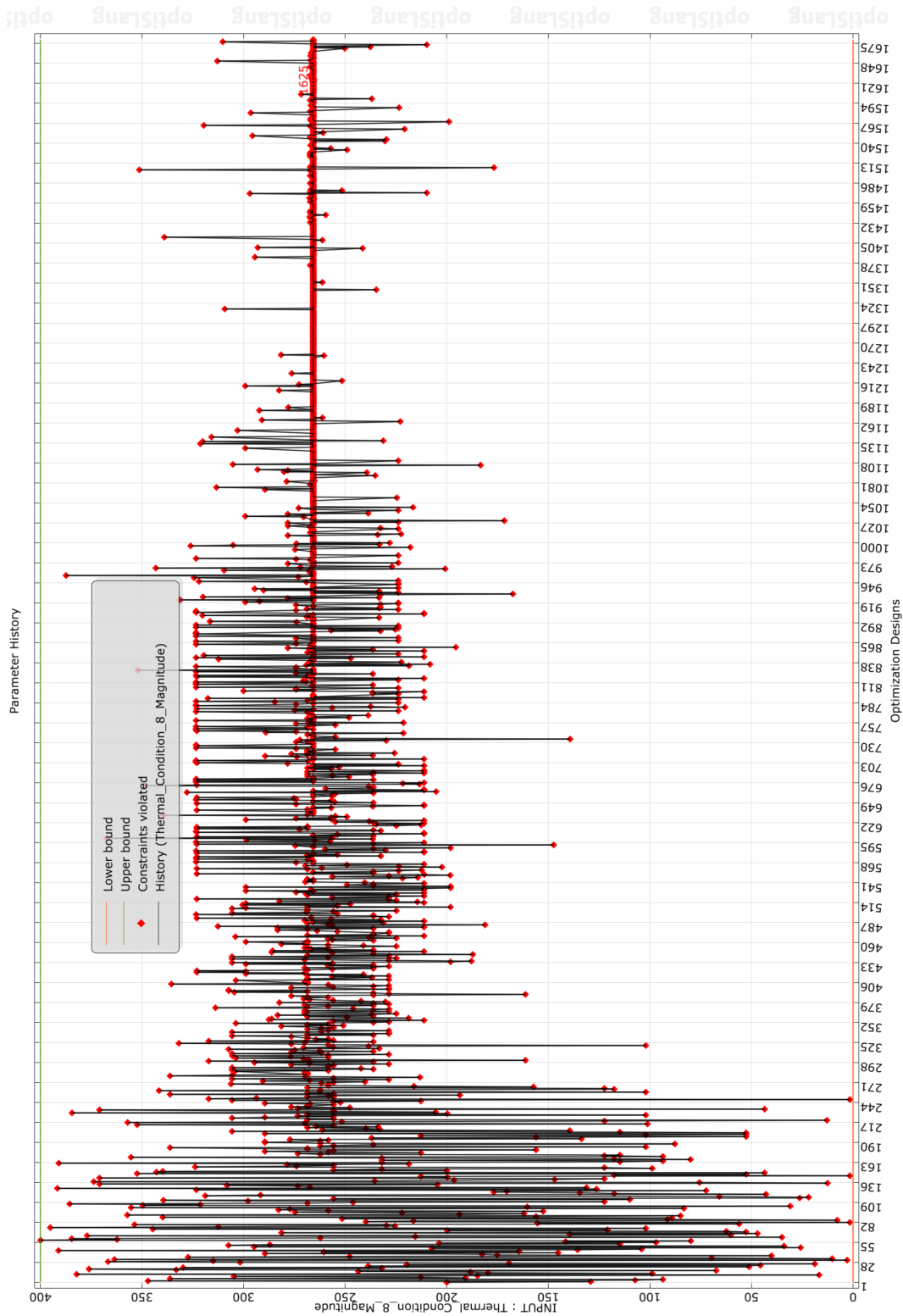


Figure 5.15: Input History for the thermal condition 8. The algorithm has practically stabilized and ceases to explore more design space.



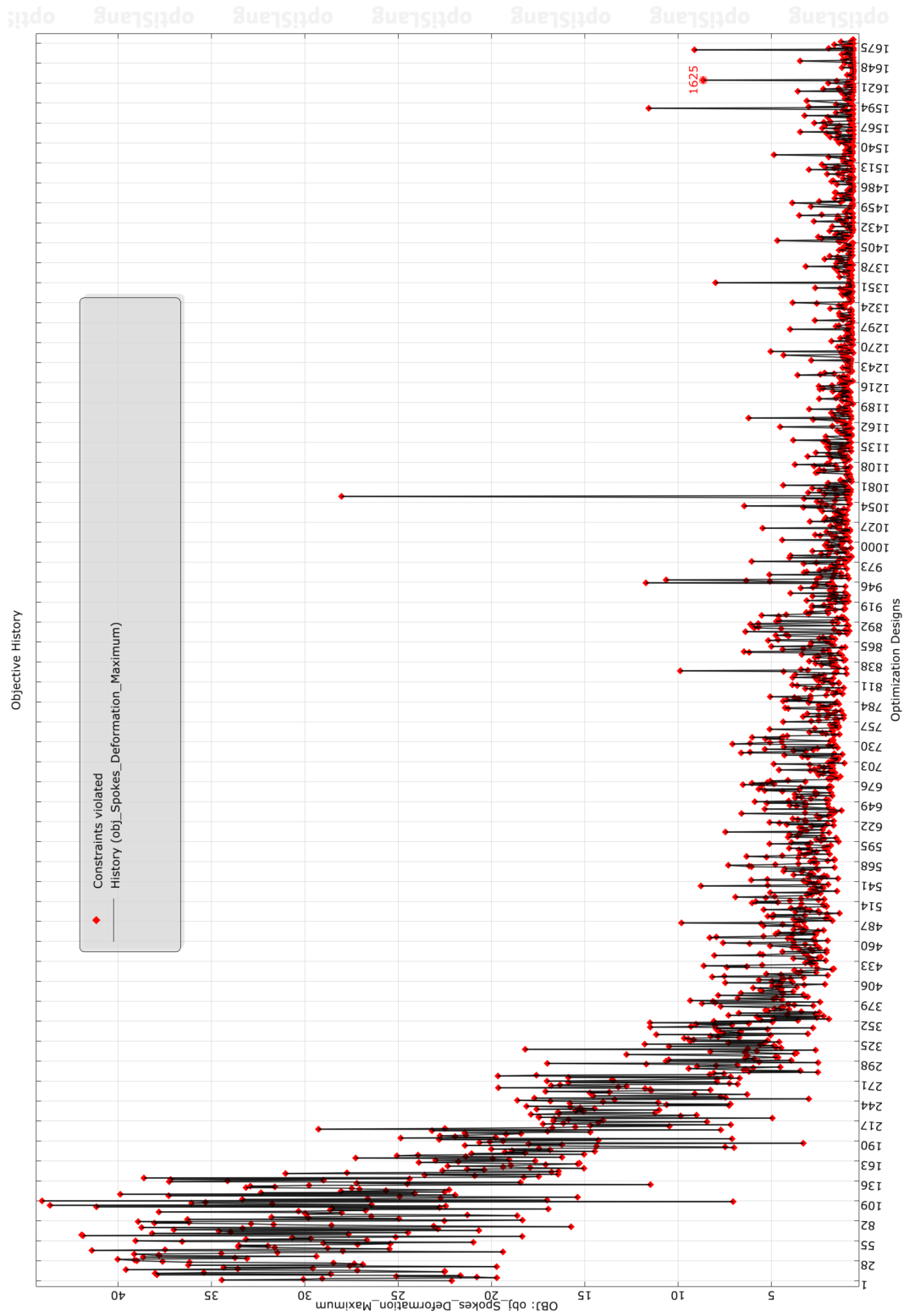


Figure 5.16: Total deformation History showing very rapid convergence in the beginning. However, the algorithm ceases to give better results after 18<sup>th</sup> generation.

## CHAPTER 5. PRELIMINARY DESIGN EXPLORATION: A METAHEURISTIC APPROACH

---

We closely monitor the variability (standard deviation) and average values within each generation (Table 5.1). The behavior of the evolutionary algorithm becomes evident as it initially explores a wide range and gradually narrows down its search domain. Specifically, after the 14<sup>th</sup> generation, the algorithm focuses on a very specific region only in the search of global optima. Surprisingly, even after reaching the 25<sup>th</sup> generation, the algorithm fails to discover any improved design points. This lack of progress is evident in Figure 5.15, where the algorithm's exploration phase comes to a halt, and it converges towards a single value, indicating stabilization. The fitness parameters can be studied with the help of following table :

Generation	Minimum value	Mean value	standard deviation
1	7.053	29.8262	7.17
2	3.29	18.50	5.24
3	2.99	12.65	4.35
4	2.49	7.14	3.09
5	1.91	4.64	1.81
6	1.66	3.81	1.81
7	1.35	3.20	1.42
8	1.35	3.07	1.37
9	1.24	2.90	1.45
10	1.08	2.586	1.53
11	0.97	2.34	1.31
11	1.08	2.34	1.31
12	0.82	2.68	1.72
13	0.72	1.63	1.01
14	0.71	1.78	0.98
15	0.63	1.31	0.91
16	0.61	1.21	0.79
17	0.61	1.04	0.62
18	0.61	1.05	0.90
19	0.61	1.16	0.79
21	0.61	1.01	0.64
22	0.61	1.24	1.39
23	0.64	0.66	0.01
24	0.64	0.66	0.01
25	0.64	0.66	0.008

Table 5.1: Minimum value, Mean value and the standard deviation of the total deformation in each generation as the evolutionary algorithm searches for global local optima in the domain.

Considering these circumstances, we make the decision to terminate the optimization process. Our final selection of the optimal value is based on the designs that exhibit the lowest total maximum deformation in spokes (Table 5.2).

CHAPTER 5. PRELIMINARY DESIGN EXPLORATION: A METAHEURISTIC APPROACH

---

Cable number	Values of Thermal condition
Cable-1	330.976
Cable-2	360.646
Cable-3	382.838
Cable-4	298.239
Cable-5	343.049
Cable-6	119.933
Cable-7	388.512
Cable-8	265.701
Cable-9	362.211
Cable-10	129.413
Cable-11	35.1225
Cable-12	335.869
Cable-13	213.717
Cable-14	189.269

Table 5.2: Values of the thermal condition used in the cables to apply the effect of prestress. Cable-1 is the outermost cable near the inner cylinder. Cable-14 is the innermost cable near the outer cylinder.

Again, using these values from Table 5.2, we can narrow our domain and start the genetic algorithm again. We use a mutation rate of 10% and use pareto dominance. However, the optimal solution did not improve (Figure 5.17). Two designs are tabulated below. Table 5.3 shows the parameters for least Maximum total deformation in the spokes. Table 5.4 shows parameters for least average deformation in spokes. These two values do not occur concurrently.

Cable number	Values of Thermal condition
Cable-1	319.81
Cable-2	354.545
Cable-3	354.37
Cable-4	314.571
Cable-5	338.287
Cable-6	148.386
Cable-7	299.983
Cable-8	223.538
Cable-9	356.852
Cable-10	184.144
Cable-11	73.4131
Cable-12	259.06
Cable-13	165.964
Cable-14	153.964

Table 5.3: Values of the thermal condition used in the cables to apply the effect of prestress. The average deformation in the spokes is 0.428763 mm and maximum deformation in the spokes is 0.56466 mm.

Cable number	Values of Thermal condition
Cable-1	319.81
Cable-2	354.545
Cable-3	354.37
Cable-4	314.222
Cable-5	338.291
Cable-6	148.336
Cable-7	299.213
Cable-8	220.979
Cable-9	393.337
Cable-10	184.144
Cable-11	73.4131
Cable-12	267.89
Cable-13	154.163
Cable-14	153.964

Table 5.4: Values of the thermal condition used in the cables to apply the effect of prestress. The average deformation in the spokes is 0.42069 mm and maximum deformation in the spokes is 0.59195 mm.

## 5.5 Conclusion

Despite the inherent efficiency of evolutionary algorithms in rapidly converging towards solutions by optimizing mutation rates, they often encounter challenges such as getting trapped in local optima or failing to discover superior solutions. Even after applying the NLPQL technique (*though not shown here*), there was not an expected improvement in the solution. Additionally, a significant discrepancy in the search domain exists between the optimal solutions presented in Table 5.2 and Tables 5.3-5.4 highlighting the need for a more extensive exploration of the domain.

However, considering the complexities arising from the nonlinearity of the problem, the constraints imposed by our available computational resources, and the criticality of achieving precise outcomes during the preliminary design phase, we make a thoughtful decision to limit the deformation to 400 microns. We find it prudent to conclude our current exploration while acknowledging the potential for future studies.



# Chapter 6

## Layered Composite Design

For many years, engineers envisioned theoretical designs that they could not build because the materials needed to construct them did not exist. The term “unobtainium” is sometimes used to identify materials that are desired but not yet available. In the field of particle detection too, scientists envisaged materials possessing reduced electromagnetic interaction with charged particles, while simultaneously ensuring their structural integrity remains adequately robust. Composite materials are the answers to the aforementioned challenges and are the preferred material for constructing this IDEA drift chamber. This chapter presents numerical modelling of layered composite structures using ANSYS Composite PrepPost (ACP). The previous chapters focused on the monolithic approach to composites, which involved simplifications that compromised the accuracy of the structure’s representation. However, this chapter offers a comprehensive and systematic approach for numerical development of layered composite materials used in our ultra light drift chamber.

### 6.1 Introduction

Composite refers to two or more materials with significantly different physical or chemical properties – categorized as “matrix” or “reinforcement” – combined in such a way to act together, yet remain separate and distinct at some level so as not to fully merge or dissolve into one another [43]. Even though composites can vary from naturally occurring wood

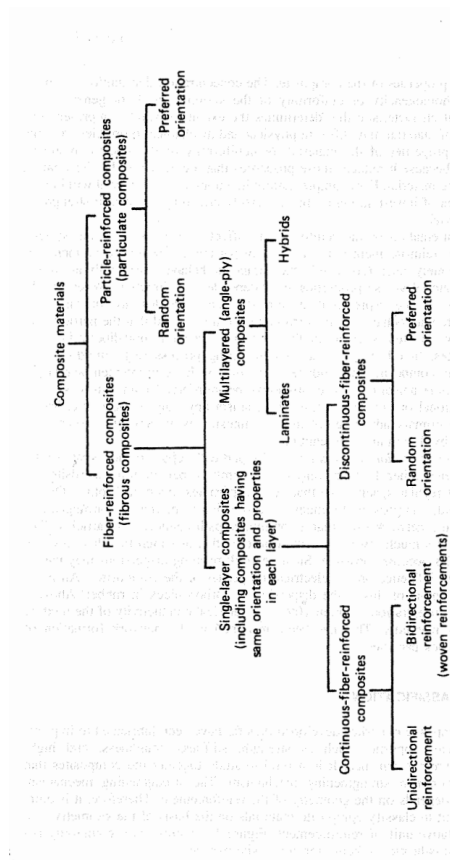


Figure 6.1: A classification chart of the composites. Adapted from *Bhagwan D Agarwal, Lawrence J Broutman, and CW Bert. Analysis and performance of fiber composites. 1981* [42].

to typically engineered products such as reinforced concrete, we focus our discussion to unidirectional composite materials, also referred to as advanced composite materials due to unusually high strength and high stiffness, or modulus of elasticity. A classification chart of the composites can be seen in Figure 6.1. The high strength fibers are also low density while occupying a large fraction of the volume. Composite materials are distinct from typical heterogeneous materials, as they are made up of strong fibers (whether continuous or not) that are surrounded by a weaker matrix material. This matrix material serves two purposes: firstly, it distributes the fibers throughout the composite, and secondly, it transmits the load to the fibers [44]. A typical carbon fiber can be seen in Figure 6.2.

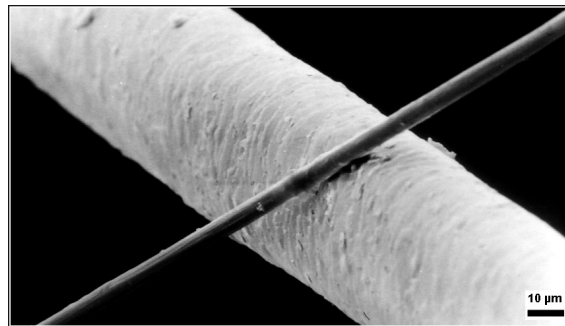


Figure 6.2: A carbon fiber of 6  $\mu\text{m}$  diameter carbon filament compared to 50  $\mu\text{m}$  diameter human hair. Adapted from *Wikipedia:Composite material* [43].

## 6.2 Need of composite material in particle detector systems

Charged particles have an electric charge, causing them to interact electromagnetically with the detector materials. The strength of this interaction depends on the charge of the particle and the atomic number ( $Z$ ) of the detector's elements. In a drift chamber, we observe the path of charged particles within a magnetic field. The curvature of their path, influenced by the magnetic field, determines the particle's momentum, which along with its mass, determines its energy. Momentum and energy are crucial parameters for understanding the complete interaction dynamics.



When the particle's trajectory is disturbed by interaction with the detector materials, our measurements become uncertain. To minimize these uncertainties, we aim to reduce both the amount of material the charged particle encounters and the atomic number of the materials used. To achieve this, we have selected helium gas as the drift chamber medium, aluminum (or carbon monofilaments) for the wires, and carbon fiber for the chamber's mechanical components. We avoid metals with higher atomic numbers because they introduce larger uncertainties, although some metallic components are necessary for electrostatic and radiofrequency (RF) shielding purposes. Structural Steel predominantly comprises 99% iron (Fe) and 0.25% carbon (C), with other lesser quantities of impurities. Iron possesses an atomic weight of around 55.845 atomic mass units (u). In case of carbon composites, the atomic weight is approximately 12.011 atomic mass units (u).

In addition to the advantages of having a low atomic number and minimal interference, composite materials offer several other benefits. Composite materials are typically lighter than metals, making them easier to handle and transport. In particle detection systems, lightweight components are desirable as they reduce the overall weight of the apparatus, making it more portable and less cumbersome to operate (*the final drift chamber will have to be assembled*). Composites can be designed to have excellent rigidity and dimensional stability, which is crucial in particle detection. Metals can be susceptible to thermal expansion and contraction, leading to potential mis-alignments and distortions in sensitive particle detection equipment. Composite materials with tailored properties can maintain their shape and integrity even under varying environmental conditions. Composite materials are often electrically insulating, unlike metals that are conductive. In particle detection systems, electrical insulation is essential to prevent interference or unwanted signals caused by the presence of electrically conductive materials. Composites can help reduce the background noise and improve the signal-to-noise ratio (SNR) in particle detection experiments. Composite materials can be engineered to have specific properties such as low thermal expansion, high radiation resistance, or minimal magnetic interference. These characteristics can be advantageous in particle detection applications where precise control over material properties is required to enhance the accuracy and

sensitivity of the detection system. Composites offer greater design flexibility compared to metals. They can be manufactured in various shapes, sizes, and forms, allowing for intricate and optimized designs of particle detectors. However, they are also extremely expensive and the wastage must be calculated beforehand. Composite materials can be molded or fabricated to conform to specific geometries. This is very important and crucial especially in developing the joints between the parts. Lastly, metals are susceptible to corrosion, which can degrade the performance and longevity of particle detection equipment. Composite materials are inherently corrosion-resistant (*except in cases where composites are in contact with aluminium where galvanic corrosion might occur [45]*), reducing the risk of degradation due to environmental factors or chemical exposure. All these attributes contribute to the long-term stability and reliability of use of the composite material in particle detection systems.

### 6.3 Historical Development of Composites

The history of composites dates back to ancient times when humans started combining different materials to create stronger and more durable structures. Mud and straw were used by ancient Egyptians to make bricks, while mud and plant fibers were used in wattle and daub construction [43]. The development of synthetic resins in the late 19<sup>th</sup> and early 20<sup>th</sup> centuries played a crucial role in the advancement of composites [46]. Carleton Ellis patented unsaturated polyester resins in 1936, which became the primary choice for composites manufacturing due to their curing properties[46]. Epoxy resins were also introduced during this time. Bakelite, one of the first synthetic resins, was created by Leo Hendrik Baekeland in 1907, leading to the development of new and improved resins in the following decades [46]. The integration of glass fibers into composites became possible in the late 1930s, when techniques to produce thin glass strands for weaving into textile fabrics were developed [46]. Ray Greene used fiberglass and polyester resin to build a dinghy in 1942, which revolutionized the boating industry [46]. During World War II, the military's need for strong and durable materials led to further advancements in the composites industry. Composite wing spars made of wood layers and plastic resin were

used in Howard Hughes' Spruce Goose plane [46].

The popularity of composites grew rapidly in the 1950s, with various products such as boats, trucks, sports cars, storage tanks, pipes, and ducts being constructed using composites. Manufacturing techniques like pultrusion, vacuum bag molding, and filament winding were developed during this time [46]. Carbon fiber, patented in 1961, took a few more years to become commercially available but revolutionized applications in aerospace, automotive, marine, and consumer goods [46]. Kevlar, invented in 1966, became known for its use in ballistic and stab-resistant body armor [46]. The 2010s witnessed the rise of 3-D printing, which allowed for the incorporation of reinforced fibers into printed products. Carbon fiber and fiberglass strands were commonly used to reinforce plastics in industries such as aerospace, automotive, medicine, and infrastructure. This technology provided the strength of composites with reduced material usage and production time.

Today, the composites industry is looking to make a significant impact by leveraging the design flexibility, durability, low weight, and corrosion resistance of composites.

### 6.4 Use of composite from Mechanical point of view

For a prismatic beam subjected to axial load,  $P$ , the axial deflection,  $u$ , is given by

$$u = \frac{PL}{AE} \quad (6.1)$$

where,  $L$ = length of the beam and  $E$  = Young's modulus of elasticity of the material of the beam.

The mass,  $M$ , of the beam is given by

$$M = \rho AL, \quad (6.2)$$

$$M = \frac{PL^2}{4} \frac{1}{E/\rho} \quad (6.3)$$

where,  $\rho$  = density of the material of the beam.

This suggests that the beam with the highest value of  $(E/\rho)$  is the lightest beam that can achieve a specific deflection under a given load [42]. Therefore, in order to quantify the mechanical advantage, the  $(E/\rho)$  ratio is computed and referred to as the specific modulus. Another parameter, known as the specific strength, is defined as the ratio of the strength ( $\sigma_{ult}$ ) to the density of the material ( $\rho$ ), that is,

$$\text{Specific modulus} = \frac{E}{\rho} \quad (6.4)$$

$$\text{Specific strength} = \frac{\sigma_{ult}}{\rho} \quad (6.5)$$

Composite materials exhibit high values for both of these ratios. For instance, consider a graphite/epoxy unidirectional composite, which can have the same strength as steel but three times the specific strength. This means that even though the cross-sectional area of the graphite/epoxy rod is equivalent to that of the steel rod, the mass of the graphite/epoxy rod is only one third of the steel rod [42]. As a result, this reduction in mass leads to decreased material and cross-sectional properties. Figure 6.3 provides a comparison of composites and fibers with traditional materials in terms of specific strength.

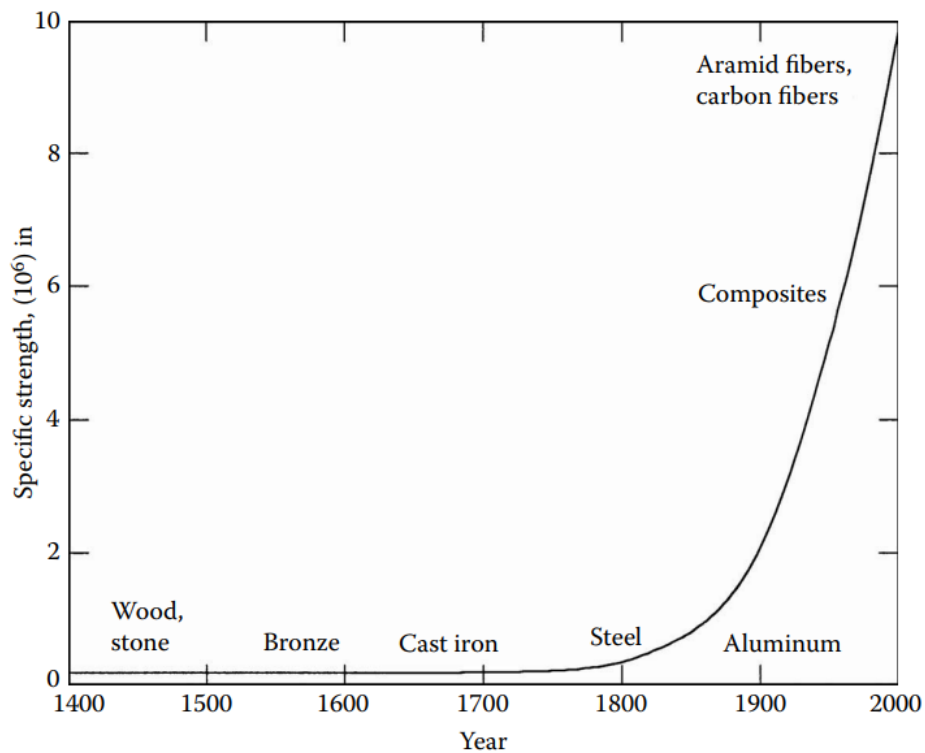


Figure 6.3: Specific strength as a function of time of use of materials. Adapted from Eager, T.W., *Whither advanced materials? Adv. Mater. Processes*, ASM International, June 1991, 25–29.

Material Units	Specific gravity	Young's modulus (GPa)	Ultimate strength (MPa)	Specific modulus (GPa-m <sup>3</sup> /kg)	Specific strength (MPa-m <sup>3</sup> /kg)
Graphite fiber	1.8	230.00	2067	127.8	1.148
Aramid fiber	1.4	124.00	1379	88.57	0.9850
Glass fiber	2.5	85.00	1550	34.0	0.6200
Unidirectional graphite/epoxy	1.6	181.00	1500	113.1	0.9377
Unidirectional glass/epoxy	1.8	38.60	1062	21.44	0.5900
Cross-ply graphite/epoxy	1.6	95.98	373.0	60.00	0.2331
Cross-ply glass/epoxy	1.8	23.58	88.25	13.10	0.0490
Quasi-isotropic graphite/epoxy	1.6	69.64	276.48	43.53	0.1728
Quasi-isotropic glass/epoxy	1.8	18.96	73.08	10.53	0.0406
Steel	7.8	206.84	648.1	26.52	0.08309
Aluminum	2.6	68.95	275.8	26.52	0.1061

Table 6.1: Specific Modulus and Specific Strength of Typical Fibers, Composites, and Bulk Metals. Adapted from Autar K Kaw. *Mechanics of composite materials*. CRC press, 2005 [47].

Table 6.1 presents specific modulus and strength values for different composite materials,

metals, and laminates. It should be noted that comparing fibers such as graphite and aramid with metals is not entirely equitable, since composites consist of both fibers and a matrix, with matrices generally having lower modulus and strength than fibers [47]. Unidirectional composites are primarily suitable for uniaxial tension or pure bending, and the strength and elastic moduli perpendicular to the fibers are significantly lower than those along the fiber direction [47]. This would be the case if we use the fibre in only one orientation. Therefore we adopt a ply stackup with a [0/0/90/0/0] orientation.

Similarly, for a constant length ( $L$ ) and load ( $P$ ) and Euler critical buckling load ( $P_{cr}$ ), the mass of the beam ( $M$ ) can be written as:

$$M = \frac{2L^2\sqrt{P_{cr}}}{\sqrt{\pi}} \frac{1}{E^{1/2}/\rho} \quad (6.6)$$

where,  $L$  is the length of the member, and  $E$  is the modulus of elasticity of the member.

This implies that, to achieve a specified stiffness, the lightest beam would have the highest value of  $E^{1/2}/\rho$  [47]. Similarly, it can be demonstrated that, for minimizing deflection in a beam under a load along its length, the lightest beam would have the highest value of  $E^{1/3}/\rho$  [47].

Material	Specific gravity	Young's modulus (GPa)	$E/\rho$ (GPa-m <sup>3</sup> /kg)	$E^{1/2}/\rho$ (Pa-m <sup>3</sup> /kg)	$E^{1/3}/\rho$ (Pa <sup>1/3</sup> -m <sup>3</sup> /kg)
Graphite fiber	1.8	230.00	127.80	266.4	3.404
Kevlar fiber	1.4	124.00	88.57	251.5	3.562
Glass fiber	2.5	85.00	34.00	116.6	1.759
Unidirectional graphite/epoxy	1.6	181.00	113.10	265.9	3.535
Unidirectional glass/epoxy	1.8	38.60	21.44	109.1	1.878
Cross-ply graphite/epoxy	1.6	95.98	60.00	193.6	2.862
Cross-ply glass/epoxy	1.8	23.58	13.10	85.31	1.593
Quasi-isotropic graphite/epoxy	1.6	69.64	43.53	164.9	2.571
Quasi-isotropic glass/epoxy	1.8	18.96	10.53	76.50	1.481
Steel	7.8	206.84	26.52	58.3	0.7582
Aluminum	2.6	68.95	26.62	101.0	1.577

Table 6.2: Mechanical properties of typical fibers and composites compared to steel and aluminum. Adapted from *Autar K Kaw. Mechanics of composite materials. CRC press, 2005 [47]*.

Table 6.2 provides typical values of these two parameters,  $E^{1/2}/\rho$  and  $E^{1/3}/\rho$ , for var-

ious materials such as fibers, unidirectional composites, cross-ply and quasi-isotropic laminates, steel, and aluminum. When comparing these values with metals, composites exhibit a greater advantage for these two parameters. Additional mechanical parameters for comparing the performance of composites to metals include fracture resistance, fatigue resistance, impact resistance, and creep resistance.

## 6.5 Fibres and Matrix

**Fibers** Fibers are composed of numerous filaments, each with a diameter ranging from 5 to 15 micrometers (Figure 6.4). Thin fibers are preferred as their strength decreases with increasing diameter. This is due to the fact that the likelihood of having inherent flaws in the fibre diminishes. While a steel plate may possess a strength of 689 MPa, a wire manufactured from the same steel plate can exhibit a strength as high as 4100 MPa [47]. On the other hand, smaller diameters enable a more effective radius of curvature in fiber bending, typically around half a millimeter[47]. Common fiber materials include Glass, Aramid or Kevlar (lightweight), Carbon (high modulus or high strength), Boron (high modulus or high strength), Silicon carbide (high temperature resistant), and more.

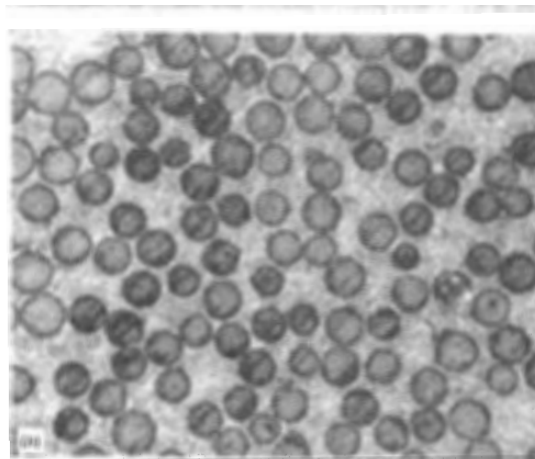


Figure 6.4: A cross-section of a unidirectional fibre of the composite embedded in matrix. Adapted from *Bhagwan D Agarwal, Lawrence J Broutman, and CW Bert. Analysis and performance of fiber composites. 1981*[42].

The fibers can have different orientations, including unidirectional, bidirectional, or multidirectional. Prior to being formed into reinforcements, the fibers undergo a surface treatment with two main objectives: reducing abrasion during the forming process and enhancing the adhesion between the fibers and the matrix material [48]. Carbon fiber, in particular, is utilized in applications that demand high performance. Carbon fiber production involves subjecting filaments made from polyacrylonitrile or pitch, derived from petroleum product residues, to a high-temperature oxidation process at approximately 300°C [45]. These filaments are then further heated to 1500°C in a nitrogen atmosphere. To achieve a high modulus of elasticity, the filaments are drawn at elevated temperatures [45]. Long fibers have enhanced impact resistance, minimal shrinkage, improved surface finish, and better dimensional stability [47]. On the other hand, short fibers are cheaper and have quick fabrication processes. As mentioned previously, they will have fewer flaws, resulting in higher strength.

**Matrix** The matrix serves to disperse the fibers and facilitate the transfer of the load onto the fibers. The matrix, although weaker than fibers, plays a crucial role in protecting and preserving the reinforcing elements from external factors such as moisture, chemicals, and physical damage. Matrices typically possess lower mechanical properties compared to fibers and the interaction between fibres and matrix affects the overall properties of the composite. The selection of a proper matrix is based upon the compatibility with the reinforcement and performance criterion such as transverse modulus and strength, shear modulus and strength, compressive strength, interlaminar shear strength, thermal expansion coefficient, thermal resistance, and fatigue strength. The materials used in composite matrix can be classified into three main categories:

i) Polymeric matrix: These are composed of thermoplastic resins (such as polypropylene, polyphenylene sulfone, polyamide, polyetheretherketone, etc.) and thermoset resins (including polyesters, phenolics, melamines, silicones, polyurethanes, epoxies) [45]. These materials provide a range of properties and can be tailored to specific application requirements. Epoxy carbon prepreg typically consists of an polymeric epoxy resin matrix



which is a thermosetting polymer that serves as the binding material, providing structural integrity and adhesion between the carbon fibers (Figure 6.5).

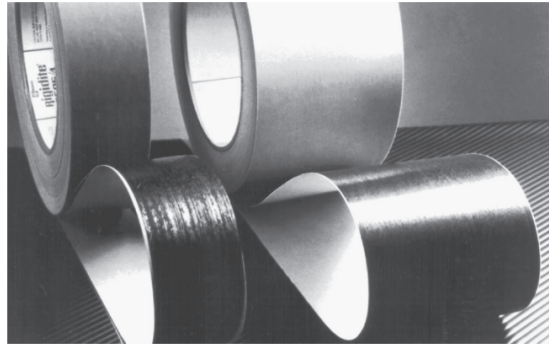


Figure 6.5: Epoxy Prepregs pre-manufactured as tapes (76 to 1270 mm) consisting of fibers embedded in a polymer matrix . Adapted from *Autar K Kaw. Mechanics of composite materials. CRC press, 2005 [47]*.

ii) Mineral matrix: This category includes materials like silicon carbide and carbon. These mineral-based matrices offer excellent performance at high temperatures, making them suitable for applications that involve extreme thermal conditions.

iii) Metallic matrix: Metallic matrices consist of materials such as aluminum alloys, titanium alloys, and oriented eutectics. These matrices are primarily used in applications where high strength and stiffness are required, along with good thermal conductivity and compatibility with metal-based components.

## 6.6 Physical Properties of Composite materials

Composite materials exhibit unique characteristics that arise from the combination of reinforcement fibres and matrix components (Figure 6.6). The final properties of composites are influenced by several factors, including the proportions of reinforcements and matrix, the form of the reinforcement, and the fabrication process employed.

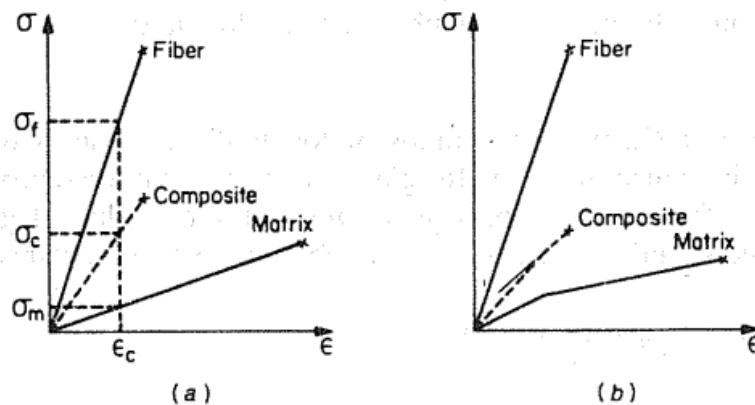


Figure 6.6: Longitudinal stress-strain diagrams for a composite with (a) linear and (b) nonlinear matrix material. *Bhagwan D Agarwal, Lawrence J Broutman, and CW Bert. Analysis and performance of fiber composites. 1981[42].*

The proportions of reinforcements and matrix play a crucial role in determining the overall behavior of composites. The volume fraction of reinforcements affects properties such as strength, stiffness, and durability. Different volume fractions can be selected to achieve specific performance requirements. The form of the reinforcement also impacts the characteristics of composites. Reinforcements can be in the form of fibers, particles, flakes, or other geometries. The geometry and arrangement of the reinforcements influence properties such as strength, stiffness, and impact resistance. The fabrication process employed during the manufacturing of composites significantly affects their final properties. Processes such as hand lay-up, filament winding, pultrusion, and resin transfer molding can be used to tailor the properties of the composite material [49]. Factors such as curing temperature, pressure, and curing time can be controlled to achieve desired characteristics.

In addition to these factors, composite materials possess other notable properties. Firstly, composites do not exhibit a yield point, meaning their elastic limits correspond to the rupture limit. This characteristic allows composites to withstand high stress levels before failure. Secondly, composite materials exhibit excellent fatigue resistance, making them suitable for applications subjected to repeated loading and cyclic stress. Composite ma-

materials can be affected by environmental factors such as humidity and heat. Epoxy resins, commonly used as matrices, can absorb water through diffusion, resulting in dimensional changes and potential degradation of properties. However, composites generally do not corrode, except in cases where there is contact between aluminum and carbon fibers, leading to galvanic corrosion. Composites are generally resistant to common chemicals used in engines, including grease, oils, hydraulic fluids, paints, solvents, and petroleum. However, epoxy resins used in composites can be susceptible to attack by paint thinners[45]. Regarding impact resistance, composites generally have medium to low levels compared to metallic materials. While composites possess excellent fire resistance when compared to lightweight alloys of the same thickness, certain matrix materials used in composites can produce toxic smoke during combustion. The properties of composite materials are therefore influenced by various factors, and careful consideration of these factors is necessary to tailor the composites for specific applications. The combination of unique characteristics, including high strength, stiffness, fatigue resistance, corrosion resistance, and fire resistance, makes composites versatile materials suitable for a wide range of industries and applications.

### **6.7 Macromechanical Analysis of composite lamina**

A lamina is a thin layer of a composite material, typically with a thickness around 0.005 inches (0.125 mm)[47]. By stacking multiple laminae together in the direction of the lamina thickness, a laminate structure is created (see Figure 6.7). When analyzing a lamina from a macroscopic perspective, we focus on its overall mechanical behavior rather than examining the individual components such as fibers and matrix. The mechanical properties of a lamina are influenced by the properties of its constituents (fibers and matrix) and how they are arranged within the lamina. However, it's important to note that mechanical properties can vary throughout the lamina due to differences in fiber properties, matrix properties, or the properties of the fiber-matrix interface.

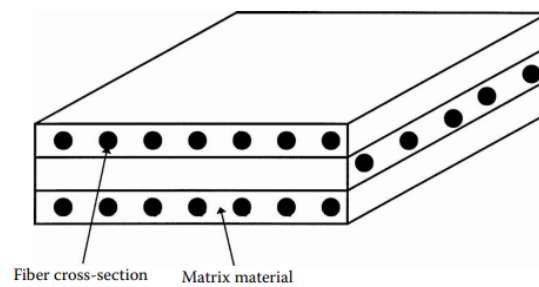


Figure 6.7: Typical laminate made up of three laminae. The direction of the fibers can be changed in each individual layer to adapt for the load bearing capacity. Adapted from *Autar K Kaw. Mechanics of composite materials. CRC press, 2005 [47]*.

Analyzing the mechanical behavior of a lamina at a microscopic level can be challenging due to these property variations. Consequently, macromechanical analysis is conducted by treating the lamina as a homogeneous material with average properties. This approach overcomes the complexity of considering point-to-point variations within the lamina. The average properties are determined either through experimental testing or analytical methods, taking into account factors such as the type, orientation, and volume fraction of fibers in the lamina, as well as the properties of the matrix material. By modelling the lamina as a simple material with uniform mechanical properties, the macromechanical analysis enables the prediction of its response to external loads. This simplification allows engineers and researchers to analyze and design laminates with greater ease and efficiency, based on the average properties of the constituent laminae.

### Isotropy and Anisotropy

The mechanical response of elastic bodies under load can be investigated by applying principles derived from elasticity theory. When an elastic body is subjected to stresses, it will exhibit reversible deformation. At any given point within the body, specific principal planes can be identified where only normal stresses are present. These principal stress directions are characterized by their respective normal directions. Additionally, when a small sphere of material surrounding a point in the body is loaded, it will transform into an ellipsoid. By considering the spatial relationship between the ellipsoid and the principal stress directions, it is possible to determine whether the material being studied is isotropic (possessing uniform properties in all directions) or anisotropic (exhibiting varying properties based on direction). This concept is visually depicted in Figure 6.8.

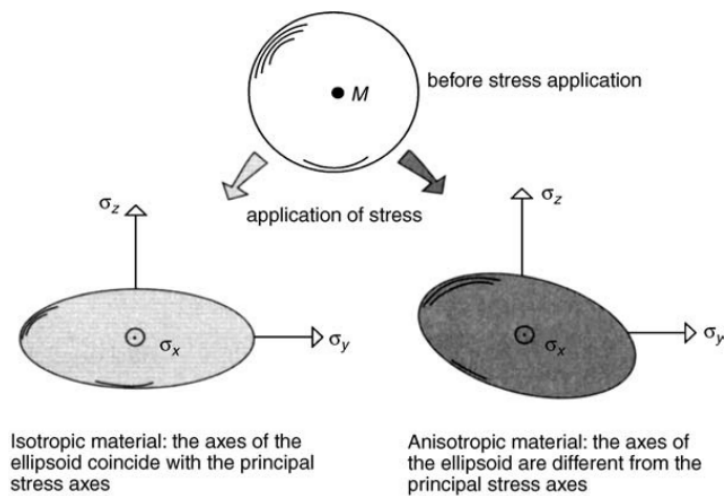


Figure 6.8: Schematic of deformation in isotropic and anisotropic material. Adapted from Daniel Gay. *Composite materials: design and applications*. CRC press, 2022[45].

The deformation characteristics of both isotropic and anisotropic samples is illustrated in Figure 6.9. In the figure, the oblique lines represent the preferred directions for fiber reinforcement. When a longitudinal load is applied to an isotropic plate, it will undergo extension in the longitudinal direction and contraction in the transverse direction. On the other hand, an anisotropic plate subjected to the same loading will not only experience

longitudinal extension and transverse contraction but also angular distortion.

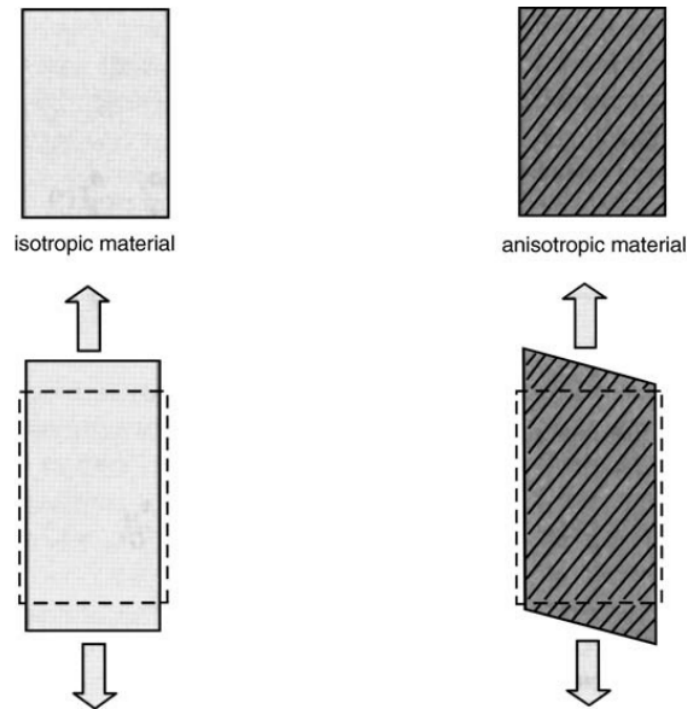


Figure 6.9: Schematic of deformation in isotropic and anisotropic material. Adapted from Daniel Gay. *Composite materials: design and applications*. CRC press, 2022 [45].

## 6.8 Hooke's law for Anisotropic, Orthotropic and Transversely isotropic material

While it is acceptable to assume that composite materials display linear and elastic behavior, it is important to acknowledge that these materials do not possess isotropic characteristics. Hence, the stress-strain relationship for such materials needs to be considered in the context of anisotropic, orthotropic, or transversely isotropic properties.

Unlike isotropic materials, which have uniform properties in all directions, composites exhibit anisotropic behavior due to the presence of distinct components with varying

properties. The mechanical response of composite materials is highly influenced by the arrangement, orientation, and distribution of reinforcing fibers within the matrix. As a result, their mechanical properties, such as stiffness and strength, can vary significantly depending on the direction of applied forces. It is crucial to consider this anisotropic nature when analyzing and designing composite structures to ensure accurate predictions of their mechanical behavior and to optimize their performance for specific applications. The stress-strain relationship for a three-dimensional body in a 1–2–3 orthogonal Cartesian coordinate system is given by:

$$\begin{bmatrix} \sigma_1 \\ \sigma_2 \\ \sigma_3 \\ \sigma_{12} \\ \sigma_{13} \\ \sigma_{23} \end{bmatrix} = \begin{bmatrix} C_{11,11} & C_{11,22} & C_{11,33} & C_{11,12} & C_{11,13} & C_{11,23} \\ C_{22,11} & C_{22,22} & C_{22,33} & C_{22,12} & C_{22,13} & C_{22,23} \\ C_{33,11} & C_{33,22} & C_{33,33} & C_{33,12} & C_{33,13} & C_{33,23} \\ C_{12,11} & C_{12,22} & C_{12,33} & C_{12,12} & C_{12,13} & C_{12,23} \\ C_{13,11} & C_{13,22} & C_{13,33} & C_{13,12} & C_{13,13} & C_{13,23} \\ C_{23,11} & C_{23,22} & C_{23,33} & C_{23,12} & C_{23,13} & C_{23,23} \end{bmatrix} \begin{bmatrix} \epsilon_1 \\ \epsilon_2 \\ \epsilon_3 \\ \epsilon_{12} \\ \epsilon_{13} \\ \epsilon_{23} \end{bmatrix} \quad (6.7)$$

where  $\sigma_i$  and  $\epsilon_i$  represent the stress and strain components in the  $i$ -th direction, respectively, and  $\sigma_{ij}$  and  $\epsilon_{ij}$  represent the stress and strain components in the  $i$ - $j$  plane, respectively. The  $6 \times 6$  matrix  $[C]$  is the stiffness matrix, which contains a total of 36 constants.

An anisotropic material is characterized by its directional dependence of properties, meaning that its mechanical characteristics, including stiffness, strength, and other properties, vary based on the direction of measurement. Unlike isotropic materials, which have identical properties in all directions, anisotropic materials exhibit different responses to applied forces along different axes. This variation in material properties can be attributed to the presence of internal structures, such as aligned fibers or crystals, that impart directional behavior to the material. When studying the mechanical behavior of an anisotropic material, a matrix format is often used to represent the stress-strain relationship. This matrix format allows for the representation of different material properties corresponding

to different directions or axes. By considering the anisotropic nature of the material, engineers and researchers can accurately analyze and predict its behavior under different loading conditions, enabling them to design structures that effectively utilize the material's unique properties in specific directions.

The stress-strain relationship for an anisotropic material is given by:

$$\begin{bmatrix} \sigma_1 \\ \sigma_2 \\ \sigma_3 \\ \sigma_{12} \\ \sigma_{13} \\ \sigma_{23} \end{bmatrix} = \begin{bmatrix} c_{11} & c_{12} & c_{13} & c_{14} & c_{15} & c_{16} \\ c_{12} & c_{22} & c_{23} & c_{24} & c_{25} & c_{26} \\ c_{13} & c_{23} & c_{33} & c_{34} & c_{35} & c_{36} \\ c_{14} & c_{24} & c_{34} & c_{44} & c_{45} & c_{46} \\ c_{15} & c_{25} & c_{35} & c_{45} & c_{55} & c_{56} \\ c_{16} & c_{26} & c_{36} & c_{46} & c_{56} & c_{66} \end{bmatrix} \begin{bmatrix} \epsilon_1 \\ \epsilon_2 \\ \epsilon_3 \\ \epsilon_{12} \\ \epsilon_{13} \\ \epsilon_{23} \end{bmatrix} \quad (6.8)$$

where  $\sigma_i$  and  $\epsilon_i$  represent the stress and strain components in the  $i$ -th direction, respectively, and  $\sigma_{ij}$  and  $\epsilon_{ij}$  represent the stress and strain components in the  $i$ - $j$  plane, respectively. The  $6 \times 6$  matrix contains a total of 21 independent material constants, which describe the material properties in different directions.

An orthotropic material is characterized by having three mutually perpendicular planes of symmetry, where each plane exhibits distinct material properties. This means that the mechanical behavior of the material varies in three orthogonal directions, while remaining consistent within each specific plane. Unlike isotropic materials, which have the same properties in all directions, and anisotropic materials, which exhibit directional dependence without specific planes of symmetry, orthotropic materials have a well-defined pattern of material properties. The distinct properties in each direction arise from the structural arrangement of the material, such as aligned fibers or grains, which give rise to different stiffness, strength, and other mechanical characteristics. When studying the mechanical response of an orthotropic material, a matrix format is commonly used to represent the stress-strain relationship. This matrix allows for the description of different



material properties corresponding to the three mutually perpendicular directions. The stress-strain relationship for an orthotropic material is given by:

$$\begin{bmatrix} \sigma_1 \\ \sigma_2 \\ \sigma_3 \\ \tau_{23} \\ \tau_{31} \\ \tau_{12} \end{bmatrix} = \begin{bmatrix} c_{11} & c_{12} & c_{13} & 0 & 0 & 0 \\ c_{12} & c_{22} & c_{23} & 0 & 0 & 0 \\ c_{13} & c_{23} & c_{33} & 0 & 0 & 0 \\ 0 & 0 & 0 & c_{44} & 0 & 0 \\ 0 & 0 & 0 & 0 & c_{55} & 0 \\ 0 & 0 & 0 & 0 & 0 & c_{66} \end{bmatrix} \begin{bmatrix} \epsilon_1 \\ \epsilon_2 \\ \epsilon_3 \\ \gamma_{23} \\ \gamma_{31} \\ \gamma_{12} \end{bmatrix} \quad (6.9)$$

where  $\sigma_i$  and  $\epsilon_i$  represent the stress and strain components in the  $i$ -th direction, respectively, and  $\tau_{ij}$  and  $\gamma_{ij}$  represent the shear stress and strain components in the  $i$ - $j$  plane, respectively. The  $6 \times 6$  matrix contains a total of 9 independent material constants, which describe the material properties in different directions and planes.

A transversely isotropic material is a specific type of orthotropic material that possesses a unique symmetry configuration. In this case, one plane of symmetry is perpendicular to the other two planes (as shown in Figure 6.10). Consequently, the material properties exhibit uniformity in two directions while differing in the third direction and the plane that is perpendicular to it. This arrangement gives rise to distinctive mechanical behaviors along these directions. The stress-strain relationship of a transversely isotropic material comprises five independent elastic constants and is given by:

$$\begin{bmatrix} \sigma_1 \\ \sigma_2 \\ \sigma_3 \\ \tau_{23} \\ \tau_{31} \\ \tau_{12} \end{bmatrix} = \begin{bmatrix} c_{11} & c_{12} & c_{12} & 0 & 0 & 0 \\ c_{12} & c_{22} & c_{23} & 0 & 0 & 0 \\ c_{12} & c_{23} & c_{22} & 0 & 0 & 0 \\ 0 & 0 & 0 & \frac{c_{22}-c_{23}}{2} & 0 & 0 \\ 0 & 0 & 0 & 0 & c_{55} & 0 \\ 0 & 0 & 0 & 0 & 0 & c_{55} \end{bmatrix} \begin{bmatrix} \epsilon_1 \\ \epsilon_2 \\ \epsilon_3 \\ \gamma_{23} \\ \gamma_{31} \\ \gamma_{12} \end{bmatrix} \quad (6.10)$$

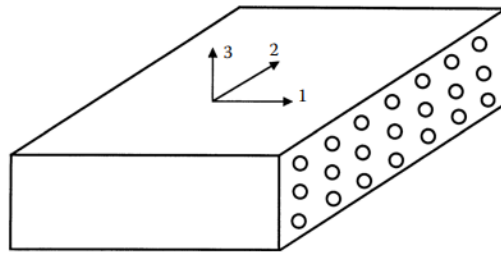


Figure 6.10: A unidirectional lamina as a transversely isotropic material with fibers arranged in a square array. Adapted from *Autar K Kaw. Mechanics of composite materials. CRC press, 2005 [47]*.

## 6.9 Hooke's Law for a Two-Dimensional Unidirectional Lamina: Plane stress Assumption

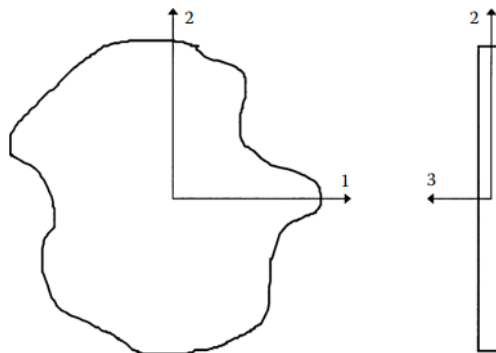


Figure 6.11: Plane stress conditions for a thin plate. Adapted from *Autar K Kaw. Mechanics of composite materials. CRC press, 2005 [47]*.

A thin plate is a prismatic member with small thickness and can be considered under plane stress if there are no out-of-plane loads (Figure 6.11) . If the upper and lower surfaces of the plate are free from external loads, then three of the stresses ( $\sigma_3, \tau_{31}, \tau_{23}$ ) can be assumed to be zero within the plate as they vary little in magnitude from the stresses at the top and bottom surfaces. This allows the three-dimensional stress-strain equations to be reduced to two-dimensional stress-strain equations. This assumption also applies to

lamina.

A unidirectional lamina falls under the orthotropic material category. If the lamina is thin and does not carry any out-of-plane loads, one can assume plane stress conditions for the lamina. Therefore, assuming  $\sigma_3 = 0$ ,  $\tau_{23} = 0$ , and  $\tau_{31} = 0$ , then the normal strain,  $\varepsilon_3$ , can be omitted from the stress-strain relationship. Also, the shearing strains,  $\gamma_{23}$  and  $\gamma_{31}$ , can be omitted because they are zero. For an orthotropic plane stress problem can then be written as

$$\begin{bmatrix} \sigma_1 \\ \sigma_2 \\ \tau_{12} \end{bmatrix} = \begin{bmatrix} S_{11} & S_{12} & 0 \\ S_{21} & S_{22} & 0 \\ 0 & 0 & S_{66} \end{bmatrix} \begin{bmatrix} \varepsilon_1 \\ \varepsilon_2 \\ \gamma_{12} \end{bmatrix}, \quad (6.11)$$

where  $S_{ij}$  are the elements of the compliance matrix. Inverting Equation (6.11) gives the stress-strain relationship as

$$\begin{bmatrix} \varepsilon_1 \\ \varepsilon_2 \\ \gamma_{12} \end{bmatrix} = \begin{bmatrix} Q_{11} & Q_{12} & 0 \\ Q_{21} & Q_{22} & 0 \\ 0 & 0 & Q_{66} \end{bmatrix} \begin{bmatrix} \sigma_1 \\ \sigma_2 \\ \tau_{12} \end{bmatrix}, \quad (6.12)$$

where  $Q_{ij}$  are the reduced stiffness coefficients, which are related to the compliance coefficients as

$$\begin{aligned} \begin{bmatrix} Q_{11} & Q_{12} & 0 \\ Q_{12} & Q_{22} & 0 \\ 0 & 0 & Q_{66} \end{bmatrix} &= \begin{bmatrix} S_{11} & S_{12} & 0 \\ S_{12} & S_{22} & 0 \\ 0 & 0 & S_{66} \end{bmatrix}^{-1} \\ &= \frac{1}{S_{11}S_{22} - S_{12}^2} \begin{bmatrix} S_{22} & -S_{12} & 0 \\ -S_{12} & S_{11} & 0 \\ 0 & 0 & S_{66} \end{bmatrix} \end{aligned} \quad (6.13)$$

$$\begin{aligned}
 Q_{11} &= \frac{1}{S_{11}} \\
 Q_{22} &= \frac{1}{S_{22}} \\
 \text{And for the reduced stiffness coefficients :} \\
 Q_{12} = Q_{21} &= -\frac{S_{12}}{S_{11}S_{22} - S_{12}^2} \\
 Q_{66} &= \frac{1}{S_{66}}
 \end{aligned}$$

## 6.10 Hooke's Law for a Two-Dimensional Angle Lamina

An angle lamina is a composite material made up of layers positioned at an angle to enhance rigidity and strength in the transverse direction [50]. The lamina is described using a coordinate system where the material axes align with the 1-2 coordinates, while the global off-axes align with the x-y coordinates, forming an angle denoted as  $\theta$ . The stress-strain behavior in the local 1-2 coordinate system has already been established, and now the relationship for the global x-y coordinate system is being developed. This is achieved through the use of a transformation matrix denoted as  $[T]$ , defined as  $[T] = [T(\theta)]$ . The specific form of the  $[T(\theta)]$  matrix is as follows:

$$[T(\theta)] = \begin{bmatrix} c^2 & s^2 & -2sc \\ s^2 & c^2 & 2sc \\ sc & -sc & c^2 - s^2 \end{bmatrix} \quad (6.14)$$

where,  $c = \cos \theta$  and  $s = \sin \theta$ . The transformation matrix can be used to convert the local stresses to global stresses or vice versa, using the relationship:

$$\begin{bmatrix} \sigma_x \\ \sigma_y \\ \tau_{xy} \end{bmatrix} = [T] \begin{bmatrix} \sigma_1 \\ \sigma_2 \\ \tau_{12} \end{bmatrix} \quad (6.15)$$

where, global stresses are denoted by  $\sigma_x$ ,  $\sigma_y$ , and  $\tau_{xy}$ , and the local stresses are denoted by  $\sigma_1$ ,  $\sigma_2$ , and  $\tau_{12}$ . To convert global stresses into local stresses, the inverse of the

transformation matrix is utilized. In the stress-strain relationship of a unidirectional lamina aligned with the material axes, there is no interaction between the normal and shearing terms of strains and stresses. However, in the case of an angle lamina, there is coupling between the normal and shearing terms of strains and stresses. When only normal stresses are applied to an angle lamina, non-zero shear strains occur, while non-zero normal strains arise when only shearing stresses are applied. This behavior gives rise to a lamina that is generally orthotropic in nature.

## 6.11 Micromechanical Analysis of Composites

The development of the macroscopic representation of the unidirectional composite involves using 13 distinct parameters that can be obtained through experimental means. Nonetheless, conducting all the required tests to determine these parameters can be costly and time-consuming. Consequently, analytical models are created to estimate these parameters by considering the specific characteristics of the composite's components, such as the fiber volume fraction, packing arrangement, and other relevant factors. This methodology, referred to as micromechanics of lamina, aids designers in choosing the most suitable composite material for a particular application.

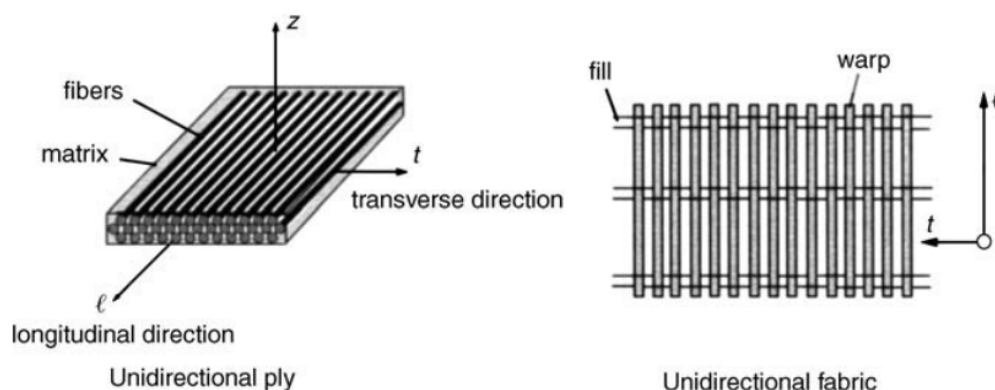


Figure 6.12: Orientation of the fibre in a unidirectional composite. Adapted from *Daniel Gay. Composite materials: design and applications. CRC press, 2022 [45]*.

**Elastic Modulus** The mechanical characteristics of the fiber/matrix mixture can be obtained based on the characteristics of each of the constituents. In the literature, there are theoretical as well as semi-empirical relations. As such, the results from these relations may not always agree with experimental values. This is due to the fact that the fibers themselves exhibit some degree of anisotropy.

**Modulus of elasticity along the direction of the fiber,  $E_\ell$**  (see Figure 6.12) is given by

$$E_\ell = E_f V_f + E_m V_m \quad (6.16)$$

or

$$E_\ell = E_f V_f + E_m (1 - V_f) \quad (6.17)$$

In practical terms, the modulus mentioned relies primarily on the longitudinal modulus of the fiber,  $E_f$ , because  $E_m \ll E_f$ .

**Modulus of elasticity in the transverse direction to the fiber axis,  $E_t$**  :

$$E_t = E_m \left[ \frac{1}{(1 - V_f) + \frac{E_m}{E_{ft}} V_f} \right] \quad (6.18)$$

where,  $E_{ft}$  represents the modulus of elasticity of the fiber in the direction that is transverse to the fiber axis.

**Shear modulus  $G_{\ell t}$**  :

$$G_{\ell t} = G_m \left[ \frac{1}{(1 - V_f) + \frac{G_m}{G_{ft}} V_f} \right] \quad (6.19)$$

where,  $G_{ft}$  represents the shear modulus of the fiber.

**Poisson coefficient  $\nu_{\ell t}$**  : The Poisson coefficient exhibits the contraction in the transverse direction  $t$  when a tensile load is applied in a longitudinal direction  $\ell$  (see Figure 6.12).

$$\nu_{\ell t} = \nu_f V_f + \nu_m V_m \quad (6.20)$$

**Modulus along any direction:** The modulus along any direction in plane  $lt$ , where  $c = \cos \theta$  and  $s = \sin \theta$ . This modulus decreases as we move away from the fiber direction (see Figure 6.14).

$$E_x = \frac{1}{\frac{c^4}{E_\ell} + \frac{s^4}{E_t} + 2c^2s^2 \left( \frac{1}{2G_{lt}} - \frac{\nu_{lt}}{E_t} \right)} \quad (6.21)$$

**Ultimate Strength of a Ply** Figure 6.13 illustrates the noteworthy differences in responses to load between metallic materials and unidirectional plies.

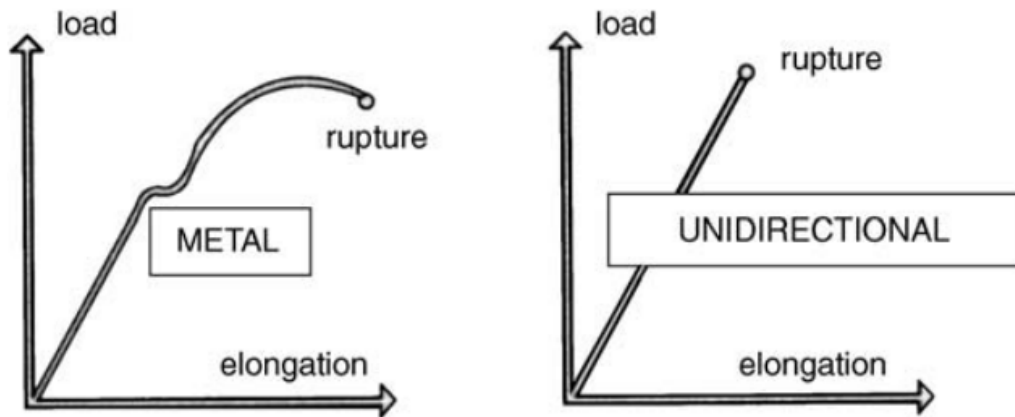


Figure 6.13: Loading Curves of Metal and Unidirectional Composite. Adapted from Daniel Gay. *Composite materials: design and applications*. CRC press, 2022[45].

Unidirectional plies exhibit a lack of plastic deformation, which is considered a disadvantage as it limits their ability to withstand and recover from deformation. On the other hand, the ultimate strength of unidirectional plies is higher compared to classical metallic materials, providing an advantage in terms of load-bearing capacity. Additionally, unidirectional plies demonstrate significant elastic deformation, which can be both advantageous or disadvantageous depending on the application. For instance, this characteristic proves beneficial in the design of springs, arcs, or poles. Moreover, in scenarios where the fibers within the composite fracture before the matrix during loading along the fiber

direction, the composite material exhibits certain properties, which require further elaboration and clarification. When the fibers break before the matrix during loading along the fiber direction, one can obtain the following for the composite:

$$\sigma_{\ell \text{ rupture}} = \sigma_{f \text{ rupture}} \left[ V_f + (1 - V_f) \frac{E_m}{E_f} \right] \quad (6.22)$$

or, approximately

$$\sigma_{\ell \text{ rupture}} \approx \sigma_{f \text{ rupture}} \times V_f \quad (6.23)$$

The ultimate strength of the unidirectional ply along any direction can be computed from the following relationship (see Figure 6.14)

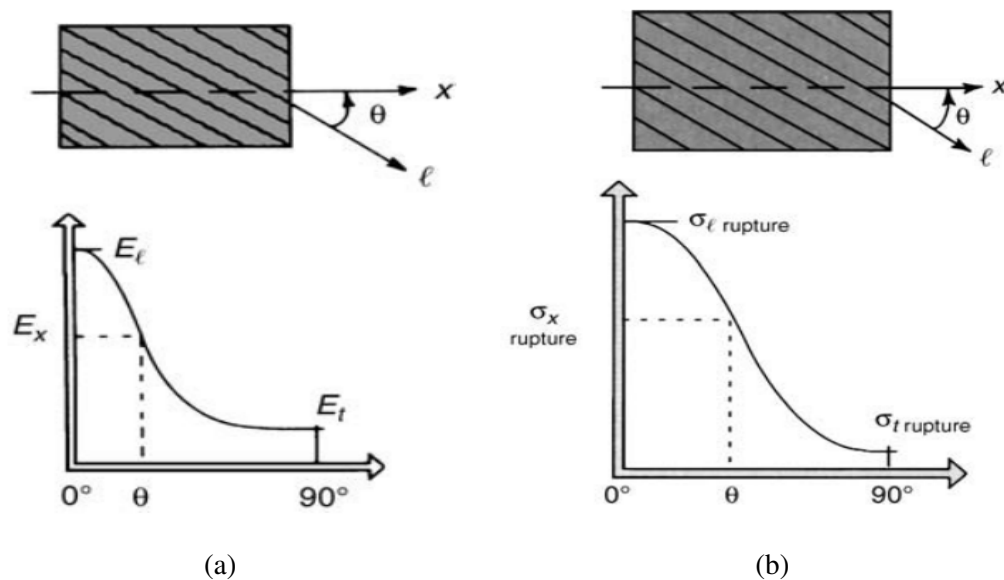


Figure 6.14: a) Off axis modulus of the composite. b) Off axis rupture strength of composite. Adapted from *Daniel Gay. Composite materials: design and applications. CRC press, 2022 [45].*



$$c = \cos \theta \quad (6.24a)$$

$$s = \sin \theta \quad (6.24b)$$

$$\sigma_{\text{rupture } x} = \frac{1}{\sqrt{\frac{c^4}{\sigma_\ell^2} + \frac{s^4}{\sigma_t^2} + \left(\frac{1}{\tau_{\ell t}^2} - \frac{1}{\sigma_l^2}\right) c^2 s^2}} \quad (6.25)$$

where,  $\sigma_l$  = Fracture strength in the direction of the fibers,

$\sigma_t$  = Fracture strength transverse to the direction of the fibers,

$\tau_{\ell t}$  = Shear strength in the plane ( $\ell, t$ ) of the ply

Also it can be noted that the compression strength along the longitudinal direction is smaller than the tensile strength along the same direction due to the micro buckling phenomenon of the fibers in the matrix [51].

## 6.12 Design of composite

When designing composite materials, it is essential to consider the functional requirements of the component and select the suitable reinforcement (usually fibers), matrix, and curing method to meet those requirements. Once the materials and process are determined, the designer must then define the architecture of the component, which involves specifying the arrangement and dimensions of the plies, consisting of layers of fibers and matrix. This step is crucial because the orientation of the fibers plays a vital role in optimizing the mechanical behavior of the component in a particular direction. Again we emphasize that composites differ from traditional metallic materials as they exhibit elastic behavior until rupture, lacking the ability to undergo local plastic deformation. Moreover, composites generally demonstrate excellent fatigue resistance.

Composite Type	Load Durability Rating
Static loading short duration	2
Static loading long duration	4
Intermittent loading over long term	4
Cyclic loading	5
Impact loading	10
High Performance	1.3 to 1.8

Table 6.3: Load Durability Ratings for High Volume and High Performance Composites. Adapted from *Daniel Gay. Composite materials: design and applications. CRC press, 2022[45]*.

To address uncertainties in the design process, the designer must incorporate safety factors, as outlined in Table 6.3. These factors account for uncertainties related to the mechanical properties of the reinforcement and matrix, stress concentrations, assumptions made during calculations, fabrication processes, and material aging. By considering these factors, the designer can ensure the component's safe and effective performance throughout its intended lifespan.

**Unidirectional Layers and fibers** Unidirectional layers provide high rigidity, efficient load transmission over long distances, and minimal material waste. However, they do have drawbacks, such as longer wrapping time and limited ability to cover complex shapes through wrapping techniques [52]. On the other hand, fabrics in composite materials contain fibers oriented in multiple directions, allowing for the shaping of intricate forms by deforming the fabric. Fabrics also offer the flexibility to combine different types of fibers within the same material. However, compared to unidirectional layers, fabrics typically have lower modulus and strength, resulting in larger amounts of waste material during the cutting process. Additionally, when using fabrics to wrap larger components, the inclusion of joints becomes necessary for proper coverage.

**Orientation of the fiber direction** Laminates possess a significant advantage when it comes to their capacity to adjust and manage the orientation of fibers, thereby enhancing their ability to withstand various loads. Understanding how the layers of the laminate contribute to its resistance is crucial, particularly in relation to their relative alignment with the direction of the applied load. Figure 6.15 illustrates both favorable and unfavorable scenarios in this regard. The concept can be further clarified by utilizing the Mohr circle, as demonstrated in the stress state depicted in Figure 6.15.

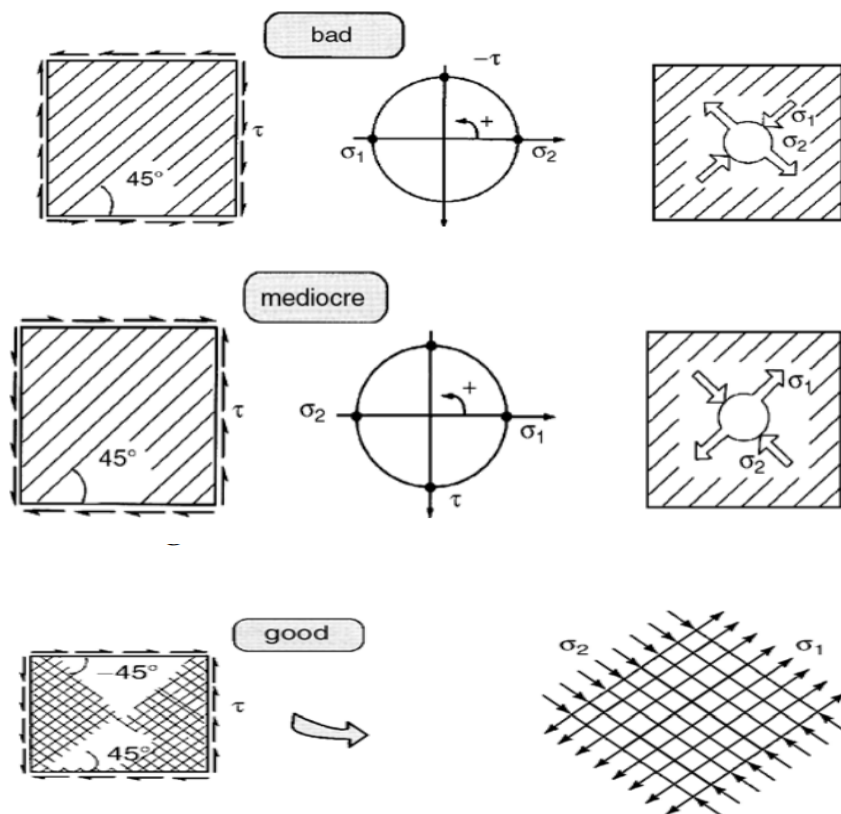


Figure 6.15: Effect of Ply orientation on composite structures. Adapted from *Daniel Gay. Composite materials: design and applications. CRC press, 2022[45]*.

In the first case, the  $45^\circ$  fibers are subjected to compression, and the resin is subjected to tension which has a relatively low fracture threshold. This is a bad design. In second figure, the fibers withstand tension, while the resin is subjected to compression. This can be a mediocre approach to design composite structures. In the last figure, fibers are positioned

at  $45^\circ$  and  $-45^\circ$  angles. Observations indicate that the  $45^\circ$  fibers can endure tension, whereas the  $-45^\circ$  fibers can withstand compression. Additionally, the resin experiences a reduced load compared to the previous scenarios. From composite design perspective, this is a good design approach [45].

**Middle Plane Symmetry** Midplane symmetry is a characteristic of laminated composites where the arrangement of layers on both sides of the central plane is identical. Essentially, this means that the composite is symmetrical with respect to the middle plane. Adoption of  $[0/0/90/0/0]$  ply orientation in our case complies with the middle plane symmetry. The significance of midplane symmetry in composite materials lies in its ability to prevent warping or distortion of the component during the cooling process.

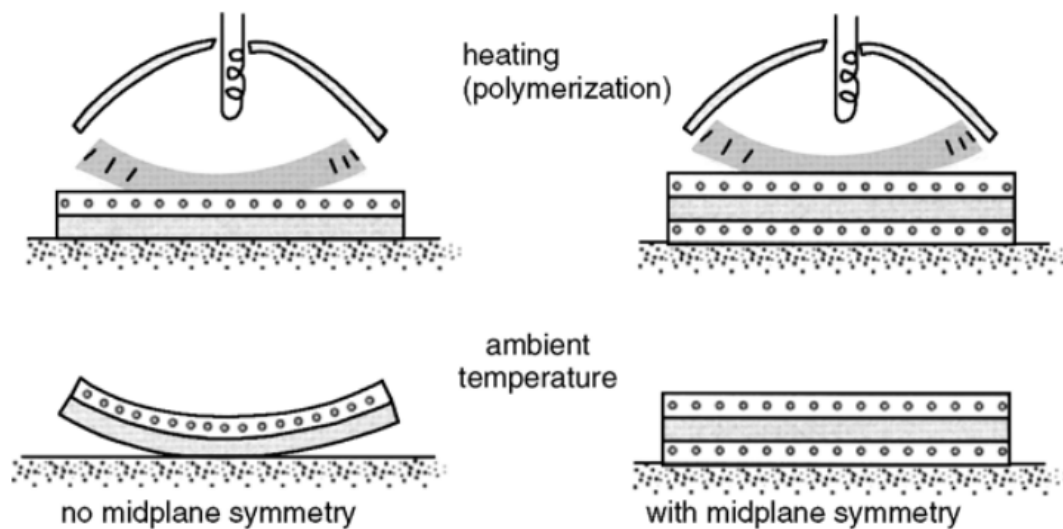


Figure 6.16: Effect of laminate lay up on the deformation. Adapted from *Daniel Gay. Composite materials: design and applications. CRC press, 2022*[45].

When composite laminates are cured, the layers are stacked at room temperature and then placed in an autoclave for the curing process. At high temperatures, the entire laminate expands uniformly without warping. However, during cooling, the individual layers contract differently based on their orientations, resulting in residual thermal stresses

(see Figure 6.16). These stresses can lead to warping or deformation of the component. By employing midplane symmetry, these stresses are imposed with symmetry, thereby averting deformations of the overall component, such as warping. Therefore, midplane symmetry holds significant importance in the design and manufacturing of laminated composite parts to ensure that they retain their desired shape and dimensions after the curing process.

### **6.13 Numerical modelling of composite structures: Micro, Macro and Meso level Approach**

When analyzing composite materials, there are different approaches available depending on the level of detail required. The most comprehensive method involves examining the microstructure of the composite. This means considering factors such as the shape and location of the fibers within the composite, as well as the properties of both the matrix material and the reinforcement materials. By analyzing the microstructure, one can gain insights into the behavior and performance of the composite material.

On the other hand, for simpler analysis that focus on specific aspects like displacements, buckling loads, or vibration frequencies and modes, a macro-scale approach can be employed. This approach treats the composite material as a homogeneous shell, assuming that its properties are uniform throughout. This simplification allows for easier calculations and analysis of these specific phenomena.

However, when it comes to analyzing strains, stresses, and failure criteria of a composite laminate, a meso-scale approach is necessary [52]. A composite laminate is made up of multiple layers of different materials, each with its own thickness and material properties. In the meso-scale approach, each layer of the composite is modelled individually, taking into account its specific characteristics. This requires detailed knowledge of the thickness and material properties of each layer. To facilitate this meso-scale analysis, we

use ANSYS Composite PrepPost (ACP). This software is specifically designed to prepare the composite design for analysis and evaluate the results obtained using the meso-scale approach. It assists in setting up the simulation, modelling the individual layers, and analyzing the composite laminate's behavior.

### 6.13.1 ANSYS Composite PrepPost Workflows

ANSYS Composite PrepPost (ACP) is an add-in that seamlessly integrates with ANSYS Workbench, providing essential analysis capabilities for modeling complex composite structures. These structures can involve multiple layers, materials, thicknesses, and orientations. This integration allows for a comprehensive approach throughout the entire process, encompassing the design of composite structures and the generation of production data. During the pre-processing stage, the geometry and finite element mesh are utilized, and boundary conditions and composite specifications are applied to the structure. Once a solution is obtained, the post-processing phase is employed to evaluate the performance of both the design and the composite laminate. If the design is found to be inadequate or if material failure occurs, adjustments may be needed in terms of the geometry or the laminate, and the evaluation process is repeated accordingly.

ANSYS Composite PrepPost (ACP) provides two modes: pre-processing and post-processing, each serving different purposes in the analysis of composite structures. In the pre-processing mode, ACP allows users to generate composite definitions and associate them with the geometry and finite element mesh. These definitions encompass important parameters such as the number of layers, material properties, orientations, and thicknesses of the composite structure. Once these composite definitions are established, they are transferred to the FE model and incorporated into the input file for the solver, enabling the analysis to consider the specific composite configuration accurately.

In the post-processing mode, after the solver completes the solution phase and produces result file, ANSYS Composite PrepPost (ACP) allows for the evaluation and visualization

of the obtained results. This includes performing failure analysis, safety assessment, and examining the strains and stresses within the composite structure. The post-processing capabilities of ACP enable engineers to gain insights into the performance and behavior of the composite material. By presenting the results visually, it becomes easier to interpret and communicate the analysis outcomes effectively. The pre-processing mode of ACP facilitates the setup and transfer of composite definitions to the analysis model, while the post-processing mode enables the evaluation and visualization of the results obtained from the analysis, providing valuable information for further analysis, design improvements, and decision-making processes.

### **6.13.2 Implementation in Workbench**

The implementation of importing a composite shell from ANSYS Composite PrepPost (ACP) into ANSYS Mechanical for analysis involves a series of steps to ensure a seamless transfer of the model. In ANSYS Workbench, the process begins by adding an ACP (Pre) system from the Component Systems list to the Project Schematic. The geometry of the composite shell is then specified, and the ACP system setup is configured according to the desired analysis requirements.

After setting up the ANSYS Composite PrepPost (ACP) system, a supported Mechanical system is added to the Project Schematic. The ANSYS Composite PrepPost (ACP Pre) Setup cell is then dragged and dropped onto the Model cell of the Mechanical system, establishing a transfer of the composite model from ACP to Mechanical. This transfer includes crucial components such as the mesh, geometry, engineering data, and composite definitions, ensuring that all necessary information is carried over for the analysis in ANSYS Mechanical.

In ANSYS Mechanical, Analysis Ply objects are created to mirror the Analysis Plies defined in ANSYS Composite PrepPost (ACP). These Analysis Ply objects represent the layers of the composite structure in the Mechanical system. The Mechanical system is

then fully defined by specifying the necessary loads, boundary conditions, and analysis settings, and subsequently solved to obtain the results.

During the implementation, certain considerations need to be taken into account. For instance, the material assignment in Mechanical becomes read-only after importing from ANSYS Composite PrepPost (ACP), meaning that material properties cannot be modified directly in Mechanical. Additionally, the editing capabilities of the mesh are limited in Mechanical, so any necessary mesh modifications should be performed in ANSYS Composite PrepPost (ACP) prior to the transfer. To scope loads and boundary conditions, criterion-based Named Selections are created in Mechanical.

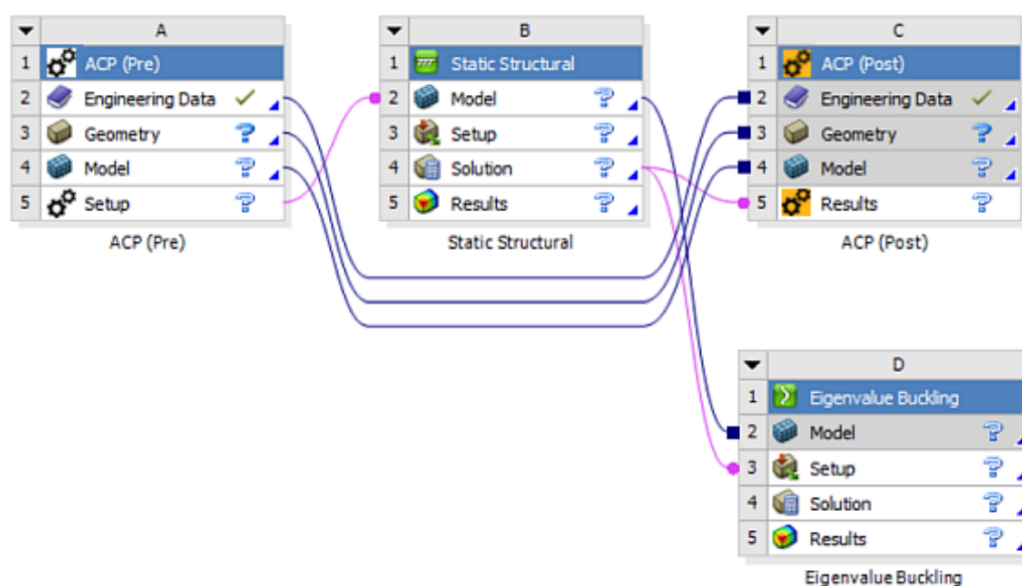


Figure 6.17: Basic Workflow in the ANSYS Composite PrepPost (ACP) including Eigenvalue Buckling Analysis

Once the analysis is complete, the results can be reviewed both in ANSYS Mechanical and ACP-Post. If additional post-processing capabilities are required, an ANSYS Composite PrepPost (ACP Post) system can be added, and the Mechanical system's Solution cell can be connected to the ACP (Post) Results cell. This enables the utilization of ANSYS Composite PrepPost (ACP)'s post-processing features for further analysis and evaluation.



Furthermore, if upstream results from Eigenvalue Buckling or Pre-Stress Modal analyses are needed, they can also be transferred to ANSYS Composite PrepPost (ACP) if desired (Figure 6.17).

## 6.14 Methodology

### 6.14.1 Geometry creation in SpaceClaim

The geometry is generated using SpaceClaim software. However, an important aspect of this methodology is that all structures are represented as surfaces. This approach allows them to function as moulds on which the layered composite material will be added in a specific direction. Specifically, the outer surface, inner surface, and spokes are created as surfaces, while the cables are formed using line elements. It is crucial to note that the geometry cannot have overlapping or shared topology. As a result, in the static structural analysis, contacts between different parts of the geometry must be manually defined. This step is necessary to ensure accurate simulation and analysis.

Figure 6.18 and Figure 6.19 display the geometry of the drift chamber showing the outer surface, inner surface, spokes created using surfaces and the cables created with line elements. Each element has to be defined as Named Selection. Even though, we can assign a certain thickness for the surfaces in SpaceClaim, this will be overridden by the composite definition in ANSYS Composite PrepPost (ACP).

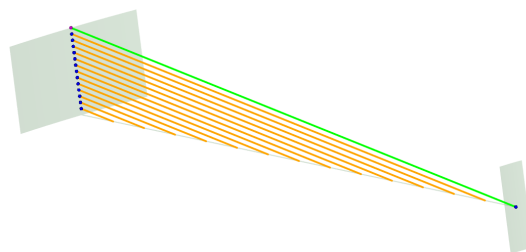


Figure 6.18: A sector of drift chamber used for the analysis.

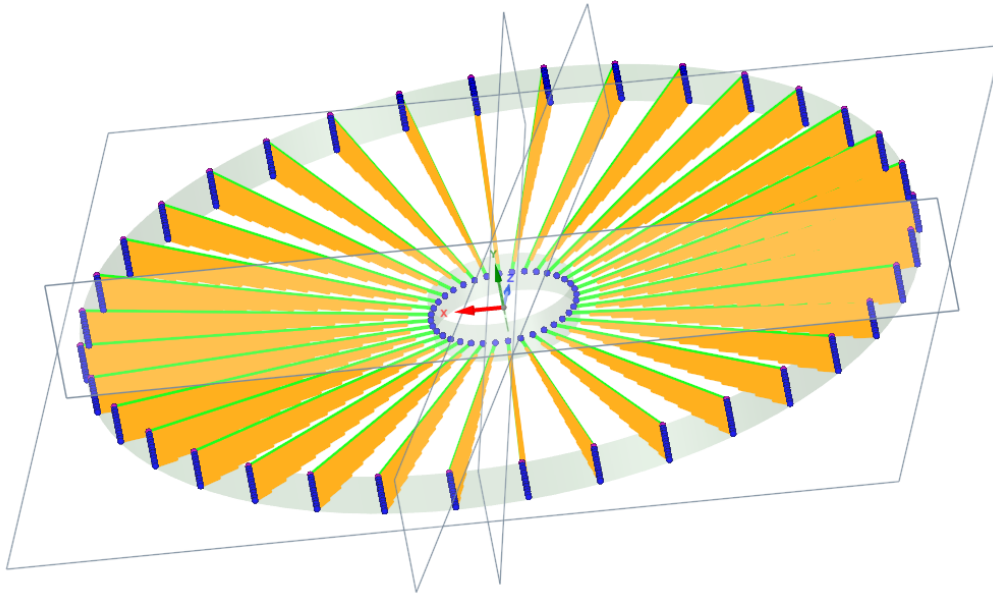


Figure 6.19: Full geometry of the drift chamber using surfaces that act as a mould for the composite layers. No topology is shared between cables and the spokes.

### 6.14.2 Meshing in ANSYS Mechanical

ANSYS Mechanical imports meshes from various systems, such as composite shell, composite solid, and cable elements. These meshes have to be combined to carry out mixed analysis in static structural. It is crucial to understand that ANSYS Mechanical imposes a restriction on the overlapping of node or element numbers across multiple systems. If meshes from different systems contain overlapping node or element numbers, the import process will encounter error and fail. To circumvent this problem, an automatic renumbering must be done to ensure that all node and element numbers are unique and avoid conflicts. All the three components of the drift chamber whose geometry were defined in SpaceClaim are now exported to three different modules of the ANSYS Mechanical (see Figure 6.20). In each ANSYS mechanical (*the whole model is imported*), the other unnecessary components are suppressed and meshing is done in the relevant component only. For example, in the first ANSYS mechanical module (*Shell Model*), we suppress the cables and the spokes. Then, on the inner and outer cylinders, we define a mesh. It is important to note that meshing cannot be done at later stage. Similar procedure

is used for cables and spokes.

### 6.14.3 Layered Composite definition in ANSYS Composite PrepPost (ACP)

The SpaceClaim geometry containing inner and outer surfaces that are to be modelled as shell elements are exported to ANSYS Composite PrepPost (ACP) for shell definition. The spokes which are also created as surfaces but will be defined as solid are exported to another schematic of ANSYS Composite PrepPost (ACP) for solid extrusion. Finally, the cable elements are exported to Mechanical. The basic workflow is shown in Figure 6.20.

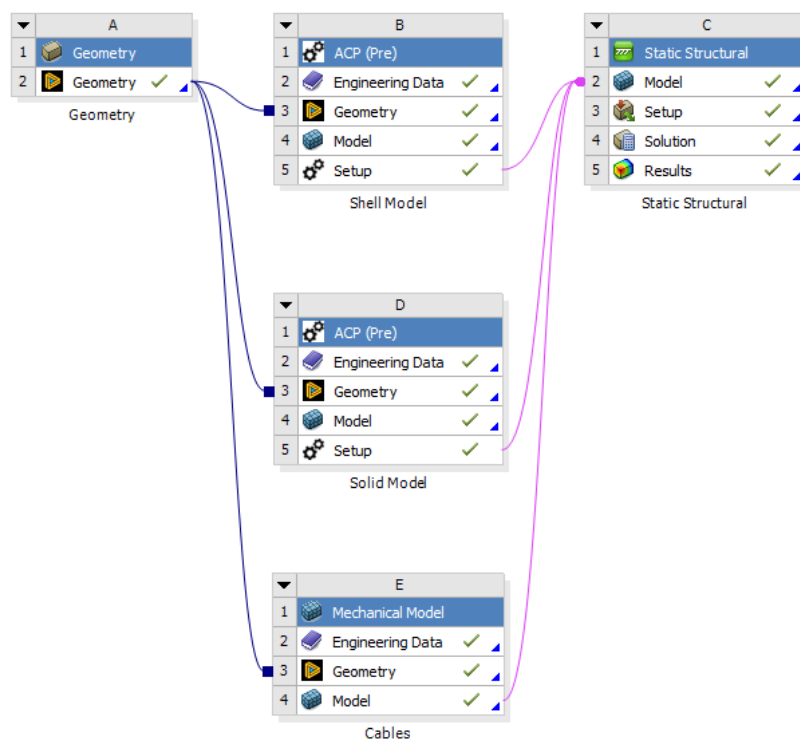


Figure 6.20: Basic Workflow of the ANSYS Composite PrepPost (ACP) workflow using different types of Model. While transferring the model to Static Structural, the type of data , "Solid" or " Shell" to be exported should also be defined.

ANSYS Composite PrepPost (ACP) features a relatively simple window layout designed to facilitate easier modelling and analysis of composite materials (see Figure 6.21) . The

## CHAPTER 6. LAYERED COMPOSITE DESIGN

software comprises various components, including the Model Tree for easy navigation through the model structure, a Graphics Window for 3D visualization and manipulation of the composite model, a Property Editor for defining and modifying material properties, a Ply Book for managing complex layups, an Analysis Setup window for configuring analysis parameters, and a Results Viewer for comprehensive display and interpretation of analysis results.

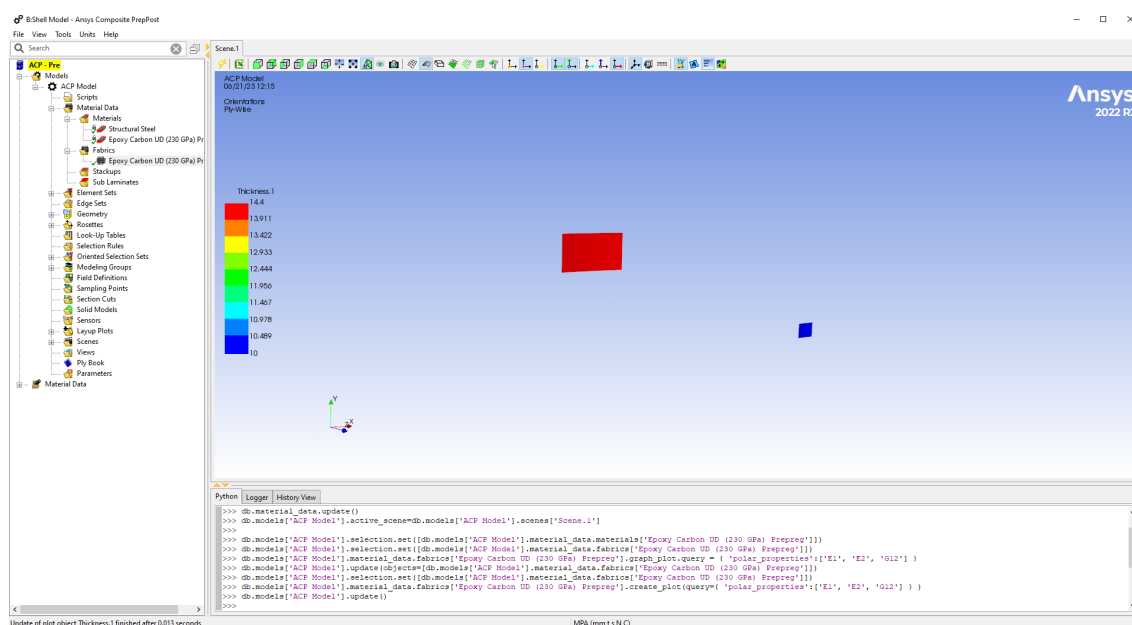


Figure 6.21: A window layout of the ANSYS Composite PrepPost (ACP) with Model Tree structure, including the composite layup, material properties, boundary conditions, and analysis settings.

A fabric is a single layer of the composite having a certain thickness. We define an Epoxy carbon prepreg fabric with 0.2 mm thickness. The definition and the polar properties are shown in Figure 6.22 and Figure 6.23 respectively. In a unidirectional composite, the modulus of elasticity,  $E_1$ , along the fiber direction is high due to the excellent stiffness provided by the fibers. It is similar to the modulus of the fiber material itself. On the other hand,  $E_2$ , the modulus perpendicular to the fibers, is generally lower as the matrix material, which has a lower modulus, plays a larger role in resisting deformation in that direction. The in-plane shear modulus,  $G_{12}$ , is typically lower than  $E_1$  and  $E_2$  since shear

deformation is more easily accommodated in the composite.

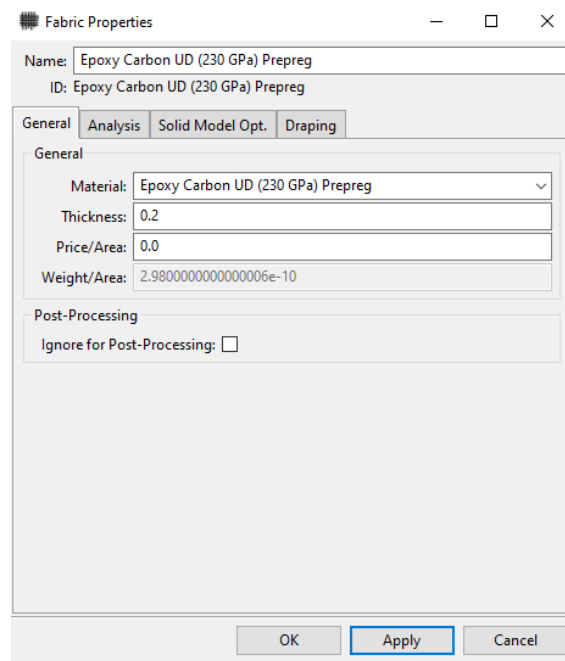


Figure 6.22: Fabric Properties for the Epoxy Carbon Prepeg.

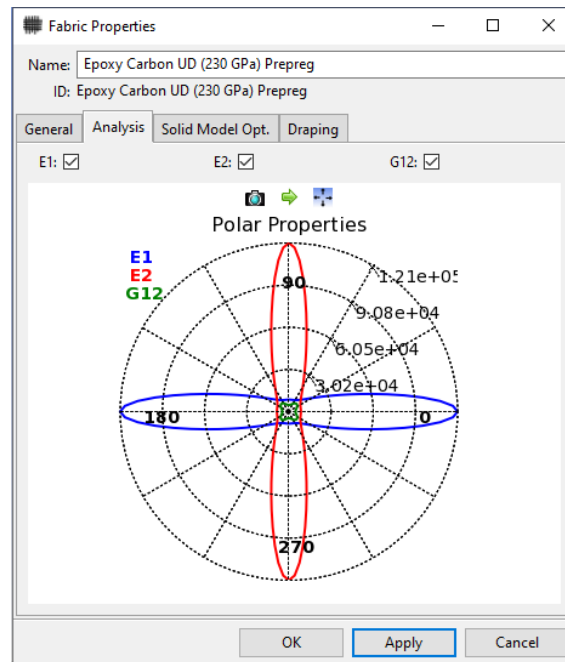


Figure 6.23: Representation of Elastic Properties of Epoxy Carbon Prepeg.

Using the fabric definition, a stackup is created with various angle of orientation. A stackup in ANSYS Composite PrepPost (ACP) refers to a non-crimp fabric that has a specific stacking sequence. In terms of production, the stackup is treated as a single ply that is applied onto the desired form. However, for analysis purposes, all the plies within the stackup are taken into account. It is necessary to provide information about the fabric type and its orientation for each individual ply within the stackup. We define a stackup with 5 fabric with a cross ply of 90 ° in the middle as in Figure 6.24. We can further assess and analyze the laminate properties of the stackup as in Figure 6.25. However, for the spokes, we define the stackup orientation only in 0° as having very short fibers in that direction would produce a lot of wastage as well as bending strength will also decrease in the preferred direction.

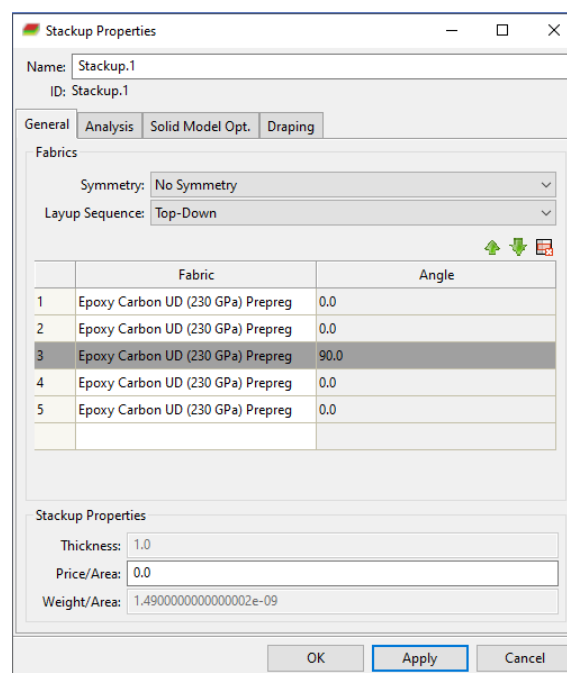


Figure 6.24: Five fabrics stacked up with a cross-ply at 90° in the middle. Each stackup has 1 mm thickness.

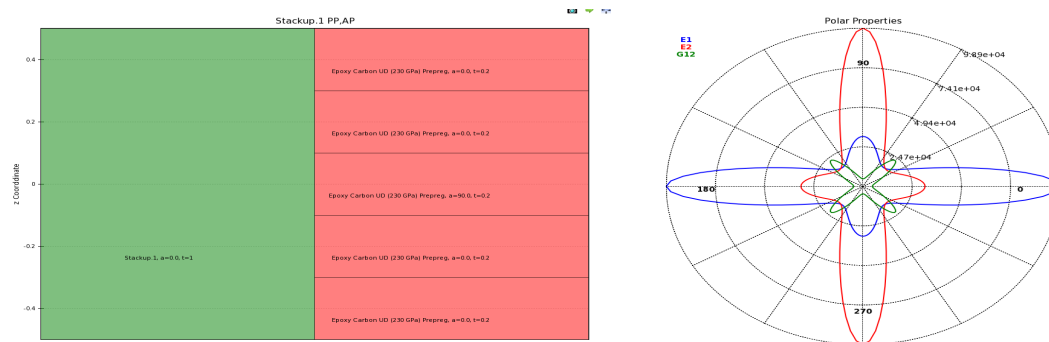


Figure 6.25: Stackup of the Production ply and Analysis ply. The polar properties of the stackup can be seen to be decreasing in  $0^\circ$  and increasing in  $90^\circ$ .

Rosettes are coordinate systems utilized to establish the reference direction for Oriented Selection Sets. They define the  $0^\circ$  orientation for the composite lay-up. Coordinate systems created in ANSYS Mechanical are automatically imported and maintain their naming in ACP. Additional Rosettes can be defined within ANSYS Composite PrepPost (ACP). The origin and directions of Rosettes are defined in the global coordinate system. It's important to note that Rosettes are independent of the mesh, meaning their properties are not affected by node and element selections. For the inner and outer surfaces the Rosettes are cylindrical whereas for the spokes the Rosettes are radial ones. One or multiple Rosettes can be employed to set the reference direction for elements within an Oriented Selected Set (OSS). The Selection Method specified in the Oriented Selection Sets (OSS) definition determines which Rosette determines the reference direction for the elements. To determine the reference direction for an individual element, the applicable Rosette is projected onto the element. Different types of Rosettes can be used to define the reference direction.

Oriented Selection Sets (OSS) play a fundamental role in ANSYS Composite PrepPost (ACP), providing the foundation for defining the lay-up of composite materials. Unlike Element Sets, plies are applied to specific areas designated by the Oriented Selection Sets (OSS). This offers independence from the finite element model and its element normals. Oriented Selection Sets (OSS) combines several crucial elements for the composite lay-up

process. Firstly, the designated area where the plies are applied is defined. Secondly, the side of the shell mesh on which the plies are positioned are selected determining their orientation. Finally, the reference direction that establishes the 0° fiber direction (see Figure 6.26-6.27) , serving as the baseline for all ply angles relative to this direction (see Figure 6.26-6.27).

Once the fabrics, stackup and the orientation of the composite layers is defined , the next thing is to define the number of layers. This is done through Modelling groups. For each component, we use a same stackup , but the number of the ply will be different hence the thickness. The table 6.4 below shows the number of ply and the corresponding thickness used :

Component Type	Orientation of Ply	No. of Stackups	No. of Ply	Total thickness (mm)
Outer Cylinder	0/0/90/0/0/	16	80	16
Inner Cylinder	0/0/90/0/0/	10	50	10
Spokes	0/0/0/0/0/	16	80	16

Table 6.4: Arrangement of the Stackup and Ply in the various components of Drift chamber



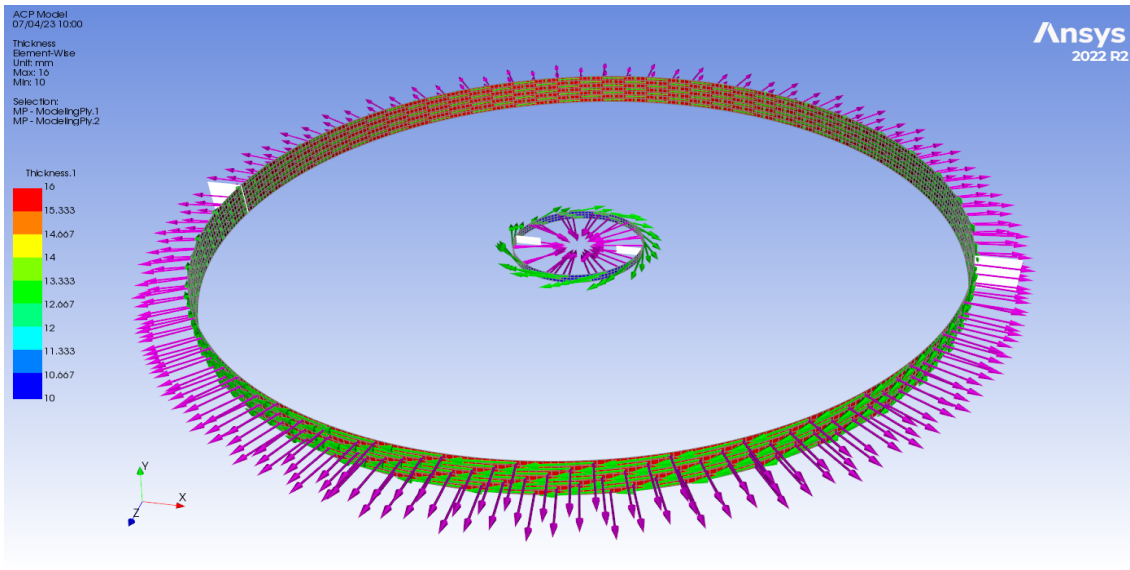


Figure 6.26: Layup direction for the composite inner and outer cylinders. The outer cylinder is extruded outwards *shown by purple arrows*. The inner cylinder is extruded inwards *shown by purple arrows*. The green arrows represent the direction of fibers. For the inner and outer surfaces the fibers are in cylindrical direction. Incorrect definition of Layup direction will produce intersecting surfaces and the solver will be unable to give an output.

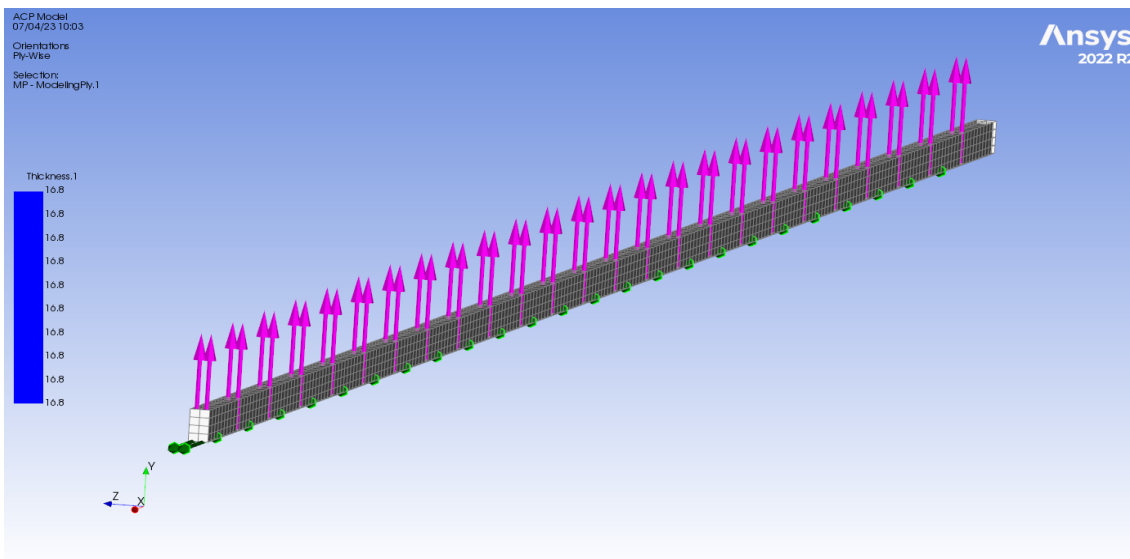


Figure 6.27: Reference direction and fiber direction for the spokes. The reference direction of spokes are in radial direction.

### Solid Modelling

Solid modeling should be used in composite analysis when the structural behavior of the composite material is primarily three-dimensional, and when the geometry consists of solid components or features embedded within the composite structure (see Figure 6.28). Solid modeling provides a more accurate representation of the three-dimensional stress distribution within the composite, making it suitable for scenarios where detailed stress analysis is required. In ANSYS Composite PrepPost (ACP), composite solids can be imported into ANSYS Mechanical for analysis by importing the mesh from ANSYS Composite PrepPost (ACP) systems and generating the geometry from the imported meshes. The process of importing a composite solid into ANSYS Mechanical is similar to that of composite shells, but with one key difference: the selection of the "Transfer Solid Composite Data" option. ANSYS Composite PrepPost (ACP) offers two approaches for solid modeling. The first approach, called Solid Model, utilizes an extrusion algorithm to create a solid mesh based on the Composite Definitions and the shell reference surface (see Figure 6.29). ANSYS Composite PrepPost (ACP) handles the entire solid mesh generation process in this case. In our case, we use the second approach, referred to as Imported Solid Model, which involves mapping the Composite Definitions onto an external solid mesh that is loaded into ANSYS Composite PrepPost (ACP). This approach provides more flexibility by allowing the use of an existing solid mesh for analysis (Figure 6.30).

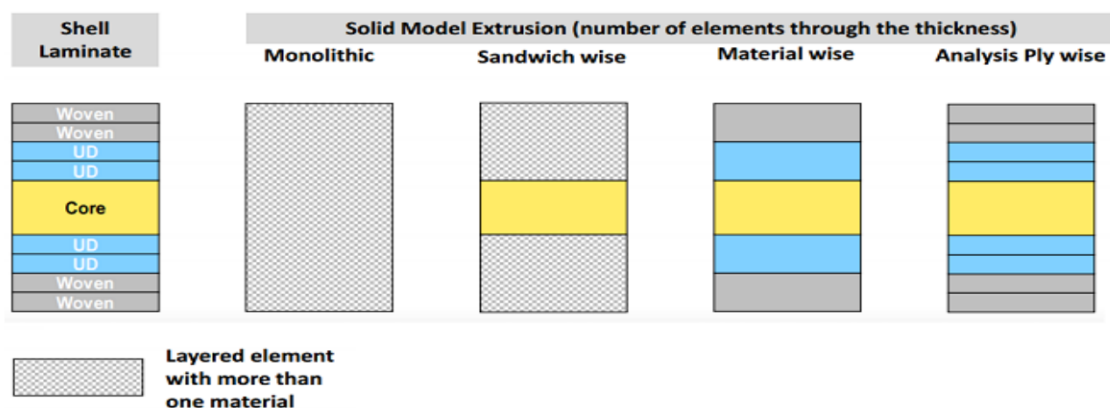


Figure 6.28: Illustration of various solid extrusion methods available in ANSYS Composite PrepPost (ACP).

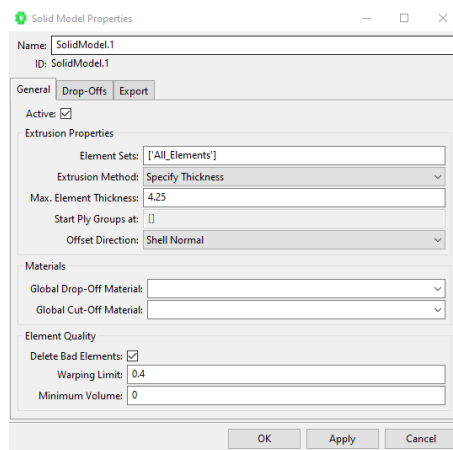


Figure 6.29: One of the spokes is defined in ANSYS Composite PrepPost (ACP) for Extrusion using thickness of the solid and shell normal is the offset direction. This is necessary for post processing the composite.

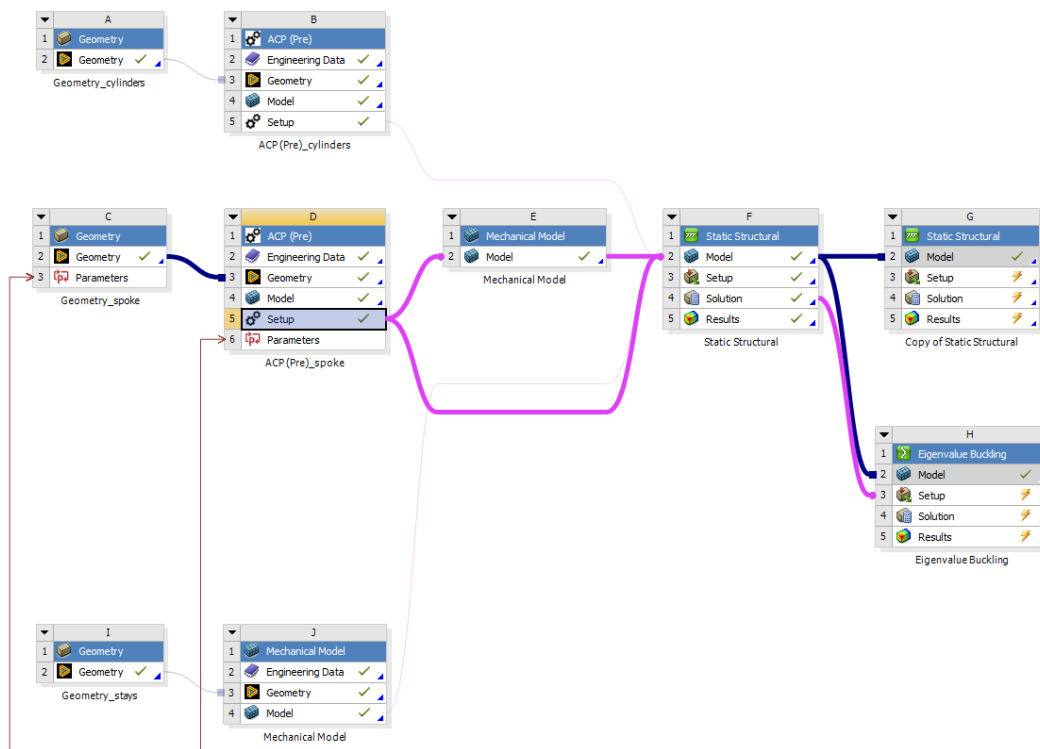


Figure 6.30: Full setup of the solid model : One of the spokes is defined in ANSYS Composite PrepPost (ACP) and extruded as solid model, whereas other 35 are defined in ANSYS Mechanical and composite properties are defined through command APDL.

Shear locking is a phenomenon that can occur in finite element analysis when modelling thin structures, particularly those with a high aspect ratio (e.g., long and slender elements). It refers to the loss of accuracy in predicting shear deformation and stress distribution, leading to erroneous results. The primary cause of shear locking is the inadequate representation of shear deformation modes in certain types of finite elements, such as the standard four-node quadrilateral or eight-node brick elements. These elements are based on a displacement-based formulation and may struggle to accurately capture shear deformation, resulting in overly stiff behavior and incorrect stress distributions. To avoid shear locking, several techniques can be employed:

1. **Reduced integration:** Using reduced integration elements, such as reduced integration quadrilateral or hexahedral elements, can help to avoid shear locking as these elements have fewer integration points and have a reduced number of degrees of freedom allowing for greater freedom of shear deformation.
2. **Selective integration:** Selective integration techniques involve using a higher-order integration scheme for certain terms of the element stiffness matrix, particularly those associated with shear deformation. By selectively applying a higher integration order for these terms, more accurate results can be obtained.
3. **Mixed or enhanced formulation:** Using mixed or enhanced formulations, such as mixed shear-flexible or mixed interpolation of strains, can help address shear locking. These formulations introduce additional degrees of freedom associated with shear deformation, allowing for improved accuracy.
4. **Specialized elements:** Employing specialized finite elements designed specifically for thin structures can effectively mitigate shear locking. Examples include the Mindlin-Reissner plate element or the MITC (Mixed Interpolation of Tensorial Components) elements, which are specifically formulated to handle shear deformation accurately.

5. Mesh refinement: Increasing the element density in regions where shear deformation is significant can help reduce the effects of shear locking. By refining the mesh and using smaller elements, more accurate representation of the shear deformation behavior can be achieved.

### **6.14.4 Exporting Model to Static Structural**

Once the individual models are fully defined in their corresponding ANSYS modules, the next thing is to export them to Static Structural where loads, symmetry and boundary conditions are applied. While transferring the inner and outer surfaces, transferring of the shell data should be selected. For the transferring of the spokes, the solid data should be selected. For transferring the cables, a direct transfer takes place as this is defined only on ANSYS Mechanical.

# Chapter 7

## Structural Analysis: A Macro Scale

### Approach

Composite materials are known for their remarkable combination of high strength, stiffness, and lightweight properties, which result from their composition of multiple layers of different materials. However, comprehensively analyzing these structures necessitates a specialized approach due to the complexity of their constituent materials and the interactions between these layers. This chapter provides an extensive overview of the methods and considerations involved in conducting structural analysis on composite layered structures. Rather than focusing on individual components such as fibers and matrix, the chapter concentrates on the overall mechanical behavior of these structures. This approach, known as macro analysis, specifically examines displacements and buckling loads. In macro analysis, the composite material is treated as a uniform shell, assuming its properties remain consistent throughout. Additionally, the chapter introduces the contact kinematics, the application of loads, and the consideration of boundary conditions.

### 7.1 Contact kinematics

When analyzing the interaction between two bodies, it is customary to designate one body's surface as the contact surface and the other body's surface as the target surface. In cases of rigid-flexible contact, the deformable body is associated with the contact surface,

while the target surface corresponds to the rigid body. In flexible-flexible contact, both the contact and target surfaces are related to deformable bodies. These paired surfaces form what is referred to as a "Contact Pair."

To establish this connection, the CONTA174 contact element is linked to the 3-D target segment elements (TARGE170) through a shared real constant set number [29]. The CONTA174 element is positioned on the surface of 3-D solid or shell elements, which are known as underlying elements [29]. The contact element possesses the same geometric characteristics as the underlying elements. It is worth noting that the contact surface can encompass either one or both sides of the shell or beam elements.

### 7.1.1 Location of contact detection

The CONTA174 contact element is designed for surface-to-surface contact analysis. It employs integration points located at nodal or Gauss points for contact detection. While the contact element is restrained from penetrating the target surface at its integration points, the target surface itself can potentially penetrate the contact surface. By default, CONTA174 utilizes Gauss integration points, which generally yield more accurate results compared to using the nodes as integration points [29]. However, using nodal contact points may lead to inaccuracies in representing uniform pressure distribution, particularly at corners where kinematically equivalent forces indicate release [29].

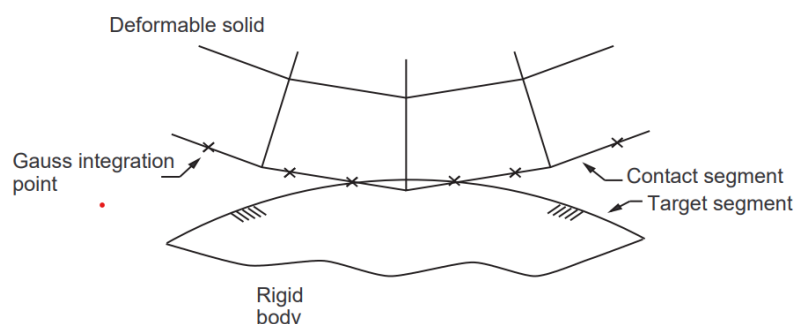


Figure 7.1: Contact Detection Point Location at Gauss Point. Adapted from ANSYS Inc. ANSYS mechanical user's guide, 2019[29].

To enhance contact constraints on overlapping regions of contact and target surfaces, the surface projection method is available for 3-D elements CONTA173 and CONTA174 [29]. This method, based on the work of Puso and Laursen, enforces contact constraints over a combined region rather than individual contact nodes or Gauss points [29]. The surface projection method passes patch tests and typically produces smoother stress distributions for both contact and underlying elements. It ensures smooth variation of contact forces during significant sliding and eliminates force jumps when contact nodes slide off target surface edges. Moreover, the surface projection method satisfies moment equilibrium for frictional or bonded contact, unlike other contact detection options that may not precisely satisfy moment equilibrium under certain circumstances, such as when there is an offset along the contact normal direction or when considering shell thickness effects or user-defined contact offsets [29].

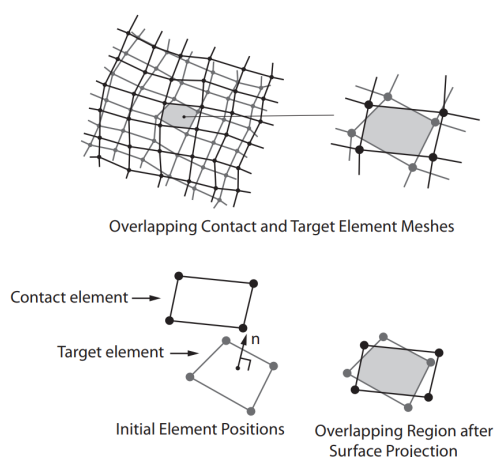


Figure 7.2: Surface-Projection-Based Contact. Adapted from ANSYS Inc. *ANSYS mechanical user's guide, 2019*[29].

### 7.1.2 Penetration

The measurement of penetration distance between the contact surface and the target surface occurs along the normal direction at integration points (Figure 7.3). This measurement is uniquely defined, even if the target surface's geometry is not smooth. Discontinuities in the target surface's geometry can result from physical corners or the numerical discretization



process, such as finite element analysis. The current method of calculating penetration distance does not impose any restrictions on the shape of the rigid target surface. Smoothing of the concave corner may not always be necessary, but it is recommended to smooth the region with abrupt changes in curvature for convex corners (Figure 7.4).

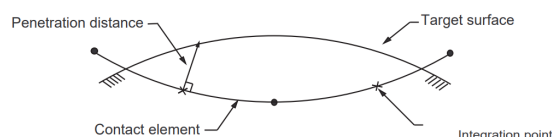


Figure 7.3: Penetration Distance. Adapted from *ANSYS Inc. ANSYS mechanical user's guide, 2019[29]*.

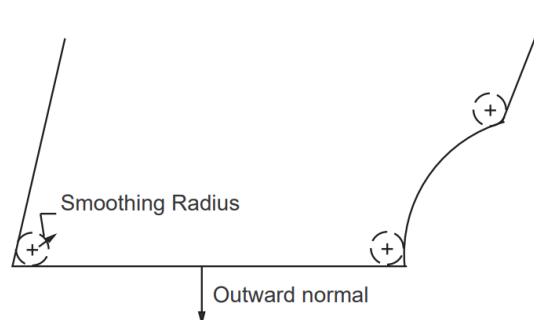


Figure 7.4: Smoothing Convex corner. Adapted from *ANSYS Inc. ANSYS mechanical user's guide, 2019[29]*.

In the surface-projection-based contact method, the detection of contact still occurs at contact nodal points, and the contact normal remains perpendicular to the contact surface. However, the computation of contact penetration distance takes place over the overlapping region in an average sense. This means that the measurement considers the overall penetration distance over the combined region, as depicted in Figure 7.2: Surface-Projection-Based Contact, rather than focusing on individual contact points.

### 7.1.3 Pinball Algorithm

The contact element's status is determined by its position and motion relative to the associated target surface. The program continuously monitors each contact element and assigns a specific status based on its behavior.

A contact element enters the near-field contact state when it enters a pinball region centered on its integration point. The computational cost of searching for contact is influenced by the size of this pinball region. Far-field contact element calculations are straightforward and have minimal computational demands. However, near-field calculations for contact elements that are either in close proximity to or in actual contact with each other are slower and more complex. The most intricate calculations occur when the elements are in direct contact.

To ensure accurate contact definitions, especially in cases where the target surface contains multiple convex regions, setting an appropriate pinball region is crucial in overcoming spurious contact. The default setting provided by the program should generally be suitable for most contact problems.

### 7.1.4 Contact Algorithms

There are four distinct contact algorithms that we can apply;

1. Pure penalty method: This method relies solely on penalty-based formulations to enforce contact constraints between surfaces. In this approach, both the contact normal and tangential stiffness are essential. However, a key limitation is that the extent of penetration between the surfaces is influenced by these stiffness values. Higher stiffness values result in reduced penetration, but they can also introduce problems such as ill-conditioning of the global stiffness matrix and convergence challenges [29]. Ideally, one seeks a stiffness value that is sufficiently high to keep contact penetration within acceptable limits, yet low enough to ensure stable convergence and prevent matrix ill-conditioning issues. Striking

the right balance is crucial to achieve a well-behaved and accurate solution. However this method is faster than Lagrangian ones.

2. Augmented Lagrangian method: Developed by Simo and Laursen, this method incorporates augmented Lagrangian techniques to handle contact conditions effectively. The augmented Lagrangian method is an iterative process that involves updating penalties to determine the Lagrange multipliers, which represent the contact tractions [29]. In comparison to the penalty method, the augmented Lagrangian method generally yields better conditioning and is less dependent on the contact stiffness coefficient's magnitude [29]. However, in certain analyses, the augmented Lagrangian method may necessitate additional iterations, particularly if the deformed mesh undergoes excessive distortion. This method is expensive in comparison to penalty based methods.

The contact pressure is defined by:

$$P = \begin{cases} 0 & \text{if } u_n > 0 \\ K_n u_n + \lambda_{i+1} & \text{if } u_n \leq 0 \end{cases} \quad (7.1)$$

where:

$$\lambda_{i+1} = \begin{cases} \lambda_i + K_n u_n & \text{if } |u_n| > \varepsilon \\ \lambda_i & \text{if } |u_n| < \varepsilon \end{cases} \quad (7.2)$$

$\varepsilon$  = compatibility tolerance

$\lambda_i$  = Lagrange multiplier component at iteration i

The Lagrange multiplier component  $\lambda_i$  is computed locally (for each element) and iteratively.

3. Pure Lagrange multiplier method: Introduced by Bathe, this method utilizes Lagrange multipliers exclusively to enforce contact constraints between surfaces.

4. Lagrange multiplier on contact normal and penalty on frictional direction: This approach combines the use of Lagrange multipliers to enforce constraints along the contact normal direction and penalty-based formulations to handle constraints related to frictional forces [29].

### 7.1.5 MPC184 - Multipoint Constraint

MPC184 is part of a broader category of multipoint constraint elements that employ Lagrange multipliers to enforce kinematic constraints. These elements can be broadly classified as either "constraint elements" or "joint elements" [29]. They are utilized in scenarios where it is necessary to impose constraints to fulfill specific requirements. By utilizing Lagrange multipliers, these elements provide access to the constraint forces and moments, which can be useful for output purposes.

## 7.2 Defining contacts

Since the models are imported from separate ANSYS modules, no topology sharing option was available between spokes, cables, inner and outer cylinders.

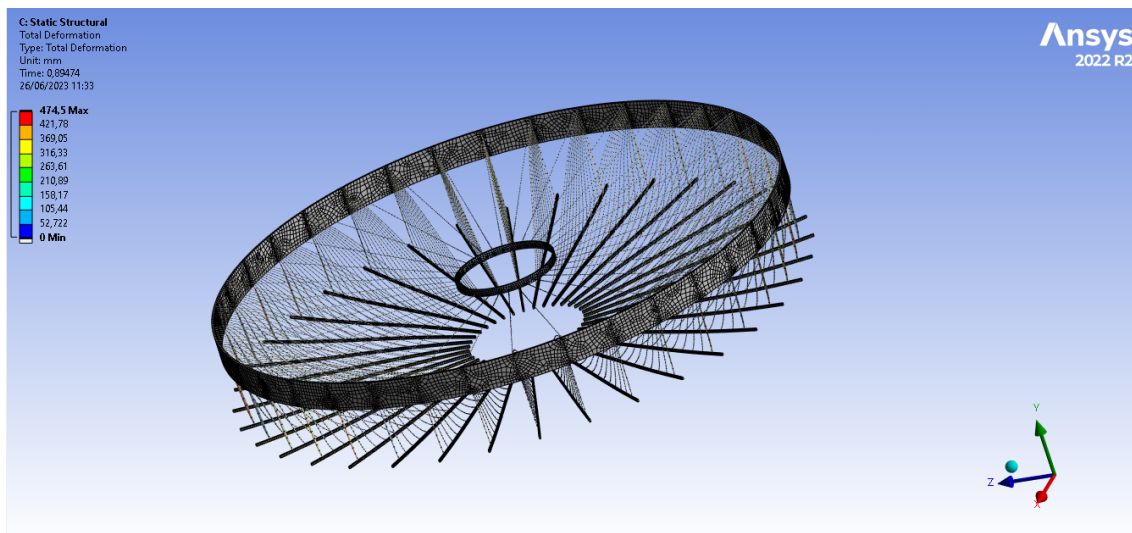


Figure 7.5: Translation of the spokes in the negative Y direction due to lack of contact between spokes and the cylinders

If the contacts are not defined properly, a rigid body motion occurs, or in some cases no solution will be generated at all. Figure 7.5 shows how the spokes completely translate in the negative Y direction due to lack of contact between spokes and the cylinders. In this case, however, the contact between cables to all other elements was defined. We define a Bonded contact with MPC184 - Multipoint Constraint based formulation. Pinball regions were defined based on the dimensions. Figure 7.6 shows a Bonded contact between the spokes and the cables. The contact must be defined on the lower surface of the spokes and the node of the cables. If we select the whole spoke and the line of the cable, the solver will try to find the solution in whole body and computation time will be very high.

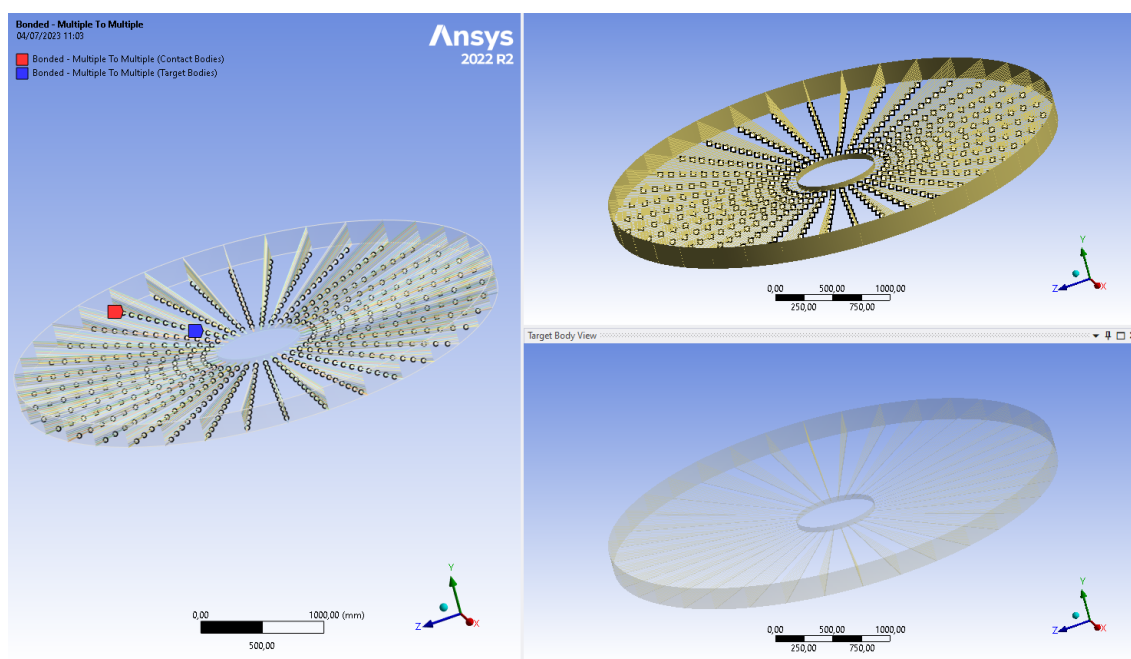


Figure 7.6: Contact definition between the lower surface of the spokes and the nodes of the cables

After the definition of the contact, we should not directly solve the model. This is due to the fact that if some issues are in contact, then an unconverged solution will be given as output after very large number of time steps. In order to avoid the convergence issues due to the contacts, penetration, gap and contact status must be checked beforehand (Figure 7.7-7.8). This can be done with contact tool.

## CHAPTER 7. STRUCTURAL ANALYSIS: A MACRO SCALE APPROACH

### Initial Information

For additional options, please visit the context menu for this table (right mouse button)

Name	Contact Side	Type	Status	Number Contacting	Penetration (mm)	Gap (mm)	Geometric Penetration (mm)	Geometric Gap (mm)	Resulting Pinball (mm)	Real Constant
Bonded - Multiple To Multiple	Contact	Bonded	Closed	468,	0,	0,	7,4593e-014	0,	2,	587,
Bonded - Multiple To outer(Copy of ACP (Pre))	Target	Bonded	Inactive	N/A	N/A	N/A	N/A	N/A	N/A	0,
Bonded - Multiple To inner(Copy of ACP (Pre))	Contact	Bonded	Closed	72,	0,	0,	0,15747	0,	5,	583,
Bonded - Multiple To outer(Copy of ACP (Pre))	Target	Bonded	Inactive	N/A	N/A	N/A	N/A	N/A	N/A	0,
Bonded - Multiple To inner(Copy of ACP (Pre))	Contact	Bonded	Closed	72,	0,	0,	0,	0,13263	5,	585,
Bonded - Multiple To inner(Copy of ACP (Pre))	Target	Bonded	Inactive	N/A	N/A	N/A	N/A	N/A	N/A	0,

### Color Legend

<b>Red</b>	The contact status is open but the type of contact is meant to be closed. This applies to bonded and no separation contact types.
<b>Yellow</b>	The contact status is open. This may be acceptable.
<b>Orange</b>	The contact status is closed but has a large amount of gap or penetration. Check penetration and gap compared to pinball and depth.
<b>Gray</b>	Contact is inactive. This can occur for MPC and Normal Lagrange formulations. It can also occur for auto asymmetric behavior.

Figure 7.7: Initial information of the contacts defined on our model. The resulting penetration and gap can be read from the table provided.

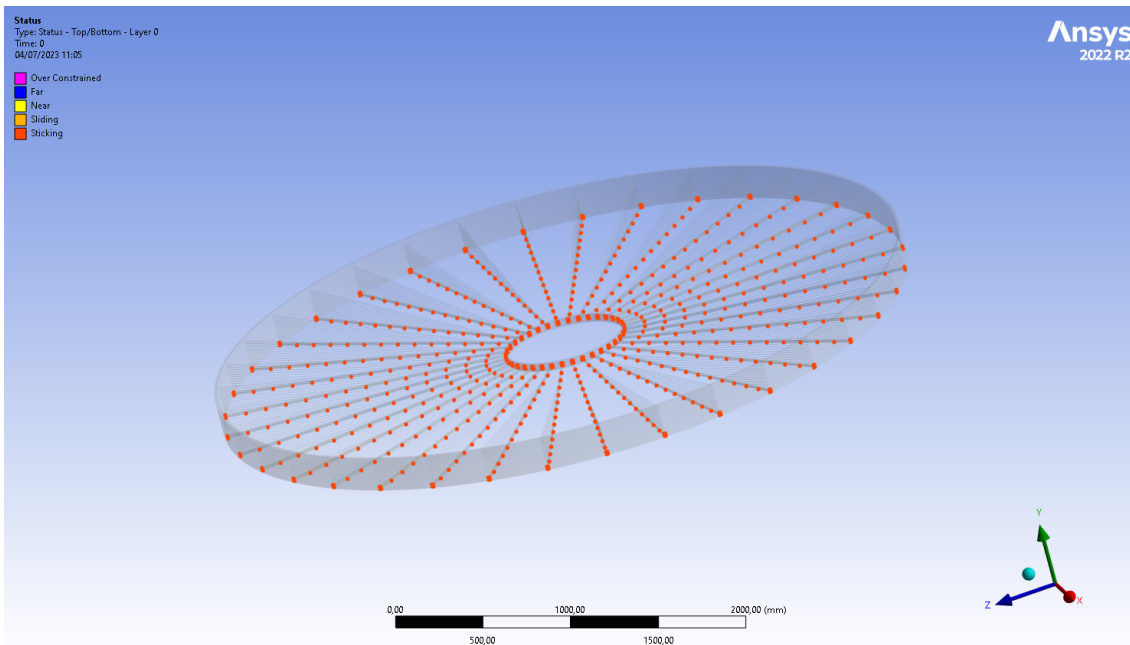


Figure 7.8: Contact status check on our model. The status can be Over-constrained, Far, Near, Sliding and Sticking.

### 7.3 Application of Pressure

Initially, in previous chapters uniformly distributed line pressure was used. However, in reality, the wires are imparting linearly increasing line pressure. But also, this pressure is

distributed as a surface pressure along the breadth (Figure 7.9). The equivalent pressure calculation is as follow:

Total load on one face of drift chamber = 100,000 N

$$\text{Total load on one spoke} = \frac{100,000}{36} = 2777.78 \text{ N}$$

This force has to be applied on a spoke with a length of 1650 mm and a breadth of 9.6 mm.

Therefore,

$$\text{Equivalent uniformly distributed pressure} = \frac{2777.78}{1650 \times 9.6} = 0.1753 \text{ MPa}$$

Linearly varying surface pressure at the outer cylinder = 0.3507 MPa

Linearly varying surface pressure at the inner cylinder = 0.00 MPa

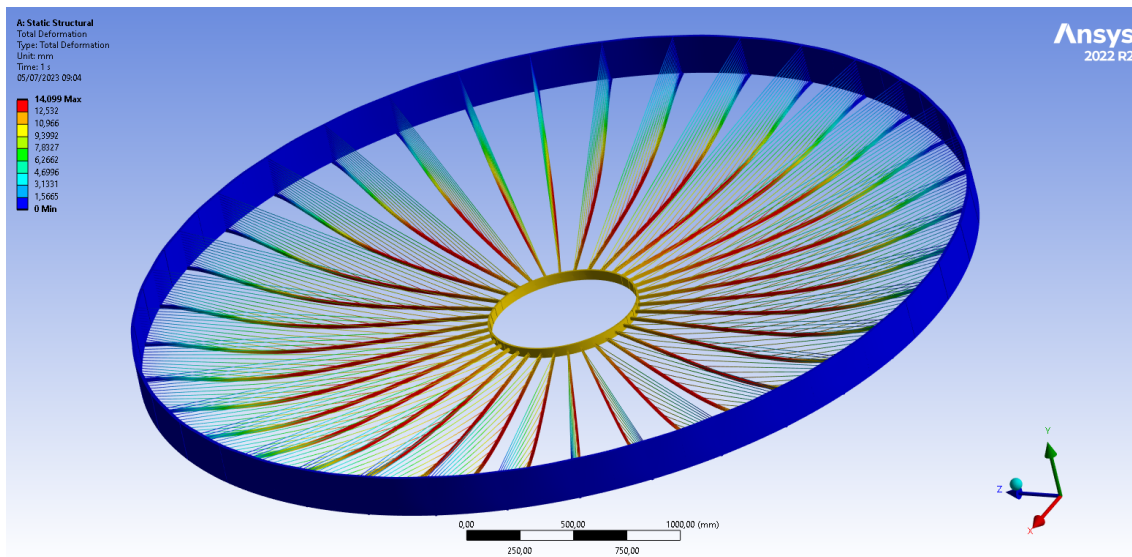


Figure 7.9: Application of linearly varying pressure of 0.36 MPa on the surface of the spokes. The application of pressure is defined using cylindrical coordinate system.

## 7.4 Application of Prestress on Cable elements

The Total deformation in the spokes without the application of prestress is around 14.099 mm. To limit this deflection, we use a cable prestressing and the values of these forces

(*thermal conditions*) were obtained by solving an optimization problem in Chapter.5. The values of the thermal conditions <sup>1</sup>

Cable number	Values of Thermal condition
Cable-1	330.976
Cable-2	360.646
Cable-3	382.838
Cable-4	298.239
Cable-5	343.049
Cable-6	119.933
Cable-7	388.512
Cable-8	265.701
Cable-9	362.211
Cable-10	129.413
Cable-11	35.1225
Cable-12	335.869
Cable-13	213.717
Cable-14	189.269

Table 7.1: Values of the thermal condition used in the cables to apply the effect of prestress. Cable-1 is the outermost cable near the inner cylinder. Cable-14 is the innermost cable near the outer cylinder.

## 7.5 Boundary condition

We are using very conservative design approach because we are fixing only the inner edge of the outer cylinder. Fixing the full face will imply a very stiff outer cylinder. However, the full drift chamber might have a different behaviour, somewhere between these two conditions. We will take a look at both of these boundary conditions.

## 7.6 Results

### 7.6.1 Total deformation of the drift chamber with the edge of the outer cylinders fixed

Without the application of the internal prestressing in the cables, the maximum total deformation of the spokes was 14.099 mm and the outer cylinders was 0.63 mm. After the

---

<sup>1</sup>The environment temperature was set to 400°C and coefficient of thermal expansion of steel as  $\alpha = 1.35 \times 10^{-5}$  per degree Celsius (°C)



application of the internal cable prestressing the maximum total deformation of the spokes was reduced to 0.61 mm whereas the total maximum deformation in the outer cylinders increased to 0.67 mm. Figure 7.10-7.14 show the total deformation for the aforementioned cases.

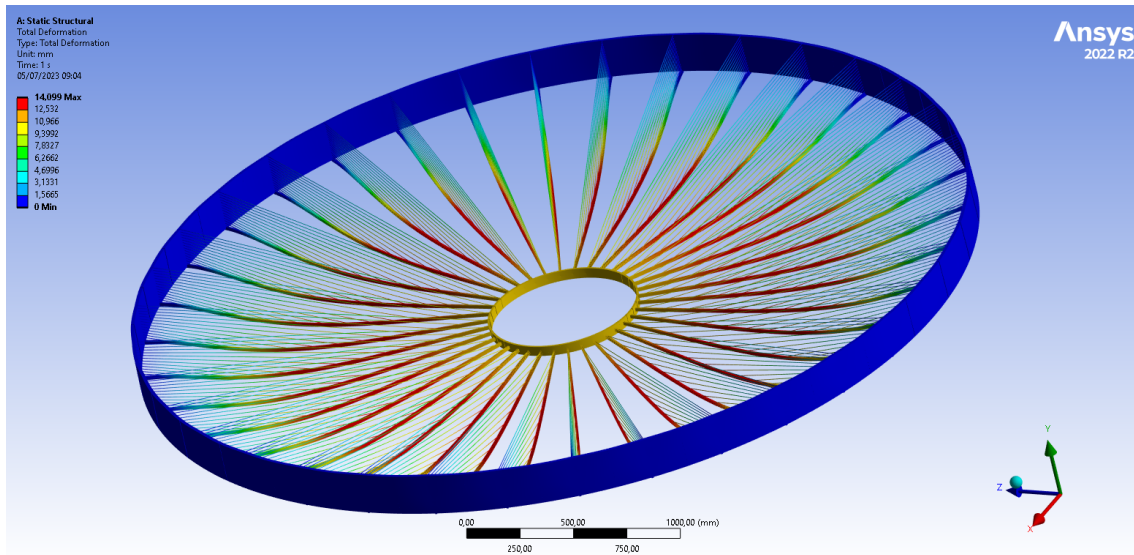


Figure 7.10: Total deformation ( $14.099\text{ mm}$ ) of the drift chamber subjected to linearly varying pressure only.

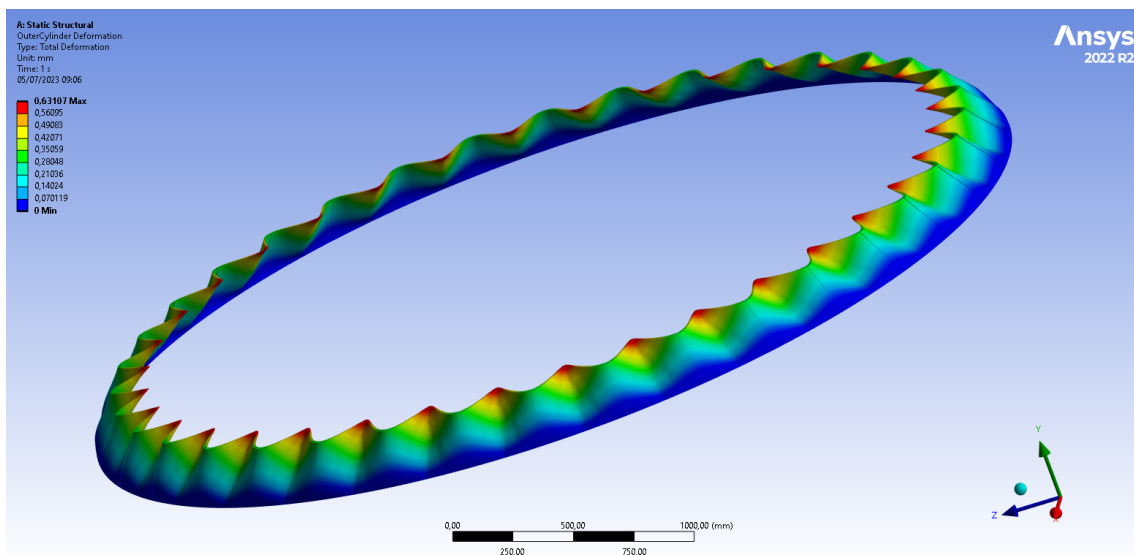


Figure 7.11: Total deformation ( $0.63\text{ mm}$ ) of the outer cylinder subjected to linearly varying pressure only.

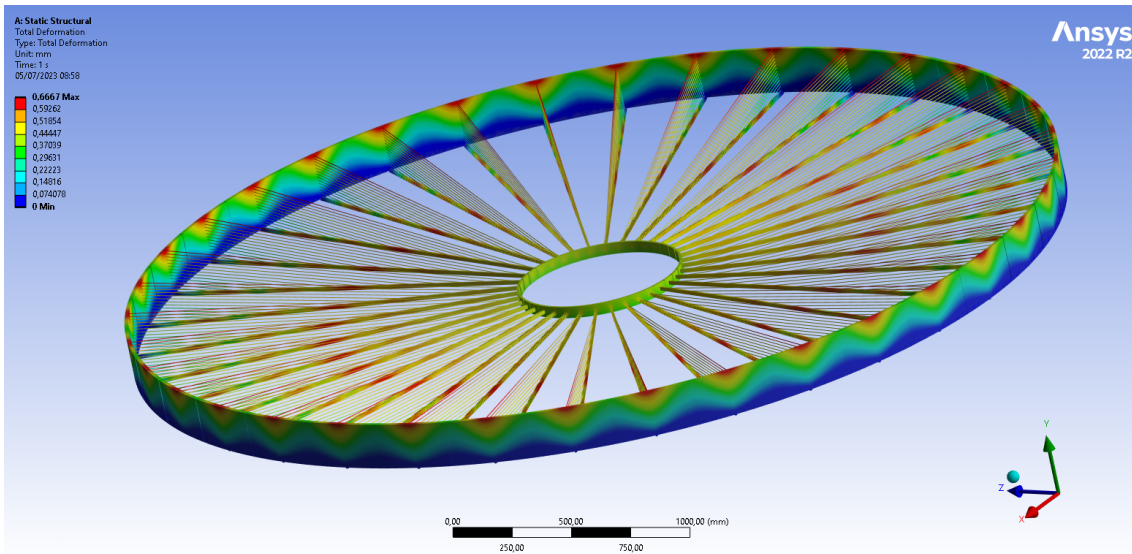


Figure 7.12: Total deformation ( $0.67\text{ mm}$ ) of the drift chamber subjected to linearly varying pressure and prestress.

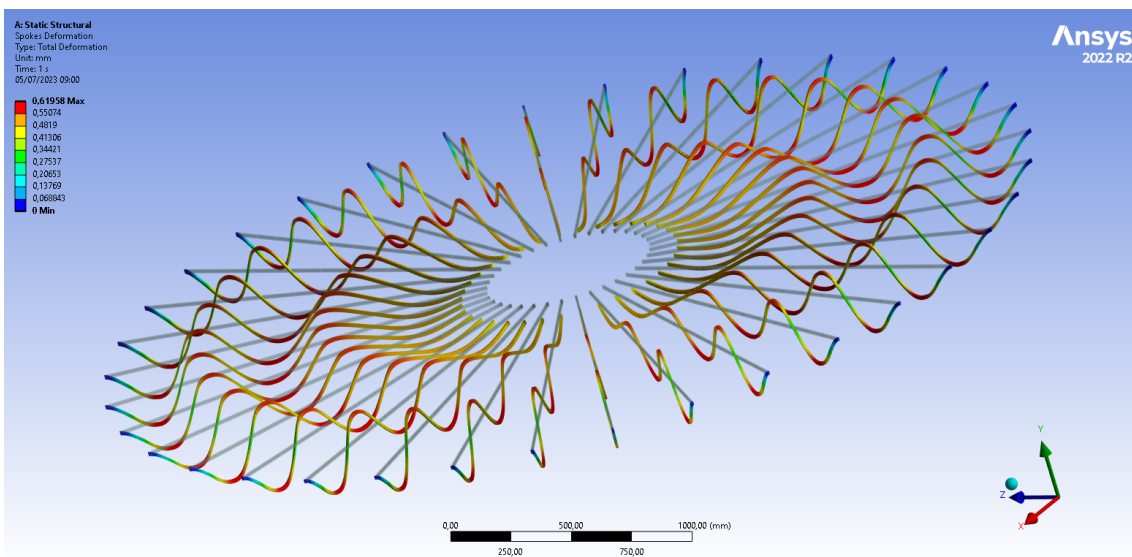


Figure 7.13: Total deformation of the spokes ( $0.62\text{ mm}$ ) subjected to linearly varying pressure and prestress. The deformation has been scaled 60 times higher otherwise it is visually imperceptible.

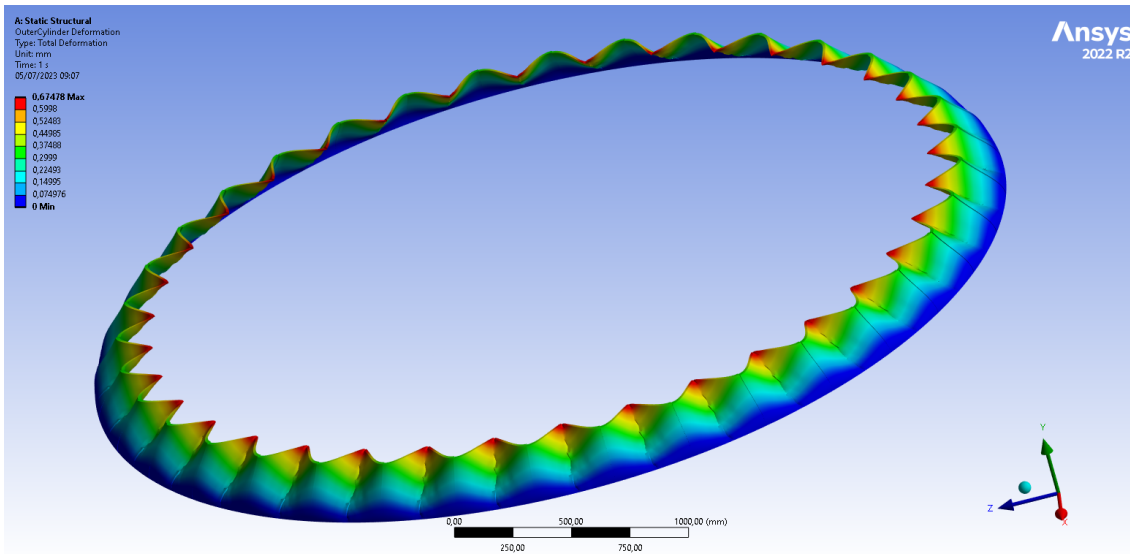


Figure 7.14: Total deformation ( $0.67\text{ mm}$ ) of the drift chamber subjected to linearly varying pressure and prestress.

## 7.6.2 Total deformation of the drift chamber with the face of the outer cylinders fixed

When a fixed boundary condition is applied on the face of the outer cylinder, then the total deformation of the drift chamber is only  $11.54\text{ mm}$  ( $3\text{ mm}$  less than that of edge fixed), so when we apply the same internal prestressing force as that of edge fixed, the drift chamber is pulled upwards and shows a very high total deformation. Figure 7.15-7.17 show the total deformation for the aforementioned cases.

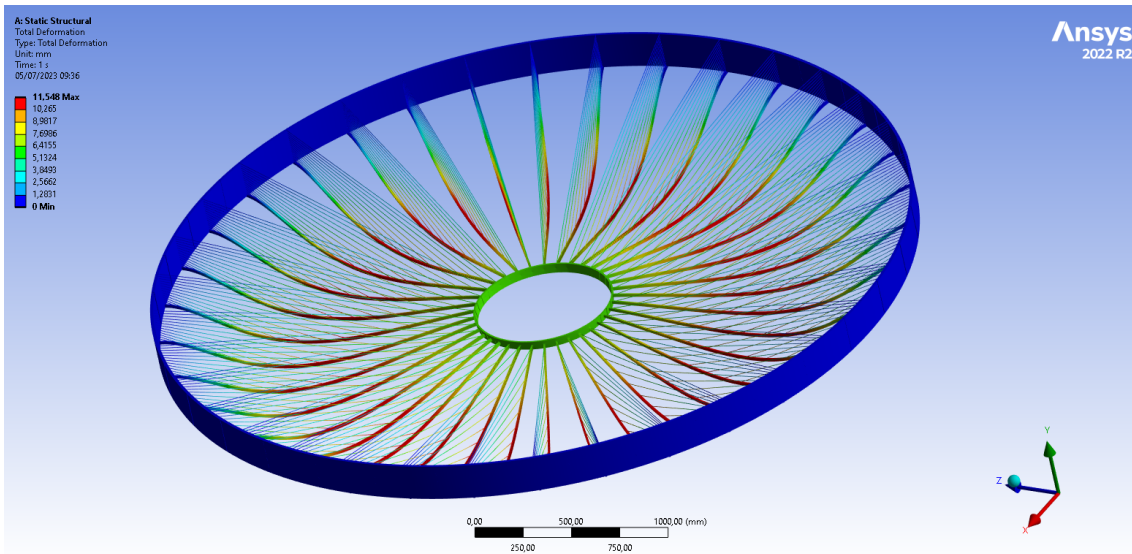


Figure 7.15: Total deformation ( $11.54 \text{ mm}$ ) of the drift chamber subjected to linearly varying pressure only with outer cylinders completely fixed

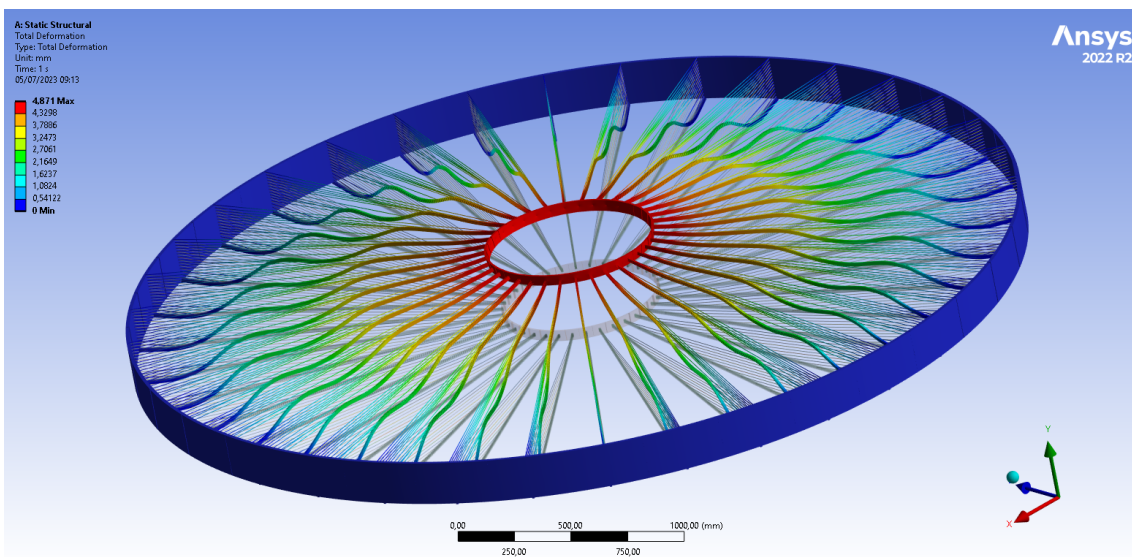


Figure 7.16: Total deformation ( $4.871 \text{ mm}$ ) of the drift chamber subjected to linearly varying pressure and prestress with outer cylinders completely fixed

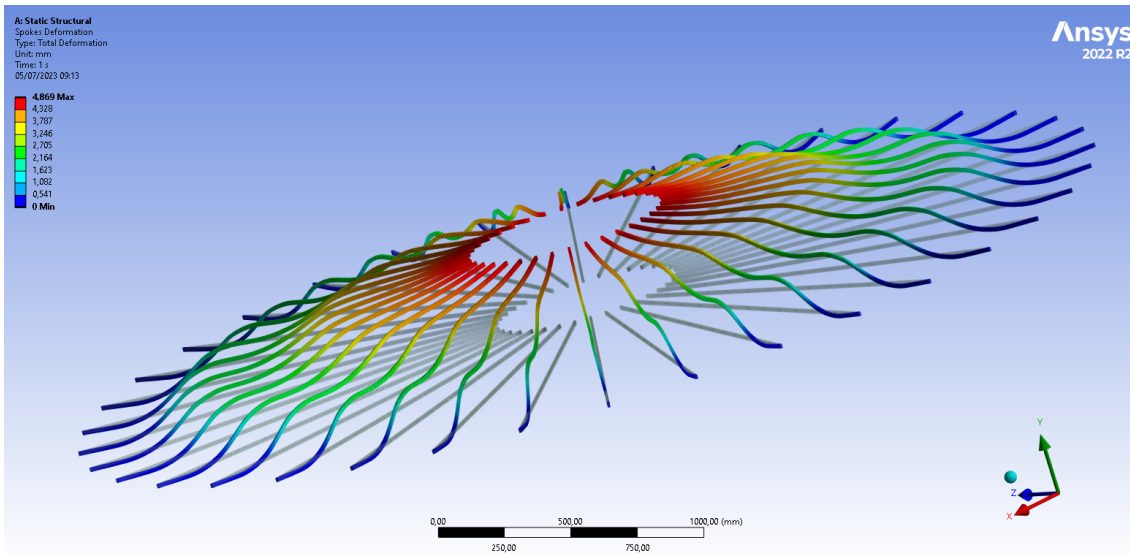


Figure 7.17: Total deformation of the spokes ( $4.869\text{ mm}$ ) subjected to linearly varying pressure and prestress with outer cylinders completely fixed.

## 7.7 Conclusion

Accurate definition of contacts is an important aspect in the analysis of composites structures. In our study, we examined the contacts in parallel with the response of the monolithic model to ensure consistent behaviour between both models. Another significant aspect is the impact of boundary conditions on the overall deformation of the spokes. It is essential to thoroughly evaluate the boundary conditions before applying optimization algorithms, as otherwise, a significant amount of computational resources would be wasted.

# Chapter 8

## Failure Analysis of Composites

Composites demonstrate exceptional mechanical strength and lightweight characteristics making them an attractive choice for structural applications, offering the potential for enhanced performance and improved efficiency. However, despite the numerous advantages offered by composites, their intricate nature and heterogeneous structure can pose challenges in understanding their failure mechanisms. The analysis of failures in composite materials is considerably more intricate compared to isotropic materials. This increased complexity arises from their orthotropic material behavior and the presence of various potential failure modes, which can involve different types of fiber or matrix failure. Numerous failure criteria exist to evaluate and, in certain instances, anticipate distinct failure modes. This chapter focuses on the failure analysis of the composite using various independent and polynomial criterion.

### 8.1 Failure criterion

Different failure criteria can be used to predict the strength of materials and material systems under multiaxial loads. These criteria establish a relationship between the material's strength limits, typically defined for uniaxial tension-compression and shear, and the overall stress-strain state resulting from multiaxial loads. Failure criteria are often presented as mathematical expressions known as failure criterion functions  $f$ . These functions depend on the stresses (or strains) and the material's strength.

### 8.1.1 Maximum strain criterion

The maximum strain criterion involves assessing the ratios between actual strains and failure strains in the principal coordinate system of the ply. This criterion is formulated as a function that determines failure.

$$f = \max \left( \left| \frac{\varepsilon_1}{X_\varepsilon} \right|, \left| \frac{\varepsilon_2}{Y_\varepsilon} \right|, \left| \frac{\varepsilon_3}{Z_\varepsilon} \right|, \left| \frac{\gamma_{12}}{S_\varepsilon} \right|, \left| \frac{\gamma_{13}}{R_\varepsilon} \right|, \left| \frac{\gamma_{23}}{Q_\varepsilon} \right| \right) \quad (8.1)$$

where:

$$\varepsilon_1 \geq 0 \Rightarrow X_\varepsilon = X_{\varepsilon t}; \varepsilon_1 < 0 \Rightarrow X_\varepsilon = X_{\varepsilon c}$$

$$\varepsilon_2 \geq 0 \Rightarrow Y_\varepsilon = Y_{\varepsilon t}; \varepsilon_2 < 0 \Rightarrow Y_\varepsilon = Y_{\varepsilon c}$$

$$\varepsilon_3 \geq 0 \Rightarrow Z_\varepsilon = Z_{\varepsilon t}; \varepsilon_3 < 0 \Rightarrow Z_\varepsilon = Z_{\varepsilon c}$$

### 8.1.2 Maximum stress criterion

The maximum stress criterion involves assessing the ratios between actual stress and failure stress in the principal coordinate system of the ply. This criterion is formulated as a function that determines failure.

$$f = \max \left( \left| \frac{\sigma_1}{X} \right|, \left| \frac{\sigma_2}{Y} \right|, \left| \frac{\sigma_3}{Z} \right|, \left| \frac{\tau_{12}}{S} \right|, \left| \frac{\tau_{13}}{R} \right|, \left| \frac{\tau_{23}}{Q} \right| \right) \quad (8.2)$$

where:

$$\sigma_1 \geq 0 \Rightarrow X = X_t \quad ; \sigma_1 < 0 \Rightarrow X = X_c$$

$$\sigma_2 \geq 0 \Rightarrow Y = Y_t \quad ; \sigma_2 < 0 \Rightarrow Y = Y_c$$

$$\sigma_3 \geq 0 \Rightarrow Z = Z_t \quad ; \sigma_3 < 0 \Rightarrow Z = Z_c$$

### 8.1.3 Quadratic Failure Criteria

Quadratic failure criteria combines all stress or strain components into a single expression. Several widely utilized criteria fall under the category of quadratic criteria, which are fully interactive in nature. The typical representation of quadratic criteria involves a second-order polynomial equation.

$$f = F_{11}\sigma_1^2 + F_{22}\sigma_2^2 + F_{33}\sigma_3^2 + F_{44}\tau_{23}^2 + F_{55}\tau_{13}^2 + F_{66}\tau_{12}^2 + 2F_{12}\sigma_1\sigma_2 + 2F_{23}\sigma_2\sigma_3 + 2F_{13}\sigma_1\sigma_3 + F_1\sigma_1 + F_2\sigma_2 + F_3\sigma_3 \quad (8.3)$$

In plane stress-state ( $\sigma_3 = 0$ ), the polynomial reduces to the simpler form

$$f = F_{11}\sigma_1^2 + F_{22}\sigma_2^2 + F_{66}\tau_{12}^2 + 2F_{12}\sigma_1\sigma_2 + F_1\sigma_1 + F_2\sigma_2 \quad (8.4)$$

The quadratic failure criteria in ACP (such as Tsai-Wu, Tsai-Hill, and Hoffman) exhibit differences in the definitions of the coefficients, represented as  $F_{ij}$  and  $F_I$ . The objective of determining these coefficients is to ensure that the failure criterion function corresponds to the material strength under a unidirectional stress condition. Nevertheless, it is worth mentioning that not all coefficients can be determined through this approach.

## 8.2 Tsai-Wu Failure Criterion

For the plane stress-state, the Tsai-Wu criterion coefficients  $F$  have the values

$$\begin{aligned} F_{11} &= \frac{1}{X_t X_c} \\ F_{22} &= \frac{1}{Y_t Y_c} \\ F_{44} &= \frac{1}{Q^2} \\ F_{66} &= \frac{1}{S^2} \\ F_1 &= \frac{1}{X_t} - \frac{1}{X_c} \\ F_2 &= \frac{1}{Y_t} - \frac{1}{Y_c} \\ F_{55} &= \frac{1}{R^2} \end{aligned} \quad (8.5)$$

Thus, the criterion can be written as:

$$f = \frac{\sigma_1^2}{X_t X_c} + \frac{\sigma_2^2}{Y_t Y_c} + \frac{\tau_{23}^2}{Q^2} + \frac{\tau_{13}^2}{R^2} + \frac{\tau_{12}^2}{S^2} + \left( \frac{1}{X_t} - \frac{1}{X_c} \right) \sigma_1 + \left( \frac{1}{Y_t} - \frac{1}{Y_c} \right) \sigma_2 + 2F_{12}\sigma_1\sigma_2 \quad (8.6)$$



The coefficient  $F_{12}$  cannot be obtained directly from the failure stresses of uniaxial load cases. For accurate results it should be determined through biaxial load tests. In practice, it is often given in the form of a non-dimensional interaction coefficient:

$$F_{12}^* = \frac{F_{12}}{\sqrt{(F_{11}F_{22})}} \quad (8.7)$$

To ensure that the criterion represents a closed conical failure surface, the value of  $F_{12}^*$  must be within the range  $-1 < F_{12}^* < 1$ . However, the value range for physically meaningful material behavior is more limited. The often used value  $-\frac{1}{2}$  corresponds to a "generalized Von Mises criterion". The final Tsai-Wu constant  $2F_{12}^*$  becomes -1. Similarly  $2F_{13}$ ,  $2F_{23}$  can be dealt with using the corresponding values  $F_{12}^*$  and  $F_{23}$ , which leads to the Tsai-Wu 3-D expression:

$$\begin{aligned} f = & \frac{\sigma_1^2}{X_t X_c} + \frac{\sigma_2^2}{Y_t Y_c} + \frac{\sigma_3^2}{Z_t Z_c} + \frac{\tau_{12}^2}{S_{xy}^2} + \frac{\tau_{13}^2}{S_{xz}^2} + \frac{\tau_{23}^2}{S_{yz}^2} \\ & - 1.0 \frac{\sigma_1 \sigma_2}{\sqrt{X_t X_c Y_t Y_c}} - 1.0 \frac{\sigma_2 \sigma_3}{\sqrt{Y_t Y_c Z_t Z_c}} - 1.0 \frac{\sigma_1 \sigma_3}{\sqrt{X_t X_c Z_t Z_c}} \\ & + \sigma_1 \left( \frac{1}{X_t} - \frac{1}{X_c} \right) + \sigma_2 \left( \frac{1}{Y_t} - \frac{1}{Y_c} \right) + \sigma_3 \left( \frac{1}{Z_t} - \frac{1}{Z_c} \right) \end{aligned} \quad (8.8)$$

In ACP, the Tsai-Wu constants are:

$$2F_{12} = XY, \text{ default } -1$$

$$2F_{13} = XZ, \text{ default } -1$$

$$2F_{23} = YZ, \text{ default } -1$$

### 8.3 Tsai-Hill Failure Criterion

Depending on the loading condition, the Tsai-Hill criterion utilizes either the tensile or compressive strengths to determine the coefficients. The coefficients are :

$$\begin{aligned}
 F_{11} &= \frac{1}{X^2} \\
 F_{22} &= \frac{1}{Y^2} \\
 F_{44} &= \frac{1}{Q^2} \\
 F_1 &= 0 \\
 F_2 &= 0 \\
 F_{55} &= \frac{1}{R^2} \\
 F_{12} &= -\frac{1}{2X^2} \\
 F_{66} &= \frac{1}{S^2}
 \end{aligned} \tag{8.9}$$

where the values of  $X$  and  $Y$  are ;

$$\begin{aligned}
 \sigma_1 \geq 0 &\Rightarrow X = X_t \\
 \sigma_1 < 0 &\Rightarrow X = X_c \\
 \sigma_2 \geq 0 &\Rightarrow Y = Y_t \\
 \sigma_2 < 0 &\Rightarrow Y = Y_c
 \end{aligned}$$

The Tsai-Hill failure criterion differentiates between UD and woven plies. The Tsai-Hill failure criterion function for UD plies can be written in the form

$$f = \left(\frac{\sigma_1}{X}\right)^2 + \left(\frac{\sigma_2}{Y}\right)^2 + \left(\frac{\tau_{12}}{S}\right)^2 - \frac{\sigma_1\sigma_2}{X^2} \tag{8.10}$$

For woven plies, the function becomes

$$f = \left(\frac{\sigma_1}{X}\right)^2 + \left(\frac{\sigma_2}{Y}\right)^2 + \left(\frac{\sigma_{12}}{S}\right)^2 - 2H\sigma_1\sigma_2 \tag{8.11}$$

where,

$$H = \frac{1}{2} \left( \frac{1}{X^2} + \frac{1}{Y^2} \right) \quad (8.12)$$

For the full 3-D case another formulation can be used:

$$(G + H)\sigma_1^2 + (F + H)\sigma_2^2 + (F + G)\sigma_3^2 - 2H\sigma_1\sigma_2 - 2G\sigma_1\sigma_3 - 2F\sigma_2\sigma_3 \dots \dots + 2L\tau_{23}^2 + 2M\tau_{13}^2 + 2N\tau_{12}^2 = 1 \quad (8.13)$$

where,

$$\begin{aligned} F &= \frac{1}{2} \left( -\frac{1}{X^2} + \frac{1}{Y^2} + \frac{1}{Z^2} \right) \\ G &= \frac{1}{2} \left( \frac{1}{X^2} - \frac{1}{Y^2} + \frac{1}{Z^2} \right) \\ H &= \frac{1}{2} \left( \frac{1}{X^2} + \frac{1}{Y^2} - \frac{1}{Z^2} \right) \end{aligned} \quad (8.14)$$

## 8.4 Hoffman failure criterion

The Hoffman criterion defines the biaxial coefficients  $F_{12}$ ,  $F_{23}$ , and  $F_{13}$  with the following material strength expressions for the 3-D stress state:

$$\begin{aligned} F_{12} &= \frac{1}{(X_t X_c)} + \frac{1}{(Y_t Y_c)} - \frac{1}{(Z_t Z_c)} \\ F_{13} &= \frac{1}{(Z_t Z_c)} + \frac{1}{(X_t X_c)} - \frac{1}{(Y_t Y_c)} \\ F_{23} &= \frac{1}{(Y_t Y_c)} + \frac{1}{(Z_t Z_c)} - \frac{1}{(X_t X_c)} \end{aligned} \quad (8.15)$$

The Hoffman failure criterion for a 3-D stress state can be written as:

$$f = \frac{\sigma_1^2}{X_t X_c} + \frac{\sigma_2^2}{Y_t Y_c} + \frac{\sigma_3^2}{Z_t Z_c} + \frac{\tau_{12}^2}{S_{xy}^2} + \frac{\tau_{13}^2}{S_{xz}^2} + \frac{\tau_{23}^2}{S_{yz}^2} - F_{12}\sigma_1\sigma_2 - F_{23}\sigma_2\sigma_3 - F_{13}\sigma_1\sigma_3 + \frac{\sigma_1}{X_t X_c} + \frac{\sigma_2}{Y_t Y_c} + \frac{\sigma_3}{Z_t Z_c} \quad (8.16)$$

The biaxial coefficient  $F_{12}$  for the plane stress state reduces to:

$$F_{12} = \frac{1}{(X_t X_c)} \quad (8.17)$$

The entire Hoffman criterion in the plane stress case reduces to:

$$f = \frac{\sigma_1^2}{X_t X_c} + \frac{\sigma_2^2}{Y_t Y_c} + \frac{\tau_{12}^2}{S_{xy}^2} - F_{12} \sigma_1 \sigma_2 + \frac{\sigma_1}{X_t X_c} + \frac{\sigma_2}{Y_t Y_c} \quad (8.18)$$

## 8.5 Reserve factor

The reserve factor (Equation 8.19) serves as an indicator of the margin to failure in a system. Multiplying the applied load by the reserve factor yields the failure load. A reserve factor greater than one signifies a positive margin to failure, while a value less than one indicates a negative margin. It is important to note that reserve factors are always greater than zero.

$$RF \times F_{\text{applied}} = F_f \quad (8.19)$$

The critical values of reserve factors range between zero and one, while non-critical values range from one to infinity. In presentations of results, whether numerical or as contour plots, non-critical values are often emphasized over critical values. For practical purposes, the inverse reserve factor (Equation 8.20) is often preferred. The non-critical values range from zero to one, while the critical values extend beyond that range.

$$IRF = \frac{1}{RF} \quad (8.20)$$

An alternative term for the reserve factor, indicating the margin to failure, is the margin of safety. The margin of safety can be obtained from the corresponding reserve factor using the relationship shown in Equation 8.21. A positive margin of safety indicates the relative amount by which the applied load can be increased before reaching the failure load, while a negative margin of safety indicates the necessary reduction in the applied load. Margins of safety are typically expressed as percentages.

$$MoS = RF - 1 \quad (8.21)$$

## 8.6 Weighting Factors

In ACP (Advanced Composite Products), various failure criteria are available to predict the mode of failure, such as determining whether fiber or matrix failure occurs first. These failure criteria can be customized by assigning weighting factors to individual failure mode criteria, which allows for a bias towards or against a specific failure mode. This tuning of failure criteria enables the design to meet specific requirements. For instance, a design may prioritize a higher safety margin against delamination rather than fiber failure, leading to an increased weighting factor for delamination.

## 8.7 Results from the failure analysis

There are several failure criterion and each of them can be turned on at once (Figure 8.1). Except the LaRC, we turn on all the failure criteria and check for the inverse reserve factor, margin of safety and safety factor (Figure 8.2-8.6). In our drift chamber , the stresses and strain are well below the material’s strength. However, some failure modes are predicted and the notations are shown in Figure 8.2. Also no delamination occurs, as the Puck criterion is also satisfied.

<b>Definition</b>	
ID (Beta)	93901
Type	Composite Failure Tool
<b>Reference</b>	
Selected Criteria ID (Beta)	93902
Defined By	Direct Input
<b>Reinforced Ply Criteria</b>	
Maximum Strain	On
Maximum Stress	On
Tsai-Wu	On
Tsai-Hill	On
Hoffman	On
Hashin	On
Puck	On
LaRC	Off
Cuntze	On
<b>Sandwich Criteria</b>	
Face Sheet Wrinkling	Off
Core Failure	Off
Shear Crimping	Off
<b>Isotropic Material Criteria</b>	
Von Mises	Off

Figure 8.1: Various failure criterion are turned on to check the composite failure

## 6.1 Failure Criteria

### Failure Criteria Terms

- e = strain    s = stress
- 1 = material 1 direction
- 2 = material 2 direction
- 3 = out-of-plane normal direction
- 12 = in-plane shear
- 13 and 23 = out-of-plane shear terms
- I = principal I direction
- II = principal II direction
- III = principal III direction
- t = tension, c = compression

### Failure Mode Abbreviations in ACP

Maximum Strain Failure modes	e1t, e1c, e2t, e2c, e12
Maximum Stress	s1t, s1c, s2t, s2c, s3t, s3c, s12, s23, s13
Tsai-Wu 2D and 3D	tw
Tsai-Hill 2D and 3D	th
Hashin	hf (fiber failure) hm (matrix failure) hd (delamination failure)
Puck (simplified, 2D and 3D)	pf (fiber failure) pmA (matrix tension failure) pmB (matrix compression failure) pmC (matrix shear failure) pd (delamination)

Figure 8.2: Notations for various failures modes for composites [29].

### 8.7.1 Results: Inverse Reserve factor

Using all the criteria, the Inverse reserve factor is very low (Figure 8.3-8.6). The maximum value is 0.7 and the critical zone is between the inner cylinder and spokes. Also probable failure mode can be maximum strain criterion as shown by e2t.

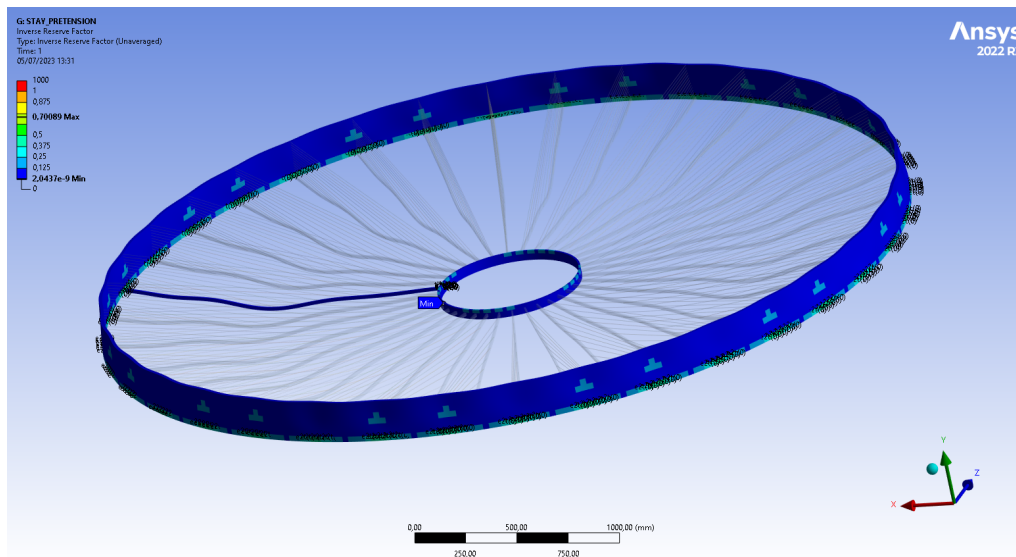


Figure 8.3: A very low inverse reserve factor indicating no failure in our composite

## CHAPTER 8. FAILURE ANALYSIS OF COMPOSITES

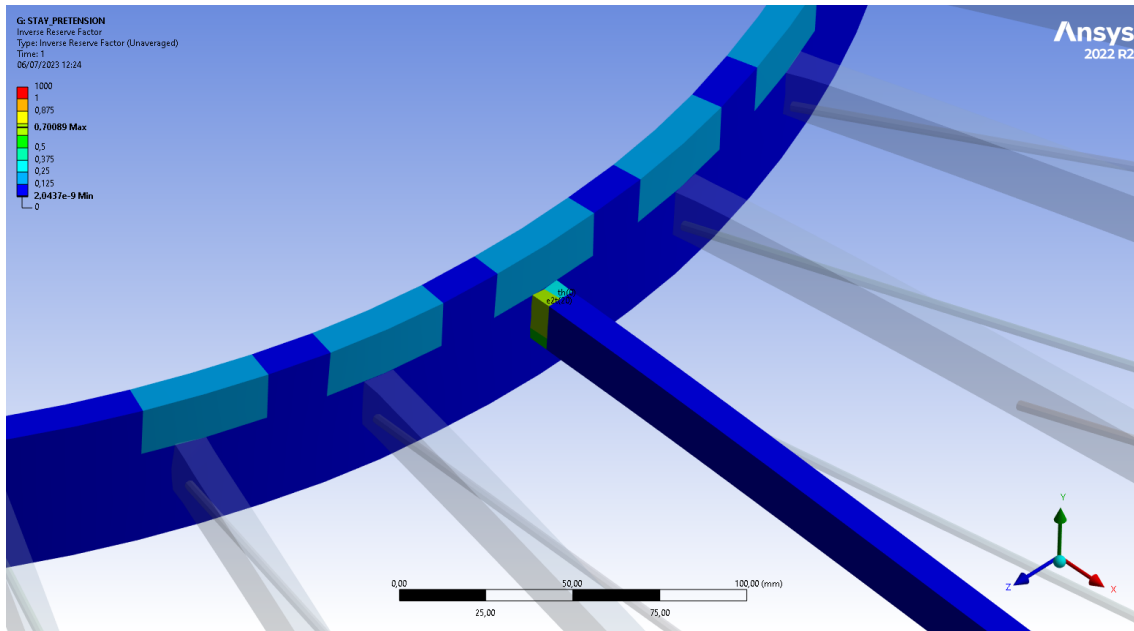


Figure 8.4: Maximum value of inverse reserve factor occurs at the contact between spokes and inner cylinder.

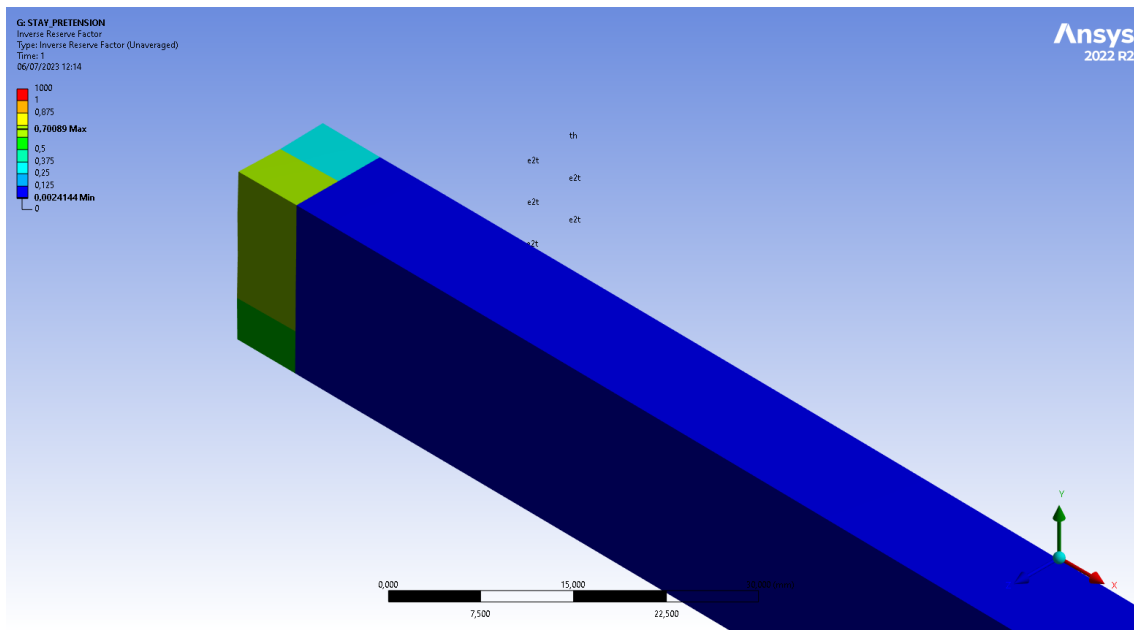


Figure 8.5: Possible Maximum strain failure mode ( $e2t$ ) and Tsai Hill ( $th$ ) failure in the spoke as given by inverse reserve factor.

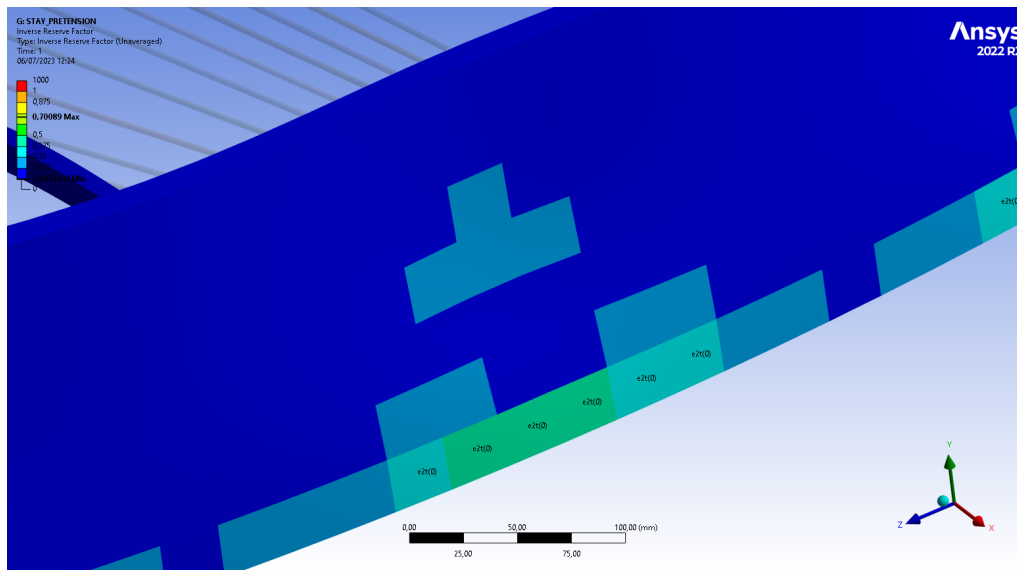


Figure 8.6: Possible Maximum strain failure mode ( $e_{2t}$ ) in the outer cylinder as given by inverse reserve factor.

### 8.7.2 Results: Safety margin

Safety margin in our structure is very high and the lowest value is 0.42 (Figure 8.7). Coherent with the inverse reserve factor, it also shows possible Maximum strain failure mode.

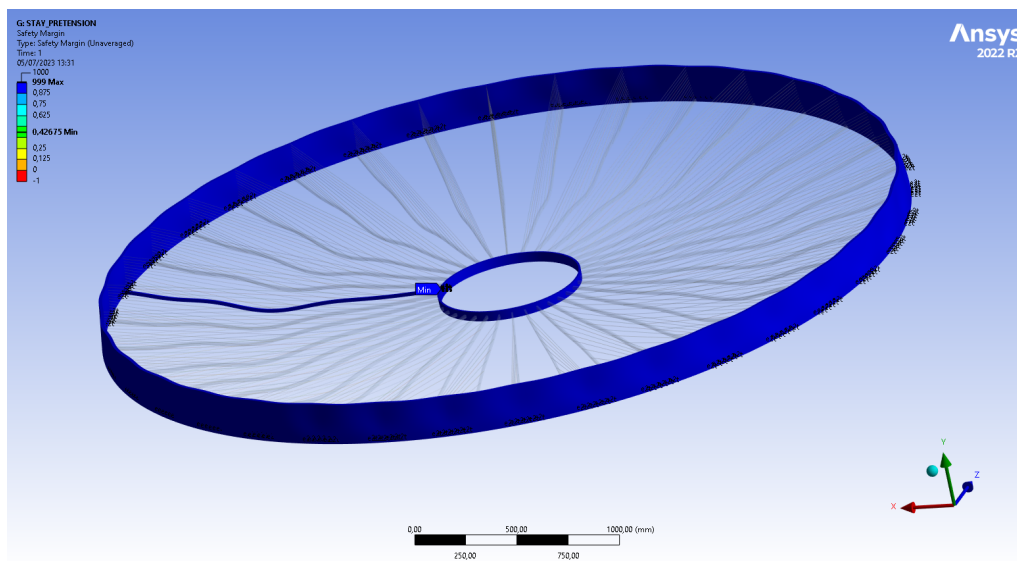


Figure 8.7: Safety margin in our composite drift chamber.



### 8.7.3 Results: Safety factor

Safety factor in our structure is very high and the lowest value is 1.42. Coherent with the inverse reserve factor and safety margin, it also shows possible Maximum strain failure mode.

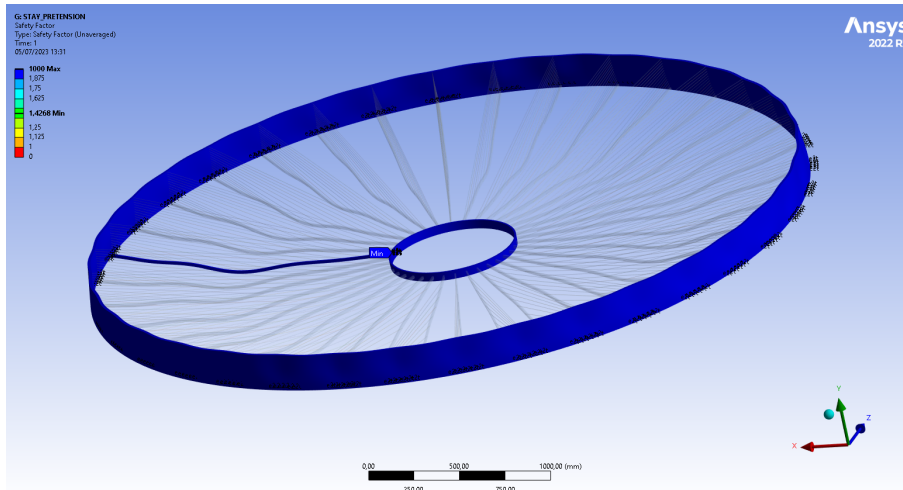


Figure 8.8: Safety factor in our composite drift chamber.

### 8.7.4 Results: Stress Analysis

The equivalent von-Mises stress is maximum at the contact between the outer cylinder and the spokes. The von-Mises stress is reported on the entire spoke (Figure 8.9) rather than on each ply. In order to calculate the stresses at ply level, we use the normal stress for which the solution is reported in element coordinate system. The results are shown in Figure 8.10-8.12.

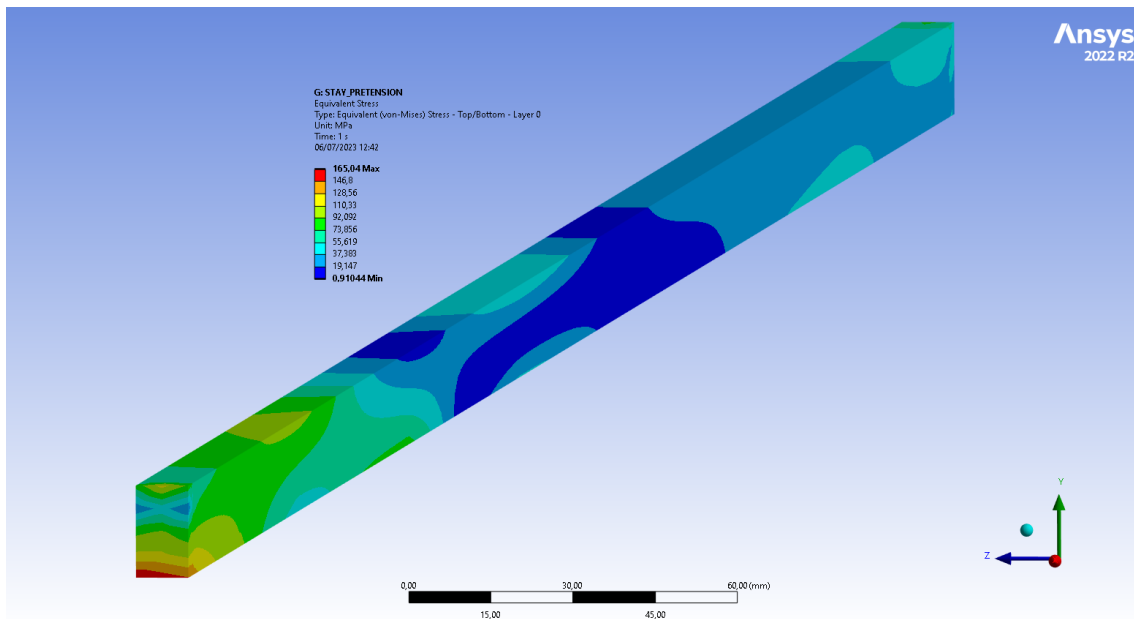


Figure 8.9: Equivalent von-Mises stress calculated on the entire spoke.

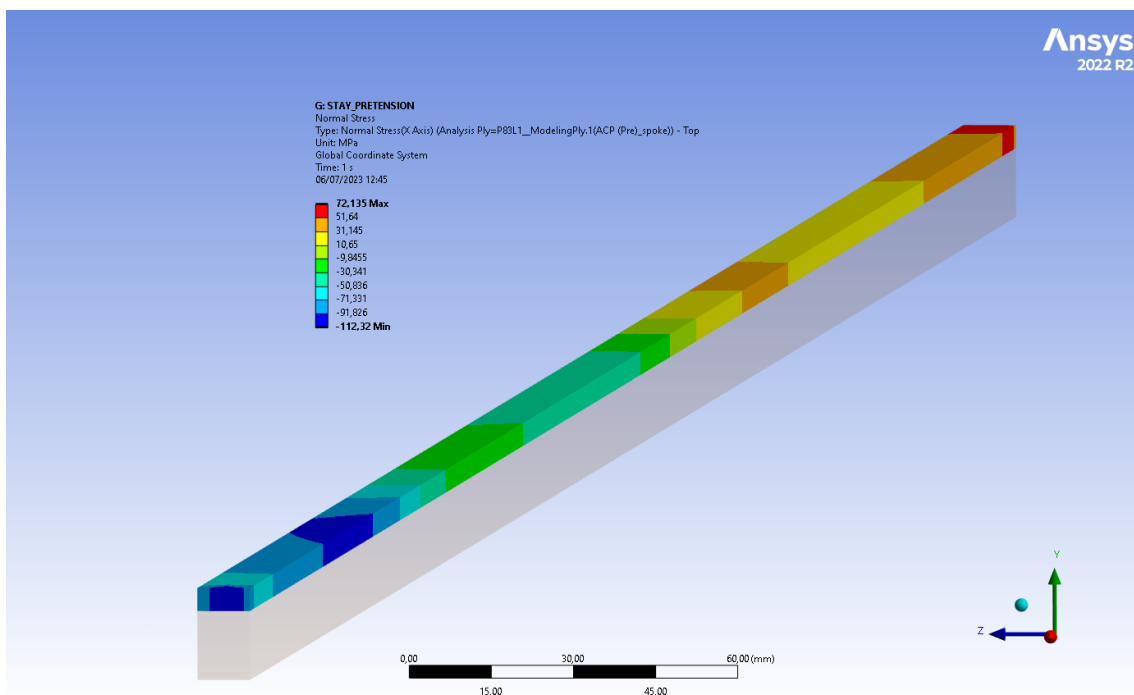


Figure 8.10: Normal stress on the Top ply reported in element coordinate system (X-axis).

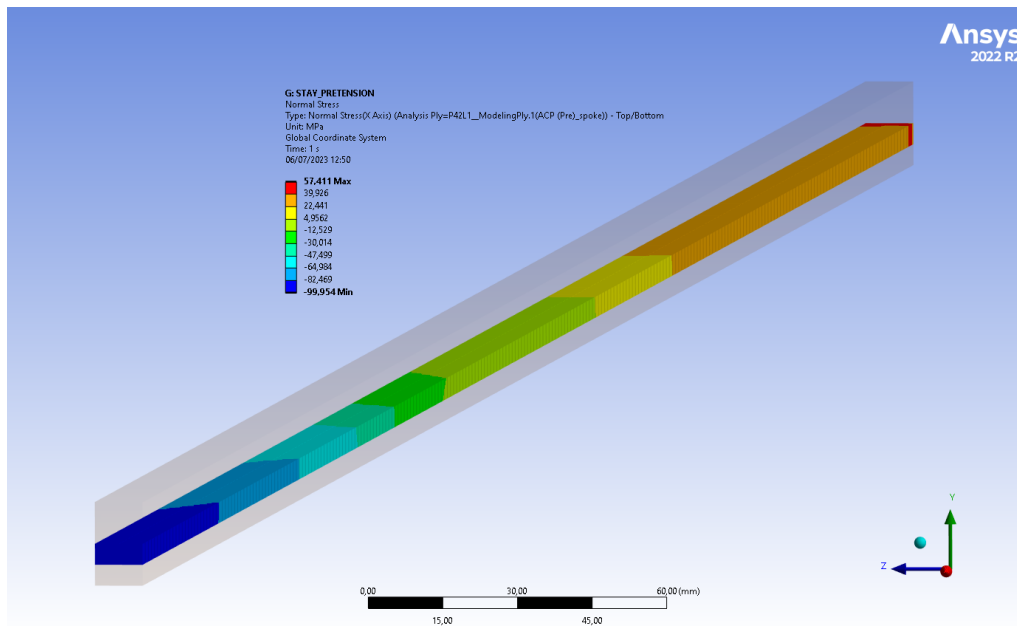


Figure 8.11: Normal stress on the Top middle reported in element coordinate system (X-axis).

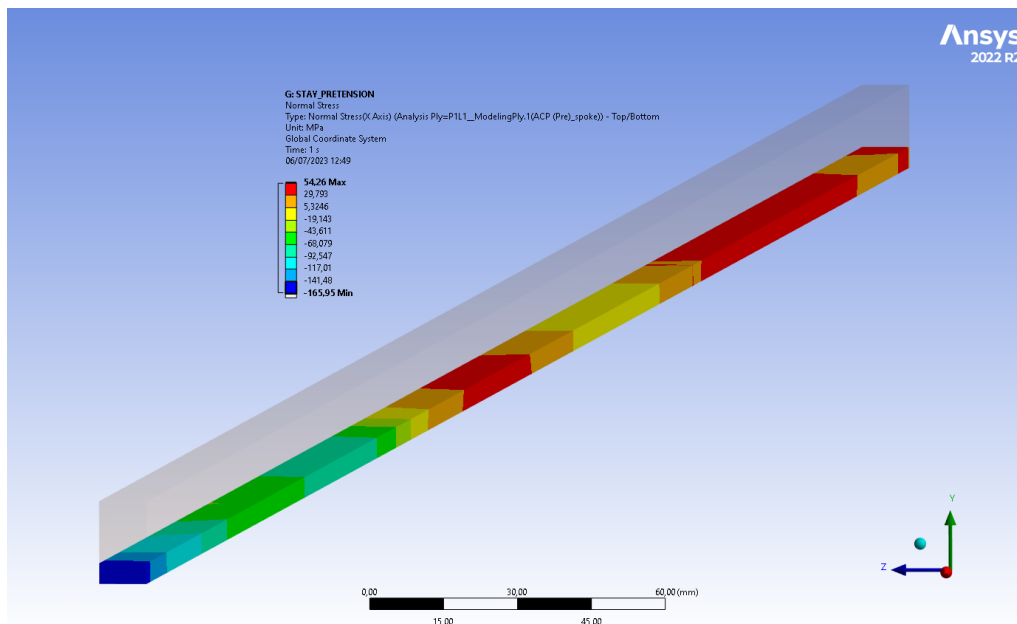


Figure 8.12: Normal stress on the Top bottom reported in element coordinate system (X-axis).

For the outer and inner cylinders, only the equivalent von-Mises stress is reported. The

results are shown in Figure 8.13-8.14.

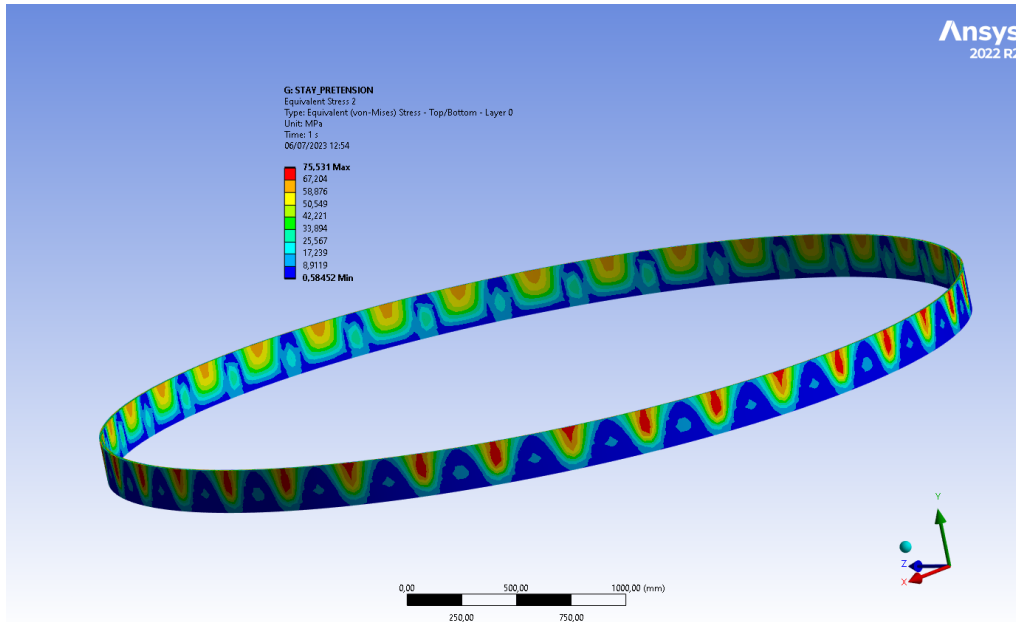


Figure 8.13: Equivalent von-Mises stress calculated on the outer cylinder.

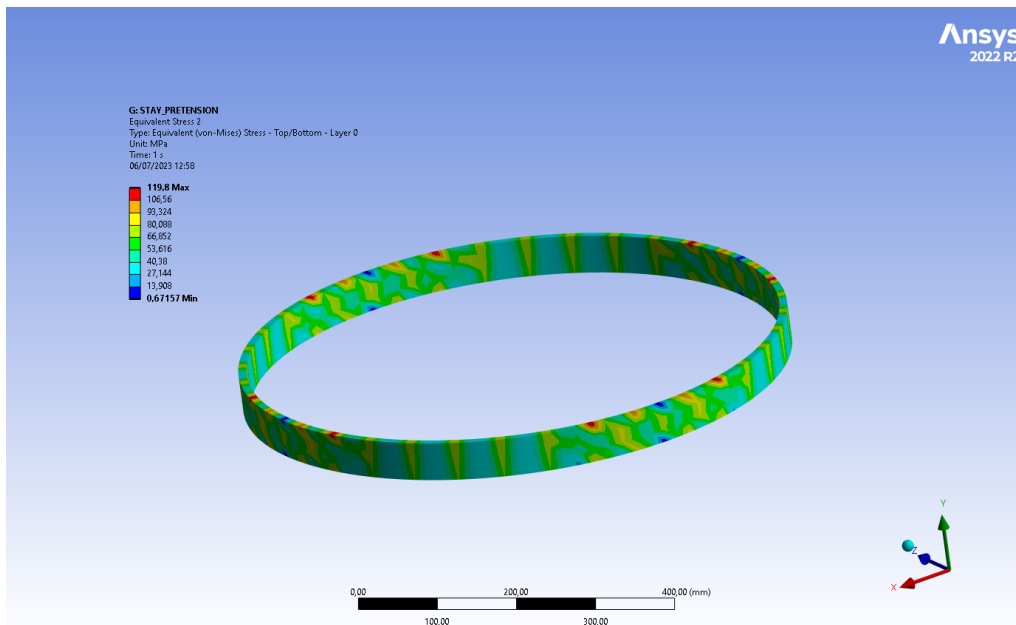


Figure 8.14: Equivalent von-Mises stress calculated on the inner cylinder.

## **8.8 Conclusion**

By utilizing different failure criteria, it becomes evident that the composite structure remains safe and free from delamination. While there are higher stresses observed at the interfaces, it is plausible that they are a result of stress concentration. The composite analysis provides only unaveraged results only and the high stress areas being very small in size and within safety margin, we choose to overlook this detail.

# Chapter 9

## Buckling Analysis

Structural stability is a crucial aspect of engineering design, ensuring that structures can withstand applied loads and maintain their integrity. Buckling analysis is a fundamental tool used to assess the stability of various structural components, ranging from slender columns to complex shell structures. Buckling refers to the sudden and catastrophic failure of a structure under compressive loads, leading to the loss of its load-carrying capacity. Understanding and predicting buckling behavior is essential for us to ensure the safety and reliability of this drift chamber. The primary objective of this chapter is to provide a comprehensive introduction, methodology and results obtained from linear and nonlinear buckling analysis. We will delve into the fundamental concepts, theories, and numerical techniques used in both approaches.

### 9.1 Introduction

Buckling refers to a structural instability phenomenon that occurs when a slender component or structure fails under compressive loads. It is characterized by sudden and excessive lateral deflections or deformations that lead to a loss of load-carrying capacity and structural failure.

In structural engineering, buckling is a critical consideration as it can result in catastrophic consequences if not properly addressed. Understanding the concept of buckling

involves examining the equilibrium between compressive forces and the structural stiffness. When the applied compressive load exceeds a critical threshold, the structure becomes unstable and experiences a rapid lateral deflection or deformation, often accompanied by a reduction in load-carrying capacity.

The concept of buckling can be illustrated using a simple example of a slender column. When a column is subjected to a compressive load, the tendency is for it to deform elastically, resulting in a uniform reduction in length without any significant lateral deflection. However, as the compressive load increases, the column's behavior changes. Beyond a certain critical load, the column becomes unstable, and a slight lateral deflection initiates a buckling mode of deformation. The lateral deflection grows rapidly, and the column loses its ability to support additional load, leading to its failure.

Buckling can occur in various structural components, including columns, beams, plates, shells, and other slender members. It is influenced by several factors, such as the material properties, geometric imperfections, boundary conditions, and the presence of initial stresses. Analyzing and predicting buckling behavior is crucial for ensuring the structural integrity and safety of engineering systems.

To assess and analyze buckling, engineers employ various analytical and numerical techniques. Linear buckling analysis assumes small deflections and linear material behavior, while nonlinear buckling analysis considers large deformations and accounts for material and geometric nonlinearity. These analyses involve determining critical loads, buckling modes, and the response of the structure after buckling, allowing engineers to design structures that can withstand compressive loads and maintain stability. In ANSYS, there are two distinct techniques available to predict the buckling load and buckling mode shape of a structure. These methods are nonlinear buckling analysis and eigenvalue (or linear) buckling analysis. It is essential to have a clear understanding of the differences between these techniques because they can yield markedly different results (see Figure 9.1).

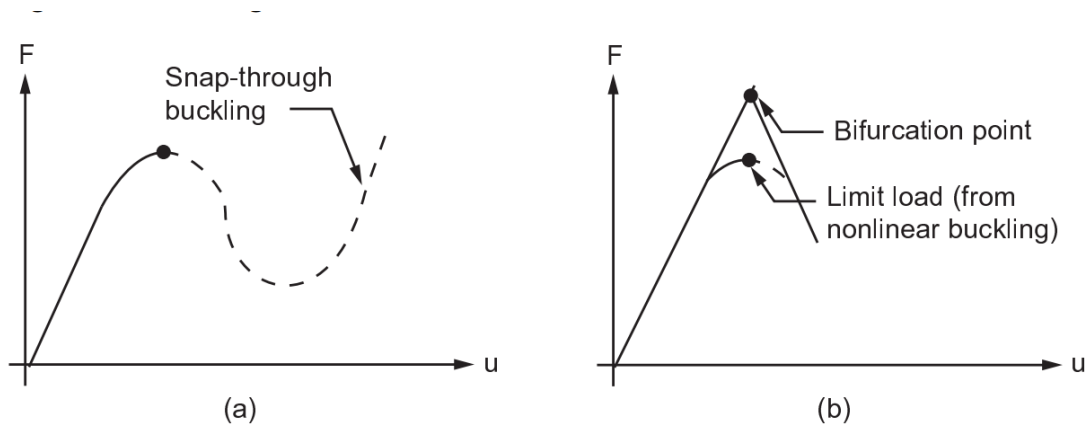


Figure 9.1: (a) Non linear load deflection curve (b) Linear (Eigenvalue) buckling curve. Adapted from *ANSYS Inc. ANSYS mechanical user's guide, 2019 [29]*.

## 9.2 Linear Buckling Theory

Linear buckling theory, also known as linear elastic buckling theory or Euler's buckling theory, is a fundamental approach used to analyze the stability of slender structural components under compressive loads. It provides a simplified and approximate method for predicting the critical buckling load and mode of deformation in linear elastic materials.

The underlying assumption in linear buckling theory is that the structural behavior remains within the linear elastic range, where the material properties and deformation are assumed to have a linear relationship. This assumption allows for the application of basic principles of mechanics and simplifies the analysis by neglecting geometric nonlinearity and large deformations.

The key concept in linear buckling theory is Euler's formula, which relates the critical buckling load to the properties of the structural member. For a perfectly straight and uniform column, Euler's formula states that the critical buckling load is given by:

$$P_{\text{critical}} = \frac{\pi^2 \cdot E \cdot I}{L_{\text{effective}}^2} \quad (9.1)$$



where;

$P_{\text{critical}}$  is the critical buckling load,

$E$  is the modulus of elasticity of the material,

$I$  is the moment of inertia of the cross-sectional area of the column,

$L_{\text{effective}}$  is the effective length of the column.

Euler's formula demonstrates that the critical buckling load is inversely proportional to the square of the effective length of the column. Longer columns have lower critical buckling loads compared to shorter columns with the same material and cross-sectional properties.

Linear buckling theory also provides insights into the mode of deformation associated with buckling. The mode shapes, or buckling modes, are sinusoidal functions that represent the shape of the deformed column under the critical buckling load. These modes are characterized by specific wavelengths and nodal patterns. While linear buckling theory provides valuable approximations for analyzing the stability of slender components, it has limitations. It assumes linear material behavior, neglects geometric imperfections, and does not account for post-buckling behavior. For more accurate predictions, nonlinear buckling analysis methods that consider material and geometric nonlinearity are employed. Nonetheless, linear buckling theory serves as a useful starting point for understanding and estimating the critical buckling load and initial mode shapes of slender structures, guiding engineers in the design process and ensuring structural stability.

### 9.2.1 Results from Linear Buckling Analysis

Although we refer to this analysis as a linear buckling analysis, it is not entirely accurate because the link elements exhibit nonlinearity and the solver produces results only when large deflection is enabled. This implies that the method resembles linear buckling analysis, but the load factor must be determined using a nonlinear approach. In this section, our objective is not solely to calculate the buckling load for our composite model; we also

## CHAPTER 9. BUCKLING ANALYSIS

aim to examine different buckling modes while varying the thickness of the outer cylinder. Consideration must be given to the effects of prestress by turning it on. When conducting a linear buckling analysis, using unit loads are typically adequate, and there is no need to specify actual load values. The eigenvalues obtained from the analysis represent scaling factors relating to the buckling loads. Thus, when a unit load is applied, the load factors correspond to the buckling loads, and all loads are adjusted accordingly.

In an eigenvalue buckling analysis, it is possible for seemingly equivalent pressure and force loads to yield different predictions for buckling loads (Figure 9.2-9.7). This is due to the fact that pressure is considered as "follower" load, whereas the force defined by vectorial components maintains its direction. Only by thoroughly understanding the nature of the load, whether the application of force or pressure is required must be decided. We consider it more realistic to represent the load as pressure in our model. Also, in the non linear analysis the perturbation load must be added to the load multiplier. Hence, in our case, eventhough the lowest load multiplier is 0.47, it is actually 1.47 (Figure 9.5).

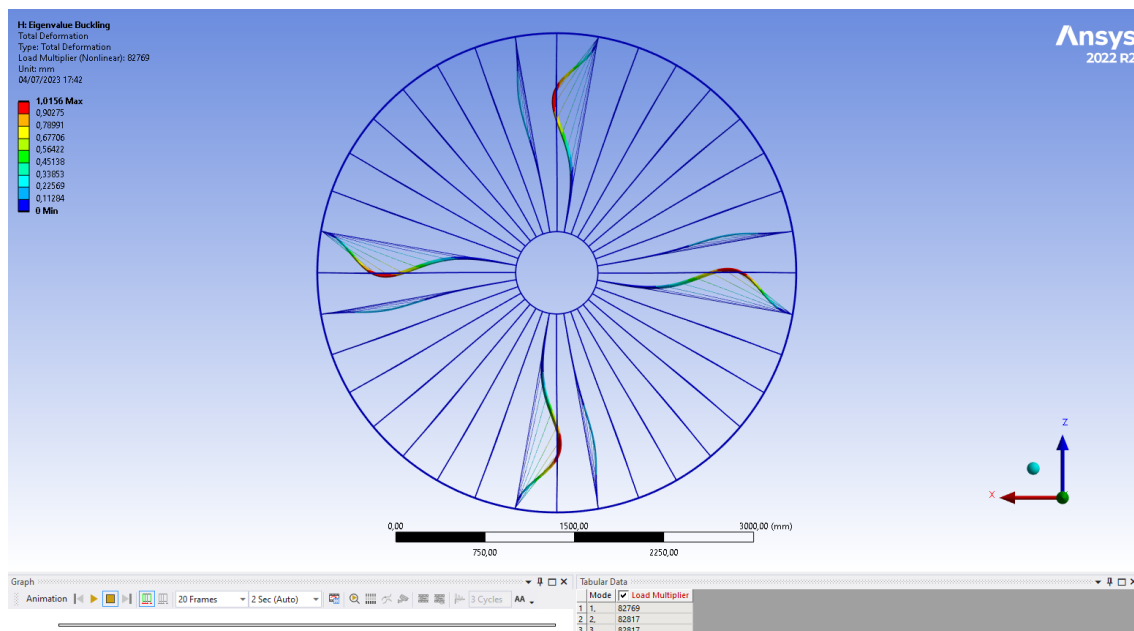


Figure 9.2: Buckling mode corresponding to first buckling load factor due to the application of force

## CHAPTER 9. BUCKLING ANALYSIS

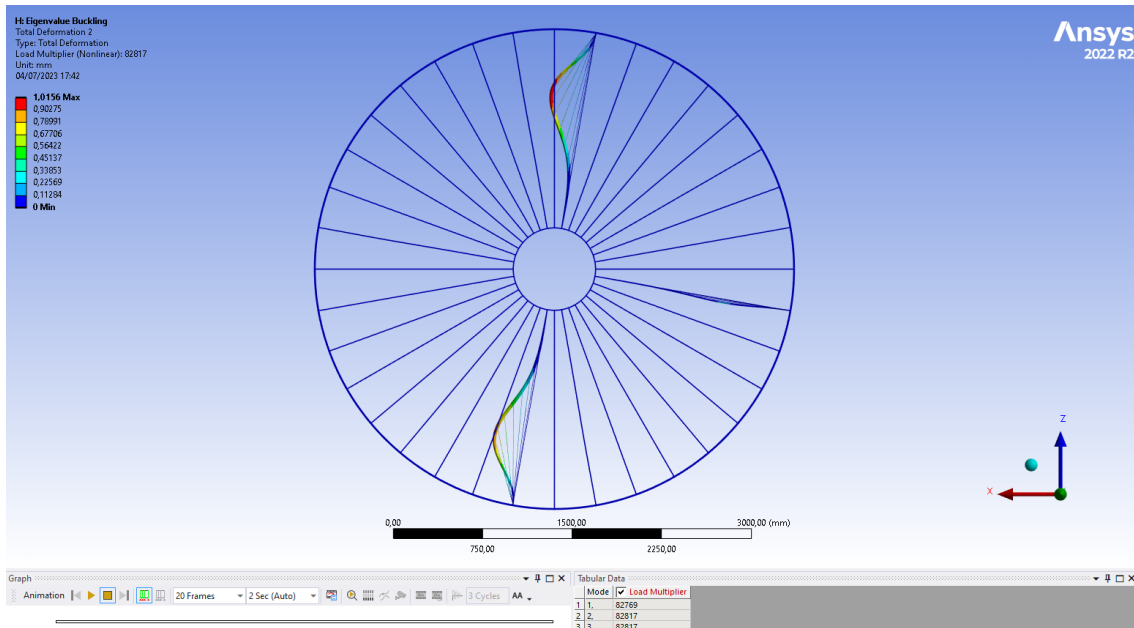


Figure 9.3: Buckling mode corresponding to second buckling load factor due to the application of force

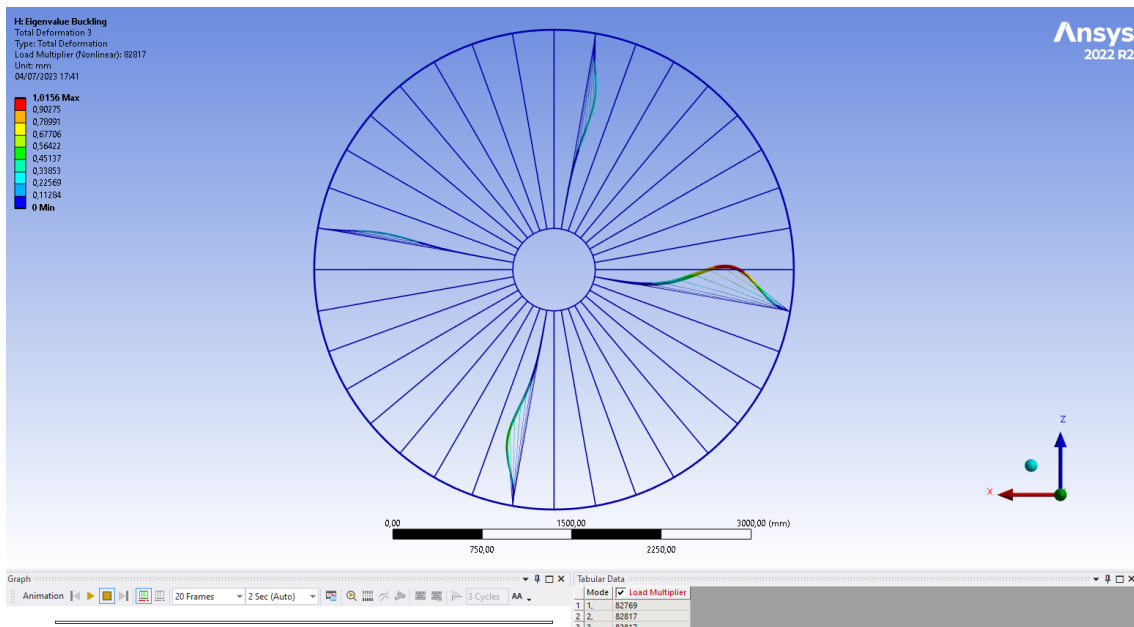


Figure 9.4: Buckling mode corresponding to third buckling load factor due to the application of force

## CHAPTER 9. BUCKLING ANALYSIS

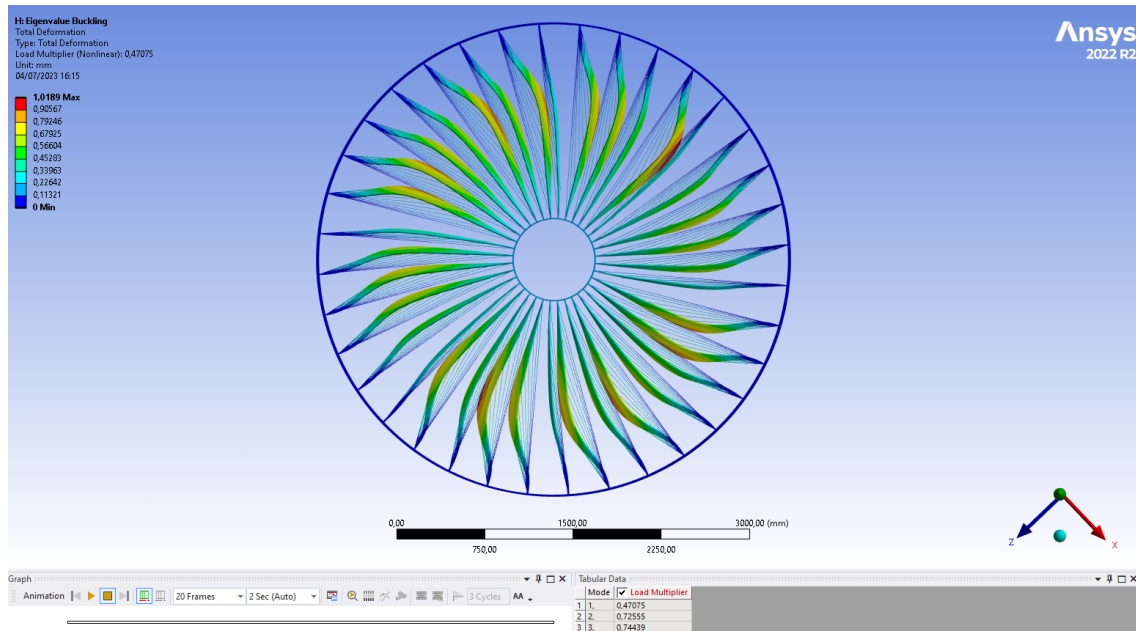


Figure 9.5: Buckling mode corresponding to first buckling load factor due to the application of uniformly varying pressure

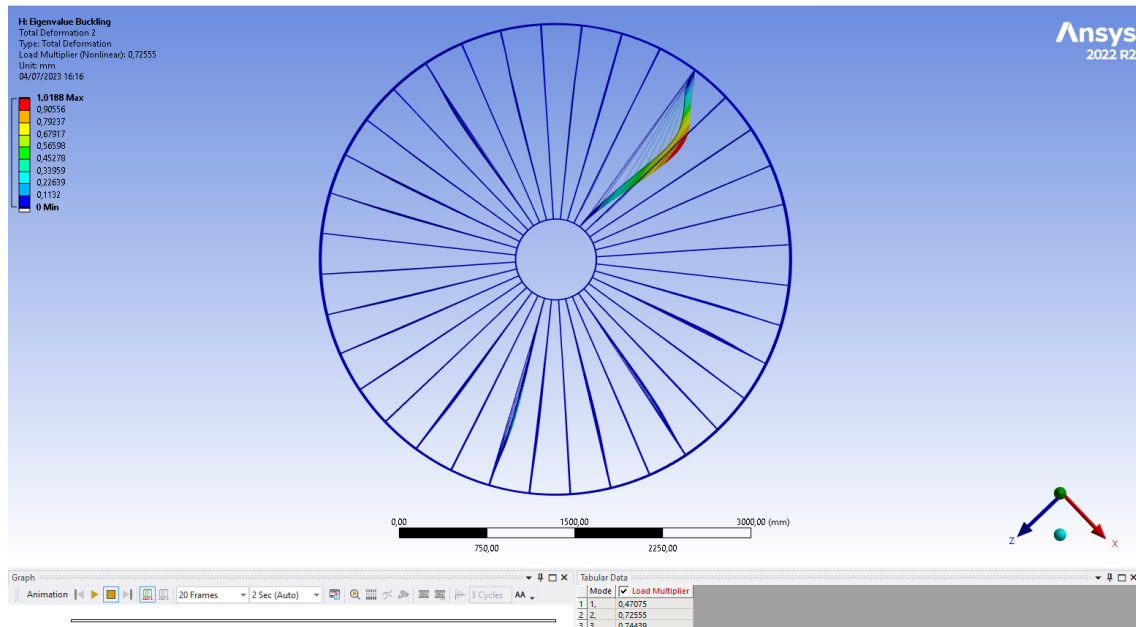


Figure 9.6: Buckling mode corresponding to second buckling load factor due to the application of uniformly varying pressure

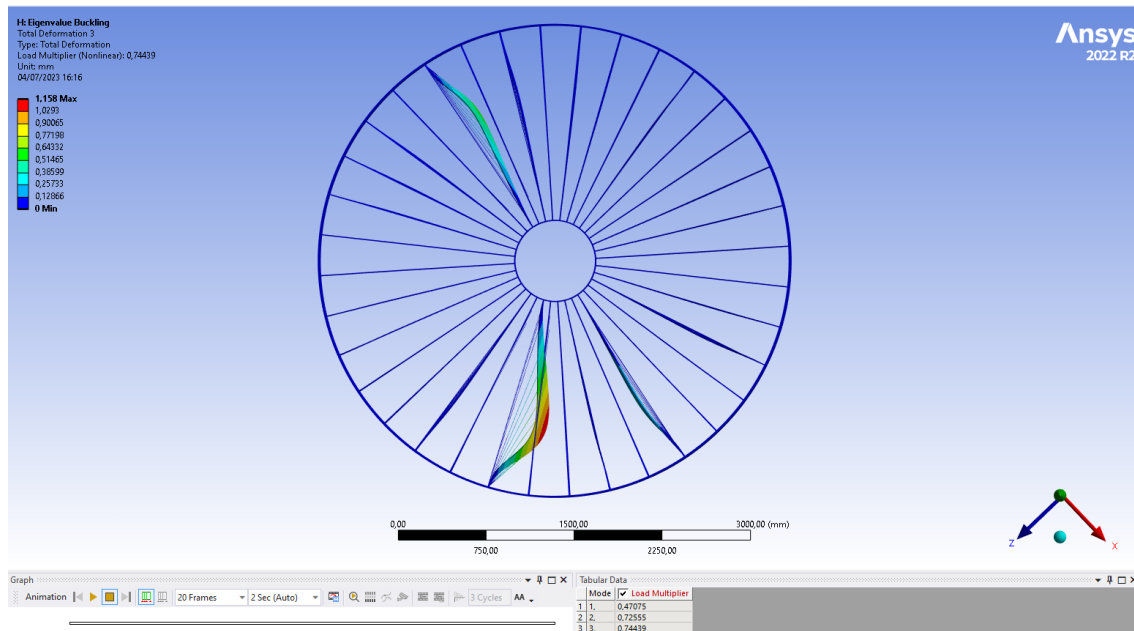


Figure 9.7: Buckling mode corresponding to third buckling load factor due to the application of uniformly varying pressure

It is worth noting that eigenvalues act as scaling factors for all loads. If certain loads remain constant (e.g., self-weight gravity loads), while others vary (e.g., externally applied loads), it is crucial to ensure that the stress stiffness matrix for the constant loads is not influenced by the eigenvalue solution.

### 9.2.2 Ovalization

The eigenvalue solution for a ring or cylindrical shell subjected to an external pressure can be written as:

$$v(\vartheta) = v_0 \cos 2\vartheta \tag{9.2}$$

This equation 9.2 illustrates the phenomenon known as ovalization, which is the deformation or alteration of a thin cylindrical or tubular structure, causing it to deviate from its initial circular form and take on an oval or elliptical shape (Figure 9.2). Ovalization commonly occurs when external loads or internal pressure are applied. In our case, the cables exert this external load causing the outer cylinder to buckle. It can be mathematically demonstrated that the second eigenshape, when of an even order, exhibits a configuration

with four lobes, as shown in Figure 9.2. In a broader context, the  $n^{\text{th}}$  eigenshape of even order will display  $2n$  lobes.

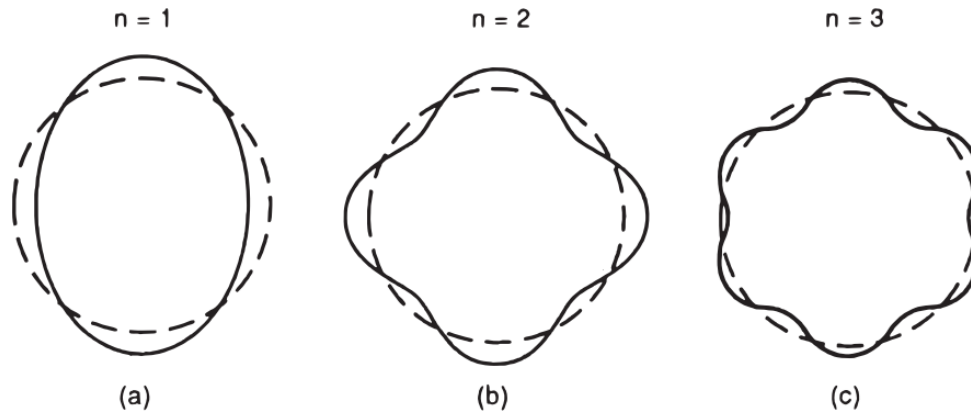


Figure 9.8: Eigenshapes of even order. Adapted from *Alberto Carpinteri. Advanced structural mechanics. CRC Press, 2017 [53].*

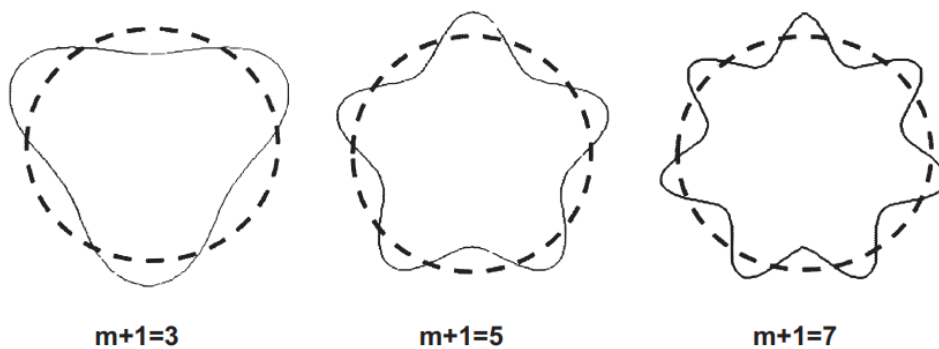


Figure 9.9: Eigenshapes of the odd order. Adapted from *Alberto Carpinteri. Advanced structural mechanics. CRC Press, 2017 [53].*

In our specific scenario (*thickness of outer cylinder 16 mm*) of linear buckling analysis, the failure primarily occurs in the spokes while the outer cylinder remains undamaged. Nevertheless, when the thickness of the outer cylinder is approximately around 10 mm to 13 mm, buckling starts to happen in the outer cylinder itself (see Figure 9.4-9.7).

## CHAPTER 9. BUCKLING ANALYSIS

Understanding this is crucial, as we need to not only evaluate the safety of the design but also anticipate potential failure modes and their interaction.

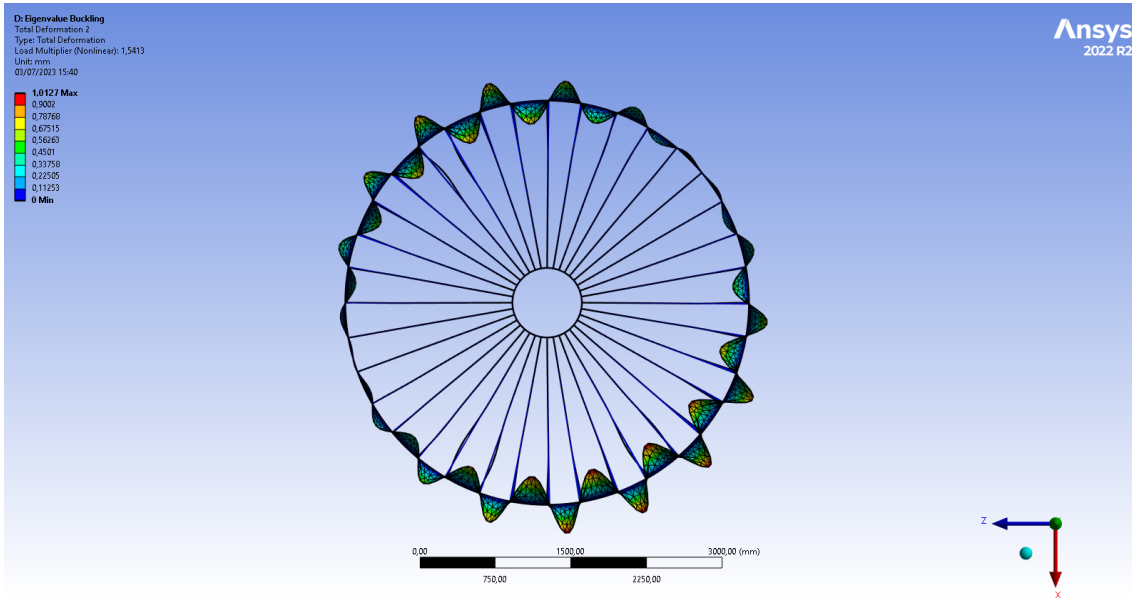


Figure 9.10: Buckling mode corresponding to first buckling load factor

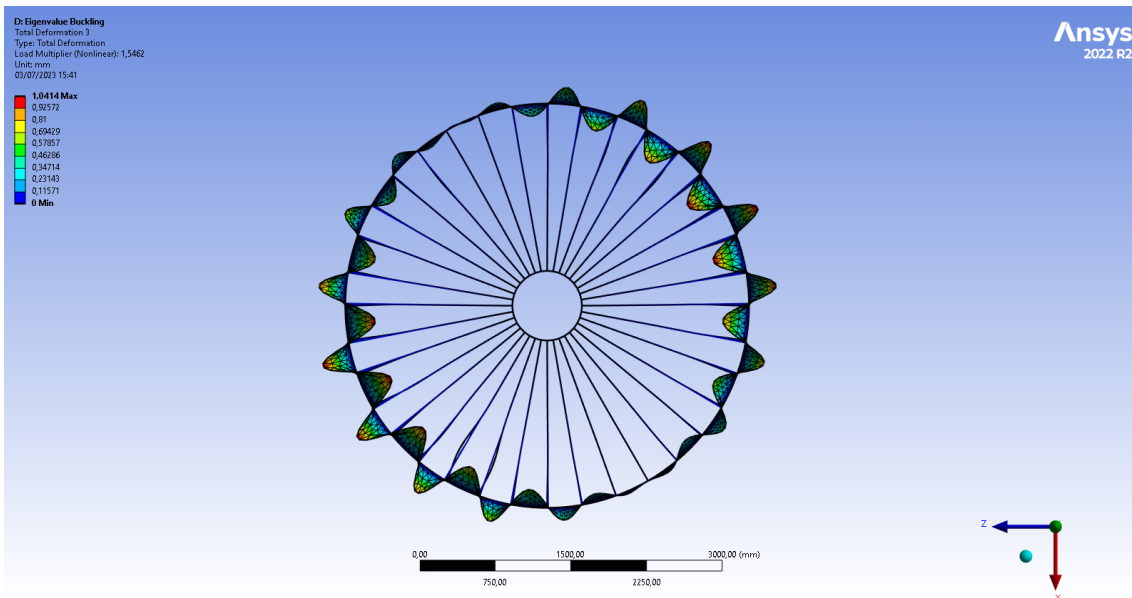


Figure 9.11: Buckling mode corresponding to first buckling load factor

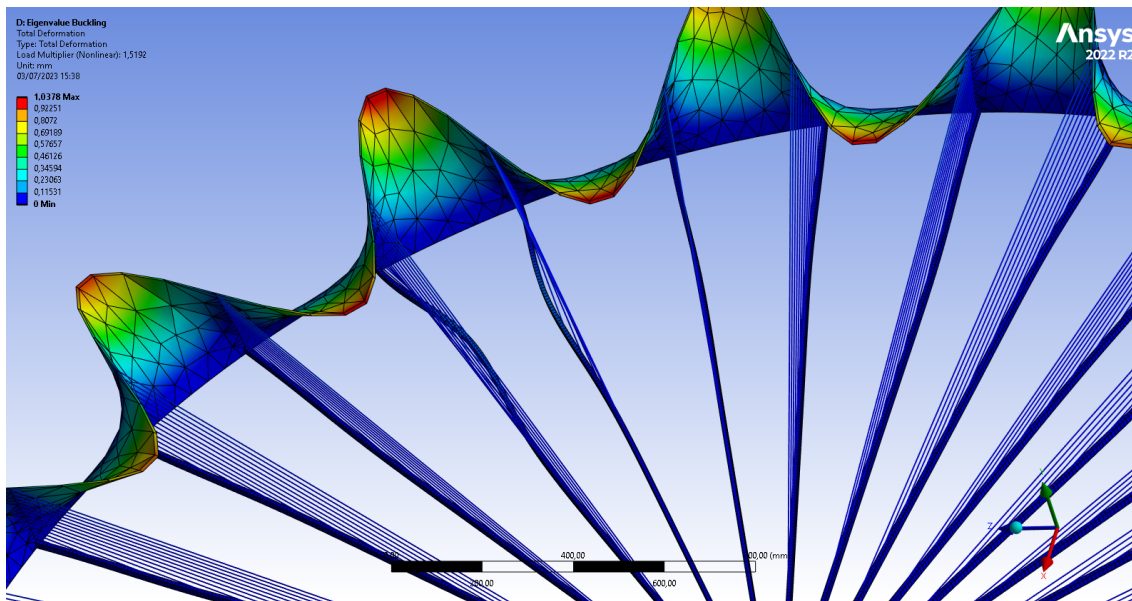


Figure 9.12: Buckling modes interact with the spokes and consequently spokes deform near the outer cylinder

### 9.3 Non linear Buckling Analysis

Nonlinear buckling analysis is a computational technique used to analyze the stability and behavior of structures under compressive loads when the structural response involves significant nonlinearities. Unlike linear buckling analysis, which assumes small deformations and linear material behavior, nonlinear buckling analysis considers large deformations, geometric nonlinearity, and material nonlinearity.

In many real-world scenarios, structural components experience large deformations and exhibit nonlinear behavior. This can arise from various factors, including material plasticity, large displacements, material strain hardening, contact and friction, and geometric imperfections. Nonlinear buckling analysis takes these factors into account to accurately predict the behavior of structures under compressive loads, particularly near and beyond the critical buckling load.



### 9.3.1 Applying Load Increments

In a nonlinear buckling analysis, the fundamental strategy involves incrementally increasing the applied loads until the solution starts to diverge. It is crucial to use a sufficiently small load increment as the applied loads approach the anticipated critical buckling load. Using a coarse load increment may result in an inaccurate prediction of the buckling load. To mitigate this issue, we can enable bisection and automatic time stepping as they can help prevent this problem [29].

### 9.3.2 Automatic Time Stepping

When automatic time stepping is enabled, the software automatically searches for the buckling load in a buckling analysis. In a static analysis with ramped loading, if the solution fails to converge at a specific load, the program utilizes load step increment bisection. It attempts a new solution at a lower load level. In a buckling analysis, such convergence failures are often accompanied by a "negative pivot" message, indicating that the load being attempted equals or exceeds the buckling load.

Typically, these "negative pivot" messages can be disregarded if the program successfully achieves a converged solution at the subsequent reduced load. The program continuously performs bisection and resolves the load until it reaches the point where the minimum time step increment is attained [29]. It is important to note that the precision of our results is directly influenced by the minimum time step.

### 9.3.3 Unconverged Solution

The inability to achieve convergence in a solution does not necessarily indicate that the structure has reached its maximum load. It could also be a result of numerical instability, which can be rectified by refining the modeling technique. To determine whether an unconverged load step signifies actual structural buckling or another issue, we have to track the load-deflection history of the structure's response.

To obtain an approximate value of the buckling load, a preliminary analysis can be conducted using the arc-length method [29]. This approximate value can then be compared to the more accurate value obtained through bisection. This comparison aids in determining if the structure has truly reached its maximum load. Alternatively, the arc-length method itself can be used to obtain a precise buckling load. However, this method necessitates manual adjustment of the arc-length radius through a series of directed reanalyses, involving trial-and-error iterations.

### 9.3.4 Performing a Nonlinear Buckling Analysis

If the loading applied to the structure is purely in-plane, meaning it only induces membrane or axial stresses, the analysis will not capture the development of out-of-plane deflections necessary for buckling initiation. To overcome this limitation, it is essential to introduce a small out-of-plane perturbation, such as a modest temporary force or specified displacement, to initiate the buckling response. Conducting a preliminary eigenvalue buckling analysis can help predict the mode shape of buckling and guide the placement of perturbations in order to stimulate the desired buckling response. It is crucial to ensure that the imperfection (perturbation) introduced aligns with the location and size of imperfections present in the real structure. The failure load is highly sensitive to these parameters. Following things must be considered while performing a nonlinear buckling analysis:

- 1) Forces and displacements should maintain their original orientation, while surface loads should be adjusted to "follow" the changing geometry of the structure as it deflects. Therefore, it is important to apply the appropriate type of loads.

- 2) It is necessary to continue the stability analysis until the critical load is identified to calculate the structure's factor of safety concerning nonlinear buckling. Merely establishing that a structure is stable at a specific load level is generally insufficient for most design practices, as a specified safety factor is usually required. This can only be

determined by establishing the actual limit load.

### 9.3.5 Performing a Post-Buckling Analysis

The post-buckling analysis is a continuation of the nonlinear buckling analysis. Once a load reaches its buckling value, the load can either remain unchanged or decrease, while the deformation continues to increase. In certain cases, after a certain amount of deformation, the structure may require additional loading to sustain further deformation, leading to a second buckling event. This cycle of increasing deformation and subsequent buckling can even repeat multiple times.

During the post-buckling stage, special techniques are necessary due to its unstable nature. Nonlinear stabilization methods can be employed for both local and global buckling, while the arc-length method is particularly useful for global buckling.

Performing a post-buckling analysis with nonlinear stabilization involves certain considerations. Since the buckling load is initially unknown, a standard nonlinear analysis can be conducted using automatic time stepping until the buckling load is reached or a convergence issue arises. At that point, stabilization can be activated during a multiframe restart to continue the analysis. If the deformation stabilizes at a later stage, the stabilization can be deactivated until the next buckling event occurs.

In cases where only local buckling occurs, the total load can still increase during buckling due to the redistribution of loading. Nonlinear stabilization is the applicable technique in such scenarios. However, it is important to note that nonlinear stabilization may not accurately detect the negative slope of a load-displacement curve and may yield less precise results for materials with history-dependent behavior. In such situations, the arc-length method should be utilized.

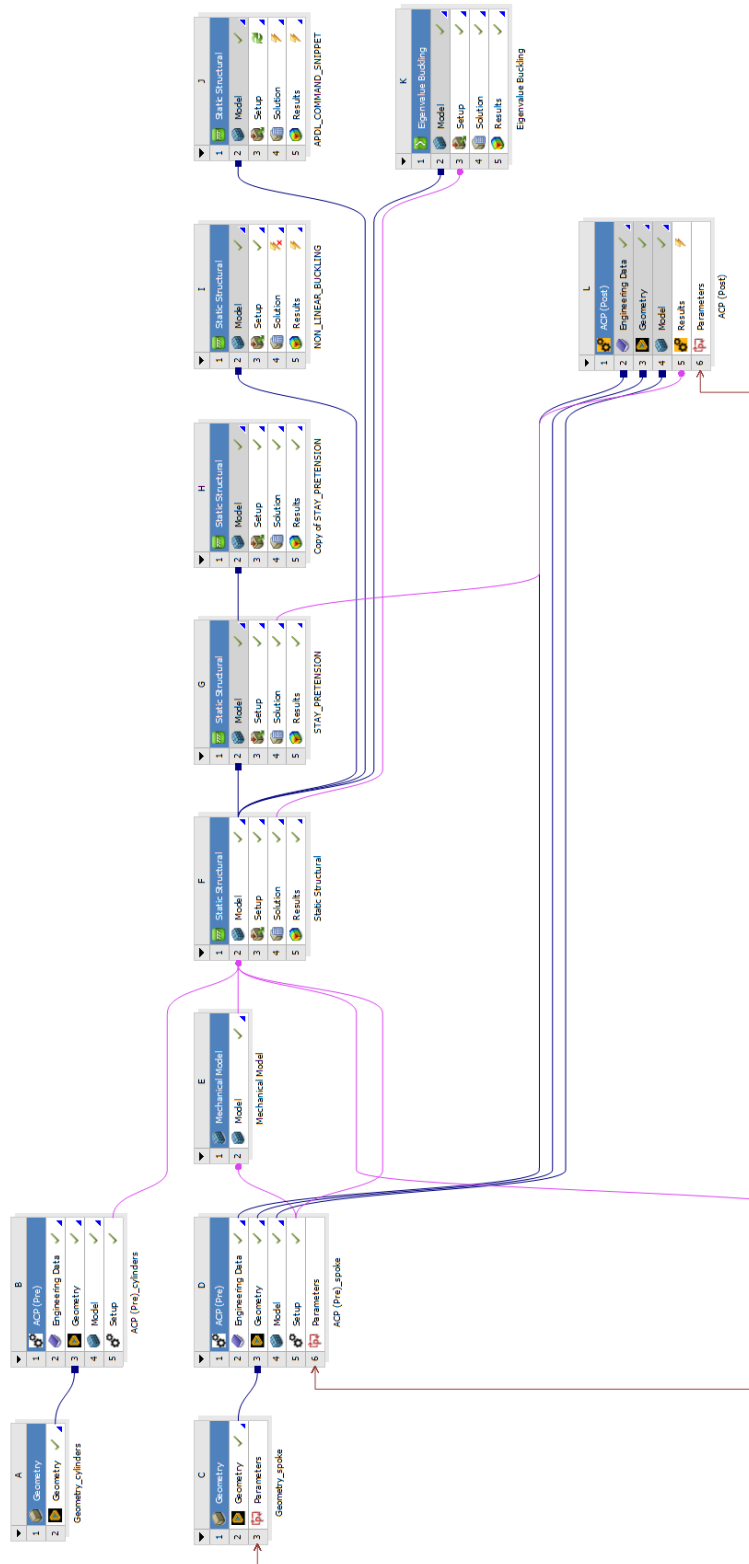


Figure 9.13: Schematic for the workflow in the ANSYS Workbench to perform Nonlinear buckling Analysis

## 9.4 Results from Nonlinear buckling analysis

The schematic to perform Nonlinear buckling or more precisely Nonlinear geometric analysis for composites is shown below (Figure 9.13). A very small time step was used and stabilization was turned on and a constant damping was introduced. The pressure used (0.65 MPa) was slightly higher than that predicted by linear buckling analysis. The results are shown from Figure 9.14-9.18

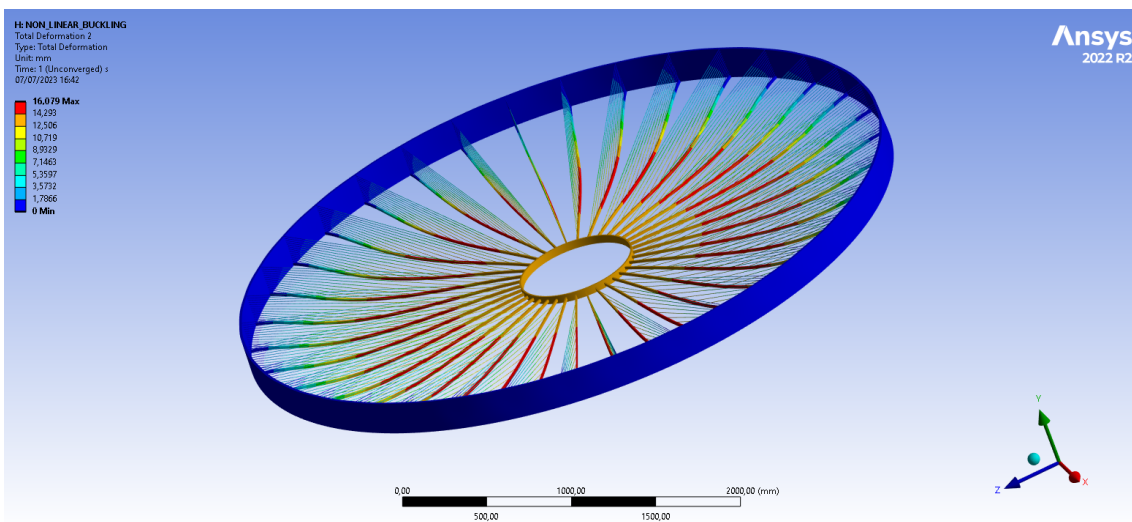


Figure 9.14: Total deformation of the drift chamber with full application of load of 0.65 MPa. A very large deflection can be seen as we are also looking at a post buckling stage.

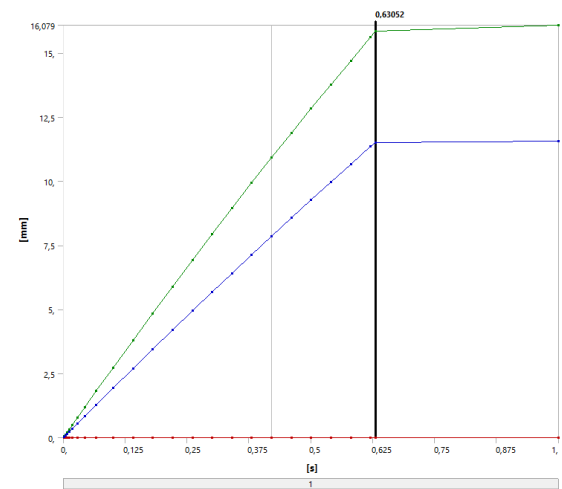


Figure 9.15: Total Deformation history of the structure

## CHAPTER 9. BUCKLING ANALYSIS

Tabular Data				
	Time [s]	✓ Minimum [mm]	✓ Maximum [mm]	✓ Average [mm]
1	2.e-003	0.	5,5096e-002	3,8921e-002
2	4.e-003	0.	0,11016	7,7827e-002
3	7.e-003	0.	0,19271	0,13616
4	1,15e-002	0.	0,31641	0,2236
5	1,825e-002	0.	0,50168	0,35463
6	2,8375e-002	0.	0,77897	0,55087
7	4,3563e-002	0.	1,1935	0,84455
8	6,6344e-002	0.	1,8121	1,2835
9	0,10052	0.	2,7327	1,9384
10	0,14052	0.	3,7989	2,6995
11	0,18052	0.	4,8527	3,4546
12	0,22052	0.	5,8939	4,2036
13	0,26052	0.	6,9225	4,9464
14	0,30052	0.	7,9383	5,6829
15	0,34052	0.	8,9412	6,4131
16	0,38052	0.	9,9313	7,137
17	0,42052	0.	10,909	7,8544
18	0,46052	0.	11,873	8,5653
19	0,50052	0.	12,825	9,2697
20	0,54052	0.	13,764	9,9677
21	0,58052	0.	14,691	10,659
22	0,62052	0.	15,605	11,344
23	0,63052	0.	15,833	11,514
24	1.	0.	16,079	11,549

Figure 9.16: Tabular data: Deformation history

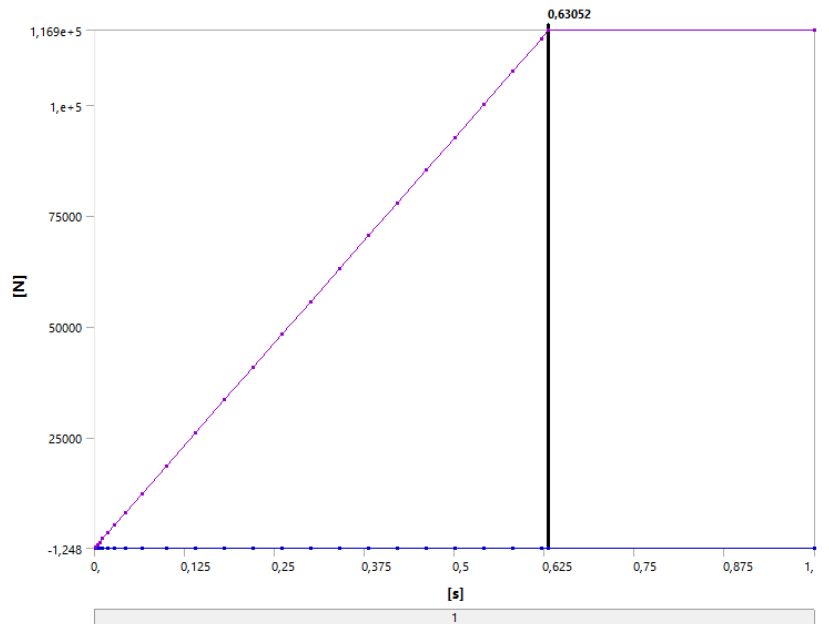


Figure 9.17: Total load history of the structure. At time 0.63 the load is 116000 N. This is slightly lower than that predicted by linear buckling theory.

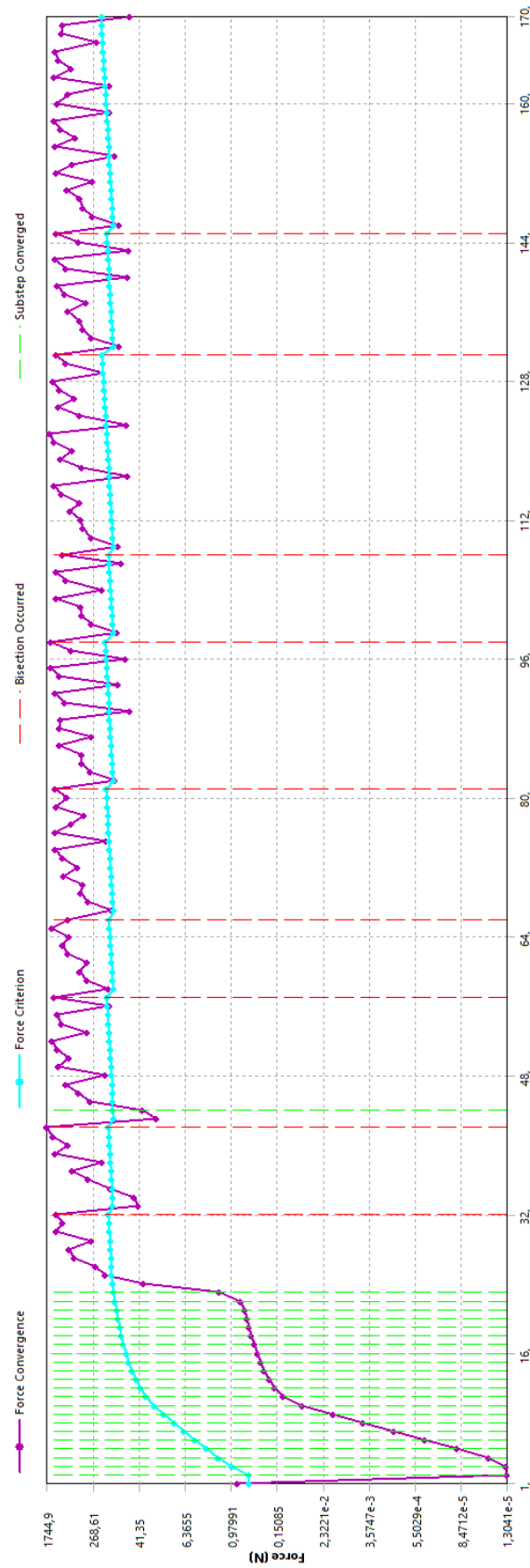


Figure 9.18: Force Convergence graph showing multiple substeps converged and bisections

## 9.5 Conclusion

The buckling loads obtained from both the linear and nonlinear approaches exhibit a certain level of consistency. However, it is crucial to conduct further investigations and gain a comprehensive understanding of our structure in order to validate these results effectively. The buckling characteristics of both the outer cylinders and spokes are highly distinctive, and their interaction holds significant importance. As the structure evolves, their buckling modes undergo significant variations. Therefore, despite having conducted numerically accurate buckling analysis, a more rigorous human understanding of the problem is required to ensure the reliability and accuracy of our findings.



# Chapter 10

## Conclusions

The design and analysis of the drift chamber for subatomic particle detection present exciting challenges that demand exceptional precision to achieve accurate results. Throughout our study, our main goal was to limit the deformation of the spokes to 200 microns while ensuring the structural integrity. Although the structure exhibited a deformation of 600 microns, falling short of our goal by 400 microns, our research has yielded valuable insights and advancements in the design and analysis of the drift chamber.

To overcome these challenges, we embraced a comprehensive approach that involved utilizing a monolithic equivalent material based on composite laminate theory. This not only provided us with an optimal and elegant design solution but also significantly reduced the simulation time, enhancing efficiency and productivity. Through numerical simulations and a preliminary design exploration using statistical concepts, we made iterative improvements to optimize the design and accurately captured the response of the drift chamber—an achievement that would have been inconceivable within a composite design structure.

To further mitigate deflection, we introduced the concept of cable prestressing and employed an evolutionary algorithm for optimization of these cable prestressing forces. Despite the highly nonlinear and sensitive nature of the problem, we successfully found

suboptimal values and also got an insight into the complexity of the problem. We recognize that during the initial preliminary design phase, such significant computational power would be wasted in the pursuit of limiting the deformation of spokes to 200 microns especially when the solution is highly sensitive to boundary conditions. However, several alternative approaches, including prestressing of spokes, can be done in the future design phases.

Even though our main focus was on limiting the deformation, we also conducted thorough investigations into various composite failure criteria ensuring the structural integrity of the drift chamber and in some cases also anticipate potential failure modes. An extensive linear and nonlinear buckling analysis is also done to anticipate probable failure modes. However, we also agree that a thorough understanding of our composite structure is necessary. Based on our comprehensive analysis, we confidently assert that the structure is safe and capable of withstanding the loads it will encounter.

Although we did not fully achieve the ambitious goal of limiting deformation to 200 microns, we celebrate the significant progress we have made in advancing the design and analysis of the drift chamber.

# Bibliography

- [1] Jost B Jonas et al. “Human optic nerve fiber count and optic disc size.” In: *Investigative ophthalmology & visual science* 33.6 (1992), pp. 2012–2018.
- [2] Hermann Kolanoski and Norbert Wermes. *Particle Detectors: Fundamentals and Applications*. Oxford University Press, USA, 2020.
- [3] Carl D. Anderson. “The Positive Electron”. In: *Phys. Rev.* 43 (6 Mar. 1933), pp. 491–494. DOI: 10.1103/PhysRev.43.491. URL: <https://link.aps.org/doi/10.1103/PhysRev.43.491>.
- [4] V. E. Barnes et al. “Observation of a Hyperon with Strangeness Minus Three”. In: *Phys. Rev. Lett.* 12 (8 Feb. 1964), pp. 204–206. DOI: 10.1103/PhysRevLett.12.204. URL: <https://link.aps.org/doi/10.1103/PhysRevLett.12.204>.
- [5] IX-B Garcia Ferreira, J Garcia Herrera, and L Villaseñor. “The Drift Chambers Handbook, introductory laboratory course (based on, and adapted from, AH Walenta’s course notes)”. In: *Journal of Physics: Conference Series*. Vol. 18. 1. IOP Publishing. 2005, p. 346.
- [6] Walter Blum, Werner Riegler, and Luigi Rolandi. *Particle detection with drift chambers*. Springer Science & Business Media, 2008.
- [7] William R Leo. *Techniques for nuclear and particle physics experiments: a how-to approach*. Springer Science & Business Media, 2012.
- [8] Walaa Elmetenawee et al. “The Tracking performance for the IDEA drift chamber”. In: *arXiv preprint arXiv:2211.12568* (2022).

## BIBLIOGRAPHY

---

- [9] GF Tassielli, IDEA Collaboration, et al. “A proposal of a drift chamber for the IDEA experiment for a future  $e^+ e^-$  collider”. In: *40th International Conference on High Energy Physics*. 2021, p. 877.
- [10] Federica Cuna et al. “A proposal of a He based Drift Chamber as central tracker for the IDEA detector concept for a future  $e^+ e^-$  collider”. In: *The European Physical Society Conference on High Energy Physics. 26-30 July 2021. Online conference*. 2022, p. 786.
- [11] Klaus-Jürgen Bathe. *Finite element procedures*. Klaus-Jurgen Bathe, 2006.
- [12] Junuthula Narasimha Reddy. *Introduction to the finite element method*. McGraw-Hill Education, 2019.
- [13] Alexander Hrennikoff. “Solution of problems of elasticity by the framework method”. In: (1941).
- [14] Frank Williamson Jr. “An historical note on the finite element method”. In: *International Journal for Numerical Methods in Engineering* 15.6 (1980), pp. 930–934.
- [15] John H Argyris and Sydney Kelsey. *Energy theorems and structural analysis*. Vol. 60. Springer, 1960.
- [16] Ray W Clough. “The finite element in plane stress analysis”. In: *Proc. 2<sup>nd</sup> ASCE Confer. On Electric Computation, 1960* (1960).
- [17] Wing Kam Liu, Shaofan Li, and Harold S Park. “Eighty years of the finite element method: Birth, evolution, and future”. In: *Archives of Computational Methods in Engineering* 29.6 (2022), pp. 4431–4453.
- [18] Charles L Fefferman. “Existence and smoothness of the Navier-Stokes equation”. In: *The millennium prize problems 57* (2000), p. 67.
- [19] Steven H Strogatz. *Sync: How order emerges from chaos in the universe, nature, and daily life*. Hachette UK, 2012.
- [20] SP Venkateshan and Prasanna Swaminathan. *Computational methods in engineering*. Elsevier, 2013.

## BIBLIOGRAPHY

---

- [21] Steven Strogatz. *Infinite powers: how calculus reveals the secrets of the universe*. Eamon Dolan Books, 2019.
- [22] Wikipedia. *Differential equation* — *Wikipedia, The Free Encyclopedia*. <http://en.wikipedia.org/w/index.php?title=Differential%20equation&oldid=1148753245>. [Online; accessed 16-April-2023]. 2023.
- [23] Wikipedia. *Finite element method* — *Wikipedia, The Free Encyclopedia*. <http://en.wikipedia.org/w/index.php?title=Finite%20element%20method&oldid=1144717530>. [Online; accessed 17-April-2023]. 2023.
- [24] C Meyer. “Lunar regolith”. In: *NASA Lunar Petrographic Educational Thin Section Set 46* (2003).
- [25] William F Rogers. *Apollo experience report: lunar module landing gear subsystem*. Tech. rep. 1972.
- [26] WR Rogers. “The Rogers’ Commission Report on the Space Shuttle Challenger Accident”. In: *US Government Accounting Office* (1987).
- [27] Mishap Investigation Board. *Mars Climate Orbiter Mishap Investigation Board Phase I Report November 10, 1999*. 1999.
- [28] Wikipedia. *Sparse matrix* — *Wikipedia, The Free Encyclopedia*. <http://en.wikipedia.org/w/index.php?title=Sparse%20matrix&oldid=1149912340>. [Online; accessed 16-April-2023]. 2023.
- [29] Ansys Inc. *ANSYS Mechanical User’s Guide*. 2019.
- [30] Alan George and Joseph W Liu. *Computer solution of large sparse positive definite*. Prentice Hall Professional Technical Reference, 1981.
- [31] Amit Amritkar et al. “Recycling Krylov subspaces for CFD applications and a new hybrid recycling solver”. In: *Journal of Computational Physics* 303 (2015), pp. 222–237.
- [32] G Mahinthakumar and S Ratnajeevan H Hoole. “A parallelized element by element Jacobi conjugate gradients algorithm for field problems and a comparison with other schemes”. In: *Applied Electromagnetics in Materials* 1.1 (1990), pp. 15–26.

## BIBLIOGRAPHY

---

- [33] Miklos Gyimesi and J Douglas Lavers. “Generalized potential formulation for 3-D magnetostatic problems”. In: *IEEE transactions on magnetics* 28.4 (1992), pp. 1924–1929.
- [34] Averill M Law. “A tutorial on design of experiments for simulation modeling”. In: *2017 Winter Simulation Conference (WSC)*. IEEE. 2017, pp. 550–564.
- [35] Douglas C Montgomery. *Design and analysis of experiments*. John wiley & sons, 2017.
- [36] Haitao Liu, Yew-Soon Ong, and Jianfei Cai. “A survey of adaptive sampling for global metamodeling in support of simulation-based complex engineering design”. In: *Structural and Multidisciplinary Optimization* 57 (2018), pp. 393–416.
- [37] Jason L Loeppky, Jerome Sacks, and William J Welch. “Choosing the sample size of a computer experiment: A practical guide”. In: *Technometrics* 51.4 (2009), pp. 366–376.
- [38] LE Scales. *Introduction to non-linear optimization*. Springer-Verlag, 1985.
- [39] Thomas V Mikosch, Sidney I Resnick, and Stephen M Robinson. *Springer Series in Operations Research and Financial Engineering*. 2006.
- [40] Dan Simon. *Evolutionary optimization algorithms*. John Wiley & Sons, 2013.
- [41] Simon Ronald. “Duplicate genotypes in a genetic algorithm”. In: *1998 IEEE International Conference on Evolutionary Computation Proceedings. IEEE World Congress on Computational Intelligence (Cat. No. 98TH8360)*. IEEE. 1998, pp. 793–798.
- [42] Bhagwan D Agarwal, Lawrence J Broutman, and CW Bert. “Analysis and performance of fiber composites”. In: (1981).
- [43] Wikipedia. *Composite material* — *Wikipedia, The Free Encyclopedia*. <http://en.wikipedia.org/w/index.php?title=Composite%20material&oldid=1156495959>. [Online; accessed 23-June-2023]. 2023.
- [44] Lauge Fuglsang Nielsen. *Composite materials: properties as influenced by phase geometry*. Springer Science & Business Media, 2005.

## BIBLIOGRAPHY

---

- [45] Daniel Gay. *Composite materials: design and applications*. CRC press, 2022.
- [46] CompositesLab. *History of Composites*. <https://compositeslab.com/composites-101/history-of-composites/index.html>. Accessed July 2, 2023.
- [47] Autar K Kaw. *Mechanics of composite materials*. CRC press, 2005.
- [48] Robert M Jones. *Mechanics of composite materials*. CRC press, 2018.
- [49] Valery V Vasiliev and Evgeny V Morozov. *Mechanics and analysis of composite materials*. Elsevier, 2001.
- [50] Vincent KS Choo. *Fundamentals of composite materials*. Knowen Academic Press, 1990.
- [51] L Kachanov. *Delamination buckling of composite materials*. Vol. 14. Springer Science & Business Media, 2012.
- [52] Young W Kwon, David H Allen, and Ramesh Talreja. *Multiscale modeling and simulation of composite materials and structures*. Vol. 47. Springer, 2008.
- [53] Alberto Carpinteri. *Advanced structural mechanics*. CRC Press, 2017.